Numerical Modelling for Underwater Excavation Process

A Method Based on DEM and FVM

Chen, X.

DOI
10.4233/uuid:40af58ca-9f3b-491f-8f21-998b45bfecb8

Publication date
2021

Document Version
Final published version

Citation (APA)
Chen, X. (2021). *Numerical Modelling for Underwater Excavation Process: A Method Based on DEM and FVM.* [Dissertation (TU Delft), Delft University of Technology]. https://doi.org/10.4233/uuid:40af58ca-9f3b-491f-8f21-998b45bfecb8

Numerical Modelling for Underwater Excavation Process

A Method Based on DEM and FVM

Numerical Modelling for Underwater Excavation Process

A Method Based on DEM and FVM

Proefschrift

ter verkrijging van de graad van doctor
aan de Technische Universiteit Delft,
op gezag van de Rector Magnificus Prof. dr. ir. T.H.J.J. van der Hagen,
voorzitter van het College voor Promoties,
in het openbaar te verdedigen op donderdag 1 april 2021 om 10:00 uur

door

Xiuhan CHEN

Master of Science in Offshore and Dredging Engineering,
Technische Universiteit Delft, Nederland
geboren te Jurong, China.

Dit proefschrift is goedgekeurd door de

promotor: Prof. dr. ir. C. van Rhee
promotor: Dr. ir. S.A. Miedema

Samenstelling promotiecommissie:

Rector Magnificus,	voorzitter
Prof. dr. ir. C. van Rhee,	Technische Universiteit Delft, promotor
Dr. ir. S.A. Miedema,	Technische Universiteit Delft, promotor
Onafhankelijke leden:	
Prof. dr. ir. D. A. Abbink,	Technische Universiteit Delft
Prof. dr. S. Fan,	Technische Universiteit Wuhan, China
Prof. dr. ir. A. Bezuijen,	Universiteit Gent, België
Dr. ir. D. L. Schott,	Technische Universiteit Delft
Dr. V. Magnanimo,	Universiteit Twente
Prof. dr. M. A. Hicks,	Technische Universiteit Delft, reservelid

Keywords: Discrete Element Modelling, Excavation Process, DEM-FVM Coupling
Printed by: Ridderprint | www.ridderprint.nl
Front & Back: Simulation of 3D dynamic underwater excavation process

ISBN 978-94-6384-204-4

An electronic version of this dissertation is available at
http://repository.tudelft.nl/.

For my father

Contents

Summary

More than 70% of the surface of our planet Earth is covered with water. Most people live near the interface between the water and land. People use the sea for transportation, but people also protect themselves from the sea, thus dikes, canals and breakwaters are built. The materials for construction are often obtained from dredging activities.

One of the most important engineering processes in dredging engineering, the underwater excavation process, is studied in this thesis. Up to about 2000, most of the modelling was carried out by either analytical or experimental methods, resulting in many semi-analytical semi-empirical models, on the contrary the development of numerical modelling was relatively slower. Because of the increase of computing power of modern computers, the study methodology has shifted to numerical models in the last decennia. In this thesis, numerical modelling is mainly carried out.

Up to about 2010, there was already the possibility of simulating fluids with Computational Fluid Dynamics (CFD) and solids with Discrete Element Method (DEM), but a real combination was not yet established. Therefore the main focus of this thesis is combining CFD and DEM. For the underwater excavation process, three types of materials are considered, which are sand, cohesive soil and rock. DEM is applied to simulate the mechanical behaviour of these three solid materials. It models the sand, cohesive soil and rock as an assembly of a large number of 3D particles. Based on their soil mechanical properties, different contact rules are created to govern the force, the velocity and displacement of every particle. To numerically model the underwater environment and the water flow, the most frequently used CFD model, the Finite Volume Method (FVM), is implemented.

The interaction between the solid and fluid phases is realized by a specially designed DEM-FVM coupling mechanism, where the fluid-particle interaction forces, the volume fraction information and the particle information are constantly updated and exchanged. In this way the solid behaviour, the fluid behaviour, and the solid-fluid interaction behaviour considered in the excavation process can all be numerically modelled, which helps the researchers to understand those transient and internal physical processes which might be very difficult to measure in experiments.

In the studies for sand cutting, the analytical model of (Miedema, 2011) shows a shear zone between the undisturbed and disturbed sand. But this phenomenon is not well presented in the normal DEM simulations since the normal DEM spherical particles have the tendency to rotate instead of shearing over each other, because rolling comes with much less resistance. Hence two special treatments are made to suppress the rotation behaviour, one is to use spherical particles with rolling friction and the other is to use a non-spherical particle model with an internal structure of regular tetrahedron. Dry sand cutting simulations are conducted and validated against the experimental results of Hatamura and Chjiiwa (1975, 1976a,b, 1977a,b), where the scaling laws derived from the Miedema (2017) are applied to compare the cutting forces.

Besides, underwater sand cutting simulations are carried out to validate against the experiments of Miedema (2017). The results from both the dry and underwater sand cutting simulations are within acceptable error margins.

Cutting of cohesive soil is fundamentally different from the cutting of sand. The main reason is that sand is cohesionless but holds a significant friction, while in the cutting of cohesive soil the process is dominated by the undrained shear strength and the adhesion, where the latter one represents the external shear strength. In this research project, to numerically model the cutting process of cohesive soil, DEM simulations to determine the mechanical properties of the cohesive soil sample have been firstly conducted, and then the simulations of cutting process in the above- and under- water conditions have been undertaken. The Simplified Johnson-Kendall-Roberts (SJKR) cohesion model is applied to create the desired cohesive DEM particles. The experimental data from the (Hatamura and Chjiiwa, 1975, 1976a,b, 1977a,b) tests are used for the validation of cohesive soil cutting in above-water environment. The numerical results match with the experimental data within acceptable error margin. Results from the underwater cutting simulations are also analysed. It is discovered that the cutting force measured on the cutting blade increases much faster with the cutting speed comparing with the empirical relation on clay cutting from dredging practice. The reason for such a phenomenon is that the permeability of the cohesive DEM soil sample has not been tuned to as low as that of dense clays in nature, which is usually in the range of $10^{-18} \sim 10^{-13}\ m^2$, so significant pressure gradients are imposed between in and out of the pores in the DEM soil sample, resulting in higher cutting forces. Unfortunately there is no experimental data available for validating the underwater cohesive soil cutting simulations. It is however still believed that in the future underwater cohesive soil cutting process can be well simulated with the DEM-FVM coupling method if the permeability of the DEM soil sample has been properly calibrated in advance.

Regarding the implementation of DEM in the dredging-relevant rock cutting process, the general applicability of using DEM to create rock samples, and the calibration of DEM rock samples have been investigated. For testing the general applicability, three types of rock samples, weak, medium strength and strong, are created respectively with DEM and compared with real rocks' mechanical properties. The results show that DEM can be widely applied to simulate the 3D mechanical behaviour of weak, medium strength and very strong rocks. For building up the calibration methodology of DEM rock samples, simulations of uniaxial compression tests and Brazilian tensile tests have been undertaken. Based on the results, relevant scaling laws between the input parameters on the micro scale (DEM particle size) to the output mechanical properties on the macro scale (samples' size) have been established. These works are essential for conducting atmospheric and underwater rock cutting simulations in the future.

In summary, the DEM-FVM coupling method gives people the ability to observe the physics of cutting process on the particle level, in other words, inside the soil. This is a big supplement to experimental and analytical studies. It is thus believed that DEM-FVM coupling provides with a bright future for researchers to understand more physics and to improve the cutting tools as well as the cutting planning of underwater excavation process.

Samenvatting

Meer dan 70% van het oppervlak van onze planeet Aarde is bedekt met water. De meeste mensen wonen in de buurt van het grensvlak tussen water en land. Mensen gebruiken de zee voor transport, maar mensen beschermen zichzelf ook tegen de zee, zo worden dijken, kanalen en golfbrekers gebouwd. De materialen voor de bouw worden vaak verkregen uit baggeractiviteiten.

Een van de belangrijkste technische processen in de baggertechniek, het onderwater graafproces, wordt in dit proefschrift bestudeerd. Tot ongeveer 2000 werd de meeste modellering uitgevoerd door analytische of experimentele methoden, wat resulteerde in veel semi-analytische semi-empirische modellen, integendeel, de ontwikkeling van numerieke modellering verliep relatief langzamer. Door de toename van rekenkracht van moderne computers is de studiemethodiek de afgelopen decennia verschoven naar numerieke modellen. In dit proefschrift wordt voornamelijk numeriek modelleren uitgevoerd.

Tot ongeveer 2010 was er al de mogelijkheid om vloeistoffen te simuleren met Computational Fluid Dynamics (CFD) en vaste stoffen met Discrete Element Method (DEM), maar een echte combinatie was nog niet tot stand gekomen. Daarom is de belangrijkste focus van dit proefschrift het combineren van CFD en DEM. Voor het uitgraven onder water worden drie soorten materialen beschouwd, namelijk zand, cohesieve grond en gesteente. DEM wordt toegepast om het mechanische gedrag van deze drie vaste materialen te simuleren. Men modelleert het zand, de cohesieve grond en het gesteente als een samenstel van een groot aantal 3D-deeltjes. Op basis van hun bodemmechanische eigenschappen worden verschillende contactregels opgesteld om de kracht, de snelheid en verplaatsing van elk deeltje te beschrijven. Om de onderwateromgeving en de waterstroom numeriek te modelleren, is het meest gebruikte CFD-model, de Finite Volume Method (FVM), geïmplementeerd.

De interactie tussen de vaste en vloeibare fasen wordt gerealiseerd door een speciaal ontworpen DEM-FVM koppelingsmechanisme, waarbij de vloeistof-deeltje interactiekrachten, de volumefractie-informatie en de deeltjesinformatie constant worden bijgewerkt en uitgewisseld. Op deze manier kunnen het vaste gedrag, het vloeistofgedrag en het vaste-vloeistof-interactiegedrag dat in het opgravingsproces in aanmerking wordt genomen allemaal numeriek worden gemodelleerd, wat de onderzoekers helpt om die voorbijgaande en interne fysische processen te begrijpen die in experimenten moeilijk te meten zijn.

Het analytische model van (Miedema, 2011) laat in de studies voor zandsnijden een afschuifzone zien tussen het ongestoorde en verstoorde zand. Maar dit fenomeen wordt niet goed weergegeven in de normale DEM-simulaties, aangezien de normale DEM-bolvormige deeltjes de neiging hebben om te roteren in plaats van over elkaar heen te schuiven, omdat rollen veel minder weerstand met zich meebrengt. Daarom zijn er twee speciale behandelingen gemaakt om het rotatiegedrag te onderdrukken, de ene is om bolvormige deeltjes met rollende wrijving te gebruiken en de andere is om een niet-

bolvormig deeltjesmodel te gebruiken met een interne structuur van een regelmatige tetraëder. Simulaties van het snijden van droog zand worden uitgevoerd en gevalideerd aan de hand van de experimentele resultaten van Hatamura and Chjiiwa (1975, 1976a,b, 1977a,b), waarbij de schaalwetten afgeleid van de Miedema (2017) worden toegepast om de snijkrachten te vergelijken. Bovendien wordt het snijproces onder water gesimuleerd om dit te valideren tegen de experimenten van Miedema (2017). De resultaten van zowel de droge als de onderwaterzandsimulaties vallen binnen acceptabele foutmarges.

Het snijden van cohesieve grond is fundamenteel anders dan het snijden van zand. De belangrijkste reden is dat zand cohesieloos is maar een aanzienlijke wrijving heeft, terwijl bij het snijden van cohesieve grond het proces wordt gedomineerd door de ongedraineerde afschuifsterkte en de adhesie, waarbij de laatste de externe schuifsterkte vertegenwoordigt. In dit onderzoeksproject zijn, om het snijproces van cohesieve grond numeriek te modelleren, eerst DEM-simulaties uitgevoerd om de mechanische eigenschappen van het cohesieve grondmonster te bepalen, en vervolgens zijn de simulaties van het snijproces in de boven- en onderwateromstandigheden uitgevoerd. Het Simplified Johnson-Kendall-Roberts (SJKR) cohesiemodel wordt toegepast om de gewenste cohesieve DEM-deeltjes te creëren. De experimentele gegevens van de (Hatamura and Chjiiwa, 1975, 1976a,b, 1977a,b) tests worden gebruikt voor de validatie van cohesieve bodemsnijdingen in een bovenwateromgeving. De numerieke resultaten komen overeen met de experimentele gegevens binnen een aanvaardbare foutmarge. Resultaten van de onderwatersnijsimulaties worden ook geanalyseerd. Er is ontdekt dat de snijkracht gemeten op het snijmes veel sneller toeneemt met de snijsnelheid in vergelijking met de empirische relatie met het snijden van klei door het baggeren. De reden voor een dergelijk fenomeen is dat de permeabiliteit van het cohesieve DEM-grondmonster niet zo laag is afgesteld als die van dichte kleien in de natuur, die gewoonlijk in het bereik van $10^{-18} \sim 10^{-13}\ m^2$ zitten, dus er worden aanzienlijke drukgradiënten opgelegd tussen in en uit de poriën in het DEM-grondmonster, wat resulteert in hogere snijkrachten. Helaas zijn er geen experimentele gegevens beschikbaar voor het valideren van de onderwater snijden van klei. Er wordt echter nog steeds aangenomen dat in de toekomst het het snijproces van cohesieve grond onder water goed kan worden gesimuleerd met de DEM-FVM-koppelingsmethode als de permeabiliteit van het DEM-bodemmonster van tevoren goed is gekalibreerd.

Met betrekking tot de implementatie van DEM voor het baggeren van gesteente (rots), zijn de algemene toepasbaarheid van het gebruik van DEM om gesteentemonsters te maken, en de kalibratie van DEM-gesteentemonsters onderzocht. Om de algemene toepasbaarheid te testen, worden drie soorten gesteentemonsters, zwak, gemiddeld sterk en sterk, gemaakt met respectievelijk DEM en vergeleken met de mechanische eigenschappen van echte stenen. De resultaten laten zien dat DEM op grote schaal kan worden toegepast om het 3D-mechanische gedrag van zwakke, middelsterke en zeer sterke rotsen te simuleren. Voor het opbouwen van de kalibratiemethodologie van DEM-gesteentemonsters zijn simulaties van uniaxiale compressietests en Braziliaanse trektests uitgevoerd. Op basis van de resultaten zijn relevante schaalwetten vastgesteld tussen de invoerparameters op de microschaal (DEM-deeltjesgrootte) en de mechanische outputeigenschappen op de macroschaal (de grootte van de monsters). Deze werken zijn essentieel voor het uitvoeren van atmosferische en onderwater simulaties van gesteente in de toekomst.

Samenvattend geeft de DEM-FVM-koppelingsmethode mensen de mogelijkheid om de fysica van het snijproces op deeltjesniveau, met andere woorden, in de bodem te observeren. Dit is een belangrijke aanvulling op experimentele en analytische studies. Er wordt dus aangenomen dat DEM-FVM-koppeling een mooie toekomst biedt voor onderzoekers om meer fysica te begrijpen en om de snijgereedschappen te verbeteren, evenals de snijplanning van het onderwateropgravingsproces.

List of Symbols

Roman symbol	Description	unit
a	Adhesive shear stress, adhesion	$[kPa]$
A	Area of the cross-section of the parallel bond	$[m^2]$
A'_b	Value of any field A' at position $\vec{r_b}$	[-]
A_p	Inter-particle overlap area	$[m^2]$
A_{plate}	Area of the loading and bottom plates in the UCS tests	$[m^2]$
$A'(\vec{r})$	Interpolated value of any field A' at position $\vec{r}$ in SPH	[-]
A_{ring}	Contact surface between the rings and the soil in the ring shear test	$[m^2]$
c	Cohesive shear strength of the soil, cohesion	$[kPa]$
c_d	Dynamic cohesive shear strength	$[kPa]$
c_{DEM}	Cohesive shear strength of the cohesive soil sample in DEM simulations	$[kPa]$
$c_{H\&C}$	Cohesive shear strength of the cohesive soil in the Hatamura & Chijiiwa experiments	$[kPa]$
c_t	Non-corrected dimensionless cutting force in underwater sand cutting	[-]
c'_t	Corrected dimensionless cutting force in underwater sand cutting	[-]
$\mathbf{c}_{new}$	Candidate positions for the new sphere's center in the (Lozano et al., 2016) method	$[m]$
C_d	Drag coefficient for fluid-solid interactions	[-]
C_f	Compressibility of the fabric, Eq. (2.1)	$[m^2/N]$
C_s	Compressibility of the solids, Eq. (2.1)	$[m^2/N]$
C_w	Compressibility of the porewater, Eq. (2.1)	$[m^2/N]$
d	Contact distance between two particles	$[m]$
d_*	Critical cutting depth	[-]
d_{avg}, D_{avg}	Average particle diameter	$[mm]$
d_{max}	Maximum particle diameter	$[mm]$
d_{min}	Minimum particle diameter	$[mm]$
d_p, D_p	Particle diameter	$[m]$
d_{50}	Medium diameter of the particles	$[m]$
D_w	Diffusion coefficient of water pressure, Eq. (2.1)	$[m^2/s]$
e	Coefficient of restitution	[-]

E	Young's Modulus of the rock sample obtained from the UCS tests	$[MPa]$
E'	Apparent Young's modulus of the assembly (2D)	$[N/m^2]$
E_b	Young's modulus of the Timoshenko beam bond element	$[MPa]$
E_c	Young's modulus of the contact between not-bonded particles	$[Pa]$
$\bar{E}_c$	Young's modulus of the bonding beam in PBM	$[Pa]$
E_p	Young's modulus of DEM particle	$[MPa]$
E_{sp}	Specific cutting energy	$[MJ/m^3$ or $MPa]$
E_{steel}	Young's modulus of steel	$[GPa]$
$\vec{f}_B$	Basset force	$[N]$
$\vec{f}_{c,ij}$	Inter-particle elastic force	$[N]$
$\overline{f}_d$	Spatial-averaged drag force	$[N]$
$\vec{f}_{d,i}$	Drag force on particle i	$[N]$
$\vec{f}_{d,ij}$	Viscous damping force between particles	$[N]$
$\vec{f}_i^{\,m}$	Sum of other particle–fluid interaction forces on particle i	$[N]$
f_m	Targeted fraction of $\bar{F}_a$ in Eq. (3.49)	[-]
$\vec{f}_{Mag}$	Magnus force	$[N]$
$\overline{f}_{\nabla p}$	Spatial-averaged pressure gradient force	$[N]$
$\vec{f}_{\nabla p,i}$	Pressure gradient force on particle i	$[N]$
$\vec{f}_{pf,i}$	Particle(solid)–fluid interaction force applied on particle i	$[N]$
$\vec{f}_{Saff}$	Lift force	$[N]$
$\vec{f}_{vm}$	Virtual mass	$[N]$
$\overline{f}_{\nabla\cdot\tau}$	Spatial-averaged viscous force	$[N]$
$\vec{f}_{\nabla\cdot\tau,i}$	Viscous force on particle i	$[N]$
$\bar{F}_a$	Mean contact normal force for the assembly	$[N]$
F_c	Total cutting force on the wedge, Eq. (2.2)	$[N]$
F_{clay}	Clay cutting force in dredging practice	$[N]$
F_{co}	Additional attractive normal force to particles in contact according to the SJKR model	$[kN]$
F_{ct}	Non-corrected overall cutting force for underwater sand cutting	$[N]$
F'_{ct}	Corrected overall cutting force for underwater sand cutting	$[N]$
F_h	Horizontal cutting force on the blade	$[N]$
F_{hz}	Contact force between two particles according to the Hertzian model	$[N]$
F_n	Normal force between two contacting particles	$[N]$

$\bar{F}_n$	Contact force in the normal direction in the bond	$[N]$
$F^{n(c)}$	Normal component of the force acting at contact (c) of particle p	$[N]$
$\bar{F}_p$	Mean contact normal force for single particle	$[N]$
$\bar{F}_s$	Contact force in tangential direction in the bond	$[N]$
$\vec{F}_{pf}^{setI}$	Source term used in the *Set I* fluid momentum equations	$[N/m^3]$
$\vec{F}_{pf}^{setII}$	Source terms used in the *Set II* fluid momentum equations	$[N/m^3]$
$\vec{F}_{pf}^{setIII}$	Source terms used in the *Set III* fluid momentum equations	$[N/m^3]$
F_{tan}	Tangential force between two contacting particles	$[N]$
F_v	Vertical cutting force on the blade	$[N]$
g	Gravitational acceleration	$[m/s^2]$
G^*	Effective shear modulus of the contact	$[MPa]$
G_b	Shear modulus of the Timoshenko beam bond element	$[MPa]$
G_p	Shear modulus of the DEM particle	$[MPa]$
G_v	Gravity force of the shear layer	$[N]$
G_1, G_2	Shear modulus of the two contacting particles	$[MPa]$
h'	SPH interpolation length	[m]
h_b	Blade height	$[m]$
$h_{b,DEM}$	Blade height in DEM simulations	$[m]$
$h_{b,H\&C}$	Blade height in the Hatamura & Chijiiwa experiments	$[m]$
h_{bs}	Sample height of the bottom half in the ring shear test	$[m]$
h_i	Cutting depth	$[m]$
$h_{i,H\&C}$	Cutting depth in the Hatamura & Chijiiwa experiments	$[m]$
$h_{i,DEM}$	Cutting depth in DEM simulations	$[m]$
h_{ts}	Sample height of the top half in the ring shear test	$[m]$
H	Hysteresis factor in Eq. (3.49)	[-]
I	Moment of inertia of the parallel bond cross-section	$[m^4]$
I_i	Moment of inertia of particle i	$[kg \cdot m^2]$
I_p	Moment of inertia of the particle	$[kg \cdot m^2]$
J	Polar moment of inertia of the parallel bond cross-section	$[m^4]$
k_c	Number of particles in interaction with particle i	[-]
k_{hydra}	Hydraulic conductivity, Eq. (2.1)	$[m/s]$

$\bar{k}_n$	PBM bond stiffness in the normal direction	$[N/m^3]$
k_n	Elastic constant for the normal contact, Eq. (3.1)	$[N/m]$
$\bar{k}_s$	PBM bond stiffness in the shear direction	$[N/m^3]$
k_t	Elastic constant for the tangential contact, Eq. (3.1)	$[N/m]$
K	Cohesion energy density	$[kPa]$
K_a	Adhesion energy density	$[kPa]$
K_{exp}	Hydraulic conductivity from laboratory measurements	$[m/s]$
K_{Ic}	Material toughness of 2D DEM sample	$[N/m]$
K_i	Initial hydraulic conductivity before cutting	$[m/s]$
K_m	Weighted average hydraulic conductivity during cutting	$[m/s]$
K_{max}	Maximum hydraulic conductivity in the dilatancy process	$[m/s]$
K_n	Circular disc contact stiffness in normal direction, Eq. (2.8)	$[N/m^2]$
K_{num}	Hydraulic conductivity from numerical modelling	$[m/s]$
$K^{n(c)}$	Normal stiffness at contact (c)	$[N/m]$
K_s	Circular disc contact stiffness in shear direction, Eq. (2.8)	$[N/m^2]$
K_{sand}	Hydraulic conductivity of sand sample	$[m/s]$
K_{sf}	Solid-fluid momentum exchange coefficient	$[N \cdot s/m^4]$
ℓ	Characteristic length of the material	[-]
l_b	Blade length	$[m]$
l_s	Sample length	$[m]$
L	Assembly length, Eq. (2.8)	$[m]$
L_{AB}	Distance between contacting particle A and B	$[m]$
m	Ductility number / the brittleness index (BI)	[-]
m^*	Effective mass of the contact	$[kg]$
m_b	Mass of the SPH particle b	$[kg]$
m_i	Mass of particle i	$[kg]$
m_R	Multiplication factor for the particles' radii	[-]
m_1, m_2	Masses of the two contact particles	$[kg]$
M_m	Influence of the surface tension force on the mixture	$[N/m^3]$
$\bar{M}_n$	Twisting torque of the bond	$[N \cdot m]$
$\vec{M_{r,ij}}$	Rolling friction torque acting on particle i by particle j	$[N \cdot m]$
$\bar{M}_s$	Bending moment of the bond	$[N \cdot m]$
$\vec{M_{t,ij}}$	Torque acting on particle i by particle j generated by the tangential force	$[N \cdot m]$
n	Porosity, fluid volume fraction	[-]

$\vec{n}$	Unit vector for the normal direction of the contact	[-]
n'	Stress distribution factor	[-]
n_{max}	Maximum porosity	[-]
n_i	Initial porosity	[-]
n_p	Number of particles in the UCS test sample	[-]
n_{p1}	Number of particles in the BTS test sample	[-]
n_0	Initial porosity of the generated assembly	[-]
N	Number of particles to generate	[-]
N_c	Number of contacts of a particle	[-]
N_p	Number of particles in the assembly	[-]
p	Fluid pressure	$[Pa]$
p_h, P_{hydro}	Hydrostatic pressure	$[Pa]$
P_m	Mixture pressure	$[Pa]$
q	Deviatoric stress of the sample	$[MPa]$
$\vec{q}$	Specific discharge representing the Darcy flow	$[m/s]$
Q_m	Mass flux in sand cutting	$[kg/s]$
r_{ac}	Ratio between adhesion and cohesion	[-]
r_p	Solid particle radius	$[m]$
r_b	Radius of the cross-section of Timoshenko beam bond element	$[m]$
$\vec{r_b}$	Position vector of the SPH particle b	$[m]$
r_{curr}	Radius of the current sphere in the (Lozano et al., 2016) method	$[m]$
r_{halo}	Radius of the spherical halo in the (Lozano et al., 2016) method	$[m]$
r_{inner}	Inner radius of the ring	$[m]$
r_{mean}	Average radius of the ring shear test machine	$[m]$
r_{new}	Radius of the new sphere to be inserted in the (Lozano et al., 2016) method	$[m]$
r_{outer}	Outer radius of the ring	$[m]$
r_s	Radius of the selected current sphere s	$[m]$
r_{50}	Medium radius	$[m]$
$\bar{R}$	Radius of the cross-section of the parallel bond	$[m]$
R^*	Effective radius of the contact	$[MPa]$
R_A, R_B	Radii of two contacting particles	$[m]$
R_{avg}	Average disc radius, Eq. (2.8)	$[m]$
$\tilde{R}^{(c,p)}$	Distance from the contact point (c) to the particle center	$[m]$
R_f	Radius of the floater particle	$[m]$
R_i, R_j	Radius of particle i, particle j	$[m]$
R_{min}, R_{max}	Minimum and maximum radii of the particles	$[m]$
R_n	Nominal radius of the particle	$[m]$
Re_p	Reynolds number of the particle	[-]
R_1, R_2	Radii of the two contacting particles	$[MPa]$
s_u	Undrained shear strength of cohesive soil	$[kPa]$

s_n	Coefficient for calculating the damping constant in normal direction in the Hertzian model	$[N/m]$
s_t	Coefficient for calculating the damping constant in shear direction in the Hertzian model	$[N/m]$
S_h	Horizontal stress on the cutting blade	$[Pa]$
$S_{overall}$	Overall stress on the cutting blade	$[Pa]$
S_t	Transverse stress on the cutting blade	$[Pa]$
S_v	Vertical stress on the cutting blade	$[Pa]$
t	Time	$[s]$
t_c	Time duration when two particles are in contact	$[s]$
t_s	Sample thickness	$[m]$
Δt	Calculation time step	$[s]$
Δt_r	Rayleigh time step	$[s]$
T_c	Constant torque in the ring shear test	$[N \cdot m]$
T_n	Bond strengths in tensile direction, Eq. (2.8)	$[N/m]$
T_s	Bond strengths in shear direction, Eq. (2.8)	$[N/m]$
$Torque_{anti}$	Extra counter-torque contribution to the particles' contact	$[N \cdot m]$
$\vec{u}$	Fluid velocity	$[m/s]$
$\vec{u}_i$	Local fluid velocity around particle i	$[m/s]$
$\vec{u_m}$	Velocity of the centre of gravity of the mixture	$[m/s]$
U_f	Velocity of the fluid	$[m/s]$
U_s	Velocity of the solid	$[m/s]$
ΔU_n	Relative displacement increment in the normal direction in the PBM bond	$[m]$
ΔU_s	Relative displacement increment in the shear direction in the PBM bond	$[m]$
v	Loading speed	$[m/s]$
$\vec{v_b}$	Velocity vector of the SPH particle b	$[m/s]$
v_c	Cutting speed, Eq. (2.1)	$[m/s]$
$\vec{v_i}$	Translational velocity of the particle i	$[m/s]$
$v_{n_{12}}$	Normal component of the relative velocity of the two particles	$[m/s]$
$v_{t_{12}}$	Tangential component of the relative velocity of the two particles	$[m/s]$
V	Loading velocity, Eq. (2.8)	$[m/s]$
ΔV	Volume of a fluid cell	$[m^3]$
V'	A given volume in Eq. (3.45)	$[m^3]$
V_{BA}	Relative velocity of particle B to particle A	$[m/s]$
V_B^c, V_A^c	Velocities of particle B and A at the center of the bonding beam in PBM respectively	$[m/s]$
V_n	Relative normal velocity between the two contacting particles	$[m/s]$
V_p	Volume of the particle	$[m^3]$

$\vec{V}_p$	P-wave propagation velocity	$[m/s]$
$V_{pullout}$	Pull-out speed of the blade in the blade pull-out test	$[m/s]$
V_s	Relative shear velocity between the two contacting particles	$[m/s]$
$\vec{V}_s$	S-wave propagation velocity	$[m/s]$
$V_{1\sim8}$	Volume of the parts of the particle in the porosity calculation	$[m^3]$
w	Width of cutter	$[m]$
$\vec{w}$	Velocity of solids	$[m/s]$
w_s	Width of sample	$[m]$
W	SPH interpolating kernel	[-]
X_μ	Static friction coefficient for particle contacts	[-]
Y^*	Effective Young's modulus of the contact	$[MPa]$
Y_1, Y_2	Young's modulus of the two contacting particles	$[MPa]$

Greek symbol	Description	unit
α, α_c	Blade cutting angle	[-]
α_{ac}	Adhesion factor	[-]
α_b	Modification factor of the Timoshenko beam bond strength	[-]
α_σ	Modification factor of the compressive strength in the Timoshenko beam bond	[-]
α_r	Random number in the Timoshenko beam bond	[-]
α_R	Scale factor for the particles' radii reduction	[-]
α_s	Solid compression coefficient, Eq. (2.1)	[-]
β	Angle of the shear plane in soil cutting	[°]
β_{emp}	Empirical shear angle	[°]
β_f	Compressibility of the fluid	$[pa^{-1}]$
β_{num}	Numerical shear angle	[°]
β_{UCS}	Macroscopic shear angle in the UCS test	[°]
β_γ	Restitution coefficient for calculating the damping constant in the Hertzian model	[-]
γ_n	Viscoelastic damping constant for normal contact	$[kg/s]$
γ_t	Viscoelastic damping constant for tangential contact	$[kg/s]$
γ_w	Specific weight of water, Eq. (2.1)	$[N/m^3]$
Γ_T	Strain vector of the Timoshenko beam bond element	[-]
δ	External friction angle	[°]

δ_{box}	Length of the side of the search box in the (Lozano et al., 2016) method	$[m]$
δ_n	Normal overlap distance of two particles	$[m]$
δ_t	Tangential overlap distance of two particles	$[m]$
ϵ	Average volume strain in the soil	[-]
ϵ_f	Volume fraction of fluid	[-]
ϵ_{vol}	Volumetric strain of the solid skeleton	[-]
$\Delta\theta_n$	Relative rotation increment in the normal direction in the PBM bond	[°]
$\Delta\theta_s$	Relative rotation increment in the shear direction in the PBM bond	[°]
κ	Permeability of the particles' layer	$[m^2]$
κ_i	Initial permeability of soil sample	$[m^2]$
κ_{max}	Maximum permeability of soil sample	$[m^2]$
κ_T	Curvature vector of the Timoshenko beam bond element	[-]
λ	Velocity strengthening factor in cohesive soil	[-]
$\bar{\lambda}$	PBM bond-radius multiplier	[-]
λ_a	Actually measured flaw size	$[m]$
λ_{HD}	Horizontal cutting force coefficients in dry sand cutting	[-]
λ_{HF}	Horizontal cutting force coefficient	[-]
λ_{VD}	Vertical cutting force coefficients in dry sand cutting	[-]
λ_{VF}	Vertical cutting force coefficient	[-]
Λ	Scaled flaw length	$[m]$
μ	Friction coefficient between the discs, Eq. (2.8)	[-]
μ_e	External friction coefficient	[-]
μ_f	Dynamic viscosity of the fluid	$[kg/(m \cdot s)]$
μ_p	Coefficient of internal friction (particle-particle)	[-]
μ_{pb}	Coefficient of external friction (particle-blade)	[-]
μ_{pw}	Coefficient of external friction (particle-wall)	[-]
μ_r	Rolling friction coefficient	[-]
μ_{steel}	Coefficient of internal friction of steel	[-]
ν	Poisson's ratio	[-]
ν'	Apparent Poisson's ratio of the assembly	[-]
ν_f	Kinematic viscosity of fluid	$[m^2/s]$
ν_{steel}	Poisson' s ratio of the steel blade	[-]
ν_p	Poisson' s ratio of DEM particle	[-]
ν_1, ν_2	Poisson's ratio of the two contacting particles	[-]
ξ_{pe}	Pore-Peclet number	[-]
ρ	Density of the disc, Eq. (2.8)	$[Ns^2/m]$
ρ_b	Density of the SPH particle b	$[kg/m^3]$
ρ_f	Fluid density	$[kg/m^3]$

ρ_m	Mixture density	$[kg/m^3]$
ρ_p	Material density of DEM particle	$[kg/m^3]$
ρ_s	Solids density	$[kg/m^3]$
σ	Normal stress on the walls	$[kPa]$
σ_{axial}	Axial stress in the Timoshenko beam bond	$[Pa]$
σ_{break}	Breakage stress of the Timoshenko beam bond	$[Pa]$
σ_c	Compressive strength in 2D	$[N/m]$
σ_c	Compressive strength in 3D	$[MPa]$
σ_{eqv}	Equivalent stress in the Timoshenko beam bond	$[Pa]$
$\bar{\sigma}_{max}$	Maximum tensile stress in the bond in PBM	$[Pa]$
σ_t	Tensile strength of the assembly, rock or soil	$[MPa]$
σ_0	Isotropic stress of the DEM assembly	$[Pa]$
τ	Internal shear stress	$[kPa]$
τ_a	External shear stress between the blade and the soil	$[kPa]$
$\bar{\bar{\tau}}_m$	Mixture shear stress tensor	$[Pa]$
$\bar{\tau}_{max}$	Maximum shear stress in the bond in PBM	$[Pa]$
$\bar{\bar{\tau}}_m^D$	Diffusion stress tensor	$[Pa]$
$\bar{\bar{\tau}}_m^t$	Mixture turbulent shear stress tensor	$[Pa]$
τ_p	Particle relaxation time	$[s]$
τ_{shear}	Shear stress in in the Timoshenko beam bond	$[Pa]$
ϕ	Internal fiction angle	[°]
ϕ^c	Contact radius at contact (c)	$[m]$
ϕ_s	Sphericity of particle	[-]
ψ_p	Coefficient of restitution (particle-particle)	[-]
ψ_{pb}	Coefficient of restitution (particle-blade)	[-]
ω	Rotational speed	$[rad/s]$
ω_A, ω_B	Rotational velocities of the contacting particles A and B respectively	$[rad/s]$
$\vec{\omega}_i$	Angular velocities of the particle i	$[rad/s]$
ω_r	Relative rotational velocity of the 2 particles	$[rad/s]$
$\omega_{r_{shear}}$	Projection of the relative rotational velocity of the 2 particles ω_r into the shear plane	$[rad/s]$
ω_1, ω_2	Rotational velocities of two contacting particles	$[rad/s]$

Abbreviation	Description
BI	Brittleness Index
BTS	Brazilian Tensile Strength
CCZ	Clarion Clipperton Zone
CDT	Constant Directional Torque
CFD	Computational Fluid Dynamics
DEM	Discrete Element Modelling

DPS	Discrete Particle Simulation
DTS	Direct Tensile Strength
FEM	Finite Element Method
FVM	Finite Volume Method
GSI	Geology Strength Index
LES	Large Eddy Simulation
LPT	Lagrangian Particle Tracking
MPI	Message Passing Interface
PBM	Parallel Bond Model
PDEs	Partial Differential Equations
PSD	Particle Size Distribution
REY	Rare Earth Elements and Yttrium
SJKR	Simplified Johnson-Kendall-Roberts
SPH	Smoothed Particle Hydrodynamics
SSI	Simple Sequential Inhibition Model
TBM	Tunnel Boring Machine
UCS	Unconfined Compressive Strength
VTS	Vertical Transport System
2D	Two-dimensional
3D	Three-dimensional

1

Introduction

Under water excavation has been considered as an important engineering process for centuries in the history of humanity. Industries like dredging and offshore drilling engineering have accumulated a lot of experience for conducting and controlling the underwater excavation. Besides in the recent decade, the term "deep sea mining" became a hot topic, which has brought many new challenges for engineering technology. The topic of this thesis, underwater excavation, is also one of the biggest challenges in deep sea mining engineering.

Chapter 1 will introduce the background of this research and the main research objectives, followed by an outline of the whole thesis.

Parts of this chapter have been published in Chen et al. (2014).

1

1.1. Dredging engineering

Dredging engineering nowadays has become a modern industry of billions of Euros turnover per year. According to International Association of Dredging Companies (IADC) (2019), the total turnover of dredging contractors, private and state- or port-owned companies in the open markets was estimated at about € 5.1 billion for 2018. Here below Fig. 1.1 shows the turnovers of dredging industry in the different areas of the world for the year 2017 and 2018.

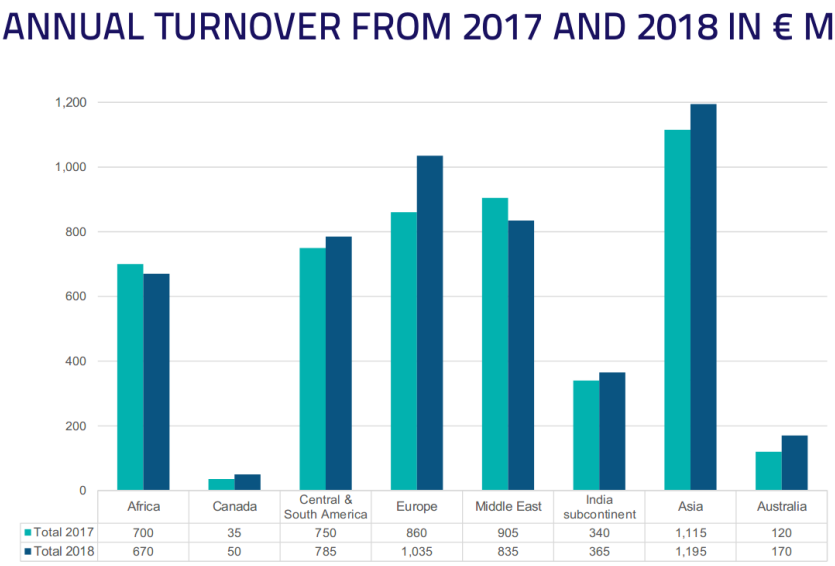

Figure 1.1: A comparison of annual turnover of the dredging industry in the open market from 2017 and 2018 according to geographical area. Source: (International Association of Dredging Companies (IADC), 2019)

During the past 20 years, dredging activities have increased dramatically, especially in Asia and Middle East. After the market booming in the period of 2006-2008, followed by a decreasing market in the years 2010-2012, the industry now has a slow increase of 0.5 to 1.0% in total turnover per year. However, according to a financial analysis from Rabobank International (2013), based on long term outlook, there will be a structural growth in the coming decades, for which, the main driving factors are:

- Growing world population, particularly in coastal areas
- Higher energy and metals consumption
- Increasing seaborne trade, particularly being shipped by larger and larger container vessels
- Growth of global tourism
- Global warming, leading to a rise of the sea level

- The installation and trenching work for offshore wind farms
- Support activities for alternative energy sources, e.g., for wave or tidal energy

All these factors are leading to the result that more land has to be reclaimed and protected, more ports should be constructed or expanded, thus there will be a lot of work for dredging companies in the following decades. Despite the huge volume of dredging industry, the term "dredging" is actually defined merely as a combination of several simple processes. It includes the excavation or loosening, mixing, lifting, transporting, and depositing or dumping of the soil that is fully or partially submerged in water, (Van der Schrieck, 2009). It can be applied for land reclamation, port construction, beach nourishment, coastal protection and etc. As shown in Fig. 1.2, it is the master piece of dredging project in the middle east, "the palm island".

Figure 1.2: Palm Jumeirah, one of the two palm islands. Source: (Wikipedia, 2005)

1.1.1. Cutter suction dredger

Currently there are more than 10 kinds of dredging vessels based on their working mechanism. In large reclamation projects, Trailing Suction Hopper Dredger (TSHD) and Cutter Suction Dredger (CSD) are most widely used. TSHD is initially designed for relatively "soft" seabed condition, e.g. sandy or muddy seabed. Nowadays they can also be used for dredging rocks underwater. The CSD is more frequently used for "harder" excavation tasks, such as when seabed consists of rock or medium to hard clay. Generally speaking, TSHD cuts into the soil by thinner layer but covers larger surface area, and CSD on the contrary cuts into the soil by thicker layer but covers smaller surface area, for example, a maintenance dredging in a canal. Fig. 1.3 shows the cutter suction dredger manufactured by IHC Holland B.V. and now owned by Royal Boskalis Westminster N.V., the "Helios", which gives an example of this kind of dredger.

Basically, cutter suction dredger uses spuds or anchors to keep its position relatively fixed during operation, and it can discharge either into barges or via slurry pipelines to the dumping site. When pipelines are used, booster pumps are also employed to

1

maintain the flow velocity inside the pipe, in this way the slurry can be transported over large distances.

Figure 1.3: The self-propelled cutter suction dredger "Helios" owned by Royal Boskalis Westminster N.V. Source: Boskalis (2017)

In this research, the excavation process is studied based on the tooth on the cutter head of the Cutter Suction Dredger. An example of the cutter head can be seen in Fig. 1.4, this is an T-series rotatory cutter head installed with the third generation cutter teeth, manufactured by VOSTA LMG. It can cut into from soft up to very hard rock, mixed soil, sand and clay, and work under cutter power from 200 kW to 8000 kW.

Figure 1.4: The T-series cutter head installed with the third generation cutter teeth manufactured by VOSTA LMG. Source: VOSTA LMG (2020)

1.2. Deep sea mining engineering and its current state

Deep sea mining, also known as offshore mining, is the engineering process to extract valuable minerals from the seabed soil. The mining sites are usually located at the seabed with more than 1500m water depth, the deepest site could reach more than 6000m water depth. This kind of area could be the deposits of poly-metallic nodules, or the neighbourhood of underwater hydrothermal vents, where massive sulphide deposits are formed up. The massive sulphide deposits consist of a variety of precious metals, such as Zn, Cu, Au, Ag, Mn, Co and etc., also many rare earth elements, for example Th, Lu, La and so on. These materials play very important roles in modern industries. Here below Fig. 1.5 shows the distribution of manganese nodules on the seabed of $4000{\sim}5000m$ water depth in the south Pacific, while Fig. 1.6 shows a seabed hydrothermal vent.

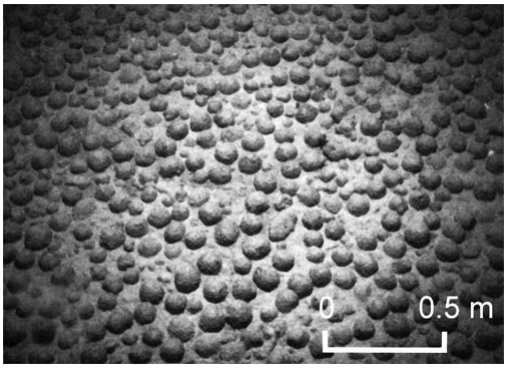

Figure 1.5: Manganese nodules on the seabed of south Pacific. (Wright, 2006)

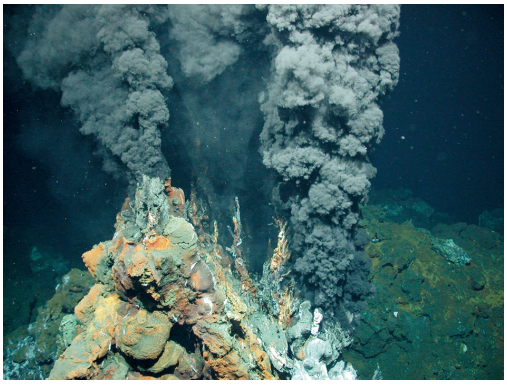

Figure 1.6: Massive sulphides form at black smokers –hot springs on the sea floor with temperatures approaching 400 degrees Celsius. (MARUM, 2010)

Currently, the hotspot of deep sea mining survey and exploitation is the middle and west Pacific regions. Fig. 1.7 has marked out the global distribution of known marine

mineral resources. Many countries have participated in the bidding of exploiting the Clarion-Clipperton Zone (CCZ) in the middle Pacific, as seen in Fig. 1.8. This area is located between the Clarion Fracture and the Clipperton Fracture, the water depth here is around 6000m. The major interest here is the polymetallic nodules.

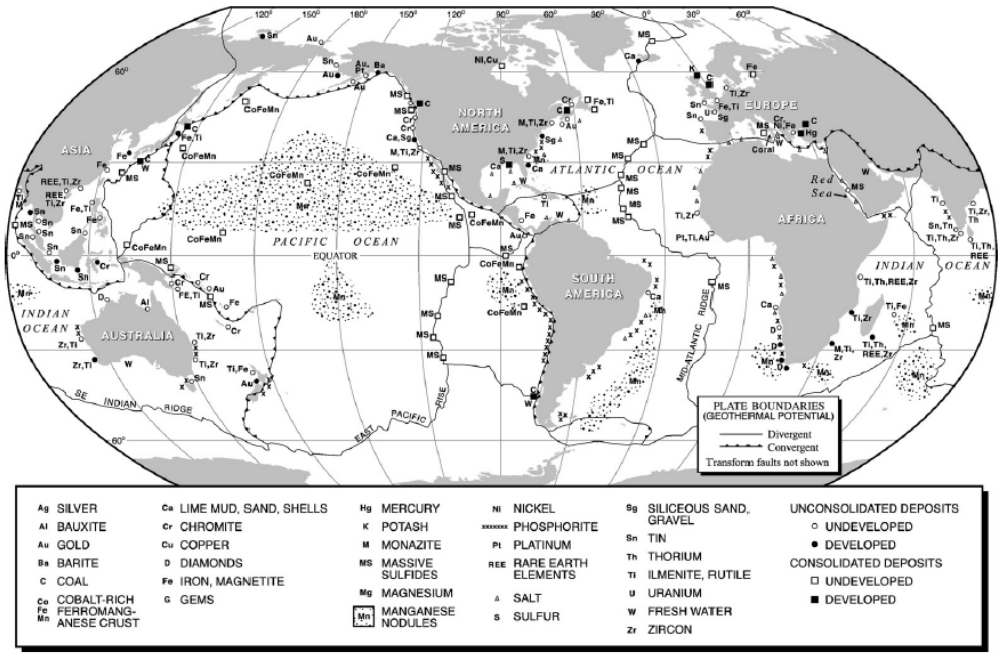

Figure 1.7: Global distribution of known marine mineral resources. (Rona, 2008)

There was a Canadian company, Nautilus Minerals, used to claim that they want to conduct the first deep sea mining project which is called the Solwara 1 Project. This project involves the recovery of high-grade polymetallic Seafloor Massive Sulphide (SMS) deposits at approximately 1600 m water depth on the seabed of the Bismarck Sea, Papua New Guinea. This company did not succeed, it went bankrupt on November 2019. But still a lot of useful information was published by this company before it gets bankrupt. According to Nautilus Minerals, a deep sea mining system would consist of the following components, as shown in Fig. 1.9:

1. A mining support vessel on the sea surface, acting as the controlling center of the whole system and the pre-processing center for the production.
2. Several seafloor mining tools on the seabed, which are moving vehicles with mounted excavation tools. These tools can be with or without the splitting functions, and they are responsible for excavating the seabed soil.
3. Vertical transport system, which transports the produced material from the seabed to sea surface. The system can be a hydraulic transport system so it

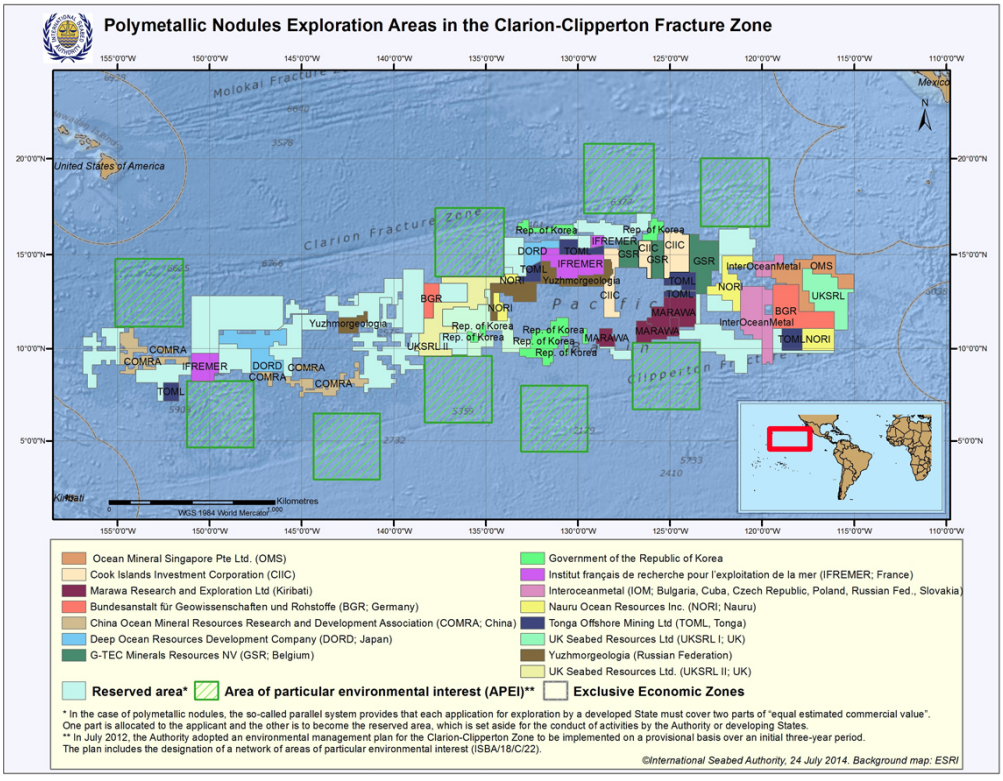

Figure 1.8: Claimed mining sites in Clarion-Clipperton Zone in the middle Pacific. Source: (International Seabed Authority (ISA), 2014)

1

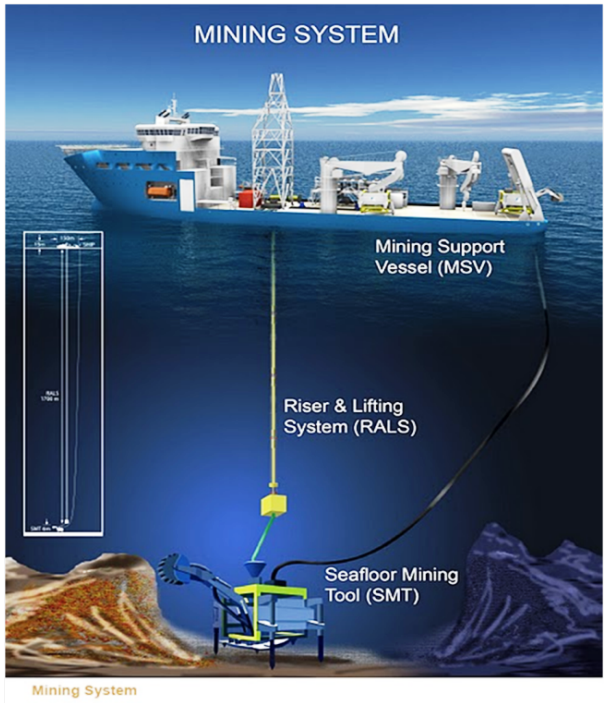

Figure 1.9: Deep sea mining system according to Nautilus Minerals, source: (Gwyther, 2008)

will consist of pipelines an booster pumps, or it can also be a mechanical transport system.
4. Umbilical system, which is responsible for controlling and transporting power from the sea surface to the bed.
5. A shuttle tanker vessel on the sea surface to transport the extracted material to shore.

It should be mentioned that the above listed out items are not fixed, alternative compositions could be to combine or separate some of these functions.

1.3. Technical challenges in the development of deep sea mining

Actually the concept of deep sea mining is not new at all. H.M.S. Challenger (Fig. 1.10), a British navy vessel, had conducted a series of scientific expeditions during 1872~1876. It was found that there are a large amount of polymetallic nodules exist in most oceans of the world.

Figure 1.10: H.M.S. Challenger. (Mitchell, 1881)

It is almost one and half century past since the discovery of rich mineral deposits in the ocean, but why there is still no deep sea mining project (water depth $>$ 1500 m) conducted yet? There are a lot of reasons behind this question, but the main reason is that there are still major technical challenges to be conquered, which will be introduced here.

The first big challenge is the vertical transport of mined material, one of the meth-

ods is hydraulic transport, currently it is the mostly recommended and studied method because it can deliver much higher production rate comparing with the other transport methods. The relevant physics and the possible phenomenons that could occur during vertical hydraulic transport have been discussed by van Wijk (2016). It is mentioned that the sizes and shapes of solid particles in the pipe do play very important roles in flow assurance. Later, Xia (2017) did the vertical slurry transport experiments in lab scale to investigate the possibility to add pneumatic driving into hydraulic transport.

The second challenge is how to provide enough power to the whole system. As shown in Fig. 1.9, the whole deep sea mining system is huge, and most of its components are operating underwater. The seabed excavation system needs huge driving power to cut through the rock of the seafloor, and also needs to make sure the size of the rock fragments are small enough so that they can be successfully transported to the sea surface. Besides that, the vertical riser and lifter system also requires big driving power to lift the mixture of about $1600 kg/m^3$ to the vessel without any blockage or plug formation. Fig. 1.11 shows the comparison of volumes of the underwater excavator and an adult man. These excavation machines weigh between $250 \sim 310$ tons. Till now it is still unclear if the whole system can work smoothly and if energy can be sufficiently transferred to every module of the system.

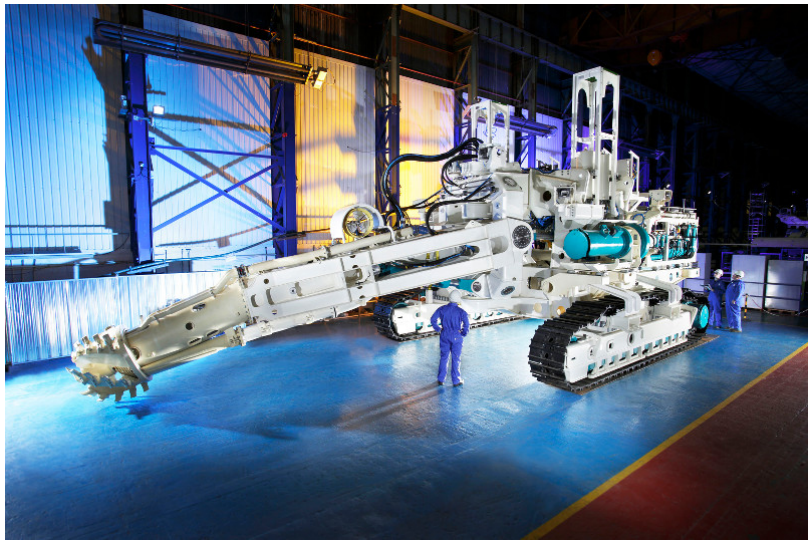

Figure 1.11: The seabed collecting excavator. Source: (Nautilus Minerals, 2016)

The third challenge is to keep the whole system structurally stable, in other words, to conquer the dynamics of the whole system. Operation in deep water means a lot of influence from hydrodynamics. Engineers must consider about all the loadings from wind, wave, current and etc. The motion of the system including all the cables and pipelines should be controlled very well. Besides, the resistance from seabed soil, especially rock, during the excavation process can also induce structural oscillation, which should also be taken into consideration. However, the biggest concern about structural safety is on the riser and lifter system, because it suffers more complex

dynamic excitation, such as slurry flow inside the pipeline, surrounding water, dynamic loads from booster pump stations and vessel motions. These kind of loads would raise up the possibility of instantaneous or fatigue-related failures (Metrikine et al., 2006). Later, to optimize the design, a numerical model is developed by Luo (2015) to calculate and predict the motion and structure behaviour of the riser and lifter system.

The fourth challenge is how to control the environmental impact of the deep sea mining operation. Predicting the environmental impact resulting from mining activities remains challenging, as the knowledge of the environment in deeper waters is relatively scarce. Decades ago, Thiel et al. (1986) made the investigations on the environmental risks for operation in the Red Sea, while Ozturgut et al. (1981) did the case study for the Clarion-Clipperton Zone in the Pacific. Recently, van Grunsven et al. (2016) studied the possible environmental damage caused by the turbidity plumes. The turbidity plumes find their source in the disturbances of the top seabed layer during the excavation process and the discharge of the return water from the vertical transport system. Due to the transport of the current, turbidity plumes may spread over several miles in various directions before achieving full sedimentation or dilution. Some mitigation measures have been proposed, e.g. change the way of discharge from discharging the return water from the deck of the vessel into the surface water to a submerged discharge of the suspended solids to avoid disturbance of the various water column processes.

The fifth challenge is to figure out the cutting process under hyperbaric conditions in deep water. Although the mechanical properties of the seabed mining sites varies a lot in different locations, the chance to encounter hard rock-like materials is still high, for example the cobalt-rich ferromanganese crusts. It is expected that the combination of high hydrostatic pressure and high cutting speed would create a large pressure difference from inside to outside of the rock, so that the cutting force on the blade would be significantly higher than cutting rock in atmospheric condition. The experiments of man-made concretes in hyperbaric chamber by Kuiper et al. (2013) have shown significant correspondence between confining pressure and the strength of the samples.

Apart from the above mentioned technical challenges, there is also a need to improve the legislations regarding deep sea mining, it is known that deep sea mining operations within 200 nautical miles from a country's baseline of the territorial sea should be governed by the domestic laws, while outside 200 nautical miles should then be governed by the International Seabed Authority (ISA) regulations, however some domestics laws do not always match well with the ISA regulations, which leads to potential double standards within one project. Thus, there is a need to set up a standard which can be generally accepted by the international communities, especially with regard to the environmental issues.

None of these challenges, not matter on technology, or on legislation, has been fully solved, but luckily a considerable amount of knowledge has been accumulated on every aspects of deep sea mining.

1

1.4. Problem definition and research procedure

Underwater excavation process plays an important role in dredging, offshore drilling, trenching, and the upcoming deep sea mining engineering. Many researches have been carried out on this topic, mostly experiments and analytical models. However, there are some deficiencies about experiments and analytical models. For a lab scale experiment, it is usually very difficult to record transient behaviours which could be very important, and there are also a lot of difficulties to track the deformation and stress level inside the soil sample, which could be because there is not enough space to place the gauge or the stress level is too high for the equipment. For analytical models, it is known that almost all the analytical solutions are derived based on stationary and two dimensional conditions, while in reality the underwater excavation is a three dimensional and dynamic process involving the interaction of cutting tools, water and soil. The physics in analytical models is often simplified, as well as the geometry of the tools, e.g., in most of the analytical models the cutting blade is assumed to be perfectly sharp.

Until now, there are mainly analytical models for soil cutting, so in order to know more about the internal behaviour of the soil deformation, it is required to develop a new kind of model. In comparison, numerical simulations are able to catch transient behaviours, to monitor the situation internally, and also to run in fully dynamic and three dimensional conditions. So it becomes necessary to develop a numerical model, as a complementary part to the analytical models, which can describe the underwater excavation process into very detailed physics. It is expected that when the numerical model is mature, it can be used to validate and improve the analytical models, and then finally to replace the experiments.

Although analytical models sometimes act like a macroscopic black-box approach, they still have their own advantage. The pros and cons are highlighted in Table 1.1.

Based on the comparison, it is decided that this research project focuses on establishing an intrinsic, three dimensional, dynamic numerical model. The deliverable will be a numerical model that can model the mechanical behaviour of sand, cohesive soil and rock, as well as their interactions with water and the mechanical tools. This model shall be able to calculate the pore water pressure and the fluid velocity field. To achieve that, the coupling mechanism between Discrete Element Modelling (DEM) and Finite Volume Method (FVM) is adopted. It is believed that this DEM-FVM coupling can describe the interaction of the cutting tools, the water and the seabed soil in a more meticulous manner. The procedure of this research is listed as following:

- First there is the literature study to gather the knowledge and basic understanding in the excavation process. The focus is to analyse the state-of-the-art solutions, from the perspectives of the physics and also the availability of the tools.
- Knowledge gained from literature study will be combined and processed to form

Table 1.1: Comparison between numerical and analytical models for excavation process

	Numerical Model	Analytical Model
Pros	1. reveal the internal behavior of the material 2. can show the transient process 3. can help to predict the extreme conditions	1. fundamental, shows the physics and the trend of the process 2. fast calculation, does not need much computation time 3. can be expanded to 3D
Cons	cannot show the trends directly, because every calculation is a full experiment, that means finally extra effort is needed to build up the empirical relation so that the trends can be displayed	1. simplified physics (2D stationary process) & simplified geometry (sharp cutter) 2. cannot tell anything about the internal behaviour of the material

up a physical model, and based on this understanding of the physics a mathematical model will be generated, which is actually a group of equations to describe the physical process.

- A design will be made for the software of this research based on the mathematical model, and correspondingly some verification studies are designed as the benchmark tests.
- Relations between the micro-input and the macro-output will be tested for building up the scaling laws
- Numerical simulations on the cutting process will be conducted, and the experimental data from literature will be used for validation.

1.5. Outline

This thesis in total consists of seven chapters. These chapters introduce the establishment of the 3D dynamic numerical model for underwater excavation process. The modules involved in the numerical model and the way they interact with each other are displayed by the flow chart in Fig. 1.12.

Here below is a detailed outline of the thesis:

- **Chapter 1 Introduction** gives an introduction of the background of this research. The general concepts of dredging engineering and deep sea mining engineering are mentioned here. At the end, a problem definition which clearly defines the task of this research will be stated.

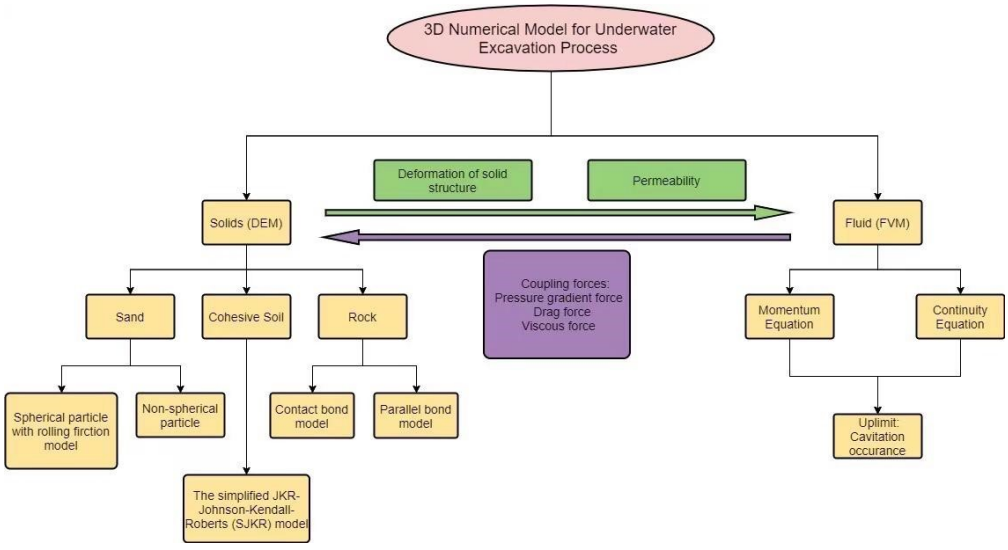

Figure 1.12: Framework of 3D Dynamic Numerical Model for Underwater Excavation Process

- **Chapter 2 Literature Review** is a review of all the literature study and also to find out the white spots, different sections represent different categories of the literature. The physics, the analytical models and numerical models will be summarised in this chapter.
- **Chapter 3 Numerical Methods** introduces the design of the 3D numerical model developed in this research. Firstly it is discussed how to choose the numerical tools, then the model is explained in the sequence that the solid modelling first, solid-fluid coupled modelling second. The equations applied and the benchmarking method are also contained in this chapter.
- **Chapter 4 Numerical Modelling of Sand Cutting Process** introduces the application of the numerical model in sand cutting process, two different ways to simulate sand particle behaviour are explained. Simulations of both above- and under- water sand cutting are validated against experimental results from literature.
- **Chapter 5 Numerical Modelling on the Cutting Process of Cohesive Soil** shows the simulations of cohesive material cutting tests, together with the validation by comparing the simulation results with experimental data from literature.
- **Chapter 6 General Applicability and Scaling Tests on Rock Samples in DEM** discusses the parameterization of simulations for rock-like materials, the tests used for calibration are uni-axial compression test and Brazilian tensile test.
- **Chapter 7 Conclusions and Recommendations** summarises all the important conclusions from the previous chapters, and gives out recommendations for the relevant future research.

2

Literature Review

This chapter is a review on the literature that previous research has been carried out. The content is mainly about rock cutting, while the literature review for sand and clay are covered in later chapters where they are specifically chosen to deal with. The physical phenomenon which may occur during the rock cutting process is discussed based on the reported cutting experiments. Then the analytical models which describe the physics are introduced.

Since numerical modelling is the focus of this research and believed to be able to display more details of the process, so more literature will be covered on how to numerically model the soil and water, and how to simulate the interaction between solid and fluid materials. This literature review is divided into a solid part and a solid-fluid coupling part.

2.1. Previous research on the physics in the cutting process

2

Generic equations have been developed in the past for calculating the cutting forces for sand, clay and rock, where a number of terms dominate for each individual type of soil. Miedema (2017) has summarized the influences of the different forces for five types of soil, as shown in Table 2.1, the dry sand, the water saturated sand, clay, the atmospheric rock and hyperbaric rock.

Table 2.1: The presence of the forces for each type of soil. (Miedema, 2017)

	Gravity	Inertia	Pore Pressure	Cohesion	Adhesion	Friction
Dry sand	■	■				■
Saturated sand			■			■
Clay				■	■	
Atmospheric rock				■		■
Hyperbaric rock			■	■		■

As mentioned before, the content of this literature review chapter is mainly about rock cutting because rock cutting represents the most complicated physics. For sand and cohesive soil the literature reviews are covered in later chapters where they are specifically chosen to deal with.

The two main mechanic properties of rock material to evaluate its strength and hardness are the Unconfined Compressive Strength (UCS) and the tensile strength. The UCS of rock is usually obtained by conducting the uniaxial compression test. The tensile strength of the rock can be obtained in different manners. The strength obtained by uniaxial tension test is called the Direct Tensile Strength (DTS), this parameter is used by the most analytical and empirical models. The strength obtained via Brazilian tension test is called the Brazilian Tensile Strength (BTS). In engineering practice, UCS and BTS are the mostly used parameters to express the rock strength, and these parameters have significant influence on determining the cuttability of rock materials. Noted here the word "cuttability" is defined as the quality or degree of being cuttable. In dredging, it is usually represented by the specific cutting energy E_{sp} $[MJ/m^3$ or $MPa]$, which is the amount of energy consumed to excavate a cubic meter volume of soil.

Many experiments have been done about rock cutting, some of which were conducted in atmospheric condition, while the others are conducted in submerged environment. The strength tests mentioned before, which are the UCS and BTS tests, are both operated in atmospheric condition, or in other words, the "dry condition".

Many rock cutting tests are also implemented in dry condition. In the early years, Roxborough and Phillips (1975) did rock excavation experiments by a disc cutter, as shown in Fig. 2.1. They measured the thrust force F_{thrust}, the rolling force F_r and some other parameters during the experiments, then an analytical model was developed and validated. They also found that the maximum separation between adjacent discs operating in array is governed by the compressive to shear strengths ratio of the rock. Later, Roxborough (1987) studied the link between some basic rock properties (compressive, tensile and shear strengths) in assessing the cuttability of the material. He found that it is very difficult to judge the rock cuttability because it is also strongly impacted by the cutter head design, cutter head operation and the heterogeneity of the rock. The relation between the rock strengths and the cuttability is quite unstable. His research preliminarily revealed the complex and difficulty of making calculation on rock cutting process.

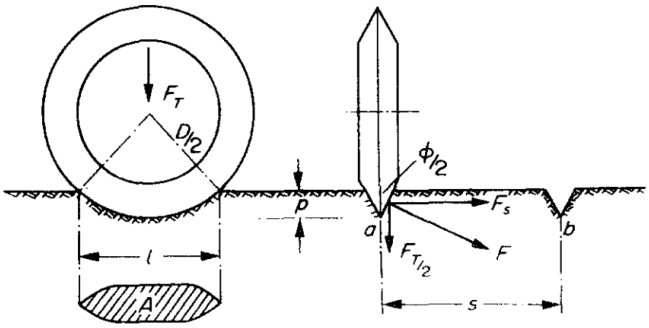

Figure 2.1: Illustration of disc cutting test by Roxborough and Phillips (1975)

Some other rock tests happen in the saturated/submerged condition. First of all, rock strength tests can also be undertaken in submerged environment. The submerged compression test is called tri-axial test, which is applied to obtain the rock strengths under different confinements. Besides, rock cutting tests have also been conducted in underwater situation and many detailed analysis has already been published. van Kesteren (1995) has pointed out that during the indentation of the cutter tooth, a crushed zone will first form up around the tip of the chisel due to the compaction, and then at the boundary of the crushed zone forces are transmitted to the intact rock as discrete point loads, resulting in the exceeding of the shear strength of the rock, so shear cracks will be developed into the virgin rock. Once the shear crack starts developing, at a certain point, the tensile strength will be exceeded and tensile cracks will occur. Hence in the end at a certain distance from the free surface the shear cracks bifurcate into tensile cracks and then chips can be formed up. So as shown in Fig. 2.2, several failure modes may occur subsequently.

Basically, van Kesteren (1995) has considered the interaction between several aspects, the solid structure of the rock, the loading of the cutter, the water inside the pores of the rock and the ambient water. According to the development of these

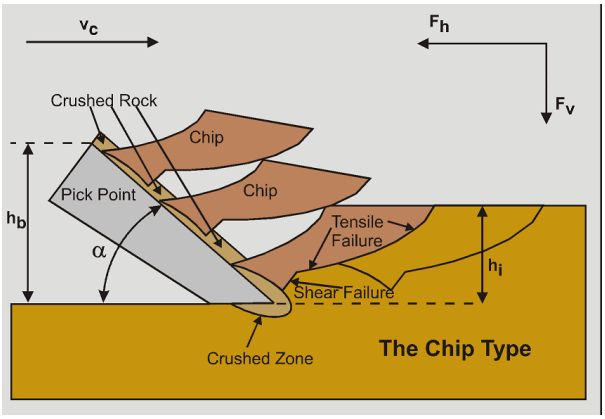

Figure 2.2: Failure modes during underwater rock cutting (Verhoef, 1997; Miedema, 2017)

interactions, he derived the equation for the pore-Peclet number ξ_{pe}:

$$\xi_{pe} = \frac{v_c h_i}{D_w} = \frac{v_c h_i [C_f - \alpha_s C_s + n(C_w - C_s)]\gamma_w}{k_{hydra}} \tag{2.1}$$

Where v_c is the cutting speed $[m/s]$, h_i is the cutting depth $[m]$, D_w is the diffusion coefficient of water pressure $[m^2/s]$, k_{hydra} is the hydraulic conductivity $[m/s]$, γ_w is the specific weight of water $[N/m^3]$, C_w is the compressibility of the porewater $[m^2/N]$, C_s is the compressibility of the solids $[m^2/N]$, C_f is the compressibility of the fabric $[m^2/N]$, which is a coefficient of proportionality usually empirically obtained, and n is the porosity and α_s is the solid compression coefficient. Based on the pore-Peclet number, he gives out two limit conditions:

- Drained condition, which is the "slow" process, will occur when $\xi_{pe} < 1$. In this condition, porewater flow due to porewater pressure gradient is possible without affecting the behaviour of the porous system itself.
- Undrained condition, which is the "fast" process, will occur when $\xi_{pe} > 10$. In this condition, porewater cannot flow fast enough through the pores, and pore water pressures will affect the stress state in the rock fabric.

The underwater excavation process could take place in dredging, trenching and deep sea mining engineering. Dredging and trenching usually operate in relatively "shallow" water ($<$ 200 m), while deep sea mining on the contrary is operating in deep water, at about 3000~6000 meters water depth. The hydrostatic pressure applied by the sea water may greatly influence the cutting process, especially when cutting seabed rock with high cutting speed, the so called "dilatancy hardening effect" (Brace and Martin Iii, 1968) could make the excavation of seabed rock much more energy-consuming. The following section explains the characteristics of hyperbaric rock cutting process in deep sea mining.

2.1.1. Characteristics of hyperbaric rock cutting for deep sea mining

Underwater rock cutting process is different from on-land rock cutting due to the influence of water, which consists of three parts:

- the confining pressure which equals to the hydrostatic pressure
- the fluid flow in the cutting area
- the pore pressure inside the pores of the seabed

It has been indicated by Miedema and Zijsling (2012) that rock which fails in a brittle mode in low confinement environment may fail in an apparent ductile mode in hyperbaric environment. To investigate into this phenomenon, Kuiper et al. (2013) carried out the experimental study on the relation between the ambient pressure and the apparent material strength of fully saturated rock, and later he pointed out that at great water depths it is easier and also more energy efficient to use a grab which excavates with slow strain rates than to use the rotating excavator. By grabbing big pieces of fragments, this method has avoided the crushing process to a large extent, thus can cut rock with much lower specific cutting energy. However, since the rotating excavator can deliver a much higher production rate, it is still necessary to figure out the cutting process with a high cutting speed.

Rock, as a bulk material, is relatively harder compared to sand and clay as bulk materials. The unconfined compressive strength (UCS) varies from around 20 MPa of sandstone to 250 MPa of granite. The cohesive force between the grains is so high that it becomes the major resistance against the excavation.

In the common dredging projects, the water depths are around 0~30 m, which means the absolute hydrostatic pressures are around 1~4 bar. Since the UCS of the rock is in the range of 200~2500 bar, the hydrostatic pressure is much smaller than the rock strength ($P_{hydro} << UCS$).

However, this is not the case in deep sea mining. In the Clarion-Clipperton Fracture Zone of the Pacific ocean, rich manganese nodules site was found at water depth ranging from approximately 4000 m in the east to 6000 m in the west (Padan, 1990; Chung et al., 1996). In the seabed around Minami-Torishima Island, soils containing very high concentration of rare earth elements and yttrium (REY) were discovered at water depth around 5600~5800 m (Suzuki, 2013). In the case of seafloor massive sulfides (SMS) deposits, the water depth is in the range of 1200~3500 m (Rona and Scott, 1993; Yamazaki, 2004).

Basically, the potential ocean mining sites which have been discovered are either around large areas of poly-metallic nodules or active and extinct hydrothermal vents, locating at about 1400~6000 m below the ocean' s surface (Ahnert and Borowski, 2000). That means the hydrostatic pressure P_{hydro} could be up to 600 bar.

Geotechnical characteristics of the soil in the potential deep-ocean mining sites

have also been investigated by many researchers in the past. It has been indicated by Chung et al. (1996) that the compressive strength of the manganese nodule samples is in the range of 3~5 MPa. Besides, Yamazaki (2004) reported that although the cobalt-rich manganese crusts are relatively loose and weak, which usually has a porosity of 0.43~0.74 and a compressive strength in the range of 0.5~16.8 MPa, the substrates could be much denser (porosity of 0.07~0.69) and harder (compressive strength of 0.1~68.2 MPa). The seafloor massive sulphide is normally stronger than the cobalt-rich manganese crust. Its porosity is mainly in the range of 0.3~0.5, while the compressive strength could be up to 38 MPa.

Extraction of valuable minerals from the seabed involves various engineering actions. In the case of poly-metallic nodules, it is designed that nodules will be sucked into the system while seabed excavation is not necessary. However, in the cases of cobalt-rich crust and SMS deposit, seabed excavation is inevitable.

As mentioned above, the hydrostatic pressure P_{hydro} of potential ocean mining sites could be up to 600 bar. For a long time, rocks with the UCS around 600 bar have been considered as the up-limit strength of being dredgable, for example some hard sandstone. Therefore the assumption $P_{hydro} << UCS$ does not hold anymore. But how will it influence the excavation process then?

It is expected that with lower porosity and higher strength, the required cutting force increases significantly. Therefore the process described below focuses on relatively dense and hard seabed rocks, e.g., seafloor massive sulphide.

In the beginning of a cutting process, when a blade is cutting into the virgin rock, cracks and fractures will develop from the blade into the rock. The propagation speed of cracks is in the same order of magnitude of the speed of sound, which is above one kilometer per second.

If the cutting speed is relatively low, e.g., in the range of 0.03~0.06 m/s, the cutter can wait for the surrounding seawater to flow into the cracks, so that the pressure inside the crack gets equal to the hydrostatic pressure outside of the crack. In this way the huge hydrostatic pressure above the seabed will not contribute much to the rock resistance. This will be the scenario of using a giant subsea grab cutter as discussed by Kuiper et al. (2013).

However, what is usually seen in dredging project is that the swing speed is around 0.3 m/s (20 m/min) and the speed on the tip of the blade could be up to 6 m/s, but keep in mind that during operation the speed on the tip of the blade sometimes can be twice the normal speed due to the torsional vibrations, i.e., up to 12 m/s. Since the propagation of cracks is much faster than the flow of seawater into those cracks, two special effects should be taken into consideration: 1) the seawater cannot be treated as incompressible; 2) the hydrostatic pressure acts as a big confining pressure which could prevent the crack to open. As mentioned before, at the ocean floor, the hydrostatic pressure could be up to 60 MPa, which is in the same order of magnitude of the strength of the rock. This makes it very difficult for the blade, at 6 km water depth, to open

the crack and then lift up the chips.

In addition, the seabed rock is porous. There are already a lot of pores or fractures inside the virgin rock. Since the seabed rock is saturated with seawater for long time, it is expected that all the pores are totally saturated with water.

In the excavation process, when the external load is small, only the shape of the pores will be distorted while the volume of the pores remains constant. But in dredging or deep sea mining practice, the purpose is to destroy the rock structure, so the external load must be big enough to break the bonds between rock grains. Thus the internal structure of rock is damaged and the pores' volume could decrease or increase. If the pore volume decreases, the local pore pressure will increase and the pore water flows out. On the other hand, if the pore volume increases, the local pore pressure will drop, attracting the surrounding water to flow in. If the pore pressure drops to the water vapor pressure, cavitation occurs. In that case, the pressure gradient between in and outside of the rock reaches a maximum value. According to the calculation of Miedema and Zijsling (2012), even under confining pressure of 1000 bar, which is approximately 10 km of water depth, cavitation could still occur. As mentioned before, due to the high cutting speed in practice, the local strain rate is so high that pore water flow is restricted. Therefore, the excavation process needs much more energy due to the big pressure difference between in and outside of the rock.

In the "fast" cutting process, both the cracks newly initiated by the blade and the pores/fractures originally in the rock can induce water under pressure.

With this under pressure, a great confining pressure develops during the cutting process. According to Vlasblom (2007), rock that behaves brittle in atmospheric condition may behave ductile in high confining pressure condition. As shown in Fig. 2.3, its apparent strength will correspondingly increase. This phenomenon has been called as the "dilatancy hardening" effect.

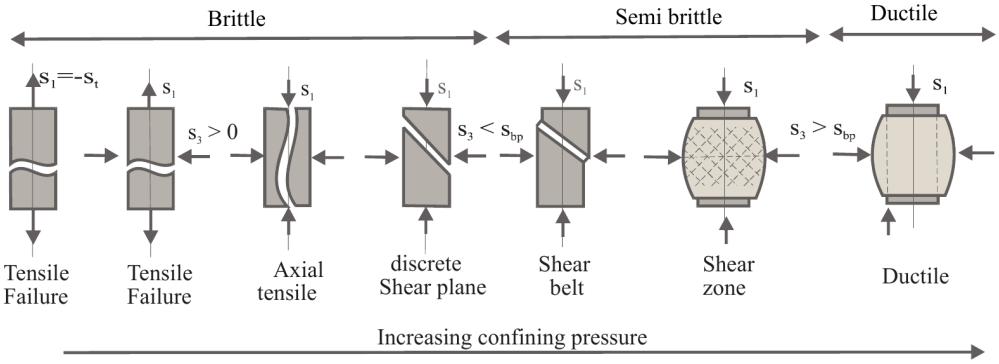

Figure 2.3: Rock failures under increasing confining pressure, (Vlasblom, 2007).

The dilatancy hardening effect (Brace and Martin Iii, 1968) due to drainage con-

ditions has been witnessed in the experiments of Duda and Renner (2012), who have applied different strain rates to three types of sandstones (Ruhr, Wilkeson and Fontainebleau). The transition from brittle failure mode to ductile failure mode under external hydrostatic pressure has been observed by Kaitkay and Lei (2005), who conducted experiments of cutting Carthage marble using a polycrystalline diamond compacts (PDC) cutter. They found that the increase in the forces from cutting under no hydrostatic pressure to cutting under 3.44 MPa (500 psi) is accompanied by an increase in chip length as clearly seen in Fig. 2.4 In hyperbaric rock cutting process, cavitation lim-

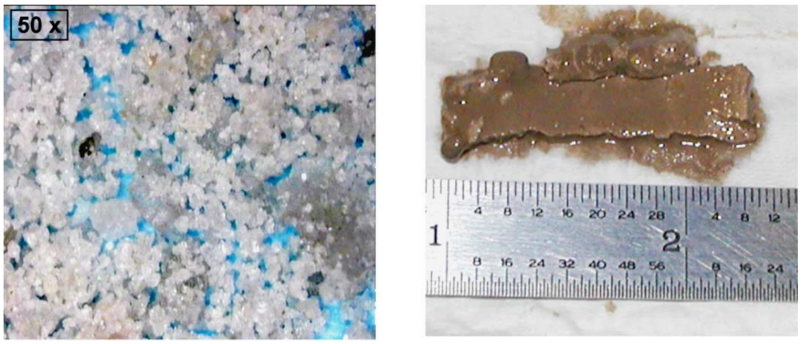

Figure 2.4: Chips from machining tests of Kaitkay and Lei (2005). Left: No confining pressure; Right: At 3.44 MPa hydrostatic pressure.

its dilatancy hardening. When the pore pressure drops to water vapor pressure, the maximum pressure difference between in and outside of the rock is reached. Another possible limit is the failure of rock grains. After the crushing of rock grains, the solid skeleton does not exist anymore. The dilatancy hardening effect cannot exceed either of these two limits.

2.2. Previous research on the analytical model of the cutting process

It is of great interests for the dredging, mining and drilling industries to quantitatively calculate the rock excavation process, mainly, the cutting force and the specific cutting energy. The specific energy E_{sp}, as mentioned before, is defined as the amount of energy used/required to excavate $1m^3$ of soil/rock (Miedema, 2017). In the early days when numerical modelling was not available, analytical models were developed to help people to estimate the required force for the rock material to fail. One of the most widely applied theory for determining rock failure is the Mohr-Coulomb theory and the Mohr's circle. The original works were published from the 18^{th} to the 19^{th} century. As shown in Fig. 2.5, several Mohr's circles are drawn based on a number of experiments, and then the envelope curves are developed for deciding where the material fails or where not, (Miedema, 2017).

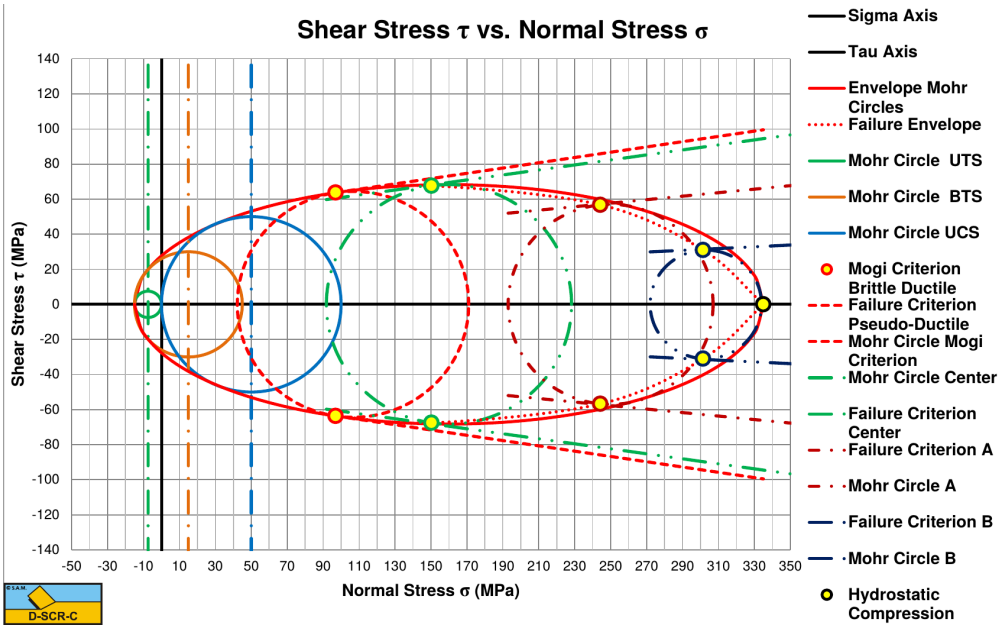

Figure 2.5: Mohr's envelope for intact rock. From left to right, circle 1 (green): uniaxial/direct tensile (UTS) test; circle 2 (yellow): Brazilian tensile test (BTS); circle 3 (light blue): unconfined compression test (UCS); circle 4 (red): tri-axial compression test where the Mogi criterion fits; circle 5 (green): tri-axial compression test where a failure envelope can be draw together with circle 1; circle 6 (dark red): tri-axial test with higher confinement; circle 7 (dark blue): hydrostatic compression test for the crushing strength of the rock, (Miedema, 2017)

2

In the 20^{th} century, some two dimensional (2D) cutting theories were developed. Evans (1965) derived an analytical model from the observations on coal breakage by a wedge cutter. As shown in Fig. 2.6, based on the tensile failure mode, he calculated the total cutting force F_c $[N]$ on the wedge as:

$$F_c = \frac{2 \cdot h_i \cdot \sigma_t \cdot w \cdot \sin(\alpha + \delta)}{1 - \sin(\alpha + \delta)} \tag{2.2}$$

where σ_t is the tensile strength $[MPa]$ of the rock, h_i is the cutting depth $[m]$, w is the width of the wedge cutter $[m]$, δ is the external friction angle, α is the blade angle.

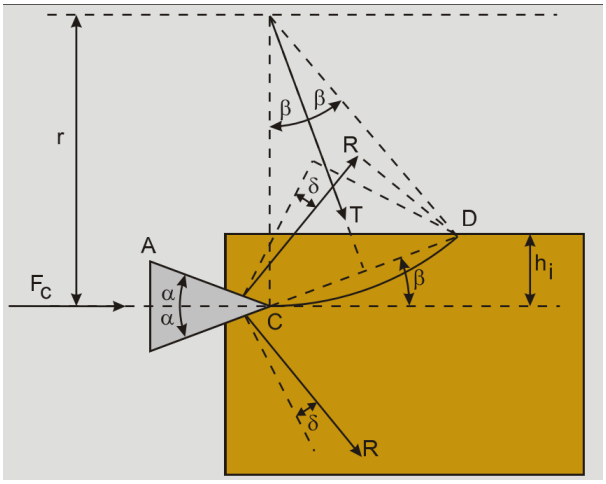

Figure 2.6: Tensile breakage theory of Evans (Miedema, 2017)

Later, Nishimatsu (1972) developed a chisel cutting model based on the mechanism of shear failure. He assumed that the shear stress is not fully mobilized everywhere along the failure plane at the same time. An illustration can be found in Fig. 2.7. Nishimatsu (1972) derived a set of equations to calculate the horizontal cutting force F_h $[N]$ and vertical cutting force F_v $[N]$ on the blade.

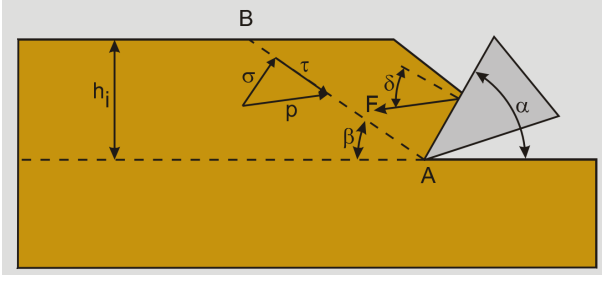

Figure 2.7: Chisel cutter induced shear failure by Nishimatsu (Miedema, 2017)

$$F_h = \frac{1}{(n' + 1)} \cdot \frac{2 \cdot c \cdot h_i \cdot w \cdot \cos(\varphi) \sin(\alpha + \delta)}{1 + \cos(\alpha + \delta + \varphi)} \tag{2.3}$$

$$F_v = \frac{1}{(n'+1)} \cdot \frac{2 \cdot c \cdot h_i \cdot w \cdot \cos(\varphi)\cos(\alpha+\delta)}{1+\cos(\alpha+\delta+\varphi)} \tag{2.4}$$

where n' is the stress distribution factor which heavily depends on the invading rake angle, for cutting angles smaller than 80 degrees n' is more or less constant with a value of $n' = 0.5$. The use of this factor is based on the fact that at the start of shear failure it is not guaranteed that the shear strength has been reached everywhere at the shear plane. Besides n', in the equations, c is the cohesive shear strength of the rock $[kPa]$ and φ is the angle of internal friction.

Decades earlier than Evans and Nishimatsu, Merchant (1944, 1945a,b) had also developed a model to calculate the steel cutting forces based on the shear failure mode. The Nishimatsu´s equations (Eq. (2.3) and (2.4)) are actually based on the Merchant model and adding the stress distribution factor n'. So the Nishimatsu model becomes the Merchant model when $n' = 0$.

Evans later further developed his model for different indentation angle using a wedge cutter, and finally using a pick point (Evans and Pomeroy, 1966). But the principle and failure mechanisms still hold the same.

All these cutting models mentioned above are established on single failure mechanisms, either shear or tensile. But rock cutting process in reality is much more complicated. Many important issues are not covered in these models, for example, the three dimensional (3D) effect, the confinement effect, the dynamic effect and the simultaneous occurrence of several failure modes.

In the 21^{st} century, a more advanced analytical model for excavation process is developed by Miedema (2014, 2017), which is called the Delft Sand, Clay and Rock Cutting Model. Miedema (2014) summarized all the rock cutting models in the past and created six cutting regimes based on the characteristics of the material and the confinement conditions. The six mechanisms are shown in the following Fig. 2.8. Two possible environments are considered in the model, the atmospheric condition and the hyperbaric condition.

In the model of Miedema (2014, 2017), these six mechanisms can cover the cutting processes of sand, clay and rock in both low confinement and high confinement situations. Miedema uses the shear mechanism to represent sand cutting process, because this corresponds with the series of experiments by Hatamura and Chjiiwa (1975, 1976a,b, 1977a,b) and his own experiments (Miedema, 1987). But to calculate the cutting forces on the blade and the specific cutting energy, the layout of the shear mechanism needs to be determined. Miedema then uses the flow mechanism to approximate the shear regime for calculating the sand cutting process, where matching results are also obtained compared with the experimental data. This approximation is feasible mainly because of that sand are in the essence many individual particles, and the particle sizes are always much smaller than the size of the mechanical tool. So although shear planes are developed during cutting, macroscopically a granular flow behaviour is observed which makes the flow regime suitable to be deployed for the

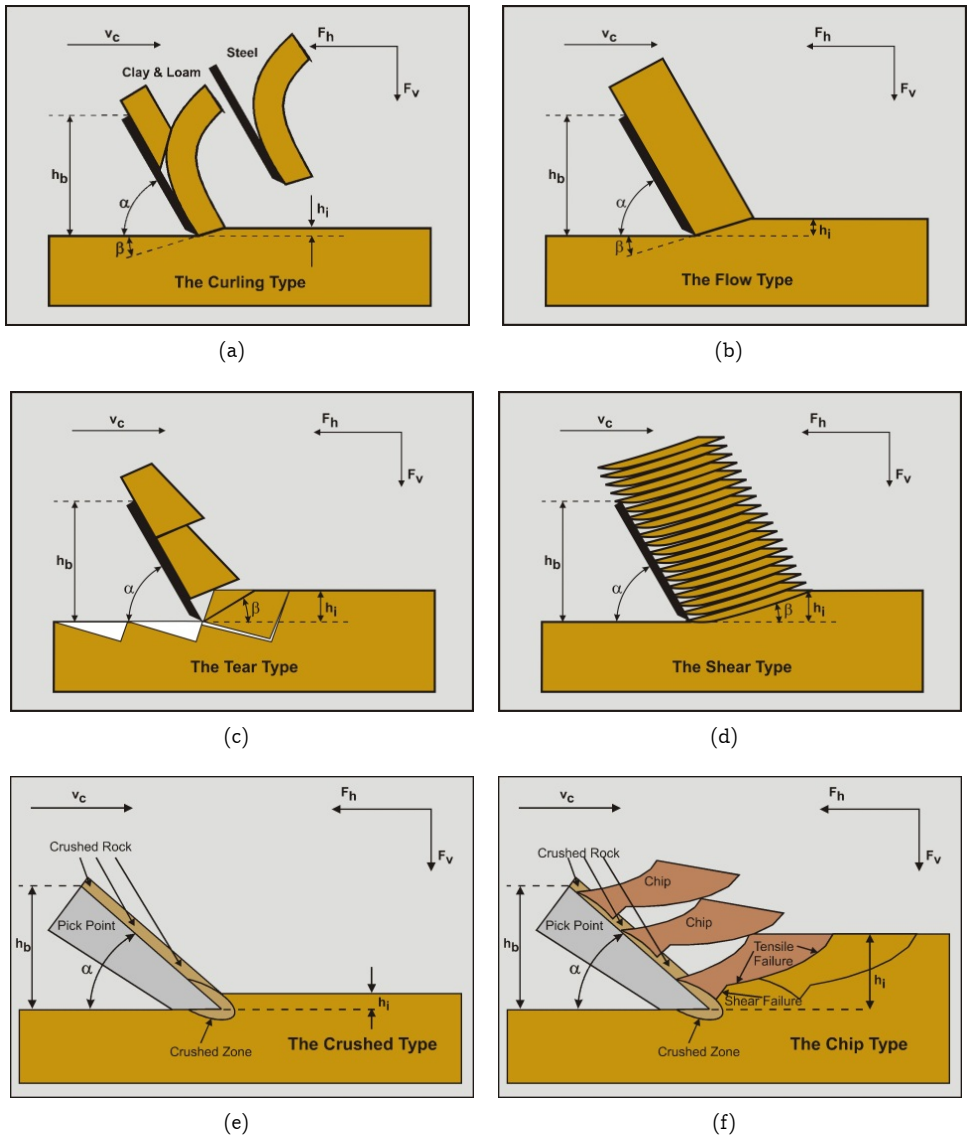

Figure 2.8: Six different types of soil cutting process (a): the curling type, (b): the flow type, (c): the tear type, (d): the shear type, (e) the crushed type, (f): the chip type. (Miedema, 2014)

calculations.

For the cutting of clay, Miedema (2014) pointed out that there are three possible regimes, the curling type, the flow type and the tear type. The curling type is seen not only in clay cutting, but also in metal and loam cutting, which follows a plastic/ductile failure mode.

The main difference between sand particles and clay grains is that clay grains can hold cohesive and adhesive stresses while sand cannot. It should be pointed out that cohesion and adhesion are not purely mechanical stresses, these stresses can also be generated based on a series of complicated electro-chemical processes. Thus the magnitudes of cohesion and adhesion are strongly linked to the water content of the clay material and the temperature. Another major mechanical difference lays in the friction angles. Pure clay hardly has any internal or external frictions during an undrained process, and it has much smaller internal and external friction angles compared with sand during an drained process. It should be mentioned that in engineering practice clay usually appears in the form of clay-sand mixture.

However, by going through the literature from soil mechanics to material science, it is discovered that people have some confusion in clearly using the terms of cohesion and adhesion. Sometimes people treat these two terms as shear stresses, but sometimes people also use them as normal stresses. Actually due to the process cohesion and adhesion are generated, they exist in both shear and normal directions. Therefore in this thesis, when cohesion and adhesion are mentioned, it will be clearly stated that if they are in the shear direction or in the normal direction, in this way confusion can be avoided.

Another often referred mechanical property of clay is the undrained shear strength, which is the overall shear strength consisting of both the cohesive shear stress and the internal friction of the clay during an undrained process. As mentioned before, for pure clay in an undrained process, its friction is negligible, so in this scenario the undrained shear strength equals the cohesion (shear).

According to Miedema (2014), clay will be cut with the flow mechanism under normal circumstances. The curling regime and the tear regime may happen with the following conditions:

- The curling regime will occur when the blade height, h_b, is large with respect to the layer thickness, h_i, the adhesive force **in the shear direction** on the blade is large with respect to the normal force in the shear plane. and the blade angle α is relatively big.
- The Tear Type will occur when the blade height, h_b, is small with respect to the layer thickness, h_i, the adhesion **in the shear direction** on the blade surface is small compared to the the normal force in the shear plane and the blade angle α is relatively small.

For rock cutting, four regimes are categorized by Miedema (2014), the tear type, the

shear type, the crushed type and the chip type, as shown in Fig. 2.8. These types, according to Miedema (2014, 2017), can cover the rock cutting regimes from atmospheric to hyperbaric conditions. The reason to distinguish the confinement conditions is that the rock materials may behave differently from low to high confinement. A transition from brittle failure mode to ductile failure mode is illustrated by Vlasblom (2007) in Fig. 2.3.

This kind of phenomenon not only occurs in tri-axial tests, but also occurs in the cutting process, as shown in Fig. 2.9, in the brittle cutting mode, the cutting force records are periodical and serrated, and big discrete fragments are created along the cutting path; however in the ductile cutting mode, the cutting force will increase to the peak value and maintain in that level, while relatively continuous chips are generated along the cutting path. This phenomenon is observed by Verhoef (1997).

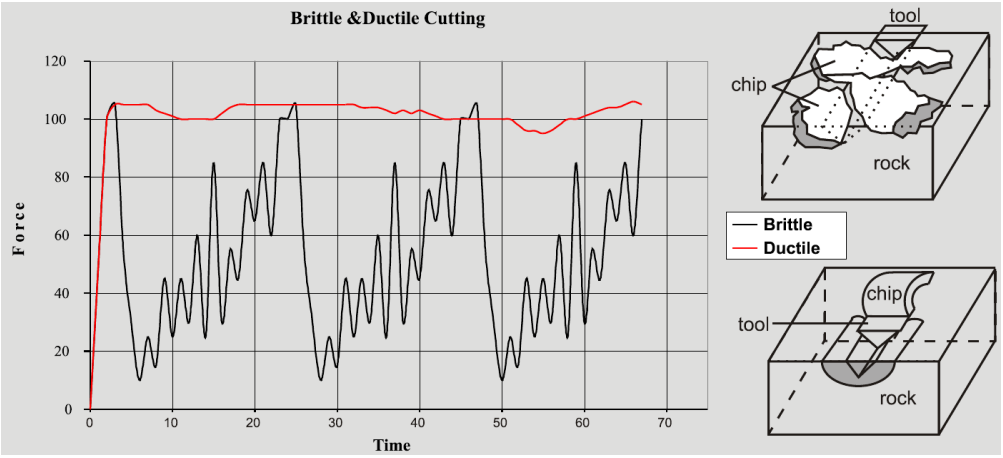

Figure 2.9: Cutting force registration of the brittle and ductile cutting modes and illustrations of the cutting process (Verhoef, 1997)

Miedema (2014, 2017) uses the ductility number to draw the boundaries between different cutting modes, the ductility number is defined as the ratio between the compressive strength over the tensile strength, as shown in Eq. (2.5). The ductility number is also called the Brittleness Index (BI). The different failure modes of rock cutting with respect to the ductility number is depicted in Fig. 2.10.

$$m = \frac{UCS}{BTS} \tag{2.5}$$

From Fig. 2.10 it can be discovered that, when the internal friction angle (φ) of the rock is fixed, not only the ductility number, but also the blade cutting angle will influence the occurrence of cutting regimes. Besides, as mentioned before, the confinements also affect the apparent failure behaviour of the rock. So all these factors should be taken into consideration when predicting the rock cutting regimes. However,

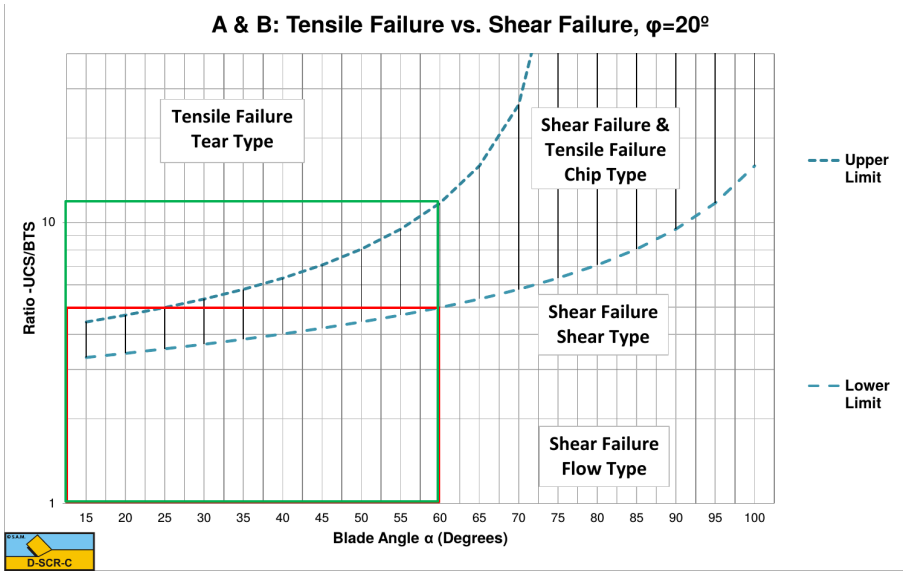

Figure 2.10: The tensile/shear failure range based on $m = UCS/BTS$ for internal friction angle $\varphi = 20^o$, (Miedema, 2017).

if certain boundaries are drawn to represent the typical dredging operation conditions, then a simplified rule can be established to determine the cutting regime. As shown by Fig. 2.11, $\varphi = 30^o$ is a typical internal friction angle of sedimentary rocks, and if the blade angle α_c is chosen as 50^o which is a typical operation angle in dredging, then the cutting regimes can be concluded that:

- Tear Type: $m \geq 10.5$. Rock fails based on 100% tensile failure.
- Chip Type: $7 \leq m < 10.5$. Rock fails based on a combination of shear failure and tensile failure.
- Shear Type: $m < 7$. Rock fails based on 100% shear failure.

The fourth regime, the Crushed Type, is based on cataclastic failure, where disintegration of the grain matrix happens. This mechanism is identified as pseudo-ductile since it shows ductile behaviour. It occurs when the cutting depth is very small ($h_i < 1mm$), and it is usually seen in offshore drilling operations. Therefore for dredging engineering, this cutting regime is not of interest.

Equations are derived by Miedema to calculate the cutting force based on the crushed type and the curling type, as shown in Eq. (2.6) and Eq. (2.7):

$$F_h = \lambda_{HF} \cdot c \cdot h_i \cdot w \tag{2.6}$$

$$F_v = \lambda_{VF} \cdot c \cdot h_i \cdot w \tag{2.7}$$

where c is the cohesive shear strength of the rock $[MPa]$, λ_{HF} is the horizontal cutting force coefficient and λ_{VF} the vertical cutting force coefficient. The cohesive shear

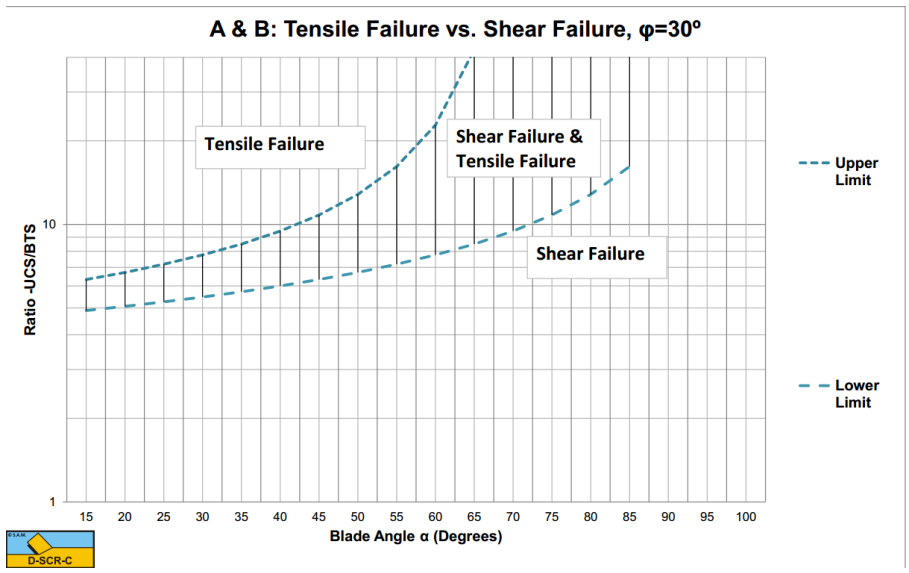

Figure 2.11: The tensile/shear failure range based on $m = UCS/BTS$ for $\varphi = 30^o$, (Miedema, 2017).

strength can be obtained by either implementing the Mohr-Coulomb failure criterion based on tri-axial tests under different confinements, or be calculated by implementing the Hoek-Brown failure criterion (Hoek et al., 2002).

The cutting force coefficients are calculated based on a combination of the internal friction coefficient, the external friction angle, the shear angle, the cutting angle and the ratio between the hydrostatic pressure to the shear strength. Fig. 2.12 shows the relation of the cutting force coefficients (λ_{HF} and λ_{VF}) and the cutting angles α under different internal friction angles ϕ.

The ductility number is treated as a material property, but it is also known that even the same material can be cut in both the brittle and the ductile modes depending on the conditions. Hence there is a confusion with regard to the ductility and the ductile failure, and also the brittleness and the brittle failure. Here below gives out the definitions of ductility and brittleness from the perspective of material science, Source: Wikipedia (2010).

- *In materials science, ductility is a solid material's ability to deform under tensile stress; this is often characterized by the material's ability to be stretched into a wire. Malleability, a similar property, is a material's ability to deform under compressive stress; this is often characterized by the material's ability to form a thin sheet by hammering or rolling. Both of these mechanical properties are aspects of plasticity, the extent to which a solid material can be plastically deformed without fracture. Ductility and malleability are not always coextensive –for instance, while gold has high ductility and malleability, lead has low ductility but high malleability. The*

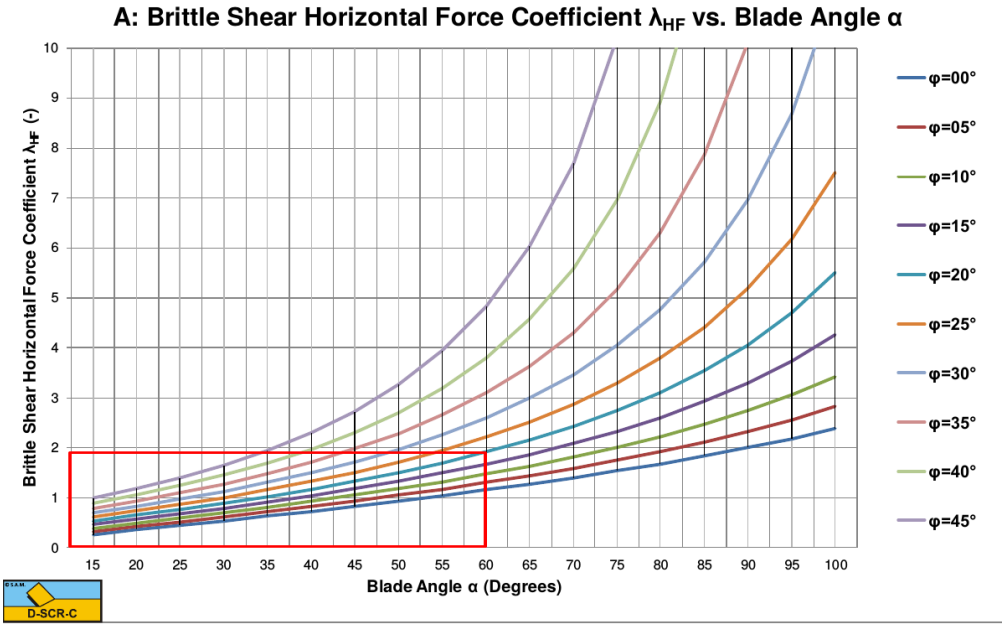

(a)

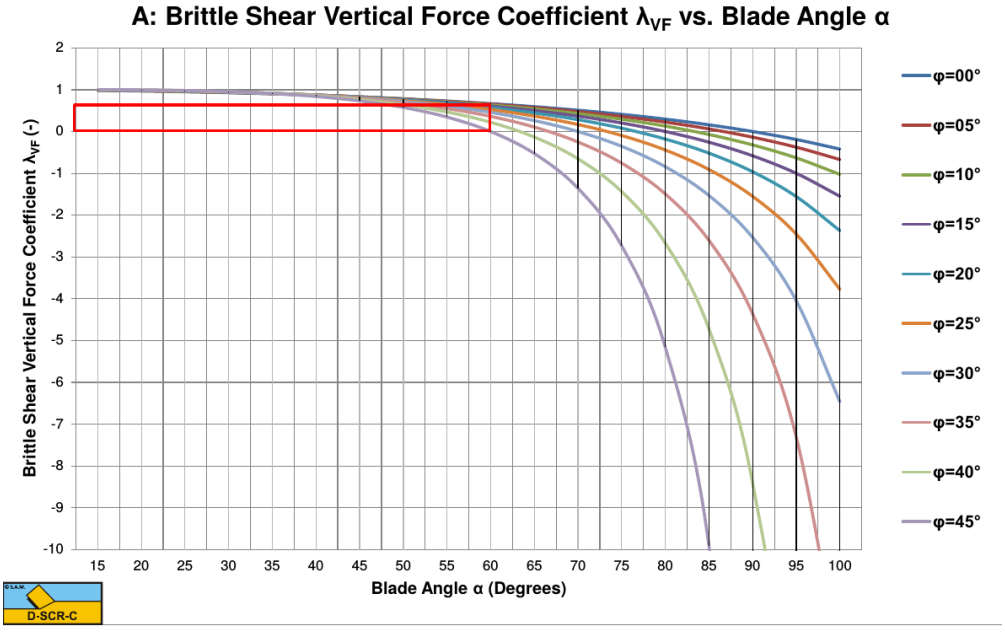

(b)

Figure 2.12: The brittle (shear failure) cutting force coefficient, where ϕ is the internal friction angle of the rock. (a): horizontal cutting force coefficient λ_{HF}, (b): vertical cutting force coefficient λ_{VF}. (Miedema, 2017)

word ductility is sometimes used to embrace both types of plasticity.

- *A material is brittle if, when subjected to stress, it breaks without significant deformation (strain). Brittle materials absorb relatively little energy prior to fracture, even those of high strength. Breaking is often accompanied by a snapping sound. Brittle materials include most ceramics and glasses (which do not deform plastically) and some polymers, such as PMMA and polystyrene. Many steels become brittle at low temperatures (see ductile-brittle transition temperature), depending on their composition and processing. When used in materials science, it is generally applied to materials that fail when there is little or no evidence of plastic deformation before failure. One proof is to match the broken halves, which should fit exactly since no plastic deformation has occurred. Generally, the brittle strength of a material can be increased by pressure. This happens as an example in the brittle-ductile transition zone at an approximate depth of 10 kilometers in the Earth's crust, at which rock becomes less likely to fracture, and more likely to deform ductile.*

From the above explanation, it is understood that the real ductile behaviour is based on plastic deformation, while the ductile failure in rock cutting is actually cataclastic breakage. Macroscopically it may look like the flow type (Fig. 2.8b), but microscopically it is just a crushing process. In other words, the rock material itself is still brittle. Researchers in the past used the macroscopic behaviours as the reference to identify if the soil fails in brittle failure mode or ductile failure mode because it is convenient and intuitive, e.g., the three cutting types from (Hatamura and Chjiiwa, 1975). More recently, inheriting this concept, Helmons (2017) has made a simpler category based on the apparent failure layout of the cutting process, the continuous and the discontinuous mechanisms, as shown in Fig. 2.13.

To make a comparison, the continuous cutting in Fig. 2.13. If the cut material is clay, then it is a ductile material and fails in a plastic and ductile way. If the cut material is rock, then it is a brittle material and fails in a microscopically brittle but macroscopically ductile way.

2.3. Previous research on numerical modelling for soil cutting

The soils on the seabed, according to their mechanical properties, are categorized into three basic groups: sand, cohesive soil and rock. The mechanical behaviour of these materials can be modelled numerically in the cutting simulations. Two main methods for modelling the solid materials are the Finite Element Modelling (FEM) and the Discrete Element Modelling (DEM).

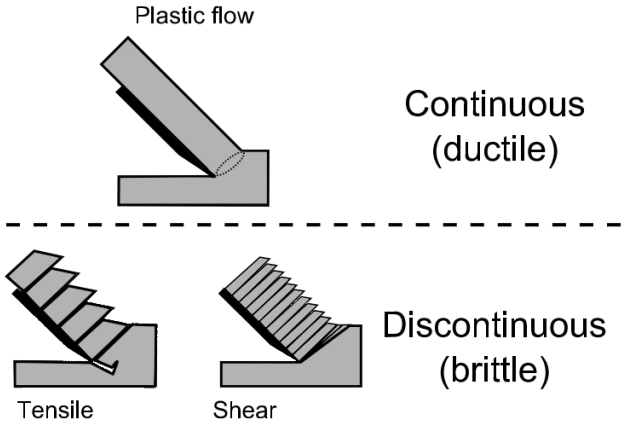

Figure 2.13: Dominant failure types in rock cutting. (Helmons, 2017)

2.3.1. Finite element modelling (FEM) for the cutting process

Fielke (1999) applied FEM to study the effect of the cutting edge geometry of the tillage implements and made comparison with the measured tillage forces, the soil failure patterns and the soil movement below the tillage depth. Two-dimensional (2D) FEM was validated by the tests conducted using 400 mm wide experimental sweeps under the controlled conditions of a tillage test track and in the field. The geometry of the cutter used in the experiments is shown in Fig. 2.14. Correspondingly, he established the 2D FEM meshes which are displayed in Fig. 2.15 The material cut in

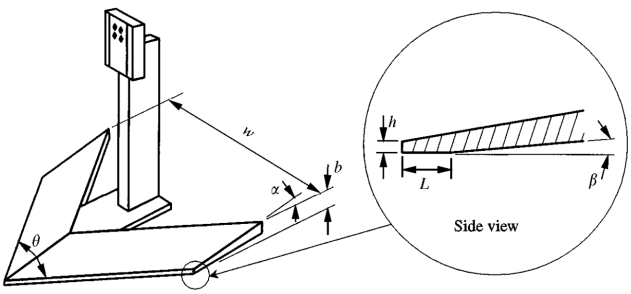

Figure 2.14: Geometry of the experimental sweep wing, where the geometry parameters are w, width; b, lift height; α, rake angle; θ, sweep angle. Cutting edge parameters of h, cutting edge height; L, length of underside rub; β, angle of underside clearance (Fielke, 1999)

the experiments is the Hoyleton soil. He found out that by tuning the Poisson's ratio of the finite elements, the failure mechanisms may change. In his model, increasing Poisson's ratio from zero (compressible soil) to 0.5 (incompressible soil) resulted in the soil which initially was failed using pressure from the top face of the tillage tool

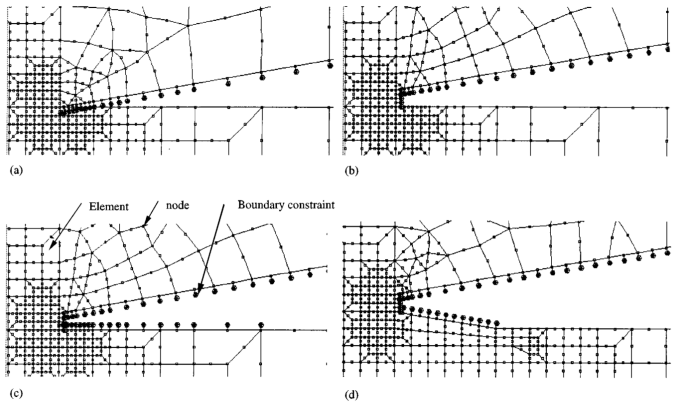

Figure 2.15: Close up of the FEM mesh of various cutting edges examined, where h is the vertical cutting edge height, L is the length of underside rub and β is the angle of underside clearance. $(a)h = 0mm; L = 0mm, \beta = 5°; (b)h = 3.1mm, L = 0mm, \beta = 5°; (c)h = 3.1mm, L = 37.5mm, \beta = 0°, (d)h = 3.1mm, L = 19mm, \beta = -9.5°$; scale of the small square elements, 1.5625 ×1.5625 mm full size (Fielke, 1999)

changing to failure from the cutting edge alone, thus resulting in larger draught and vertical up forces.

Jaime et al. (2015) implemented FEM into three-dimensional rock cutting simulation. They combined a plasticity-damage model and an element erosion scheme which can remove the damaged element when its energy release equals the fracture energy. He conducted both the scratch and the deep cut tests, and compared the results with the laboratory tests on Berea sandstone. The scratch test is shown in Fig. 2.16, and the deep cutting test is shown in Fig. 2.17, both by the polycrystalline diamond cutters (PDC).

The size of the element mesh increases from the surface to the bottom, because small elements size is necessary to capture the details of rock fragmentation process. The research shows that both the fragmentation process and the cutting forces were deemed reasonable, but it is not clear yet about how to scale up the model to fit engineering needs.

Several modified FEM techniques were developed during the last decade to study the soil deformation problem, such as the particle finite element (PFEM) (Oñate et al., 2011) and the material point method (Alonso et al., 2015; Ceccato, 2015; Bandara and Soga, 2015). These methods have applied their own constitutive laws on soil mechanics which govern the relation between the stress and strain in the soils.

Several commercial codes are also developed to solve soil mechanical or engineering problems using FEM, for example, the PLAXIS family, the Abaqus family and etc.

Many investigations of the numerical modelling on soil mechanics applications have been conducted with the coupling with finite element method and discrete element method (DEM). In most of these numerical models, FEM is used to simulate the

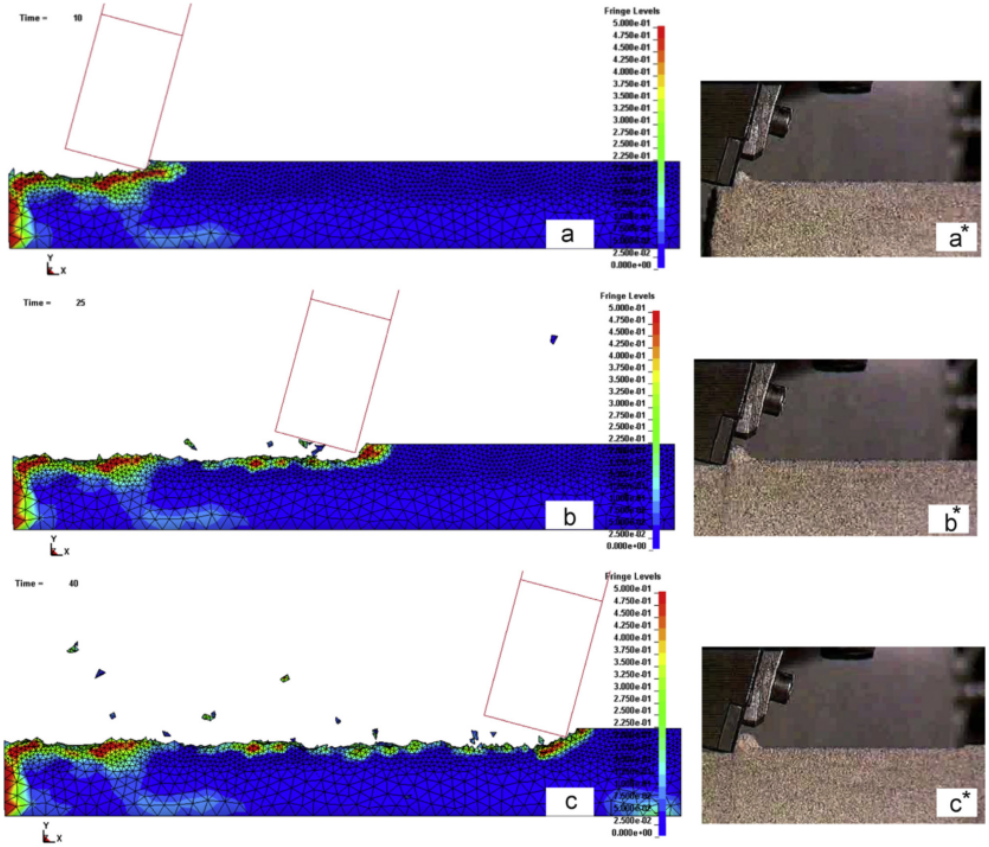

Figure 2.16: A comparison of failure/fragmentation pattern for shallow cut, d = 0.3 mm. On the left: FEM results on Vosges sandstone; on the right, laboratory tests of Berea sandstone. (Jaime et al., 2015)

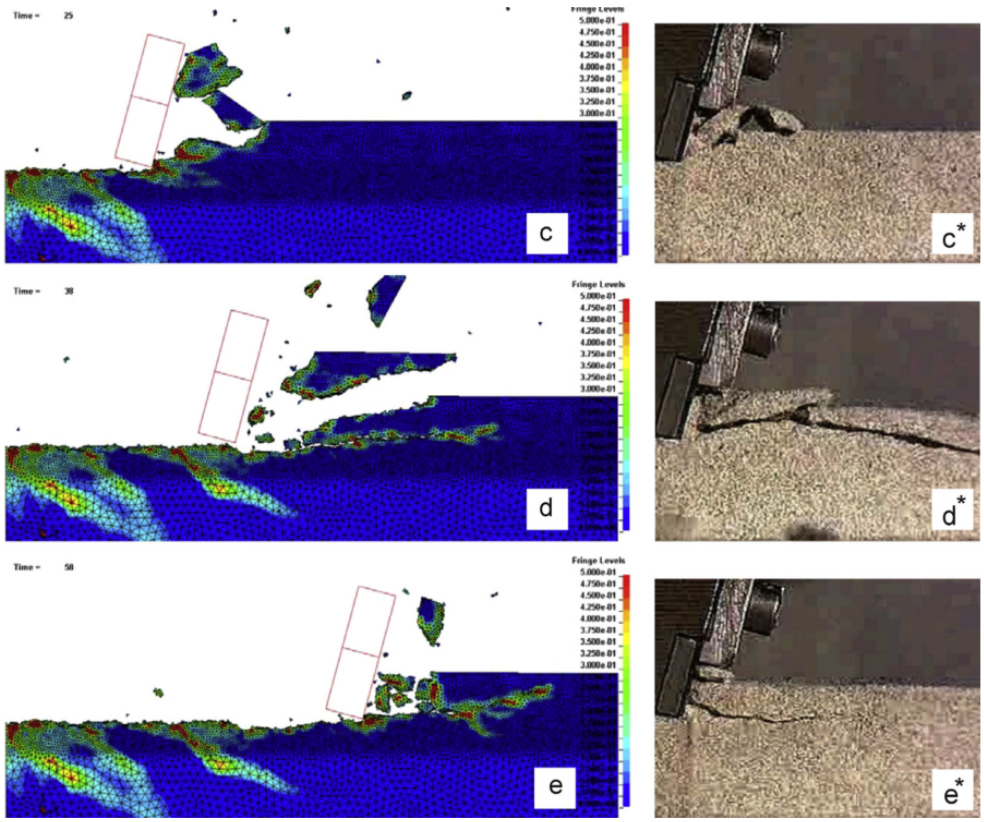

Figure 2.17: A comparison of failure/fragmentation pattern for the deeper cut. On the left: FEM results on Vosges sandstone, d = 3.6mm w.r.t cutter advances; on the right, laboratory tests of Berea sandstone, d = 4mm (Jaime et al., 2015)

behaviour of the far field and the boundary conditions to reduce the computational effect, while the core of the deformation process is calculated by DEM. So this part of the literature review will be covered in the next subsection, the review on the discrete element modelling (DEM) application for the cutting process.

2.3.2. Discrete element modelling (DEM) for the cutting process

Discrete element modelling (DEM), also called discrete element method, is a family of numerical methods for computing the motion of a large number of particles of micrometer-scale size. DEM makes it feasible to describe the behaviour of each particle. The basics of the interaction between two different particles in DEM comprises two dashpot systems, each consisting of a spring and a damper working between the particles on the normal and tangential directions respectively, as depicted in Fig. 2.18. The first application of this method is done by Cundall (1971b) in his PhD thesis to solve some problems in relation to rock mechanics.

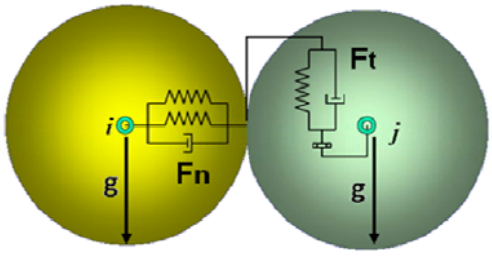

Figure 2.18: Schematics of normal and tangential dashpot system for particle-particle interactions in DEM, (Goniva et al., 2009).

The DEM method has been developed rapidly since 1980s. In the field of micromechanics of granular material, reference is made to Savage (1983); Satake and Jenkins (2013) , Biarez and Gourvès (1989), Thornton (1993) and Siriwardane and Zaman (1994). In the field of geo-mechanics, important contributions are made by Mustoe et al. (1989), Williams et al. (1993) and Shimizu et al. (2010).

Although the theory of DEM has been developed for 40 years, due to the limitation of computer, the practical application of DEM in simulation has not been done until about 15 years ago. From that time on, DEM simulations for a big number of particles in a computer are feasible. Nowadays, by using super computers and implementing the parallel computing technique, DEM simulations with more than 10^7 particles can be carried out. Besides, simulations of smaller size ($< 10^6$) can already be run by common PCs or workstations.

Cundall (1971a,b); Cundall and Strack (1979) generated the equations for calculating the contact forces between circular discs and applied them into the simulation

of granular assemblies. A software package named BALL was developed and used to calculate the forces in a 2D discs assembly. The results were compared with the force vectors obtained photoelastically for verification, although the comparison is primarily qualitative, DEM showed good potential for its application in complicated granular problems.

Huang (1999) and Huang et al. (1999) systematically studied the application of DEM in the mechanical tool - rock interaction process. She summarised all the previous contact models and applied the point contact bond model to generate rock-like material in DEM. She used the software PFC^{2D}® (Particle Flow Code in 2 Dimensions) to conduct indentation and cutting test on rock-like materials. In her PhD thesis, Huang applied the Buckingham-π theorem to determine the parameters for the DEM model for rock-like material, which is quite important for establishing the relation between the input parameters of micro scale and the output strength of macro scale. Several independent dimensionless parameters governing the elastic response and the failure behaviour of the 2D assembly are shown below in Eq. (2.8).

$$\{\frac{K_n R_{avg}}{T_n}, \frac{T_s}{T_n}, \mu, \frac{K_s}{K_n}, n, \frac{R_{avg}}{L}, \frac{V}{\sqrt{K_n/\rho}}\} \tag{2.8}$$

in which K_s $[N/m^2]$ and K_n $[N/m^2]$ are the circular disc contact stiffness' s in shear and normal direction respectively, T_s $[N/m]$ and T_n $[N/m]$ are the bond strengths in shear and tensile direction respectively, R_{avg} $[m]$ is the average disc radius, L $[m]$ is the assembly length, V $[m/s]$ is the loading velocity, ρ $[Ns^2/m]$ is the density of the disc, μ $[-]$ is the friction coefficient between the discs, n $[-]$ is the porosity of the assembly.

Relations between the dimensionless numbers have been established between:

- $K_s/K_n \sim E'/K_n$
- $K_s/K_n \sim \nu'$
- $K_n R_{avg}/T_n \sim \sigma_c R_{avg}/T_n$
- $K_n R_{avg}/T_n \sim \sigma_t R_{avg}/T_n$
- $K_n R_{avg}/T_n \sim \sigma_c/\sigma_t$
- $T_s/T_n \sim \sigma_c R_{avg}/T_n$
- $T_s/T_n \sim \sigma_t R_{avg}/T_n$
- $T_s/T_n \sim \sigma_c/\sigma_t$
- $\mu \sim \sigma_c R_{avg}/T_n$

Here E' $[N/m^2]$ is the apparent Young's modulus of the assembly, ν' $[-]$ is the ap-

parent Poisson's ratio of the assembly, σ_c $[N/m]$ and σ_t $[N/m]$ are the compressive and tensile strength of the assembly respectively. The units of some variables in Huang's research are different from engineering practice because her analysis was made in 2D domain.

Later, Huang et al. (2013), Huang and Detournay (2013) studied the transition from a ductile to a brittle failure mode in the rock cutting and the rock indentation tests respectively. The discrete element code PFC^{2D}® was used for conducting the 2D DEM simulations. For the rock cutting test, it is discovered that the failure mode transits from a ductile to a brittle failure when increasing the cutting depth, a critical cutting depth d_* is derived as Eq. (2.9), where K_{Ic} $[N/m]$ denotes the material toughness, σ_c its unconfined compressive strength and ℓ $[-]$ represents the characteristic length of the material. For the indentation test, it is concluded that the initiation of the brittle fractures after the ductile compression is governed by the scaled flaw (crack) length Λ $[m]$, as shown in Eq. (2.10). It is the ratio between the actually measured flaw (crack) size λ_a $[m]$ and the characteristic length of the material ℓ.

$$d_* \propto \ell \quad , \quad where \quad \ell = (K_{Ic}/\sigma_c)^2 \tag{2.9}$$

$$\Lambda = \frac{\lambda_a}{\ell} \quad , \quad where \quad \ell = (K_{Ic}/\sigma_c)^2 \tag{2.10}$$

Potyondy et al. (1996) and Potyondy and Cundall (2004) systematically developed the computational methodology of modelling the rock deformation and fracture behaviour via DEM. Their model consists of the grain contact part and the bonding contact part. Using the software PFC^{2D}® and PFC^{3D}®, a series of simulations were done based on the material properties of the Lac du Bonnet granite. The numerical model of Potyondy and Cundall (2004) will be further discussed in Chapter 3.

In the 21^{st} century, more and more research on DEM has been published each year. To establish the correspondent relation between the macroscopic quantities like the velocity-field, the stress or strain and the "microscopic" quantities like contact-forces, deformations and particle displacements, Luding et al. (2001) conducted quasi-2D DEM simulations of shearing tests, as shown in Fig. 2.19.

Through the tests, they found out that the bulk modulus of the assembly is proportional to the density of the particle and the coordination number. Here the coordination number of an assembly is defined as the average number of contacts per particle. On the other hand, the fabric-, the stress- and the strain tensors are not co-linear with each other. It is also discovered that the displacement rate in the shear zone decays exponentially with the distance from the moving wall which applies the shear.

Procházka (2004) studied the DEM application in the rock bursts process. In deep mining engineering sudden release of accumulated potential energy occurs under special conditions. This phenomenon is known as bumps or rock bursts. Instead of spheres (3D) or round discs (2D) which are usually seen in DEM studies, he argued that the hexagonal elements with elastic, or elastic-plastic contacts can better describe the rock behaviour from the perspective of keeping the consistence of the stiffnesses of the

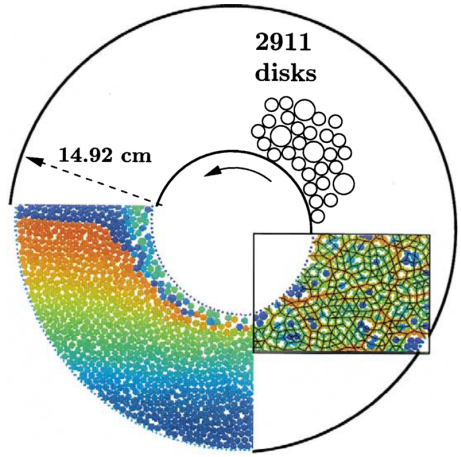

Figure 2.19: Sketch of the model system from the quasi-2D shearing test of (Luding et al., 2001). The left color inset shows the shear zone after one half rotation - particles with the same vertical coordinate had the same color initially. The right color inset shows the stress chains, where large, medium and small contact-forces are coloured red, green and blue, respectively.

springs. The assembly he generated is shown in Fig. 2.20. He thus made comparison between the free hexagonal element method and the statical particle flow code which used circular discs (2D). In his conclusion, he claimed that both methods have delivered reasonable results. But it must be pointed out that there is a big downside on this hexagonal element method, that is the created rock sample is very anisotropic. It can be clearly concluded from Fig. 2.20 that there are big differences between the sample's mechanical properties on the horizontal direction and the vertical direction. Imagining a force is loaded from the left side to the right side in the horizontal direction, then the contact surfaces on the discrete elements will be perpendicular to the loading. However, if the force is loaded from the top side to the down side, then the contact surface will be serrated, consisting many tilted faces from the discrete elements.

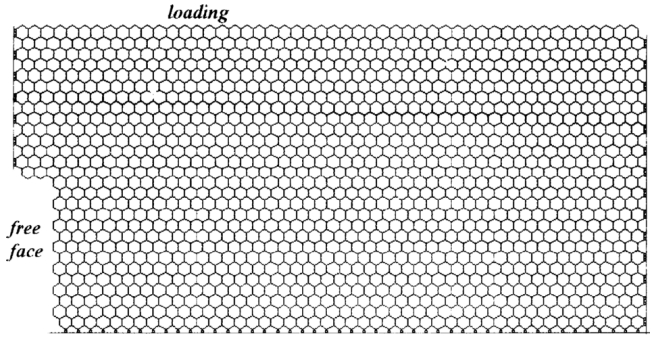

Figure 2.20: Sample made by the hexagonal elements, (Procházka, 2004).

Lei and Kaitkay (2003) and Kaitkay and Lei (2005) conducted both numerical

modelling and experiments on confined rock cutting. The numerical simulation is done by using DEM. The commercial software PFC^{2D}® is used to generate the rock specimen to approximate Carthage marble. For applying the hydrostatic pressure as the confinement, two methods were introduced in their work, one for the biaxial test and one for the cutting test. In the biaxial test, two lateral plates are used to maintain the compression at the boundaries to mimic the influence of hydrostatic confining pressure, as shown in Fig. 2.21. For the cutting process, a special algorithm consisting of two steps is developed to model the influence of confining pressure. At first, the particles located at the specimen boundary are detected, and then the second step is the application of confining pressure to the boundary particles, which is realized by applying an equivalent force on each particle with the inwards directions.

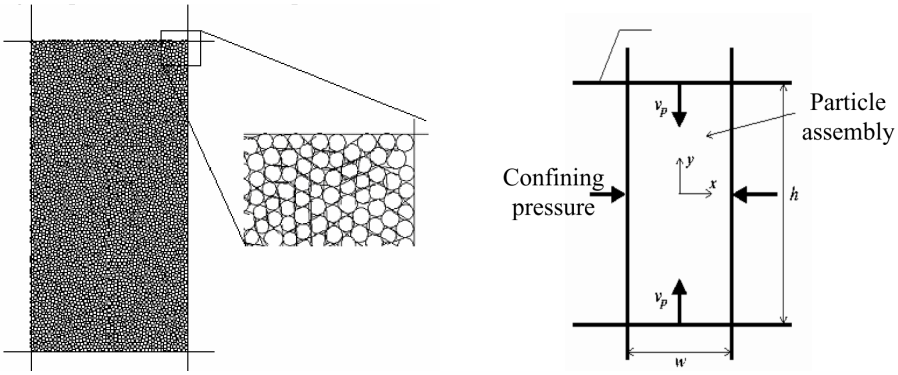

Figure 2.21: Left: rock specimen generated in PFC^{2D}®, right: Biaxial test environment, (Lei and Kaitkay, 2003).

The research was done mainly for offshore drilling purposes, so the cutting depth is only 0.8mm. However, the cutting forces still show significant difference from unconfined to confined conditions, as shown in Fig. 2.22. $F_x[kN/m]$ and $F_y[kN/m]$ are the horizontal and vertical cutting force respectively, $\alpha[-]$ is the invading rake angle. The force record shows very strong fluctuations, which is realistic because the breaking of the rock sample is an discontinuous process.

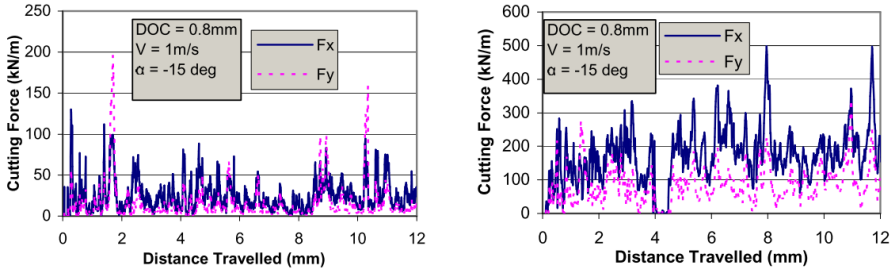

Figure 2.22: Force records from DEM simulation. left: without confining pressure, right: with a 34.5MPa confining pressure, (Lei and Kaitkay, 2003).

Alassi (2008) in his PhD thesis, developed a DEM model ($PFC^{2D®}$) to monitor an oil/gas reservoir. He found out that the boundary conditions cannot be applied properly by purely using DEM, so he implemented a continuum coarse grid to track the stress level in the far field. There are still limitations on such kind of methods, which are:

1. the maximum P-wave/S-wave ratio is limited by ($\vec{V}_p/\vec{V}_s < 3$), here $\vec{V}_p$ $[m/s]$ and $\vec{V}_s$ $[m/s]$ are the propagation velocities of the pressure wave (P-wave) and shear wave (S-wave) respectively.
2. it is difficult to derive relations for failure properties just like it was done for elastic properties, and numerical tests have to be done each time a geo-mechanical model is built.
3. there are always difficulties in building geo-mechanical models and installing complicated initial stress conditions, usually given for hydrocarbon reservoirs, using DEM.

Alassi (2008) also developed a modified discrete element approach, where in a geo-mechanical cluster the micro stiffness matrix ($\mathbf{K}$) are derived based on rock properties given by the macro stiffness matrix ($\mathbf{C}$). Then he coupled this modified DEM with a Finite Difference fluid model in which fluid is allowed to flow in a network of pipes to simulate the whole reservoir behaviour. Several case studies were done and the results have shown a big improvement.

A series of research on rock excavation has been done by Rojek (2007), Rojek and Oñate (2007), Labra et al. (2008), Rojek et al. (2008), Rojek et al. (2011), Rojek et al. (2013). In this series of publications, Rojek, together with his co-authors, published a software package which simulates the rock excavation process in both 2D and 3D domain with parallel computation. The software is based on pure DEM or a coupling mechanism between DEM and FEM. In the case of DEM/FEM coupling, DEM is usually used to calculate the interaction part with the tool because it can capture the deformation and fracture process, while FEM is used to simulate the far-field or boundary material to reduce computational cost. Fig. 2.23 shows the difference between the two calculation methods. In the DEM/FEM coupling, DEM and FEM represent the different sub-bodies of the rock respectively, but they can also have some overlap on the interface for the coupling calculation. It is claimed that such kind of coupling reduces the simulation time significantly. Several validation tests were carried out, mainly on pure DEM computations, like the unconfined compression test, the Brazilian tensile test, the pick-point cutting test and etc.

To better describe the internal heterogeneity of rock material in DEM, Rojek et al. (2013) proposed a methodology for installing a constant initial stress to an arbitrary shaped DEM sample. Macroscopic virgin stresses can be installed to a DEM sample by applying certain displacements to the particles to create the particle contact forces corresponding to the required stress/strain field. This method has been successfully tested in 2D domain.

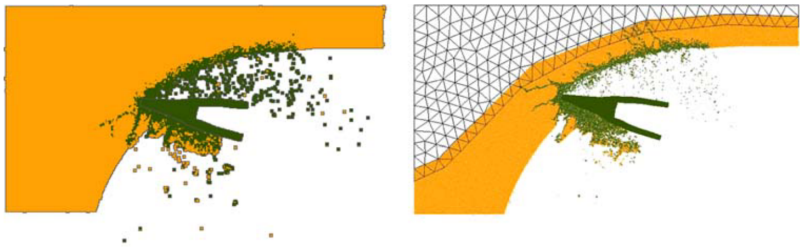

Figure 2.23: 2D simulation of rock cutting. left: DEM model, right: DEM/FEM coupling model Labra et al. (2008)

Munjiza (2004) published another DEM/FEM coupling method. In their model, each discrete element is discretized into finite elements, in this way there is a finite element mesh associated with each discrete element, and these meshes define the shape of discrete elements. A software package Y-code was developed with this model. 2D simulations of triaxial test have been conducted using this code and the results are published by Mahabadi et al. (2010).

2.4. Previous research on numerical models for solid-fluid interaction in soil mechanics applications

Now the technique to numerically model the solids has been investigated, it is time to check how to bring the solids modelling into the underwater environment. For modelling the underwater excavation process, three major components are taken into consideration: the excavation tool, the seabed soil and the pore water. Numerical models for the interaction between the solids and the fluids are examined here.

Traditionally solids and fluids are treated differently. Solids behave according to the solid mechanics, e.g., soil mechanics, while fluids behave according to the fluid mechanics. Coupling these fields is a challenge. Four methodologies are available for solving this problem numerically, the Eulerian-Eulerian method, the Lagrangian-Eulerian method, the Lagrangian-Lagrangian method and the single Eulerian method.

2.4.1. The Eulerian-Eulerian method

The representative of the Eulerian-Eulerian method is the two fluid model, which can also be referred as the two-phase model, in which the solid and the fluid are seen as two different continuums. Each continuum has its own continuity and momentum equations, which means this model consists of at least four equations, the coupling between the equations are the solid volume concentration for the continuity equation and the momentum exchange term for the momentum equations. These governing

equations can be found in (Van Wachem and Almstedt, 2003).

This method has been widely applied in dredging and coastal engineering relevant researches. For example, Nguyen et al. (2009) performed large scale simulations to study the suspended-sediment transport process in the Seine estuary area of France, while Nguyen et al. (2012) used the two fluid model to simulate the release process of dredged sediment into ambient water, where relatively good agreement was found between the experimental plume expansion and the numerical modelled plume expansion, as seen in Fig. 2.24.

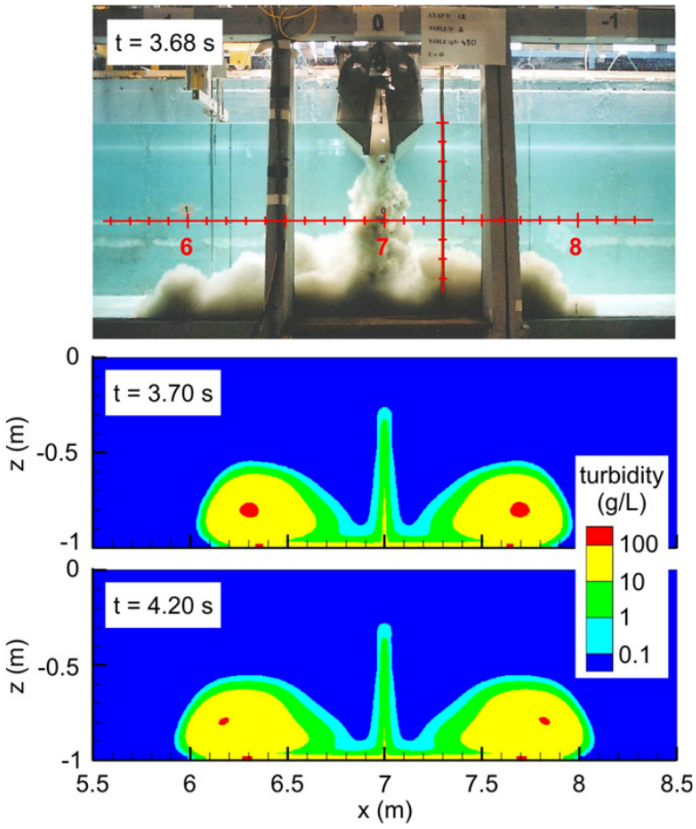

Figure 2.24: Comparison between an experimentally observed plume expansion and the numerical results: (a) picture taken at t=3.68s by laboratory tests; (b) sediment cloud calculated at t=3.70s; and (c) sediment cloud calculated at t=4.20s. (Nguyen et al., 2012)

2.4.2. The Lagrangian-Eulerian method

The Lagrangian-Eulerian method is based on the concept that the fluid is treated as continuum (the Eulerian part) while the solids are treated as dis-continuum (the

Lagrangian part). The Eulerian part could be any of the computational fluid dynamics (CFD) models, like the finite volume method (FVM), the volume of fluid method (VOF), the lattice Boltzmann method (LBM) and etc. The Lagrangian part is basically DEM. However, DEM is the name used in the field of granular materials and soil mechanics. In the field of fluid dynamics, the Lagrangian part is usually called the Lagrangian particle tracking method (LPT) or the discrete particle simulation method (DPS). In the essence, DEM and LPT/DPS are the same things, applying Newton's law of motion to calculate the interaction and movement of particles. The main difference is just that the LPT/DPS method is always used for tracking Lagrangian particles within an Eulerian phase while for DEM it is not necessary.

The recent development of the theory of LPT/DPS can be found in (Mahdavi-manesh et al., 2013), where the options for forces acting on the solid particles from the fluid side are listed. Several coupling codes have been developed between LPT and CFD, Vallier et al. (2011) applied the LPT-VOF coupling to study the break-up procedure of a cavitation sheet on hydrofoils. Lopez (2014) used the LPT-VOF coupling in the software OpenFOAM® to simulate the erosion process in a bended pipeline. He also showed a case study of a single bubble travelling in a horizontal pipeline.

Zhou et al. (2010) summarises the governing equations of DEM-CFD coupling. For the solid phase, Newton's law of motion governs the particles' motion. The translational and rotational motions of particle i with mass m_i and moment of inertia I_i can be written as Eq. (2.11) and Eq. (2.12):

$$m_i \frac{d\vec{v}_i}{dt} = \vec{f_{pf,i}} + \sum_{j=1}^{k_c} (\vec{f_{c,ij}} + \vec{f_{d,ij}}) + m_i \vec{g} \tag{2.11}$$

$$I_i \frac{d\vec{\omega}_i}{dt} = \sum_{j=1}^{k_c} (\vec{M_{t,ij}} + \vec{M_{r,ij}}) \tag{2.12}$$

where $\vec{v}_i$ and $\vec{\omega}_i$ are, respectively, the translational and angular velocities of the particle, and k_c is the number of particles in interaction with the particle. The forces involved are: the particle–fluid interaction force $\vec{f_{pf,i}}$, the gravitational force $m_i \vec{g}$, and inter-particle forces between particles which include the elastic force $\vec{f_{c,ij}}$ and viscous damping force $\vec{f_{d,ij}}$. The torque acting on particle i by particle j includes two components: $\vec{M_{t,ij}}$, generated by the tangential force, and $\vec{M_{r,ij}}$, commonly known as the rolling friction torque.

The Eulerian part contains the continuity and momentum equations, in which the momentum equations can be written in several different forms. Detailed explanation can be found in (Zhou et al., 2010).

Several software packages are developed for enabling the DEM-CFD coupling. The commercial code EDEM® and FLUENT® are coupled for this purpose. Many studies

have been done using the EDEM-FLUENT coupling. Adema et al. (2010) studied the solid particles - gas mixture flow in an iron blast furnace, where they also tried different geometries of the particles (Fig. 2.25) to find out the influence of the shapes on particles' movement.

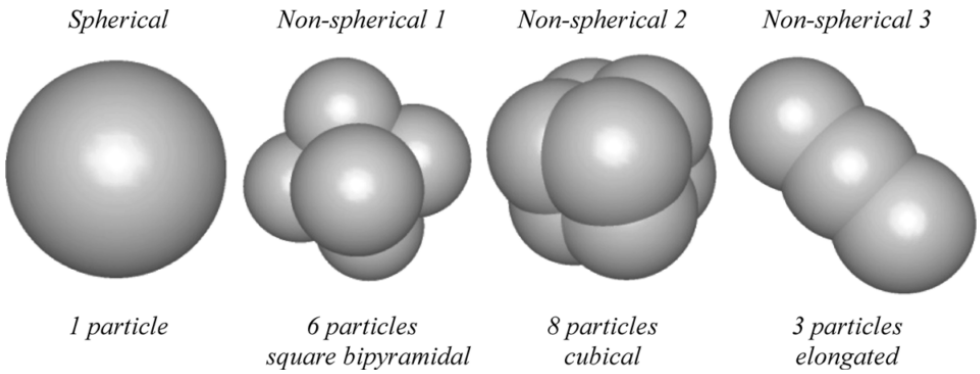

Figure 2.25: Particle shapes designed by Adema et al. (2010)

In dredging relevant research, Abdeli et al. (2010) applied the similar technique as (Adema et al., 2010). They used non-spherical particles, which are formed by several small and identical spherical particles, to conduct sand cutting simulations. Besides, they developed an algorithm to calculate the pore volume change during the sand cutting process in the 2D domain. This pore volume calculation method provides the possibility to bring the simulation into underwater environment where the fluid flow through the pores must be calculated. However it should be mentioned that Abdeli et al. (2010) did not specify the internal structure of their non-spherical particle and they did not manage to calculate the pore volume change in the 3D domain. It is thus difficult to implement their methodology.

Another important dredging process is the slurry transport by pipeline and pumps. Huang et al. (2015) applied the DEM-FVM coupling using the EDEM-FLUENT software package to simulate the slurry flow passing through a centrifugal pump. The velocity fields of both the fluid and particle phases, the volume fraction distributions and trajectories of the solid particles, and the pressure field in the centrifugal pump can all be calculated.

Apart from the commercial codes, open-source software is also developed for DEM-CFD coupling, Goniva et al. (2010) developed a package called CFDEM, which is a coupling between DEM software LIGGGHTS and CFD software OpenFOAM®. LIGGGHTS stands for LAMMPS Improved for General Granular and Granular Heat Transfer Simulations. LAMMPS is a classical open-source molecular dynamics code distributed by Sandia National Laboratories, an US Department of Energy laboratory. Later, Hager et al. (2013) compared the different algorithms in CFDEM based on the ratios between the particle size and the fluid cell size. Hindered settling and fluidized

bed simulations were conducted and compared with experimental data, proving that this CFDEM package can well describe the dynamics of both solid dominant and fluid dominant multiphase processes.

Schmeeckle (2014) studied the sand transport process in water by combining a large eddy simulation (LES) with DEM. With CFDEM, the momentum coupling of each particle on the fluid was calculated at the LES cell who contains the particle, and the fluid velocity and pressure, interpolated to each particle center, was used to derive fluid force on each DEM particle. Fig. 2.26 shows the numerical domain. According to Schmeeckle (2014), this combined LES-DEM model can be used to predict the bed-load sediment transport rates. The simulations show an exponential distribution of the velocities of the particles from the bed layer to the suspended layer, which qualitatively agrees with known physics. However, it must be pointed out that these simulations have not been validated against experimental data.

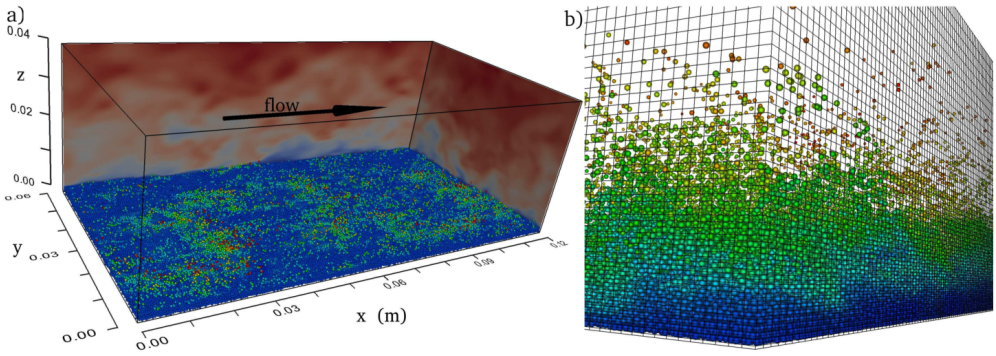

Figure 2.26: Visualization of the numerical domain. a) Shows the extent of the domain, the particles and the fluid velocity on two side edges of the domain. b) shows the grid and particles. (Schmeeckle, 2014)

Other coupling codes are also developed based on the same DEM-CFD concept. Chen et al. (2011) coupled the two open source codes, YADE-OpenDEM and OpenFOAM®, based on the DEM-FVM interaction concept, and verified this method with classical soil mechanics problems: the upward seepage flow problem and the Consolidation problem.

2.4.3. The Lagrangian-Lagrangian method

The Lagrangian-Lagrangian method is to model both the fluid and solid phases by discrete particles. The solid phase is modelled by DEM and the fluid phase by the smoothed particle hydrodynamics (SPH) method. SPH is a particle based method for modelling the coupled fluid flows. SPH particles represent the 'blobs' of discretized fluid that moves in response to the fluid or solid stresses produced by the interaction with other particles. The advantage of SPH is that this method can solve systems

of partial differential equations (PDEs) without using any grids or meshes. Cleary and Prakash (2004) explained the concept of SPH and compared the advantage and disadvantage between DEM, SPH and other numerical techniques. Case studies like flooding of a river valley, coastal inundation by a tsunami, volcanic lava flow and landslides were done with DEM or SPH. Basically, the SPH interpolation works in such a way: a particle 'b' has properties: mass m_b, position $\vec{r}_b$, density ρ_b and velocity $\vec{v}_b$. The interpolated value of any field A' at position $\vec{r}$ is approximated using information from these particles by

$$A'(\vec{r}) = \sum_b m_b \frac{A'_b}{\rho_b} W(\vec{r} - \vec{r}_b, h') \tag{2.13}$$

where W is an interpolating kernel, h' is the interpolation length and the value of A' at $\vec{r}_b$ is denoted by A'_b. The sum is over all particles 'b' within a radius $2h'$ of $\vec{r}_b$. $W(\vec{r}, h')$ is a spline-based interpolation kernel of radius $2h'$.

Ebrahimi et al. (2013) compared coupled DEM-CFD and SPH-DEM methods in single and multiple particle sedimentation test cases. It was found that for DEM-CFD coupling, a lower ratio between the fluid time-step to particle time-step ensures better coupling and information exchange between 2 phases, although computational costs are higher. On the other hand, SPH-DEM suffered with inability to resolve the porosity field near the edge of the domain, resulting in a incorrect porosity field in this region. High porosity gradients give rise to fluctuations in SPH fluid velocity leading further to fluctuations in the pressure field, thus causing numerical errors in the calculation of the pressure gradient force, the buoyancy force.

Fakhimi and Lanari (2014) proposed a numerical model based on DEM-SPH coupling to simulate the rock blasting process. The DEM particles are glued together with certain bond strengths to mimic the rock behaviour, while the SPH particles are used to model the continuous gas flow. The interaction of gas particles with the rock grains is designed to follow a perfect plastic collision model. It is shown that the DEM-SPH hybrid model is capable of simulating the induced shock waves in the gas together with wave propagation in the rock material.

Recently, Helmons et al. (2016a,b); Helmons (2017) conducted 2D numerical simulations of the triaxial test and the underwater excavation on rock by using DEM-SPH coupling software. The particles used in his code represent DEM and SPH particles simultaneously, in this way it avoids the effort to generate two sets of particles. With the SPH particles the local pressure gradients can be calculated thus the DEM particles will suffer the pressure gradient force from the fluid phase. The results show that the damage in the solid structure and the pore pressure distribution can both be well described, as shown in Fig. 2.27.

2.4.4. The single Eulerian method

The single Eulerian method is actually the method to treat the solid and fluid together, so it is also called the mixture model, the concept is mainly based on the drift flux

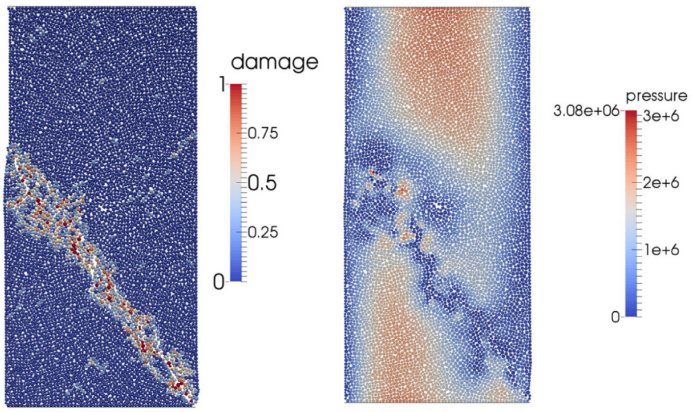

(a) Damage distribution. (b) Pore pressure distribution.

Figure 2.27: Simulation results of artificial rock tested with pore pressure = confine pressure = 0.1MPa. Results shown at the moment of failure of the rock. (a) Damage distribution and (b) pore pressure distribution. (Helmons et al., 2016b)

model. The full derivation can be found in Ishii and Hibiki (2005). The governing equations are the sum of the continuity and momentum equations of all the materials, as shown in Eq. (2.14) and Eq. (2.15)

$$\frac{\partial \rho_m}{\partial t} + \nabla \cdot (\rho_m \vec{u}_m) = 0 \tag{2.14}$$

$$\frac{\partial (\rho_m \vec{u}_m)}{\partial t} + \nabla \cdot (\rho_m \vec{u}_m \vec{u}_m) = -\nabla p_m + \nabla \cdot (\bar{\bar{\tau}}_m + \bar{\bar{\tau}}_m^t + \bar{\bar{\tau}}_m^D) + \rho_m \vec{g} + \vec{M}_m \tag{2.15}$$

Here $\rho_m[kg/m^3]$ is the mixture density, $\vec{u_m}[m/s]$ is the velocity of the centre of gravity of the mixture and $p_m[Pa]$ is the mixture pressure. $M_m[N/m^3]$ is the influence of the surface tension force on the mixture, $\bar{\bar{\tau}}_m[Pa]$ and $\bar{\bar{\tau}}_m^t[Pa]$ are the mixture shear stress tensor and the turbulent shear stress tensor respectively, $\bar{\bar{\tau}}_m^D[Pa]$ is the diffusion stress tensor due to the differences between phase velocities and mixture velocity.

This method was used frequently in the dredging relevant researches. For example, Weij et al. (2016) studied the breaching process in the bank of the river, Goeree et al. (2016) applied this method to study the concentration and velocity profiles of sediment-water mixture flows.

3

Numerical Methods for Underwater Excavation Process

This chapter will first analyse the characteristics of the underwater excavation process, and then explain the procedure of choosing the numerical tools. This chapter also contains a full description on the methodology of this research, including the DEM modelling of sand, clay and rock, and the DEM-FVM coupling algorithm.

For sand, two possible methods to suppress the rotation behaviour are introduced, namely the rolling friction model and non-spherical particle model. For clay, the cohesion model will be introduced. For rock, two bonding models are discussed, ¨point contact + rolling friction¨ model and the parallel bond model. Methods to generate the initial packing for rock sample by DEM are also presented. For the DEM-FVM coupling part, the governing equations for the coupling, the forces which could be applied on the solid particles are introduced.

Parts of this chapter have been published in Chen et al. (2014).

3.1. Characteristics of the problem and choices of numerical tools

The analytical models for rock/soil cutting process, as introduced in Chapter 2, are mainly based on the assumption of stationary and 2D processes. Apart from Miedema's chip type (Fig. 2.8), most of these models are based on a single failure mechanism, either tensile failure, shear failure or crushing failure. But it is known that in reality, excavation is a dynamic and 3D process, and different failure modes could occur simultaneously. Fig. 2.5 in Chapter 2 has already revealed the relation between the shear and normal stresses when rock fails. Here below in the *p-q* diagram (Fig. 3.1) from (Verhoef, 1997), it can be found that crushing, shearing and tensile failure can all happen in a confined rock cutting process.

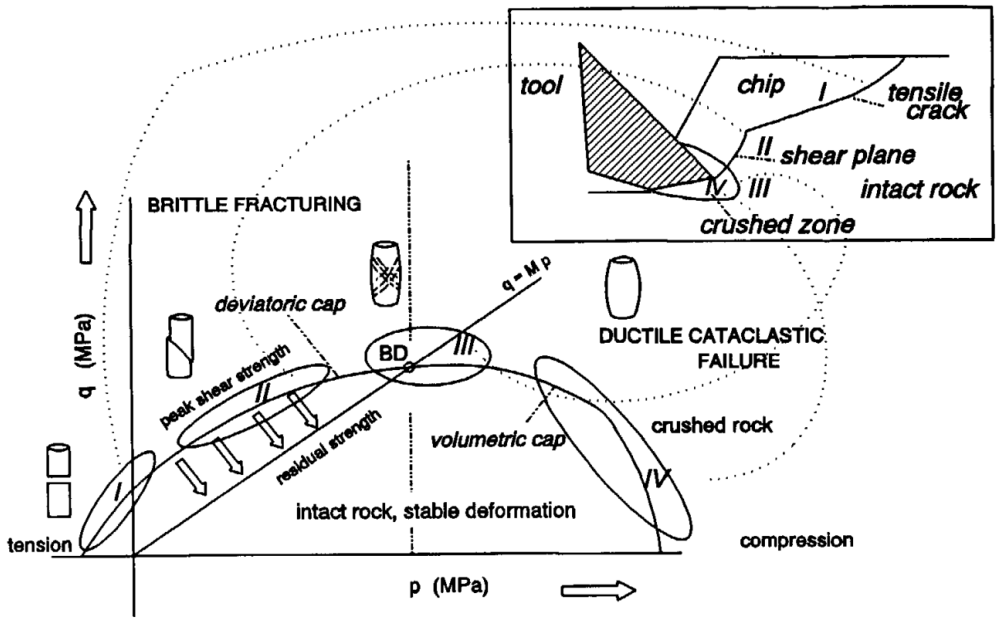

Figure 3.1: Failure during rock cutting involves the entire failure envelope, where the horizontal axis indicates the isotropic stress of the sample and the vertical axis indicates the deviatoric stress. (Verhoef, 1997)

Numerical modelling can simulate the cutting process in 3D, while catching the transient behaviour of different materials. It can describe the disorder and irregularity in the solid structure, and present the possible different failure mechanisms simultaneously, so a numerical model is required for underwater excavation process.

For numerical modelling, methods and tools must be chosen and developed. The modelling methods for solid material, as introduced in Chapter 2, are FEM and DEM.

FEM depends heavily on its mesh. For Lagrangian-based FEM, the large deforma-

tion that happens during the excavation process will distort the mesh. For Eulerian-based FEM, although it is possible to implement the Arbitrary Lagrangian-Eulerian (ALE) model to ensure the mass balance during the cutting process, still the need for frequent re-meshing makes it difficult for FEM to describe the fracturing and fragmentation process in 3D domain.

On the other hand, DEM is a meshless method. It is much easier to simulate processes like big deformation, fracturing and fragmentation with DEM than with FEM. DEM can perform different failure mechanisms spontaneously without the need of extra macro constitutive laws. Hence it is decided that DEM is chosen for modelling sand, clay and rock in this research project.

For the fluid part, it is introduced in Chapter 2 that there are Lagrangian and Eulerian methods. The Lagrangian method mentioned is SPH , which requires relatively dense distribution of the SPH particles to ensure the whole domain is covered. The two ways of using DEM-SPH coupling to simulate the underwater excavation process are analysed and compared here:

1. **DEM particles and SPH particles are two separate sets of particles.** In this case, new contact laws need to be established between DEM and SPH particles. For initial placement, SPH particles (representing the seawater) need to be very carefully inserted into the pores of the seabed soil (DEM particles) since DEM and SPH particles cannot have big spatial overlap with each other. The insertion of the SPH particles between the solid particles must also ensure a relatively high distribution density of the SPH particles to guarantee the continuity and accuracy for the fluid calculation. In underwater excavation process, the seawater above the seabed creates an open water condition. To realize that environment in 3D numerical modelling, a huge amount of SPH particles are needed to fill the space.

2. **Particles are representing DEM and SPH particles simultaneously.** This is the method used by Helmons (2017). With this method, only one set of particles is needed. Particles are representing the solid and fluid phases simultaneously. To use this method to simulate underwater excavation, initially there are no particles above the seabed, and then during the cutting process, some fragments or chips are generated and spread into open water. In numerical simulation, it means some DEM particles are moving away from the densely compacted particles' bed, but it also means that the SPH particles are moving into the open area, where they can hardly find sufficient neighbours within their influencing radii.

Comparing these two methods, the first one is apparently not suitable for modelling the underwater excavation process due to all the difficulties mentioned above. The second method, according to Helmons (2017), can successfully predict the cutting forces on the blade. But till so far it is still not able to describe the whole fluid field or the post-failure behaviour when DEM particles are dispersed into the ambient water.

In comparison, if the fluid phase is modelled by Eulerian method, then the ambient water, especially the part above the soil bed, can be well included. In this way it offers the possibility of modelling the post-failure behaviour of the soil particles. Furthermore, in computational fluid dynamics (CFD), finite volume method (FVM) is the most generic and mature numerical method. FVM can be used with different types of continuity and momentum equations. Therefore based on these considerations, it is decided in this research project, the Eulerian method, FVM, is chosen for modelling the fluid phase. The DEM-FVM coupling will be implemented to simulate the underwater excavation process.

Now the numerical method is determined, the next step is to choose the software. The DEM-FVM coupling for underwater excavation process is complicated, several existing or new models are applied for different materials. It requires the code to be fully accessible and modifiable to allow all kinds of designed treatment. From this point of view, open-source software or self-developed codes can fit the requirements. Besides, it is expected to be computationally very time consuming to calculate all the contacts between DEM particles, thus parallel computation is a must.

Goniva et al. (2010) developed an open-source software package named CFDEM which combines the strengths of two open-source software, the DEM software package LIGGGHTS (LAMMPS Improved for General Granular and Granular Heat Transfer Simulations) and the CFD software package OpenFOAM® (Open Field Operation And Manipulation). Here LAMMPS (Large-scale Atomic/Molecular Massively Parallel Simulator) was originally developed by the American Sandia National Laboratories for molecular dynamics research. By using Message Passing Interface (MPI), LIGGGHTS, OpenFOAM® and CFDEM run fully parallel on distributed-memory clusters and can be used to simulate the physical processes in 3D domain. Using CFDEM will save the effort to develop new software from scratch. Both LAMMPS and OpenFOAM® are used by a big group of users and developers, while the number of users of CFDEM and LIGGGHTS also increase rapidly.

However, it should be mentioned that parallel computation can also be realized by the help of powerful GPU (graphics processing unit). According to Helmons (2017), software developed based on CUDA (Compute Unified Device Architecture) framework can also reduce the simulation time significantly.

Comparing the two methods, currently in CFDEM, the implementation of Message Passing Interface (MPI) is more mature, it is thus decided that MPI is chosen to enable the parallel computation of CFDEM for modelling underwater excavation process.

3.2. DEM for non-cohesive material

Sand grains are non-cohesive, which means they are not bonded or glued together. No matter cutting sand in dry (atmospheric) or underwater conditions, the failure mechanism follows the shear type, but according to Merchant (1944), it can be calculated as the Flow Type, because the shearing happens continually with more or less

the same size. Fig. 3.2 gives an illustration in a 2D view.

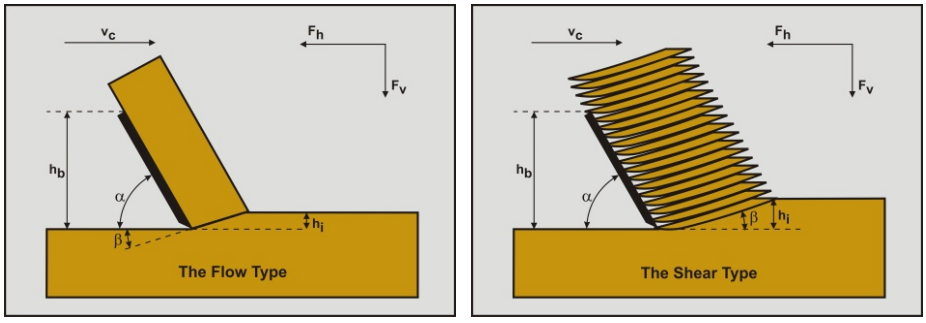

(a) (b)

Figure 3.2: Sand cutting models: (a) flow type & (b) shear type (Miedema, 2014)

In sand cutting process, due to dilatancy in the shearing in the sand layer, the pore volume will change. The sand body which originally was densely compacted becomes loose due to the effect of dilatancy. Fig. 3.3 shows the occurrence of dilatancy, where it can be observed that the pore volume increases after the shearing. In dry condition, the dilatancy phenomenon will not influence the soil strength. However, in saturated condition, the pore volume change induces local fluid flow, so that the apparent soil strength could increase due to pore under pressure.

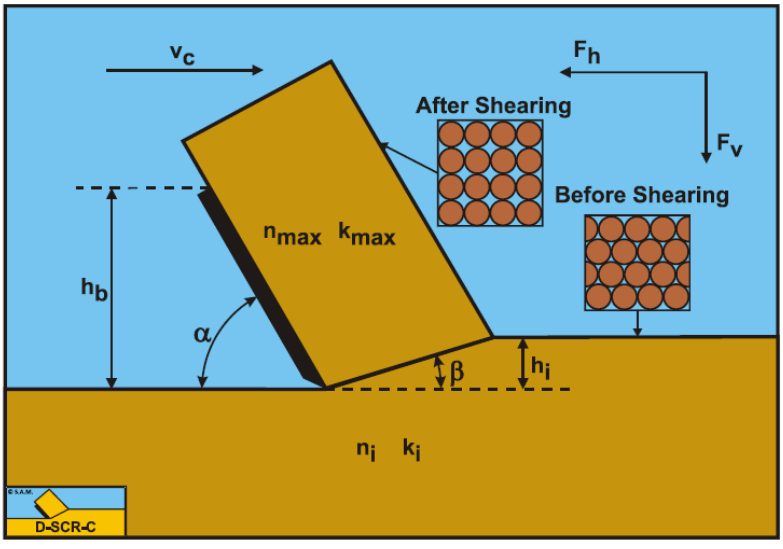

Figure 3.3: Dilatancy effect in shearing zone during cutting of dense sand (Miedema, 2014)

In DEM, sand can be simulated as many individual particles having six degrees of freedom. The interparticle forces between the DEM sand particles can be calculated by several models, among which two mainstream DEM contact models are considered

here: the Hertzian Model (Hertz, 1882; Brilliantov et al., 1996) and the Hooke Model (Radjaï and Dubois, 2011).

In the Hooke model, the contact stiffness's in the normal and shear directions are set to be equal to each other. In the Hertzian model they are treated differently, where the contact stiffness of the normal direction is linked to the Young's moduli of the two contacting particles, while that of the shear direction is linked to the shear moduli of the two particles. It is believed by Flores and Lankarani (2016) that the Hertzian model offers with more possibilities for tuning the contact force in the shear direction, making it the preferred model in the DEM modelling for free-moving soil particles. The governing equations of the Hertzian model will be introduced later in Chapter 3.2.1.

Usually in DEM spherical particles are used. But in reality sand particles' behavior is heavily influenced by their natural shapes. Simply put, as shown in Fig. 3.4, they are not spherical, and that is the reason why shearing is more dominant than rotation between sand particles. Two methods are used to overcome this problem. The first one is to add extra rolling friction to spherical particles, the other one is to use non-spherical particles.

Figure 3.4: Rounded and fine-grained eolian sand sample from the Gobi Desert (near Dalanzadgad in Mongolia). The width of the view is 10 mm (Sepp, 2011)

3.2.1. The Hertzian model for spherical particles

A DEM simulation starts with inserting all the particles with a certain orientation and a possible initial velocity into the designated space in the simulation domain. As mentioned before, the Hertzian model is chosen for calculating the contact forces between the DEM sand particles (Hertz, 1882; DCS Computing Gmbh, 2018b). This contact model calculates the normal and tangential forces between two DEM particles when the distance d between the particles is less than the sum of their radii ($d \leqslant R_1 + R_2$), as shown in Fig. 3.5. There is no force between the particles when the distance is larger than the sum of their radii ($d > R_1 + R_2$). To calculate the contact

force F_{hz} between two particles the following formula, Eq. (3.1), is used. A depiction of this contact can be found in Fig. 3.6, where the spring-damper systems of both the normal and shear directions, and the slider determined by the friction coefficient μ are all illustrated.

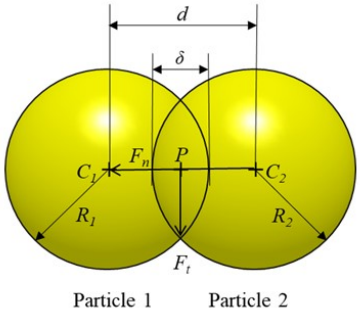

Figure 3.5: Two DEM particles in contact with each other, Particle 1 with radius R_1 and Particle 2 with radius R_2. C_1 and C_2 are the centres of the two particles respectively, d is the distance between the particles and δ is the overlap between them (Yeom et al., 2019).

$$F_{hz} = \underbrace{\left(k_n \boldsymbol{\delta_n} - \gamma_n \boldsymbol{v_{n_{12}}}\right)}_{\text{Normal Force}} + \underbrace{\left(k_t \boldsymbol{\delta_t} - \gamma_t \boldsymbol{v_{t_{12}}}\right)}_{\text{Tangential Force}} \tag{3.1}$$

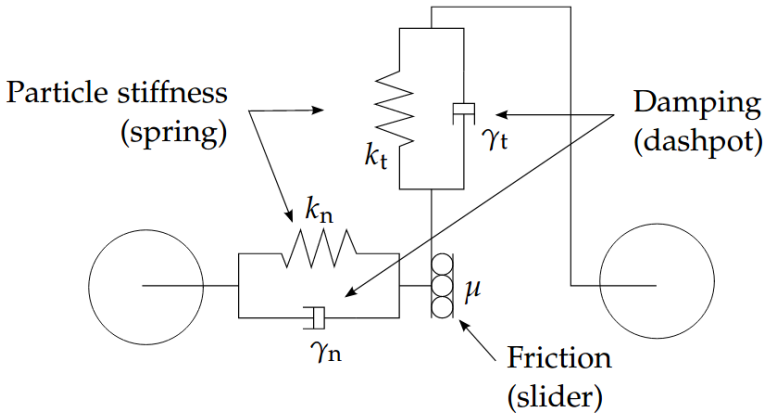

Figure 3.6: Schematics of normal and tangential dashpot systems for particle-particle interactions in DEM (Hærvig, 2017).

Eq. (3.1) contains of a normal force and a tangential force. The normal force consists of a contact force and a damping force and the tangential force consists of a shear force and a damping force. Where k_n is the elastic constant for the normal contact and k_t for the tangential constant, $\boldsymbol{\delta_n}$ is the normal overlap distance of two particles and $\boldsymbol{\delta_t}$ the tangential overlap distance, γ_n is the viscoelastic damping constant

for normal contact and γ_t the viscoelastic damping constant for tangential contact, $\boldsymbol{v}_{\boldsymbol{n}_{12}}$ is the normal component of the relative velocity of the two particles and $\boldsymbol{v}_{\boldsymbol{t}_{12}}$ the tangential component.

The normal overlap distance $\boldsymbol{\delta_n}$ can be easily calculated as:

$$\boldsymbol{\delta_n} = R_1 + R_2 - d \tag{3.2}$$

While the tangential overlap distance $\boldsymbol{\delta_t}$ needs to be calculated in an incremental way. It is calculated by integrating the relative tangential velocity at the contact point ("P" in Fig. 3.5) over time duration (t_c) when the two particles are in contact, as shown in Eq. (3.3).

$$\boldsymbol{\delta_t} = \frac{\boldsymbol{v}_{\boldsymbol{t}_{12}}}{|\boldsymbol{v}_{\boldsymbol{t}_{12}}|} \cdot \int_0^{t_c} |\boldsymbol{v}_{\boldsymbol{t}_{12}}| dt \tag{3.3}$$

The constants are calculated with the material properties using the following formulas:

$$k_n = \frac{4}{3} \cdot Y^* \sqrt{R^* \delta_n} \tag{3.4}$$

$$\gamma_n = -2\sqrt{\frac{5}{6}} \beta_\gamma \sqrt{s_n m^*} \geq 0 \tag{3.5}$$

$$k_t = 8G^* \sqrt{R^* \delta_n} \tag{3.6}$$

$$\gamma_t = -2\sqrt{\frac{5}{6}} \beta_\gamma \sqrt{s_t m^*} \geq 0 \tag{3.7}$$

Where Y^* depends on the Young's modulus of the materials, G^* depends on the Shear modulus. R^*, s_n, s_t, β_γ and m^* are coefficients which calculate the constants in Eq. (3.1) according to the following formulas:

$$s_n = 2Y^* \sqrt{R^* \delta_n} \tag{3.8}$$

$$s_t = 8G^* \sqrt{R^* \delta_n} \tag{3.9}$$

$$\beta_\gamma = \frac{ln(e)}{\sqrt{ln^2(e) + \pi^2}} \tag{3.10}$$

$$\frac{1}{Y^*} = \frac{(1-\nu_1^2)}{Y_1} + \frac{(1-\nu_2^2)}{Y_2} \tag{3.11}$$

$$\frac{1}{G^*} = \frac{2(2-\nu_1)(1+\nu_1)}{Y_1} + \frac{2(2-\nu_2)(1+\nu_2)}{Y_2} \tag{3.12}$$

$$\frac{1}{R^*} = \frac{1}{R_1} + \frac{1}{R_2} \tag{3.13}$$

$$\frac{1}{m^*} = \frac{1}{m_1} + \frac{1}{m_2} \tag{3.14}$$

Where Y is the Youngs modulus of the material, R is the radius, G is the shear modulus, ν is the poisson ratio and e is the coefficient of restitution and m is the mass of the particle.

3.2.2. The rolling friction model

The motivation to use the rolling friction model is very simple: if rolling behaviour of the spherical particles is significantly restricted, then the spherical particles will shear along each other. For a spherical particle, the resistance against the rotational movement is much smaller than in the shear movement, because the latter one is dominated by the frictional force. Thus without rolling friction, spherical particles will always choose to rotate instead of shearing along each other.

The Constant Directional Torque (CDT) (Ai et al., 2011; DCS Computing Gmbh, 2018a) adds rolling friction to rounded particles. This model creates an extra counter-torque contribution, $Torque_{anti}$, to the particles' contact. In this way when a particle is going to rotate over another particle or along a geometry, an anti-torque will be added to this particle, in the opposite direction of the rotational movement. This anti-torque can be calculated as:

$$Torque_{anti} = -\mu_r \cdot k_n \cdot \delta_n \cdot R^* \cdot \frac{\boldsymbol{\omega}_{r_{shear}}}{|\boldsymbol{\omega}_{r_{shear}}|} \tag{3.15}$$

in which μ_r is the rolling friction coefficient, δ_n is the overlap distance of two particles, $\boldsymbol{\omega}_{r_{shear}}$ is the projection of the relative rotational velocity of the 2 particles $\boldsymbol{\omega}_r$ into the shear plane. $\boldsymbol{\omega}_r$ can be calculated with:

$$\boldsymbol{\omega}_r = \boldsymbol{\omega}_1 - \boldsymbol{\omega}_2 \tag{3.16}$$

Where $\boldsymbol{\omega}_1$ is the rotational velocity of the first particle and $\boldsymbol{\omega}_2$ the rotational velocity of the second particle. In Eq. (3.15), the rolling friction coefficient μ_r is

an input parameter of a DEM simulation if the CDT model is activated, it links the contact in the normal direction to the suppression of the rotational movement of both particles. This coefficient is used as a tuning factor for determining to what extent the rotational motion of DEM particles is suppressed.

3.2.3. The non-spherical particle model

To simulate real sand behavior, the particles are made "less" rounded by using non-spherical / multi-spherical particles. In reality, the movement of sand particles is strongly affected by their shapes and material properties. The natural shape of a sand particle can never be a perfect sphere, usually it is of some crystalline geometries.

In the past, Rahman et al. (2011) has conducted DEM simulations of passive soil failure test and sand cutting process. He tried geometry of four spheres combination (Rahman et al., 2010) and later seven spheres combination (Rahman et al., 2011), but he did not clearly explain the construction of his non-spherical particles.

To create reasonable DEM particles to represent sand grains, (Chen et al., 2013; Chen and Miedema, 2013) carried out a series of comprehensive research. In total six different geometries to imitate a sand particle were created, as shown in Table 3.1. A group of cutting simulations has been undertaken in 3D by the software EDEM^{TM} to find out with which particle geometry, the simulation has the maximum similarity with experimental observations.

Results from (Chen et al., 2013; Chen and Miedema, 2013) show that, **Type 4**, the particle made by four combined spheres with a inner structure of tetrahedron (Fig. 3.7), is the best particle shape to imitate the natural sand particle.

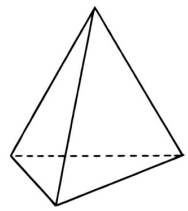

Figure 3.7: Regular tetrahedron: the optimal inner structure for DEM sand particle

It should be mentioned that there are actually countless ways to create a non-spherical particle, but since the purpose is to give out some easy designs which can be quickly implemented into many other sand-related applications, there is no need to create more complicated geometries. Combining identical spheres on easily recognizable internal structure gives the design much broader adaptability. If the design is made by using different-sized spheres, or is based on a very complicated internal structure, or contains more than six spheres, then the adaptability of the design is reduced and the required computational time will be much longer.

Table 3.1: Descriptions and pictures of the six types of particles (Chen et al., 2013)

Construction of the particle	Pictures of the particle
Particle Type 1: A spherical particle.	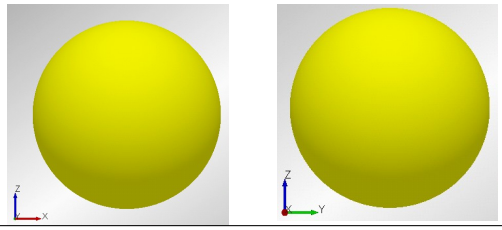
Particle Type 2: A non-spherical particle made by two partially merged spheres. These two spheres are identical to each other. The distance between the two centers of the spheres equals to the radius of each sphere.	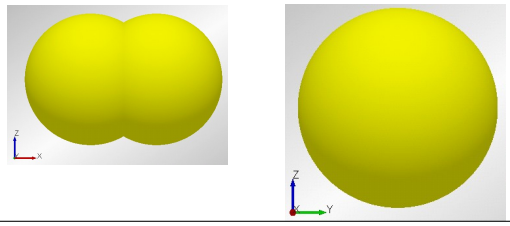
Particle Type 3: A non-spherical particle made by three combined spheres. These three spheres are identical to each other and partially overlapped. The internal structure of this particle is a regular triangle. On each vertex there located a sphere whose radius equals to the side length of the regular triangle.	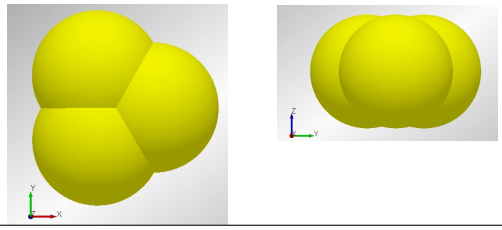
Particle Type 4: A non-spherical particle made by a combination of four identical spheres. The internal structure of this geometry is a regular tetrahedron, where each vertex is the center of a sphere. The radius of the sphere equals to the side length of this regular tetrahedron.	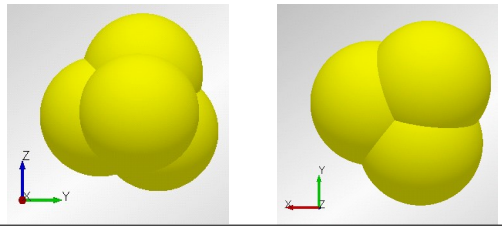
Particle Type 5: A non-spherical particle made by five identical spheres. The basic structure is two identical regular tetrahedrons with shared bottom face. So in total there are five vertexes and on each vertex there is a sphere located. The sphere' s radius equals to the side length of the regular tetrahedron.	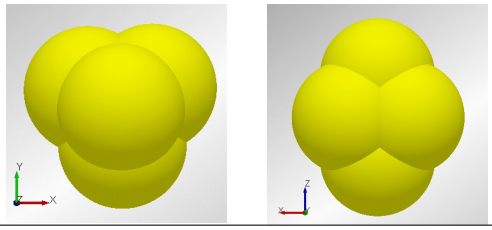
Particle Type 6: A non-spherical particle generated from six identical spheres. The internal structure is two identical square pyramidal pentahedrons who share their square bottom face with each other. All the side lengths in the structure are the same to each other. In total there are six vertexes, and on each vertex there is a sphere center located. The sphere' s radius equals to side length of the pentahedron.	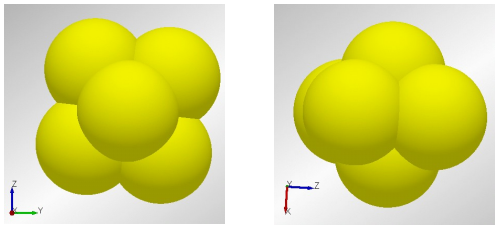

What should also be noticed is that here the expression "combined spheres" is used instead of "bonded spheres". The reason for that is bond is a special contact status in DEM which could be broken when the contact force exceeds the maximum bond strength. On the contrary, here the combined spheres are actually partially merged with each other, the connection is unbreakable, which is the most important distinction from bond contact.

3.3. DEM for cohesive material

Cohesive material can also be modelled by DEM. In soil mechanics, a typical cohesive material is clay. Cohesive soil possesses cohesive properties between the particles and adhesive properties to other materials. Cohesion is the part of the shear strength that is independent of inter-particle friction in the cohesive soil. It is the force that holds the fine-grained particles together by electrostatic bonds and cementing agents between the particles (Chen et al., 2015; Lal, 2006). Adhesion is the phenomenon of cohesive soil sticking to another material; it is a measure of the 'stickiness' of the soil. This adhesion between cohesive soil and other materials is partly due to direct attraction between the soil particles and the foreign material and partly due to adhesive action of the water in the cohesive soil, but the latter force is strongly dominant (Fountaine, 1954).

To describe the contact of cohesive particles in DEM, the core equation is still Eq. (3.1). As introduced before in Chapter 3.2, the Hertzian contact model is applied because it offers more flexibility for tuning the contacts in different directions. Thus Eq. (3.4) to (3.14) are again used to calculate the interparticle forces.

Apart from the Hertzian model, an extra layer is needed to express the cohesive and adhesive forces between the cohesive DEM particles, "the sticky part". In this research project, the Simplified Johnson-Kendall-Roberts (SJKR) cohesion model is chosen for this part. The SJKR cohesion model adds an additional attractive normal force to particles in contact which resists separation. The force on a particle by cohesion is proportional to the overlap area and can be simply modelled as stated in Eq. (3.17), where K is the cohesion energy density $[Pa]$ and A_p the interparticle overlap area $[m^2]$ (Flores and Lankarani, 2016). A_p can be calculated by using the distance L_{AB} between contacting particle A and B, and the radii of both particles R_A & R_B, as shown in Eq. (3.18).

$$F_{co} = K \cdot A_p \tag{3.17}$$

$$A_p = \frac{\pi}{4} \cdot \frac{(L_{AB} - R_A - R_B) \cdot (L_{AB} + R_A - R_B) \cdot (L_{AB} - R_A + R_B) \cdot (L_{AB} + R_A + R_B)}{L_{AB}^2} \tag{3.18}$$

Eq. (3.17) determines the cohesion and adhesion force in the normal direction. F_{co} is then combined to the normal force component in the Hertzian model (Eq. (3.1)) to

obtain the total normal force F_n. It should be noted that F_{co} is an attractive force while the normal force component in the Hertzian model (Eq. (3.1)) is a repulsive force, so they are in the opposite direction.

For the tangential direction, the tangential force F_{tan}, as calculated in Eq. (3.1) ~ (3.14) according to the standard Hertzian model, is restricted by:

$$F_{tan} \leq X_\mu F_n \tag{3.19}$$

where X_μ is the static friction coefficient and F_n is total normal contact force.

As stated in Eq. (3.17), the cohesive force between two particles is the product of the cohesive energy density K and the overlap area A_p. At the microscopic scale, which is the spatio-scale of the DEM particle, the cohesive force computed by the SJKR-model qualitatively and quantitatively agrees with the physical phenomena taking place between two grains. However, at the macroscopic level, the SJKR-model has difficulty to generate large cohesive forces (Del Cid, 2015).

The reason is that the DEM particles used in this research project is the stiff particles for which deformation is forbidden. It only allows very small overlapping depth between two particles. From Eq. (3.18) it can be found that A_p is calculated by using the overlap depth and the particle radii. Since the allowed overlap depth between stiff particles is very small, while the particle radii, in common practice of applying DEM into soil mechanics, is also at a small level of ~ 1 mm. the overlap area A_p between spherical particles will thus be significantly small. Therefore, at the macroscopic scale, the mechanic behaviour can be dominated by the larger gravitational and frictional forces.

One way to overcome this problem is by increasing the cohesion energy density K to increase the normal force between two particles. The second way is to scale up the particle size because the interparticle overlap area A_p increases when the particles' radii increase (Eq. (3.18)). In this research it is preferred to tune the particle size to reach the expected cohesion, as increasing the cohesion energy density K can easily lead to numerically unstable situations.

In dredging, engineers often assume clay has no internal or external friction, which means the internal or external friction coefficients will be zero. If $X_\mu = 0$ in Eq. (3.19), then there is no room for F_{tan} to develop. However, what people have mostly encountered in nature is cohesive soil which consists of both clay and sand, not pure clay. It is reported in the earlier publications of the author ((Chen et al., 2019a) and (Chen et al., 2019b)) that in lab experiments, the two types of cohesive soils studied have internal friction coefficient up to 0.35. Therefore, in this research, the X_μ between cohesive DEM particles is set to 0.35. This is considered as a reasonable value which satisfies the needs of numerical modeling and also reasonably matches the reality.

When all forces on the particles are computed, the *NVE* integration (constant number (N), volume (V), and energy (E) integration, where the sum of kinetic and potential

energy is conserved) is performed to compute the change in particle position, linear velocity and angular velocity during the specified time step, governed by Newton's laws of motion. Subsequently, the updated positions and velocities are used to compute the forces during the next time step. This process continues until the end time of the simulation is reached.

3.4. DEM for rock-like material

Rock is a complicated solid material. According to its formation process, rock can be divided into sedimentary rock, metamorphic rock and igneous rock, as previously introduced in Chapter 2. It is the most complicated soil type for DEM simulations, especially considering the fact that natural rock usually contains certain disorder and irregularity in its internal solid structures, such as pre-existing fractures. The internal heterogeneity makes the natural rock mechanically anisotropic.

In this part of the research, DEM is used to model the rock-like material, which means to mimic the mechanical behaviour of rock. It is possible to create different heterogeneities in DEM rock samples. For example, Scholtès and Donzé (2012) developed a series of constitutive laws to model the joint-band and the pre-existing flaws in DEM samples for rock. They plugged pre-existing discontinuities as a discrete fracture network (DFN) into the DEM rock sample. They also modified the basic contact model so that the joints in the heterogeneous rock can be presented. Fig. 3.8 shows the comparison of experiments from the laboratory and the numerical simulation with modified DEM.

However, to model the underwater excavation process, the influence of water becomes a big concern. It is more reasonable to use isotropic material as the starting point. Thus this research does not take anisotropy into account. Isotropic rock samples are generated with DEM in this research. Pre-existing fractures are only recommended for future study.

3.4.1. The bond models

Isotropic rock can be seen as homogeneous material consisting of many bonded grains. Based on this concept, bonding models are developed for enabling DEM to model rock behaviour. In a DEM rock sample, all the neighbouring particles are initially bonded together at their contact points, where the bonds limit the particles' motion. During loading, when the maximum strength of a bond is exceeded, this bond will break and cannot be recovered. After the bond is broken, the interaction between these two particles shifts from the bonding model to the collision model, which means the contact between these particles changes from the bonded behaviour to the grain behaviour. In this way the rock failure process can be simulated.

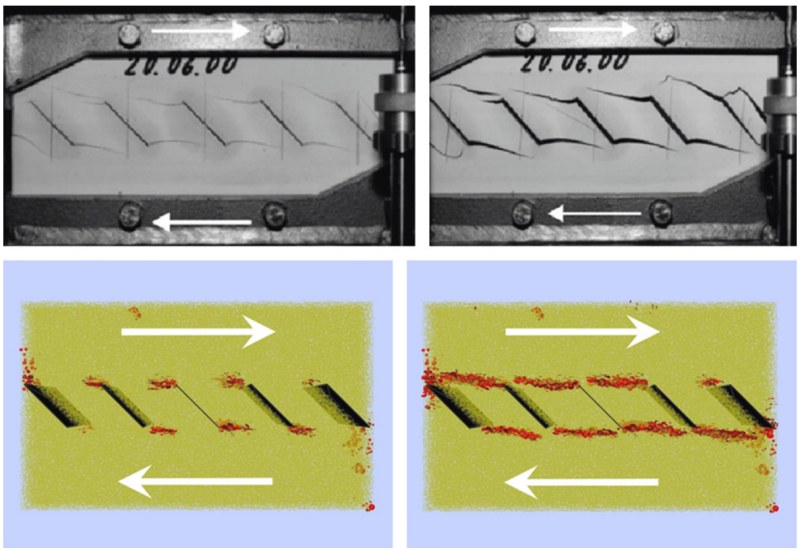

Figure 3.8: Fracture propagation and coalescence of intermittent rock joints: (top) successive snapshots from experiments made by Gehle and Kutter (2003), (bottom) numerical prediction from the DEM. (Scholtès and Donzé, 2012)

Potyondy and Cundall (2004) developed the bonded particle model (BPM) for simulating rock in DEM. BPM consists of the bonding model and the collision model. The bonding model describes the cemented behaviour between bonded particles, while the collision mode describes the grain interaction between unbonded particles. Potyondy and Cundall (2004) proposed two bonding models, the contact bond model and the parallel bond model (PBM), as shown in Fig. 3.9.

A contact bond is based on a point contact between two particles, thus only the normal force and the shear force can be transferred. A parallel bond is based on the assumption that there is a beam connecting the two bonded particles. With this beam, not only the normal and shear forces, but also the twisting torque and the bending moment can be transferred between particles.

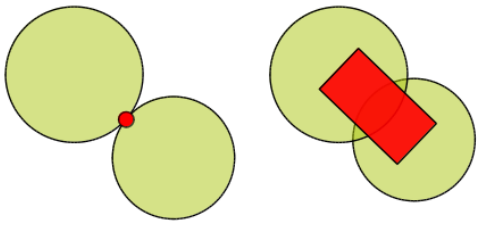

Figure 3.9: Bond between DEM particles, left: contact bond. right: parallel bond

In a contact bond model, twisting and bending between bonded particles are not restrained. For relatively weak rock, e.g., some limestone and shale, this model is sufficient. However, that does not hold for strong rocks, e.g. granite with a UCS greater than 100MPa. PBM is more suitable because it also restricts the twisting and bending. This offers the rock sample a higher resistance against structure failure. PBM is more widely applicable hence it is the chosen bonding model for this research.

PBM assumes that two particles are bonded on microscopic scale with a connecting beam. According to Potyondy and Cundall (2004), this connecting beam satisfies the criterion of an Euler–Bernoulli beam, which means the cross-section should always be perpendicular to the axial axis. The maximum tensile and shear stresses at failure in the beam's periphery are calculated by Eq. (3.20) and Eq. (3.21). If either the maximum tensile stress exceeds the tensile strength of the bond ($\bar{\sigma}_{max} \geqslant T_n$) or the maximum shear stress exceeds the shear strength of the bond ($\bar{\tau}_{max} \geqslant T_s$), the bond, in other words, the Euler–Bernoulli connecting beam will break.

$$\bar{\sigma}_{max} = \frac{-\bar{F}_n}{A} + \frac{|\bar{M}_s|\bar{R}}{I}, \text{ bond breaks when } \bar{\sigma}_{max} \geqslant T_n \tag{3.20}$$

$$\bar{\tau}_{max} = \frac{|\bar{F}_s|}{A} + \frac{|\bar{M}_n|\bar{R}}{J}, \text{ bond breaks when } \bar{\tau}_{max} \geqslant T_s \tag{3.21}$$

Basically, in this model, the beam has certain length to connect the two particle centres, and a circular cross-section with a radius equal to a fraction of the radius of the smaller particle of the two. In Eq. (3.20) and Eq. (3.21), $\bar{\sigma}_{max}$ is the maximum tensile stress in the bond $[N/m^2]$ and $\bar{\tau}_{max}$ is the maximum shear stress $[N/m^2]$, $\bar{F}_n$ is the contact force in the normal direction in the bond $[N]$ and $\bar{F}_s$ is the contact force in tangential direction in the bond $[N]$, A and $\bar{R}$ are the area $[m^2]$ and the radius $[m]$ of the cross-section of the parallel bond respectively, I and J are the moment of inertia $[m^4]$ and polar moment of inertia $[m^4]$ of the parallel bond cross-section respectively, $\bar{M}_s$ and $\bar{M}_n$ are the bending moment $[N \cdot m]$ and twisting torque $[N \cdot m]$ of the bond respectively.

But the Euler–Bernoulli beam is not the only choice, Obermayr et al. (2013) used the Timoshenko beam to establish the bond between particles to mimic the cemented sandstone behaviour, in this way the cross-section of the beam is deformable, not always perpendicular to the axial direction. The linear displacements, the twisting and bending are still constrained, the calculation with the Timoshenko beam theory is much more complicated. Obermayr et al. (2013) applied quaternion to calculate the relative motion and position between the particles and the Timoshenko beam, which actually means all the properties of motion and position of the bond need to be interpreted into the quaternion system for calculation. To determine the failure of the bond thus becomes more complicated, as shown in Eq. (3.22), (3.23) (3.24), (3.25) and (3.26).

$$\sigma_{axial} = E_b \cdot \Gamma_{T,x} + \sqrt{(E_b \cdot \kappa_{T,y} \cdot r_b)^2 + (E_b \cdot \kappa_{T,z} \cdot r_b)^2} \tag{3.22}$$

$$\tau_{shear} = G_b \cdot \kappa_{T,x} \cdot r_b + \sqrt{(G_b \cdot \Gamma_{T,y})^2 + (G_b \cdot \Gamma_{T,z})^2} \tag{3.23}$$

$$\sigma_{eqv} = \begin{cases} \sqrt{\sigma_{axial}^2 + 3 \cdot \tau_{shear}^2} & \text{, if } \sigma_{axial} \text{ is tensile stress} \\ \sqrt{3 \cdot \tau_{shear}^2} & \text{, if } \sigma_{axial} \text{ is compressive stress} \end{cases} \tag{3.24}$$

$$\alpha_b = \begin{cases} \alpha_r \cdot \alpha_\sigma & \text{, if } \Gamma_{T,x} < 0 \\ \alpha_r & \text{, else} \end{cases} \tag{3.25}$$

$$\sigma_{eqv} > \alpha_b \sigma_{break} \tag{3.26}$$

E_b, G_b are the Young' s and shear modulus of bond element, i.e., the Timoshenko beam, respectively. Γ_T and κ_T are the strain and curvature vector of the bond beam, r_b is the radius of the cross-section of the beam, α_b, α_σ are modification factor of the bond strength and the compressive strength respectively, α_r is the random number. σ_{eqv} is the equivalent stress in the beam. In this model, the curvature and the strain of the bonding beam are obtained via the quaternion calculation and then interpreted back to the coordinates system (usually Cartesian), next the von Mises criterion is applied to get a equivalent stress in the beam. Finally if this equivalent stress (σ_{eqv}) exceeds the product of the bond modification factor (α_b) and the breakage stress of the bond (σ_{break}), the bond will fail.

Although both beams can be used to build up the parallel bond between particles, the implementation of the Euler–Bernoulli beam is easier and simpler than the Timoshenko beam. Besides, in (Potyondy and Cundall, 2004)'s theory, the bonding model has a relatively better consistency with the collision model since both of them are based on the linear elasticity theory, while in the model of Obermayr et al. (2013), the bonding model is calculated with quaternion but the collision part is calculated with the motion functions of a spring-damper system. So taking these two factors into consideration, it is decided that the bond model proposed by Potyondy and Cundall (2004) is chosen for this research.

The bonding forces and moments in Eq. (3.20) and (3.21) are calculated in an accumulative way. If two particles are bonded, particle A with a radius R_A and particle B with a radius R_B. it should be mentioned that R_A does not necessarily equal R_B, which means the two particles can be of different sizes. Then the incremental bonding force in the normal direction $\Delta\bar{F}_n$, the incremental bonding force in the shear direction $\Delta\bar{F}_s$, the incremental bonding moment in the normal direction $\Delta\bar{M}_n$ and the incremental bonding moment in the shear direction $\Delta\bar{M}_s$ can be calculated via Eq. (3.27) to (3.30).

$$\Delta\bar{F}_n = -\bar{k}_n A \Delta U_n \tag{3.27}$$

$$\Delta\bar{F}_s = -\bar{k}_s A \Delta U_s \tag{3.28}$$

$$\Delta\bar{M}_n = -\bar{k}_s J \Delta\theta_n \tag{3.29}$$

$$\Delta\bar{M}_s = -\bar{k}_n I \Delta\theta_s \tag{3.30}$$

in which $\bar{k}_n$ and $\bar{k}_s$ are the normal and shear stiffness of the bond respectively, ΔU_n and ΔU_s are the relative displacement increment in normal and shear directions respectively, $\Delta\theta_n$ and $\Delta\theta_s$ are the relative rotation increment in normal and shear directions respectively. Equations to obtain all the required parameters are listed here:

$$A = \begin{cases} 2\bar{R}t_s, \ t_s = 1, & (2D) \\ \pi\bar{R}^2, & (3D) \end{cases} \tag{3.31}$$

$$I = \begin{cases} \frac{2}{3}\bar{R}^3 t_s, \ t_s = 1, & (2D) \\ \frac{1}{4}\pi\bar{R}^4, & (3D) \end{cases} \tag{3.32}$$

$$J = \begin{cases} NA, & (2D) \\ \frac{1}{2}\pi\bar{R}^4, & (3D) \end{cases} \tag{3.33}$$

$$\bar{R} = \bar{\lambda}\min(R_A, R_B) \tag{3.34}$$

$$\bar{k}_n = \frac{\bar{E}_c}{R_A + R_B} \tag{3.35}$$

$$\bar{k}_s = \frac{\bar{k}_n}{\bar{k}_n/\bar{k}_s} \tag{3.36}$$

$$\Delta\theta = (\omega_B - \omega_A)\Delta t \tag{3.37}$$

$$V_{BA} = V_B^c - V_A^c \tag{3.38}$$

$$\Delta U_n = V_n \Delta t = V_{BA} \cdot \vec{n} \cdot \Delta t \tag{3.39}$$

$$\Delta U_s = V_s \Delta t = (V_{BA} - V_n) \cdot \Delta t \tag{3.40}$$

Here $\bar{\lambda}$ is the bond-radius multiplier, $\bar{E}_c$ is the Young's modulus of the bonding beam, ω_A and ω_B are the rotational velocities of particles A and B respectively. V_{BA} is the relative velocity between particle B to A, V_B^c and V_A^c are the velocities of Particle B and A at the center of the bonding beam respectively, V_n and V_s are the relative normal and shear velocities between the two particles respectively, $\vec{n}$ is the unit vector for the normal direction of the contact, Δt is the calculation time step.

3.4.2. Generation of rock sample

In DEM, a rock sample consists of a pre-defined space filled with many DEM particles, and depending on the way it is generated, the neighbouring particles may or may not have overlaps with each other. As introduced in the previous section, the overlap between particles will generate bonding and contact forces. If particles have big overlaps with each other in the initial packing, then initially both the microscopic and the macroscopic stresses level will be very high, in this way the sample will be unstable from the beginning. Later if external loads are applied, there is a high possibility that

the particles will be just shot out or explode. Such kind of DEM sample cannot be used for studying the excavation process because it does not match reality at all, a good DEM rock sample should not contain very high initial stress level. To achieve that, the placement of particles should be arranged in such a way that no big overlap between the particles exists in the packing.

Besides, to appropriately simulate the rock behaviour, the initial packing of the DEM sample should be as dense as possible. There are two reasons why this is necessary:

- To guarantee a good connecting network for transmitting the forces. The coordination number of an assembly c is defined as the average number of contacts per particle. According to Bagi (2005), the coordination number in 2D should be around $3.9 \sim 4.3$ to realize a good connectivity, while in 3D it is proposed by Lozano et al. (2016) that the coordination number is usually above 5.7 to reach a good connectivity. If the coordination number is too low, the external loading cannot be sufficiently transmitted into the whole rock sample on time, thus the material will show anisotropic behaviour.
- To avoid too much void space inside the DEM rock samples. In a loosely packed DEM sample, many pores occupy a large portion of the total volume. During loading of such kind of assembly, the particles will just move into the pores to fill the space instead of breaking into chips and fragments. Thus the process becomes a pure compaction and dispersion. Discrete failure of rock will not occur.

Based on all the arguments mentioned above, it is required for rock simulation to have a densely compacted DEM sample with a reasonable coordination number. A good DEM rock sample is the starting point for rock-relevant simulations and can be used for many different processes. It should be noted that even following the same generation procedure and the same input parameters, but due to the randomness of generation procedure itself, the generated samples may still show slight differences macroscopically. As long as they fit for the criterion mentioned above, then they are still good DEM rock samples. What is usually seen is that there are variations in the results of the simulations for mechanical properties of these rock samples, but the bandwidths are very narrow. In other words, these not-exactly-identical DEM rock samples will show the same mechanical behaviour. From this perspective, numerical experiments are the same as laboratory experiments. Because in laboratory experiments, rock samples obtained from the same site also show some variations in their mechanical properties.

Several different methods can be applied to achieve a good DEM rock sample. In general, by using spherical particles with a range of radii, the packing methods can be divided into two categories, the static method and the dynamic method, in which static methods are also referred as "the constructive algorithms".

In the static method the assembly is based on purely geometrical calculations, without the effort of running DEM simulations. Stoyan (2002) made an overview

on the static methods from the early years. The Stienen model (Stienen, 1982), the lily-pond model (Meester et al., 1996), the simple sequential inhibition model (Evans, 1993), the Metropolis-Hastings algorithm (Metropolis et al., 1953; Hastings, 1970), and the sedimentation technique (Jodrey and Tory, 1985), are all briefly introduced. Bagi (2005) later developed the inwards packing method and made several comparisons with previous models.

The Stienen model (Stienen, 1982) starts with randomly placing N points in the 2D or 3D domain. For each point the distance from its nearest neighbour is determined. Then a circle/sphere is defined around the point, with a radius equal to the half of this distance. Meester et al. (1996) developed the lily-pond model which also starts from a set of randomly located points. A circle/sphere is defined around each point initially with zero radius. The radii are then increased with a uniform speed, and the growth of a certain particle stops when it comes into contact with another particle.

The simple sequential inhibition (*SSI*) model developed by Evans (1993) generates circles or spheres of equal or user-defined diameter sequentially at random positions in the 2D or 3D domain, the insertion of a new particle is rejected if it intersects a previous one.

The Metropolis-Hastings algorithm based on (Metropolis et al., 1953) and (Hastings, 1970) are initiated with a random placement of spheres, and then three probabilities are calculated, which are the probability for inserting a new sphere p^{ins}, for deleting an existing sphere p^{del} and for re-locating an existing sphere $(1-p^{ins}-p^{del})$. Later these proposed actions are accepted with the probabilities called the Hastings-ratios.

Jodrey and Tory (1985) proposed the sedimentation techniques, where a bottom layer of particles are initially placed and new particles are generated and translated downwards until it touches an existing sphere, the new particle will roll itself until it is stably supported by three previous spheres. Although the terms "translated" and "roll" are mentioned, only geometrical calculation is carried out in this model, so it is still a static method since it does not involve dynamic simulations.

Bagi (1993) proposed a dropping method as shown in Fig. 3.10, which is actually the 2D version of the sedimentation algorithm. Feng et al. (2003) developed the open front method and the closed front method. The open front method is similar to the dropping method, thus the same principle as the sedimentation technique. The closed front method is to fill up the desired 2D domain along an outwards spiral from a triangle of three touching particles in the middle of the domain, as shown in Fig. 3.11.

Cui and O' Sullivan (2003) developed a triangulation based approach for specimen generation. In this method, a random mesh of triangles (2D) / tetrahedron (3D) is firstly generated, then particles are generated as the incircles/inspheres of the triangles/tetrahedron or around the nodes.

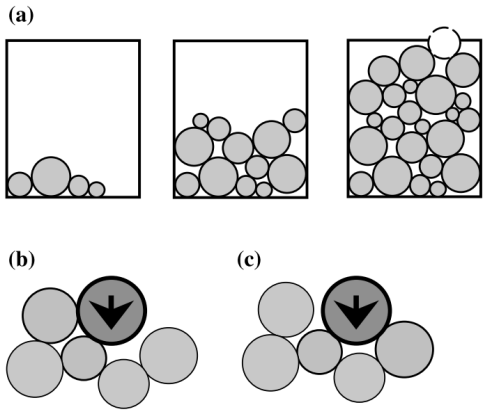

Figure 3.10: The dropping method: (a) The general idea of the algorithm; Unstable (b) and stable (c) position of a new grain (Bagi, 2005)

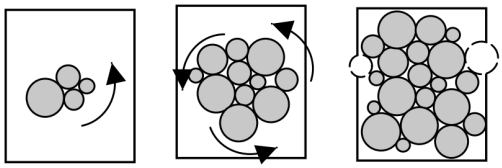

Figure 3.11: The closed front method of Feng et al. (2003), (Bagi, 2005)

Among the static methods mentioned above, only the ones with the sedimentation process and the closed front can generate a dense sample with a reasonable coordination number, but they still have major difficulties in filling the gap with the boundaries of the domain. As shown in Fig. 3.11, in the final step the particles are too big to fit within the boundaries, thus there are significant gaps between the sample and the domain. To solve this issue, Bagi (2005) developed the 2D inwards packing method where the edges of the domain are firstly filled up so a closed chain of particles is formed. This chain is called the initial front (Fig. 3.12). Later every new particle is placed inwards along the initial front with two contacts to the existing particles. Finally some small particles are generated to fill in the middle gap of the domain (Fig. 3.13). The process stops when no more particles can be inserted. Bagi compared this method with the dropping method and the dynamic deposition method, the results shows the inwards packing method delivers satisfactory results with much shorter computational time. The coordination number obtained is 3.98, and the lowest porosity obtained is 14.2%. This method satisfies both the requirements on coordination number and porosity. Therefore, it is suitable for generating 2D rock sample for DEM simulations.

Lozano et al. (2016) developed the static method to generate random sphere assembly in 3D domains. This method starts with three spheres tangent to each other located at the center of mass of the domain, these spheres are the active front and considered the seed spheres. Then the algorithm selects a sphere in the active front to be the "current sphere" and builds up a neighbourhood square box around it, the size

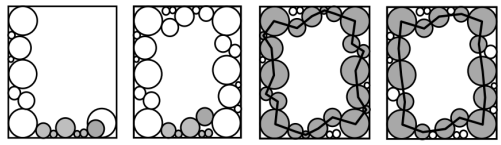

Figure 3.12: Generation of the initial front in the inwards packing method. (Bagi, 2005)

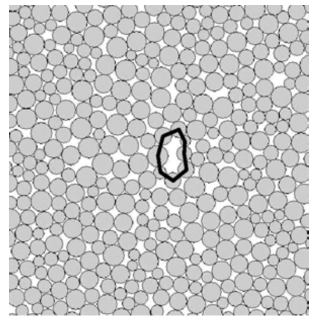

Figure 3.13: The middle region with a gap area in the sample generated by the inwards packing method (Bagi, 2005)

of the box δ_{box} is calculated by Eq. (3.41), where r_{curr} is the radius of the current sphere and r_{new} is the radius of the new sphere to be inserted. Existing spheres who intersect or touch the box are seen as the neighbours of the current sphere.

$$\delta_{box} = 2(r_{curr} + 2r_{new}) \tag{3.41}$$

To determine the candidate positions for the new sphere's center, $\mathbf{c}_{new}$, a spherical halo is created with the radius r_{halo}, centred at the centres of the current sphere $\boldsymbol{s}$, here r_{halo} is calculated by Eq. (3.42). A point that belongs to the surface of the halo of the current sphere and two others halos of spheres in the neighbourhood is a candidate for the new sphere center, as shown in Fig. 3.14. If there are two or more valid candidate points the algorithm proceeds selecting one by the shortest distance to the first of the three seed spheres. Hence the new sphere will be created on the point closer to the starting sphere to guarantee a compact and concentric pattern of the sample (Fig. 3.15).

$$r_{halo} = r_s + r_{new} \tag{3.42}$$

Similar to the closed front method of Feng et al. (2003), Lozano et al. (2016) keeps attaching new spheres in an outwards spiral pattern, meanwhile making sure the particles generated are fully contained in the domain. Densely compacted samples without any particle overlaps can be created with this method. According to Lozano et al. (2016), the coordination number is between 6.0 to 6.1 and the lowest porosity achieved is 42% to 43%. Since this is a static method, the computation time is shorter than most of the dynamic methods. It is seen as one of the options for generating 3D rock DEM samples for this research.

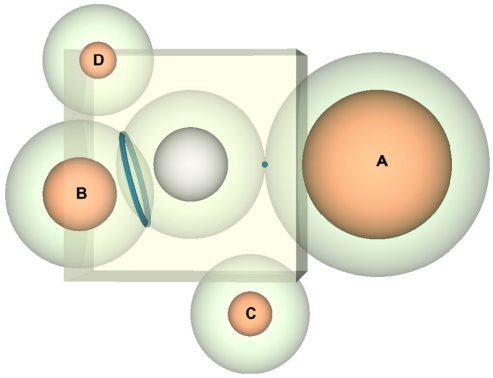

Figure 3.14: Neighborhood box around the current sphere (gray). Neighbor spheres: A, B and D. Not neighbor: C. Sphere A yields a single position. The halo intersection between the current sphere and the sphere B yields a circle of points. Spheres C and D do not generate points. (Lozano et al., 2016)

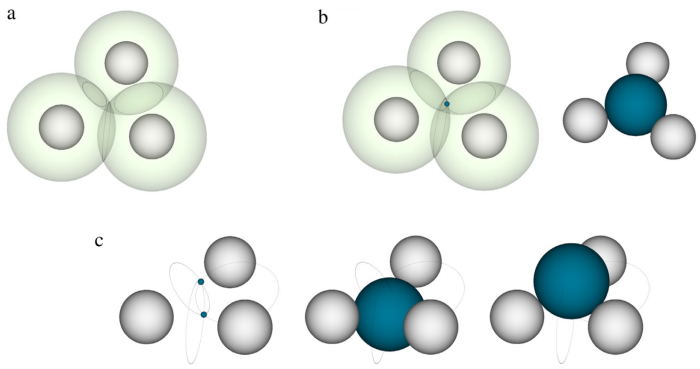

Figure 3.15: Placing a sphere in contact with three other spheres. (a) No valid intersection between the halos. (b) A single valid point of intersection between the halos. (c) Two valid points of intersection between the halos. (Lozano et al., 2016)

Dynamic methods are also common for generating 3D DEM samples, e.g., for rock-like materials. A typical model is to simulate a gravitational deposition process. Particles are created with required radii and dropped into the domain which acts as a container. Once they find their equilibrium positions under the effort of gravity, all the particle contact forces previously calculated by the collision models are set to zero, and then bonds are established between the contact particles, meanwhile the contact law shifts from the collision model to bond model. The commercial software EDEM® implemented this method (DEM Solutions, 2016). There are two drawbacks of this method.

- Gravitational deposition will create more contacts in the vertical direction than in the horizontal direction, in this way an initial anisotropy exists in the sample. The stiffness in the vertical direction is definitely higher than in the horizontal

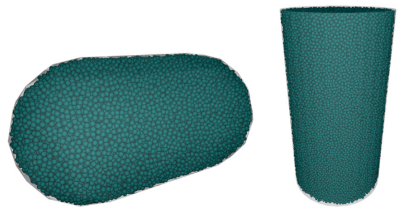

Figure 3.16: DEM samples of capsule shape and cylindrical shape, generated with the method of Lozano et al. (2016)

direction.

- Particles have overlaps in the gravitational direction in the initial packing, while both the calculations of the collision model and the bond model are based on the overlap and relative displacement between the particles. Thus manually setting all the forces to zero for the shift from the collision model to the bond model will significantly damage the consistency of the energy conservation and the calculation itself.

Based on the considerations mentioned above, the gravitational deposition method is not recommended in this research. Another dynamic method for generating dense samples in 3D is proposed by Potyondy and Cundall (2004). In their method, particles radii follow uniform distribution in the range $[R_{min}, R_{max}]$. To fill a given volume V' with a defined porosity n, the number of particles N required is calculated by Eq. (3.43).

$$N = \frac{3V'(1-n)}{4\pi\bar{R}^3} \text{ , with } \bar{R} = \frac{R_{min} + R_{max}}{2} \tag{3.43}$$

$$m_R = (\frac{1-n}{1-n_0})^{1/3} \tag{3.44}$$

To begin with, particles are generated with radii following a uniform distribution in the range $\frac{1}{2}[R_{min}, R_{max}]$ and randomly placed in the domain without any overlap with each other. Next, the porosity of the generated assembly, n_0, is computed, and the radii of all particles are multiplied by the factor m_R as in Eq. (3.44), now the system is allowed to rearrange itself with zero particle-particle or particle-wall frictions in the holding container.

In this method, the expected initial assembly stress is restricted to be maximumly 1% of the expected UCS. So particle radii need to be reduced to reach less overlaps, thus also lower assembly stress. After the rearrangement, the isotropic stress of the assembly σ_0, which is defined as the average of all the three direct stresses, can be calculated via Eq. (3.45), where $F^{n(c)}$ is the normal component of the force acting at contact (c) of particle p, $\tilde{R}^{(c,p)}$ is the distance from the contact point to the particle

center.

$$\sigma_0 = \frac{\bar{\sigma}_{kk}}{3} = -\frac{1}{3V'}\sum_{N_p}\sum_{N_c}\tilde{R}^{(c,p)}F^{n(c)} \tag{3.45}$$

$$\Delta R^p = \alpha_R R^p \tag{3.46}$$

$$\Delta F^{n(c)} = \alpha_R K^{n(c)}\phi^c, \quad where \quad \phi^c = \begin{cases} R^A + R^B, & \text{particle-particle contact} \\ R^p, & \text{particle-wall contact} \end{cases} \tag{3.47}$$

Assuming by reducing the radii of all particles with a scaled factor α_R (Eq. (3.46)), the assembly can reach the expected initial overall stress, the reduced normal contact force $\Delta F^{n(c)}$ is then calculated via Eq. (3.47). Hence finally α_R can be calculated via Eq. (3.48).

$$\alpha_R = -\frac{3V'\Delta\sigma_0}{\sum_{N_p}\sum_{N_c}\tilde{R}^{(c,p)}K^{n(c)}\phi^c} \tag{3.48}$$

In Eq. (3.48), $K^{n(c)}$ and ϕ^c are the normal stiffness and contact radii, respectively, at contact (c), and $\Delta\sigma_0$ is usually set to be 99% of the expected UCS. This reduction of the particle radius needs to be taken several times, and α_R also needs to be recalculated each time, to reach the low stress level as required, the reason is that it is a dynamic method, so inevitably some particle rearrangements occur.

After the radii reduction process, the magnitude of the internal forces in the sample when bonds are initiated would also be much smaller, ensuring it is safe to remove the container to let the sample relax itself. However, there is still one more step before the bonds can be installed, that is to eliminate the "floater" particles, which are defined as the particles with less than three contacts in 3D domain. These floaters will reduce the coordination number of the sample and damage the connectivity of the solid structure.

To eliminate the floaters, first particles with less than three contacts are found out and marked as the floaters, and then all the non-floaters are fixed and given zero velocities. Floaters' radii are then increased by a large amount (30%) to ensure contact with all of their immediate neighbours. After a period of relaxation the floaters will find their local equilibrium, then again the radii of the floaters are modified with ΔR_f, calculated via Eq. (3.49), in which $\bar{F}_a$ is the mean contact normal force for the assembly; $\bar{F}_p$ is the mean contact normal force for single particle; H is the hysteresis factor; f_m is the target fraction of $\bar{F}_a$, normally set to 0.1; k_n is the particle normal stiffness.

$$\Delta R_f = -2(\bar{F}_p - H\bar{F}_a f_m)/k_n \tag{3.49}$$

With this radii reduction, it is expected that the mean contact normal force of the floaters are significantly reduced to be below one tenth of the mean contact normal force of the assembly $(f_m\bar{F}_a)$. If this goal is reached for a floater, then this floater is seen as "inactive", it will not shrink any more. For those who still has less than

3 contacts, meanwhile also holds a mean contact normal force bigger than a fraction of the mean contact normal force of the assembly, i.e., $H\bar{f}_m F_a$, this radii reduction process will continue for several rounds until the criterion is met. It is highly possible that at the end of the floater elimination process, there are still some floaters cannot reach a contacts number of 3 or more, it might be induced by the phenomenon that some floaters can be positioned almost exactly between two non-floaters such that the two contact directions are nearly coaxial. In such a situation, the floater elimination process should stop, and then a dense sample with a good coordination number, as well as low initial stress level can be obtained. The target porosity for this method in 3D is usually around 35%.

In conclusion, the addition methods of Lozano et al. (2016) will be used in this research; the dynamic method of Potyondy and Cundall (2004) will be used for the research. Chapter 6 shows which one is the best for this research based on detailed comparison of simulations of unconfined compression tests.

3.4.3. Governing parameters and scaling laws

In the DEM calculations for rock, one of the major issues is to determine the relation between some of the most important parameters. Especially, to establish the link between the input material parameters at micro scale and the output material parameters at macro scale. These relations are built by conducting material scaling tests, which are also the calibration tests. These tests are of great importance for choosing the right simulation settings to obtain the expected rock material.

As shown by Eq. (2.8) in Chapter 2, seven dimensionless combinations are composed by ten input parameters for the situation with the contact bond model. With the parallel bond model, the bond radius should also be added to the list of input parameters. Actually it is unnecessary to tune all the parameters, because in reality many different combinations of microscopic physics could lead to the same macroscopic physics, for example, the forming processes and the compositions of a sandstone and a shale are very different, but their UCS values, or the BTS values could be the same. This is the same story in DEM, for DEM rock samples, the mechanical properties, e.g., the UCS and BTS, are the most important characteristics. Therefore as long as the expected mechanical properties can be achieved, the less parameter tuning the better. So in this research, some of the input parameters will be calibrated while the others will be determined by a number of empirical relations. Potyondy and Cundall (2004) carried out simulations of compression tests and Brazilian tension tests with different average particle diameters (D_{avg}), while the PSDs all follow uniform distribution and the R_{max}/R_{min} ratio is fixed. It is discovered that the smaller the D_{avg} is, the better the accuracy of the simulation results can be. Table 3.2 shows the simulation results from PFC3D®. The simulation is to mimic the mechanic properties of the Lac du Bonnet granite sample tested in the laboratory. The granite samples have an average UCS of 200 MPa. Table 3.2 shows that by reducing D_{avg}, the simulated compressive strength (σ_c) agrees better with the experimental value, and the variation reduces. The Lac du Bonnet rock sample modelled in Table 3.2 is a cuboid of size "63.4mm

Table 3.2: Effect of particle size on PFC3D® macroproperties

D_{avg} (mm)	Macroproperty (63.4 ×31.7 ×31.7 mm^3 specimens, n=10, mean and coefficient of variation)											
	E (GPa, %)		ν (-,%)		σ_c (MPa, %)		ϕ (deg, %)		c (MPa, %)		σ_t (MPa, %)	
5.95	57.3	10.0	0.231	21.2	127.9	11.9	25.9	14.2	40.0	11.4	43.6	27.8
3.05	64.0	3.8	0.254	8.1	169.6	3.4	30.6	9.8	48.4	7.6	35.4	26.1
2.04	67.6	1.8	0.255	5.8	186.9	1.5	32.3	9.2	51.6	6.9	33.0	21.9
1.53	69.2	1.2	0.256	5.5	198.8	3.6	32.1	7.4	55.1	7.6	27.1	13.7

×31.7mm ×31.7mm", filled with DEM particles.

In the simulation using the smallest particles (D_{avg} = 1.53 mm), the obtained σ_c is 198.8 MPa, which is very close to the practical value of 200 MPa, Potyondy and Cundall (2004) considered that this level of particle size is sufficiently small for a sample of such size, so that the DEM particles can be seen as soil grains.

On the contrary, if the DEM particles are too big, then the total number of particles and the total contact number of the sample would be much smaller. As a result, the external loading cannot be efficiently transmitted to every corner of the sample and the internal structure of the solid will be much looser. Such kind of sample cannot be used to model the behaviour of rock.

However, it is not known if σ_c will continue increasing with particles even smaller than 1.53 mm. In the tests of Potyondy and Cundall (2004), the shortest dimension of the cuboid sample of Table 3.2 is 31.7 mm, considering the case of the smallest D_{avg} 1.53 mm, it means that there are approximately 21 layers of DEM particles along the shortest dimension. The simulation results revealed that it is necessary to have at least so many layers of particles along the shortest dimension of the sample to capture the internal solid structure of the rock. Based on this concept, to further guarantee that the size of the DEM particles will not influence the accuracy of the global properties of the rock, it is determined that in this research the ratio between the shortest length scale of the sample and the D_{avg} for DEM rock sample is set to 30.

The uniform PSD and the fixed R_{max}/R_{min} ratio, 1.66, are used for the rock modelling of this research. However it must be pointed out that this arrangement is only for creating the DEM rock samples, in other dredging relevant DEM applications, e.g., simulation for sand cutting, this arrangement is not required.

In the original PBM, for 3D simulations, the shear bond strength T_s and the tensile bond strength T_n are set to be equal to the expected UCS, the units for these variables are [MPa], while in 2D the units will be [MN/m]. According to Table 3.2, σ_c matches well with the expected UCS, on the contrary, σ_t (27.1 MPa) is much larger than the BTS (9.3 MPa). As introduced before in Eq. (2.5), the ratio between the UCS and the BTS is a reflection of the ductility, or the brittleness in other way, of the rock material. That is the expression of ductility in macro scale, in which the UCS test will

show a major shear failure and the BTS test a major tensile failure. To establish a link from the macro to the micro scale, i.e., the particle scale in DEM, it is pointed out that the calculation of the shear and normal forces between particles are mostly determined by the shear and normal stiffness of the bond respectively. Potyondy and Cundall (2004) claim that they set the ratio of normal to shear stiffness, $\frac{\bar{k}_n}{\bar{k}_s}$, to match the expected Poisson's ratio. However, in their paper, the Poisson's ratio of the granite rock is 0.26±0.04, while the $\frac{\bar{k}_n}{\bar{k}_s}$ ratio is set to be 2.5, yet there is no explanation for the difference between 0.26±0.04 and 2.5. So in this research we considered that $\frac{\bar{k}_n}{\bar{k}_s}$ is an important parameter to be calibrated, besides it is already expected that a relation should be established between the $\frac{\bar{k}_n}{\bar{k}_s}$ ratio and the $\frac{\sigma_c}{\sigma_t}$ ratio to study the ductility the of the DEM rock sample into details.

Apart from the ratio $\frac{\bar{k}_n}{\bar{k}_s}$, the strengths of the bond (T_n, T_s) also significantly influence the mechanical behaviour of the rock sample. According to Potyondy and Cundall (2004), the settings are $T_n = T_s =$ *the expected UCS value*. In this research, the $T_n = T_s$ part is kept because it can reduce the number of the parameters to tune, but the value of the bonding strengths is set to be a fraction of the Young's modulus of the bonding beam instead of the expected UCS value. This allows certain freedom to tune the strength of the rock. For the Young's modulus, two types are used in the PBM, one is E_c, the Young's modulus of the grains (for unbonded particles), another one is $\bar{E}_c$, the Young's modulus of the bonding beam (for bonded particles). In (Potyondy and Cundall, 2004), it is set $E_c = \bar{E}_c =$ *the measured Young's modulus*. This setting is also applied in this research because it helps to simplify the problem. To conclude, in this way, with a known $\bar{E}_c$, by tuning the bond strength T_n, two micro-macro relations are built, which are $\{\frac{\bar{E}_c}{T_n}, \frac{\sigma_c}{T_n}\}$ and $\{\frac{\bar{E}_c}{T_n}, \frac{\sigma_t}{T_n}\}$. These relations will help the users of the numerical model to find out the appropriate setting for bond strengths.

3.5. DEM-FVM coupling mechanism

As pointed out in Chapter 3.1, a DEM-FVM (Discontinuum-Continuum) coupling method is applied in this research for underwater excavation process. Through the previous sections in Chapter 3, the mathematical expressions in the DEM part for sand, clay and rock have been explained meticulously. In this section, the coupling between the solid (DEM) and fluid (FVM), and the governing equations in the FVM part will be introduced.

3.5.1. Momentum equation in the fluid phase

The governing equations of the fluid phase for this research are the momentum and mass conservation equations, in which the latter one is referred as the continuity equation. Among the two, the momentum equation has more varieties. Three sets of possible momentum equations have been summarized by Zhou et al. (2010)

Set I (the original momentum equation):

$$\begin{aligned}
&\frac{\partial(\rho_f \epsilon_f \vec{u})}{\partial t} + \vec{\nabla}\cdot(\rho_f \epsilon_f \vec{u}\vec{u}) = -\vec{\nabla}p - \vec{F}_{pf}^{setI} + \vec{\nabla}\cdot\bar{\bar{\tau}} + \rho_f \epsilon_f \vec{g}, \\
&\text{where } \vec{F}_{pf}^{setI} = \frac{1}{\Delta V}\sum_{i=1}^{n}(\vec{f}_{d,i} + \vec{f}_{\nabla p,i} + \vec{f}_{\nabla\cdot\tau,i} + \vec{f}_i''') \\
&\text{and } \vec{f}_{pf,i} = \vec{f}_{d,i} + \vec{f}_{\nabla p,i} + \vec{f}_{\nabla\cdot\tau,i} + \vec{f}_i'''
\end{aligned} \tag{3.50}$$

Set II (derived from Set I by splitting the local mean value of the fluid-on-particle force into two components):

$$\begin{aligned}
&\frac{\partial(\rho_f \epsilon_f \vec{u})}{\partial t} + \vec{\nabla}\cdot(\rho_f \epsilon_f \vec{u}\vec{u}) = -\epsilon_f\vec{\nabla}p - \vec{F}_{pf}^{setII} + \epsilon_f\vec{\nabla}\cdot\bar{\bar{\tau}} + \rho_f \epsilon_f \vec{g}, \\
&\text{where } \vec{F}_{pf}^{setII} = \frac{1}{\Delta V}\sum_{i=1}^{n}(\vec{f}_{d,i} + \vec{f}_i''') \\
&\text{and } \vec{f}_{pf,i} = \vec{f}_{d,i} + \vec{f}_{\nabla p,i} + \vec{f}_{\nabla\cdot\tau,i} + \vec{f}_i'''
\end{aligned} \tag{3.51}$$

Set III (obtained by substituting the rewritten Set II into Set I):

$$\begin{aligned}
&\frac{\partial(\rho_f \epsilon_f \vec{u})}{\partial t} + \vec{\nabla}\cdot(\rho_f \epsilon_f \vec{u}\vec{u}) = -\vec{\nabla}p - \vec{F}_{pf}^{setIII} + \vec{\nabla}\cdot\bar{\bar{\tau}} + \rho_f \epsilon_f \vec{g}, \\
&\text{where } \vec{F}_{pf}^{setIII} = \frac{1}{\epsilon_f \Delta V}\sum_{i=1}^{n}(\vec{f}_{d,i} + \vec{f}_i''') - \frac{1}{\Delta V}\sum_{i=1}^{n}(\rho_f V_{p,i}\vec{g}) \\
&\text{and } \vec{f}_{pf,i} = \frac{(\vec{f}_{d,i} + \vec{f}_i''')}{\epsilon_f} - \rho_f V_{p,i}\vec{g}
\end{aligned} \tag{3.52}$$

where ϵ_f is the volume fraction of fluid, the subscript notation f indicates the fluid phase, ρ_f is the fluid density $[kg/m^3]$, $\bar{\bar{\tau}}$ is the viscous shear stress tensor $[N/m^2]$, $\vec{F}_{pf}^{setI}$, $\vec{F}_{pf}^{setII}$ and $\vec{F}_{pf}^{setIII}$ are the source terms used in the fluid momentum equations, representing particle(solid)–fluid interaction force in the three different sets respectively $[N/m^3]$, ΔV is the volume of a fluid cell $[m^3]$.

On the particles side, $\vec{f}_{pf,i}$ is the particle(solid)–fluid interaction force applied on particle i. $\vec{f}_{d,i}$ is the drag force, $\vec{f}_{\nabla p,i}$ is the pressure gradient force, $\vec{f}_{\nabla\cdot\tau,i}$ is the viscous

force, and $\vec{f}_i''' = \vec{f}_{vm,i} + \vec{f}_{B,i} + \vec{f}_{Saff,i} + \vec{f}_{Mag,i}$ is the is the sum of particle–fluid interaction forces on particle i, other than the drag, pressure gradient and viscous forces which are often regarded as the dominant forces in particle–fluid flow. Here $\vec{f}_{vm}$ is the virtual mass force, $\vec{f}_B$ is the Basset force, $\vec{f}_{Saff}$ represents the lift force and $\vec{f}_{Mag}$ is the Magnus force.

Set I is the original momentum equation, Set II is derived from Set I by splitting the local mean value of the force on particle i by its surrounding fluid into two components: 1) a component due to 'macroscopic' variations in the fluid stress tensor on a large scale compared with the particle spacing, e.g., $\vec{f}_{\nabla p,i}$ and $\vec{f}_{\nabla\cdot\tau,i}$; 2) a component representing the part of the total fluid–particle interaction force per unit bed volume arising from the detailed variations in the stress tensor induced by fluctuations in velocity as the fluid passes around individual particles and through the interstices between particles. It mainly includes $\vec{f}_{d,i}$ in the direction of the relative velocity $(\vec{u}_i - \vec{w}_i)$, and $\vec{f}_{vm}$ proportional to the mass of fluid displaced by a particle. Here $\vec{u}_i$ is the local fluid velocity around particle i, $\vec{w}_i$ is the velocity of particle i.

Set III is obtained by putting the rewritten Set II into Set I, meanwhile assuming the fluid acceleration term approaches zero or much smaller than the other terms in the equation. Detailed explanation can be found in (Zhou et al., 2010).

These three sets of equations are in essence similar, but in the perspective of implementation, cautions should be taken on their respective requirements. In general, two hydrodynamic models for particle-fluid flow are applied based on these three sets, model A and model B (Bouillard et al., 1989; Gidaspow, 1994; Enwald et al., 1996). Model A attributes the pressure source term to both the fluid and solid phases, while model B only attributes the pressure source term to the fluid phase. As explained in Chapter 2.1.1, the fluid pressure gradient plays an important role in the deep water cutting process, so the fluid pressure source term must be included into the momentum equation of the solids. It is thus decided that model A will be applied in this research.

Nowadays model A is mostly used by researchers, partially because the commercial software packages FLUENT and CFX both use model A. It is also explained by Zhou et al. (2010) that in principle, model A is consistent with set II, and model B with set I and III. CFDEM® offers the options of both model A and B, according to (CFDEM, 2018), model A requires the models for the pressure gradient force and viscous force, whereas model B requires the "Archimedes" force model. This Archimedes force model calculates the Archimedes' volumetric lift force stemming from density difference of fluid and particle.

It should be pointed out that DEM-FVM coupling is not the only way to calculate the pore pressures and model the water flow penetrating through the seabed soil. Another method was proposed by Shimizu et al. (2011). They introduced a rock-fluid interaction algorithm based on a 2D channel-domain network for simulating the hydraulic fracturing process. As shown in Fig. 3.17, the fluid flows are described as pipe flows which only exist around the contact point between two DEM particles and pore pressure values are saved at the center of the domains which are also surrounded by

the DEM particles. The simulation results show a good agreement with experimental results. However, the deformation of solid skeleton in hydraulic fracturing is much

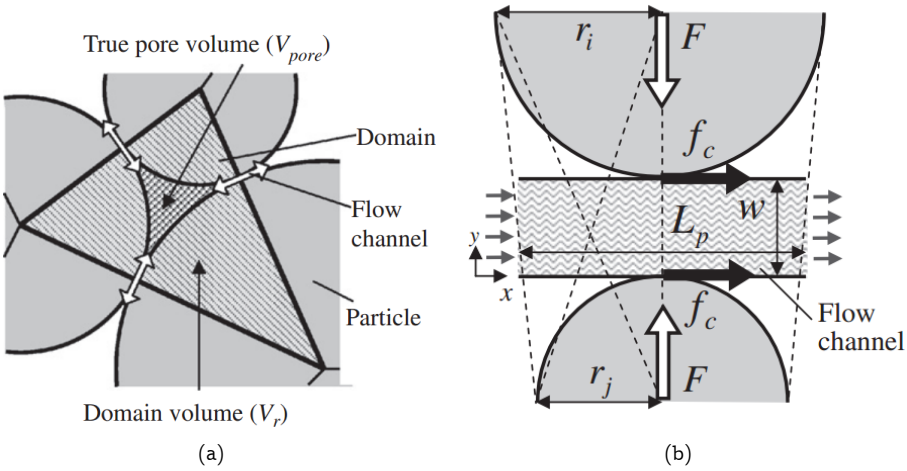

Figure 3.17: Left: Channel-Domain model; Right: Fluid flow in a channel. (Shimizu et al., 2011)

smaller than that in excavation process. The whole channel-domain network will be gone when big deformation happens in excavation process. Besides it is very difficult to upgrade this method into 3D world, thus it is not suitable for simulating the solid-fluid interaction in underwater excavation process. But it is important to notice, from their method, that the seepage through the seabed soil can be modelled as Darcy flow in porous media, which helps to simplify the problem.

By carefully examining the equations of set I, II and III, it is discovered that the momentum exchange between the fluid and the particles is mutual, which means the fluid will apply certain amount of force $\vec{f}_{pf,i}$ on the particles, while the particles will reversely apply certain forces on the fluid ($\vec{F}_{pf}^{setI}$, $\vec{F}_{pf}^{setII}$ and $\vec{F}_{pf}^{setIII}$). The coupling is so complicated so that it is necessary to investigate what specific equations should be formed up for this research.

For numerical simulation of underwater excavation process, according to Fig. 3.18, in the solid-dominant zone, seepage flow will penetrate into the solid structure where the pressure gradient force and viscous force could significantly influence the particle behaviour. In the fluid-dominant zone, the cut solid material will be spread into the water so that the drag force will be dominant. These two scenarios are now discussed separately.

For the solid-dominant zone, the dominant influence from the solid phase to the fluid phase is the solid skeleton change. From the consolidation theory of Verruijt and van Baars (2005), the specific discharge $\vec{q}[m/s]$, representing the Darcy flow, can be

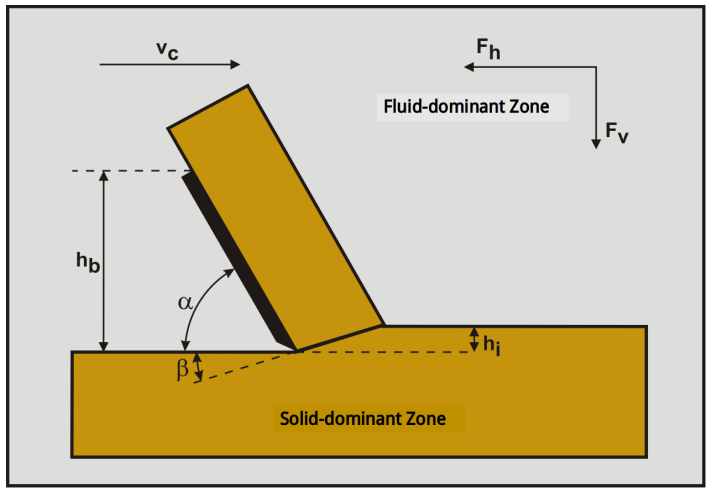

Figure 3.18: Illustration of the solid-dominant and fluid-dominant zones during the cutting process

calculated by

$$\vec{q} = n(\vec{u} - \vec{w}) = \epsilon_f(\vec{u} - \vec{w}) \tag{3.53}$$

Where $\vec{u}$ is the fluid velocity [m/s], $\vec{w}$ is the solid velocity [m/s] and n is the porosity of the solid skeleton, which equals to ϵ_f in Eq. (3.50), (3.51) and (3.52). Based on this the momentum equation of the fluid is designed in such a form,

$$\rho_f \frac{\partial(\epsilon_f \vec{u})}{\partial t} + \rho_f \vec{\nabla} \cdot (\epsilon_f \vec{u}\vec{u}) = -\epsilon_f \vec{\nabla} p + \vec{\nabla} \cdot (\epsilon_f \bar{\bar{\tau}}) - K_{sf}(\vec{u} - \vec{w}) \tag{3.54}$$

Comparing with Set II of (Zhou et al., 2010) (Eq. (3.51)), in this equation, the gravitational acceleration is neglected in the fluid phase, simply because this term is much smaller compared with the other source terms, especially the last one representing the particle-fluid interaction force. Another difference is that in this momentum equation the fluid density ρ_f is treated as constant because the compressibility of water is very small ($\beta_f \approx 5 \times 10^{-10} pa^{-1}$).

In Eq. (3.54), K_{sf} is the solid-fluid momentum exchange coefficient. The term $K_{sf}(\vec{u} - \vec{w})$ represents $\vec{F}_{pf}^{setII}$ in Eq. (3.51). To determine K_{sf}, the solid-dominant region and the fluid-dominant region are treated respectively. For the solid-dominant zone, the Kozeny-Carman Equation (Kozeny, 1927a; Carman, 1937b, 1956a) and Ergun Equation (Ergun, 1952; Akgiray and Saatçı, 2001) are the possible choices. It is known that the Kozeny-Carman Equation is only valid for laminar flow, while the Ergun Equation contains both the laminar part and the turbulent part.

In seabed excavation process, it is possible for turbulence to occur in the transition area between the solid-dominant to fluid-dominant zone, even when the solid volume fraction is still high. Based on this consideration, the Ergun Equation is used to

determine K_{sf} in the cutting zone and the seabed soil.

$$K_{sf} = \frac{150\mu_f(1-\epsilon_f)^2}{{\phi_s}^2 D_p^2 {\epsilon_f}^3} + \frac{1.75\rho_f(1-\epsilon_f)|\vec{u}-\vec{w}|}{\phi_s D_p {\epsilon_f}^3}\text{ , when } \epsilon_f \leq 0.8 \tag{3.55}$$

In Eq. (3.55), ϕ_s is the sphericity of the particles in the bed describing the level that the particle shape is close to sphere, and D_p is the equivalent diameter of the particles.

After being excavated, the cut soil particles will either be dispersed into water or move along the blade surface. These post failure behaviours also affects the cutting force. According to Gidaspow et al. (1991), the Wen and Yu (1966) equations can be used to calculate the momentum exchange coefficient in the fluid-dominant phase, which leads to:

$$\begin{aligned} &K_{sf} = \frac{3}{4}C_d\rho_f\frac{\epsilon_f(1-\epsilon_f)|\vec{u}-\vec{w}|}{D_p}{\epsilon_f}^{-2.65}\text{ , when } \epsilon_f > 0.8 \\ &\text{where } C_d = \frac{24}{\epsilon_f Re_p}[1+0.15(\epsilon_f Re_p)^{0.687}], \text{ in which } Re_p = \frac{\rho_f|\vec{u}-\vec{w}|D_p}{\mu_f} \end{aligned} \tag{3.56}$$

In Eq. (3.56), Re_p is the Reynolds number of the particle [-], μ_f is the dynamic viscosity of the fluid $[kg/(m\cdot s)]$.

To enable Eq. (3.54), (3.55) and (3.56) to also cover the extreme situations, the possibility of the occurrence of cavitation in underwater excavation process is considered. A penalty function is implemented to make sure the lowest fluid pressure value is at water vapor pressure. It means, if the calculated value of fluid pressure in a fluid cell is lower than 0.6 kPa, which is the vapor pressure of water at the temperature $0°C$, it will be automatically set to 0.6 kPa. This function limits the maximum under pressure in the simulations.

3.5.2. Continuity equation in the fluid phase

Only in the case of hyperbaric rock cutting, the compressibility of seawater needs be taken into consideration. From the consolidation theory of Verruijt and van Baars (2005), a storage equation based on mass conservation of both the solid and fluid phases is given.

$$-\epsilon_f\beta_f\frac{\partial p}{\partial t} - \frac{\partial \epsilon_{vol}}{\partial t} = -\vec{\nabla}\cdot\vec{q} \tag{3.57}$$

Where ϵ_{vol} is the volumetric strain of the solid skeleton, t is the time [s], ϵ_f is the fluid volume fraction, which equals to the porosity (n) of the solid skeleton, β_f is the compressibility of the fluid $[m^2/N]$, p is the fluid pressure [pa] and $\vec{q}$ is the specific discharge [m/s] which is calculated by (3.53).

The volumetric strain rate can be represented by

$$\frac{\partial \epsilon_{vol}}{\partial t} = -\vec{\nabla} \cdot \vec{w} \tag{3.58}$$

Substitution of Eq. (3.58) and Eq. (3.53) into Eq. (3.57) leads to:

$$\vec{\nabla} \cdot [(1-\epsilon_f)\vec{w}] + \vec{\nabla} \cdot (\epsilon_f \vec{u}) + \epsilon_f \beta_f \frac{\partial p}{\partial t} = 0 \tag{3.59}$$

According to Verruijt and Broere (2011),

$$\vec{\nabla} \cdot [(1-\epsilon_f)\vec{w}] = \frac{\partial \epsilon_f}{\partial t} \tag{3.60}$$

So the fluid mass conservation can be written as:

$$\frac{\partial \epsilon_f}{\partial t} + \vec{\nabla} \cdot (\epsilon_f \vec{u}) + \epsilon_f \beta_f \frac{\partial p}{\partial t} = 0 \tag{3.61}$$

It should be noticed that Eq. (3.59) does not have the time derivative term of porosity as Eq. (3.61), instead it uses the solid particle velocity. From the perspective of mathematics and physics, these two equations are equal. But in discretization, they can generate some difference. In DEM-FVM coupling, Eq. (3.59) reads in all the particles' velocities and calculates the average solid velocity of each fluid cell. This makes the computation much heavier and it is also sensitive to the mesh size. However, Eq. (3.61) does not need to deal with particle velocity which makes it the preferred equation to use. In the excavation of dredging engineering, the compressibility of water is negligible, thus the $\epsilon_f \beta_f \frac{\partial p}{\partial t}$ term can be neglected, leading to:

$$\frac{\partial \epsilon_f}{\partial t} + \vec{\nabla} \cdot (\epsilon_f \vec{u}) = 0 \tag{3.62}$$

In this research project, Eq. (3.62) is implemented as the mass conservation equation for the fluid phase. Eq. (3.61) is expected to be implemented in future researches which specifically focus on hyperbaric rock cutting.

3.5.3. Calculation of the volume fraction of solid particles in fluid cell

The volume fraction of the solid particles (DEM) in the fluid cells (CFD) should be calculated so that the momentum equation (Eq. (3.54)) and the continuity equation (Eq. (3.61)) can be solved. Two methods are available for this calculation, namely the divided calculation method and the center calculation method.

Divided calculation method for the solid volume fraction

A numerical model was made by (Rahman et al., 2010) to determine the pore volume change in 2D sand cutting simulations. The limitation of his model is that all the particles must be identical circular disks, which is not suitable for 3D simulations. To determine the porosity change during the 3D sand cutting simulation, the simulation zone is meshed by a Cartesian grid system, in which all the grid cells are identical cubes. Fig. 3.19 shows the grids in the cutting zone. To calculate the volume of solid particles in fluid cells, four possible situations regarding the relevant positions between the particle and the cell are studied.

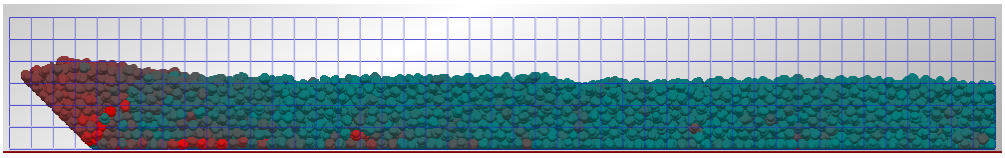

Figure 3.19: Illustration of the simulation domain with a Cartesian mesh

The first situation, as shown in Fig. 3.20a, is that a particle is totally inside a cell, namely, this particle does not interact with any boundary of the cube. In this case, the whole volume of this particle V_p belongs to this cell. **The second situation**, as shown in Fig. 3.20b, is that a particle only interacts with one boundary of the cell, not matter if it is in x, y or z direction. In this case, this particle is owned by two neighbouring cells. Now assuming the local coordinates of the particle center is (a, b, c), and this particle center is located in part 2 of the particle. Then Eq. (3.63) is derived to separately calculate the volume of part 1 (V_1) and part 2 (V_2).

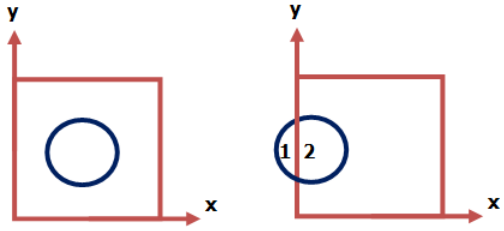

Figure 3.20: Positions of the particle with respect to the cubic cell. a): **situation 1**: Particle interacts with no boundary, b): **situation 2**: Particle interacts with one boundary

$$\begin{cases} V_1 = \dfrac{V_p}{2} - \pi \cdot a \cdot (R_n^2 - \dfrac{a^2}{3}) \\ V_2 = \dfrac{V_p}{2} + \pi \cdot a \cdot (R_n^2 - \dfrac{a^2}{3}) \end{cases} \tag{3.63}$$

The third situation, as shown in Fig. 3.21, is that a particle interacts with two

boundary faces of the cube. In this case, this particle is jointly owned by four cubic grid cells. Again we assume the particle center is located in part 2, and its local coordinates is (a, b, c), then Eq. (3.64) is generated to calculate the volume of each part.

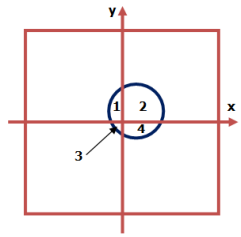

Figure 3.21: **Situation 3** –Particle interacts with two boundary faces of the cell

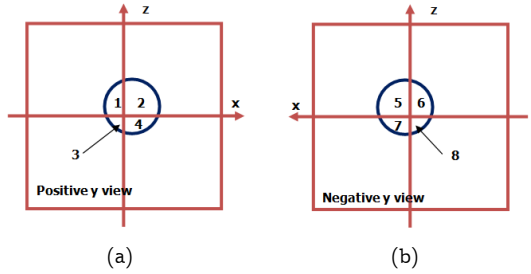

Figure 3.22: **Situation 4** –Particle interacts with three boundary faces of the cell

$$\begin{cases} V_3 \approx (\sqrt{R_n^2 - a^2} - b) \cdot (\sqrt{R_n^2 - b^2} - a) \cdot (\sqrt{R_n^2 - a^2 - b^2}) \\ V_1 = \dfrac{V_p}{2} - \pi \cdot a \cdot (R_n^2 - \dfrac{a^2}{3}) - V_3 \\ V_4 = \dfrac{V_p}{2} + \pi \cdot b \cdot (R_n^2 - \dfrac{a^2}{3}) - V_3 \\ V_2 = V_p - V_1 - V_3 - V_4 \end{cases} \tag{3.64}$$

The fourth situation, as shown in Fig. 3.22, is that a particle interacts with the boundaries of all the three directions (x, y and z) of the grid cell, in this way one particle is shared by eight cells. Assuming the local coordinates of the particle center is (a, b, c), which is located in part 5, then Eq. (3.65) is derived to calculate the volume of each part of the particle.

$$\begin{cases} V_3 \approx \frac{\pi}{6} \cdot (\sqrt{R_n^2 - a^2 - b^2} - c) \cdot (\sqrt{R_n^2 - a^2} - b) \cdot (\sqrt{R_n^2 - b^2} - a) \cdot (1 - \frac{c}{\sqrt{R_n^2 - a^2 - b^2}})^2 \\ V_1 \approx (\sqrt{R_n^2 - a^2} - b) \cdot (\sqrt{R_n^2 - b^2} - a) \cdot (\sqrt{R_n^2 - a^2 - b^2}) - V_3 \\ V_4 \approx (\sqrt{R_n^2 - c^2} - b) \cdot (\sqrt{R_n^2 - b^2} - c) \cdot (\sqrt{R_n^2 - c^2 - b^2}) - V_3 \\ V_8 \approx (\sqrt{R_n^2 - a^2} - c) \cdot (\sqrt{R_n^2 - c^2} - a) \cdot (\sqrt{R_n^2 - c^2 - a^2}) - V_3 \\ V_6 = \frac{V_p}{2} - \pi \cdot a \cdot (R_n^2 - \frac{a^2}{3}) - V_1 - V_8 - V_3 \\ V_2 = \frac{V_p}{2} - \pi \cdot b \cdot (R_n^2 - \frac{b^2}{3}) - V_1 - V_4 - V_3 \\ V_7 = \frac{V_p}{2} - \pi \cdot c \cdot (R_n^2 - \frac{c^2}{3}) - V_4 - V_8 - V_3 \\ V_2 = V_p - V_1 - V_2 - V_3 - V_4 - V_6 - V_7 - V_8 \end{cases} \tag{3.65}$$

The nominal radius (R_n) of the particle is used because the sand particles created in DEM simulation could be non-spherical (Chapter 3.2.3). This nominal radius is based on the approximation to treat a non-spherical particle as a spherical particle with the same volume.

Center calculation method for the solid volume fraction

The center calculation model is different from the divided calculation. In the center calculation, as long as a particle's center is located in a fluid cell, then the whole volume of this particle will be considered to be in this fluid cell. If a particle has a part of it in a fluid cell, but that part does not contain the particle center, then this particle will not be considered for this fluid cell at all.

The divided calculation offers with a higher accuracy than the center calculation method since the former one considers more scenarios into details. It has been tested in (Chen and Miedema, 2013). But it should also be noted that the divided calculation requires much higher computational effort.

In this project, The side length of the fluid cell is set to at least two times of the diameter of the particle. So the maximum number of particles in one cube is eight. This is a reasonable scale to monitor the local porosity change due to the deformation of the solid skeleton. If the cells are set too big, then the porosity is just an average over a large area, on the other hand, if the cells are too small, then the porosity is concentrated on a single particle which cannot reflect the local pore volume change. Based such a consideration, it is believed that the center calculation is good enough since the accuracy can be compensated by the neighboring cells while the computation effort is much smaller. Thus the center calculation method is chosen for calculating the volume fraction of the solid particles in fluid cells.

3.5.4. Fluid-Particle interaction

In the DEM-FVM coupling, the communication between the two phases is designed in the following way:

- From solid to fluid: DEM will transfer the information about the change of the solid skeleton to FVM, such as DEM particles' positions, velocities and the local porosities of each fluid cell.
- From fluid to solid: FVM will update the fluid pressure and velocity fields based on mass and momentum conservation equations, and then apply the corresponding fluid-driven forces to DEM particles, such as the pressure gradient force, the viscous force and the drag force.

Based on the information from the DEM side, local porosity values can be obtained. The Kozeny-Carman Equation are used to calculate the permeability κ $[m^2]$, which is a quite important soil mechanic property determining the fluid-soil interaction ability.

The Kozeny-Carman Equation was initially suggested by Kozeny (1927b) and then modified by Carman (1937a) and Carman (1956b). It links the pressure drop and the superficial velocity of a laminar fluid flow through a solid bed.

$$\nabla p = -\frac{180 \cdot \mu_f}{{\phi_s}^2 \cdot {D_p}^2} \cdot \frac{(1-n)^2}{n^3} \cdot v_s \tag{3.66}$$

in which v_s is the superficial velocity, On the basis of Darcy's Law (Darcy, 1856), the expression of Kozeny-Carman Equation can be altered to explain that "flow is proportional to pressure gradient and inversely proportional to dynamic viscosity". This leads to Eq. (3.67).

$$v_s = -\frac{\kappa}{\mu_f} \cdot \nabla p \tag{3.67}$$

Then the expression of the permeability κ can be derived from Eq. (3.66) and (3.67).

$$\kappa = \frac{{\phi_s}^2}{180} \cdot \frac{n^3 \cdot {D_p}^2}{(1-n)^2} \tag{3.68}$$

In Eq. (3.67), the sphericity coefficient ϕ_s will be tuned for calibration purpose. It has been stated before that in the soil bed, the fluid volume fraction ϵ_f is equal to the porosity n. Therefore substitution of Eq. (3.68) into Eq. (3.55) leads to Eq. (3.69).

$$K_{sf} = \frac{5\mu_f}{6\kappa} + \frac{1.75\rho_f(1-\epsilon_f)|\vec{u}-\vec{w}|}{\phi_s D_p {\epsilon_f}^3} \text{ , when } \epsilon_f \leq 0.8 \tag{3.69}$$

The forces applied on the solid particles from the fluid side are the pressure gradient force $\vec{f}_{\nabla p,i}$, the viscous force $\vec{f}_{\nabla\cdot\tau,i}$ and the drag force $\vec{f}_d$. In CFDEM, when model A

is applied, the pressure gradient force model and the viscous force model must be activated. These two are the components due to 'macroscopic' variations in the fluid stress tensor on a large scale compared with the particle spacing (Zhou et al., 2010). Besides, the Gidaspow drag force is also applied. This force arises from the detailed variations in the stress tensor.

This research project has not included many other force models, e.g., the virtual mass force $\vec{f}_{vm}$, the Basset force $\vec{f}_B$, the Saffman lift force $\vec{f}_{Saff}$ or the Magnus force $\vec{f}_{Mag}$. The reason is that the main focus of the underwater excavation simulations is to obtain the cutting forces, while those force models mainly take effect when particles are dispersed into water, thus contribute little to the cutting forces. Therefore they are not included.

The pressure gradient force $\vec{f}_{\nabla p,i}$, the viscous force $\vec{f}_{\nabla\cdot\tau,i}$, and the Gidaspow drag force $\vec{f}_d$ are calculated in the following way in which V_p is the volume of a solid particle $[m^3]$:

$$\vec{f}_{\nabla p,i} = -\vec{\nabla} p \cdot V_p \tag{3.70}$$

$$\vec{f}_{\nabla\cdot\tau,i} = -\vec{\nabla}\cdot\bar{\bar{\tau}}\cdot V_p \tag{3.71}$$

$$\vec{f}_d = -K_{sf}(\vec{u}-\vec{w})\cdot V_p \tag{3.72}$$

4

Numerical Modelling of Sand Cutting Process

In dredging engineering, the sand cutting process is one of the key processes which can give dominant influence on the equipment design and production rate. This chapter introduces the numerical modelling for underwater sand cutting process. In this chapter, the DEM model for sand particles is firstly explained, and then the sand cutting simulations will be discussed under dry conditions, which are to be compared with the experimental results of Hatamura and Chjiiwa (1975, 1976a,b, 1977a,b).

Scaling laws derived from the Miedema (2017) are introduced to compare the cutting forces recorded from the simulations. Finally, underwater sand cutting simulations are carried out under various conditions, the simulated cutting forces are compared with the experimental results of Miedema (1987). Comparison shows that the cutting forces obtained from the simulations match the experimental results well.

Parts of this chapter have been published in (Chen et al., 2013; Chen and Miedema, 2013).

4.1. Sand cutting experiments from Hatamura & Chijiiwa

One of the first detailed researches on sand cutting is from Hatamura & Chijiiwa in the 1970s, they determined three failure mechanisms in soil cutting by conducting experiments. Their results are published in a series of reports (Hatamura and Chjiiwa, 1975, 1976a,b, 1977a,b). One of the experiments is pushing a blade through soil in a miniature bin shown in Fig. 4.1. The observed failure mechanisms are called the Shear, Flow and Tear type (Hatamura and Chjiiwa (1976b)).

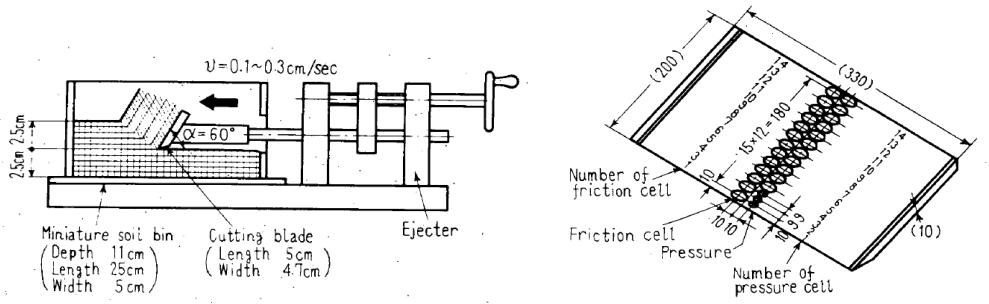

Figure 4.1: Experiment setup used in the tests of (Hatamura and Chjiiwa, 1975, 1976a,b, 1977a,b). a): Miniature Soil Bin Experiment, b): Blade used with pressure and friction cells

To determine the cutting force and the distribution of stresses on the blade, Hatamura & Chijiiwa measured the forces and stresses on the blade using pressure and friction cells (Figure 4.1b). They tested different types of soil in the experiment, like dry quartz sand and plastic loam. The quartz sand they used has a mean grain size of $0.2mm$ and an internal friction angle of $38°$. The density of the sand constituent is $2.67g/cm^3$ and the bulk density of the sample is $1.46g/cm^3$. The blade is $20cm$ long and $33cm$ wide. In the experiment the blade angle, cutting speed and layer thickness were varied as listed in Table 4.1.

The results of the dry quartz sand experiment are shown in Fig. 4.2. It shows the magnitude of the cutting force F in kg on the normal direction to the blade. The influence of the cutting angle is shown in the left side of the figure, the influence of the cutting depth in the middle and the influence of the cutting speed in the right side of the Figure.

Table 4.1: Sand cutting experiments conducted by Hatamura & Chijiiwa

Blade Angle [°]	Cutting speed [cm/s]	Layer Thickness [cm]
30	5	10
45	5	10
60	5	10
75	5	10
90	5	10
60	5	5
60	5	10
60	5	15
60	5	10
60	10	10
60	14	10

4.2. Analytical model of Miedema and the wedge theory

Miedema (2014) derived the equations for sand cutting forces according to the flow type (Fig. 3.2(a)) and the shear type (Fig. 3.2(b)). The horizontal cutting force F_h and the vertical cutting force F_v on the blade are expressed as:

$$F_h = \rho_s \cdot g \cdot {h_i}^2 \cdot w \cdot \lambda_{HD} \tag{4.1}$$

With:

$$\lambda_{HD} = \frac{sin(\alpha_c + \beta)}{sin(\beta)} \cdot \{\frac{(\frac{h_b}{h_i} + sin(\alpha_c))}{sin(\alpha_c)} + \frac{cos(\alpha_c + \beta)}{2 \cdot sin(\beta)}\} \cdot \frac{sin(\beta + \phi) \cdot sin(\alpha_c + \delta)}{sin(\alpha_c + \beta + \delta + \phi)} \tag{4.2}$$

$$F_v = \rho_s \cdot g \cdot {h_i}^2 \cdot w \cdot \lambda_{VD} \tag{4.3}$$

With:

$$\lambda_{VD} = \frac{sin(\alpha_c + \beta)}{sin(\beta)} \cdot \{\frac{(\frac{h_b}{h_i} + sin(\alpha_c))}{sin(\alpha_c)} + \frac{cos(\alpha_c + \beta)}{2 \cdot sin(\beta)}\} \cdot \frac{sin(\beta + \phi) \cdot cos(\alpha_c + \delta)}{sin(\alpha_c + \beta + \delta + \phi)} \tag{4.4}$$

in which, ρ_s is the density of sand, h_i is the thickness of the layer cut, w is the width of the blade, α_c is the blade angle, β is the shear angle, ϕ and δ are the internal and external friction angles.

He compared the cutting forces from the experiments of Hatamura & Chijiiwa with his theory (Figure 4.3). It can be found that there is a good match between the theory and the measured values, only at large blade angles (75° and 90°) the forces are overestimated. This is because the angles in the denominator of Eq. (4.2) and (4.4) have dominated the trend of the curve. When the sum of the blade angle, the shear angle, the internal friction angle and the external friction angle are approaching or even

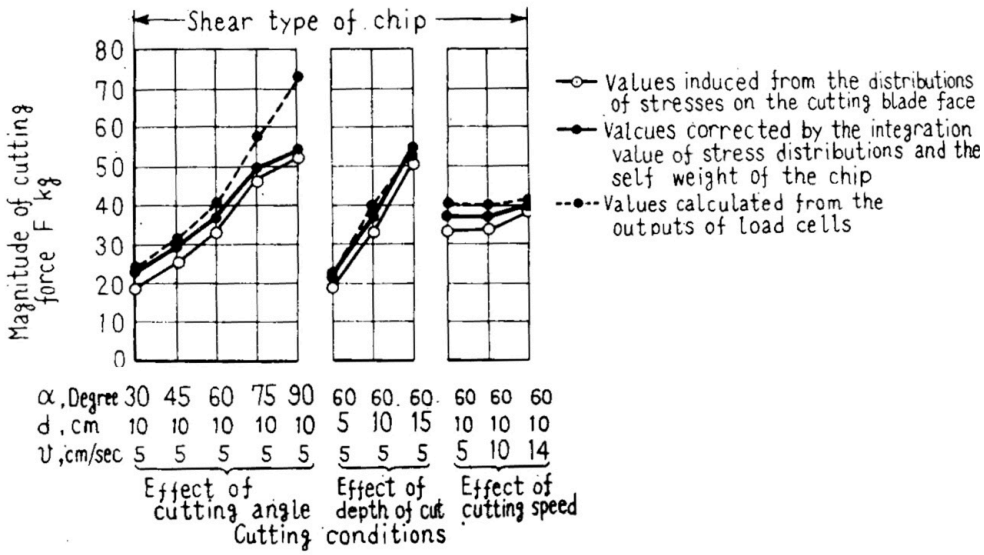

Figure 4.2: Forces acting on the cutting blade according to (Hatamura and Chjiiwa (1976b)).

over 180°, the value of the sine function will become 0 or turns negative, leading to an infinity in the value of the cutting force. This will not happen in reality. Miedema argues that, instead of an increase in the force, nature will find another mechanism with relatively smaller cutting forces. In the case of sand cutting, it appears to be the wedge mechanism. A wedge will form in front of the blade which leads to a actual decrease in the force on the blade. As shown by Fig. 4.4, a wedge forms to behave like a pseudo blade (A-C) with a smaller blade angle in front of the real blade.

In this research project, besides the small and medium cutting angles, sand cutting simulations with large cutting angles will also be conducted to find out whether the wedge phenomenon will occur or not.

4.3. Calibration - the test of angle of repose

Spherical DEM particles can be used to model sand particles when the rolling friction model is applied. The rolling friction model has been introduced in Chapter 3.2.2. To find out the correct μ_r in Eq. (3.15), the angle of repose tests have been carried out in the LIGGGHTS program. The angle of repose, or critical angle of repose, of a granular material is the steepest angle of descent or dip relative to the horizontal plane to which a material can be piled without slumping (Mehta and Barker, 1994).

The test inserts particles on a layer with a specific height (Fig. 4.5). When the particles are settled, it creates a gap in the middle of the layer and then the particles

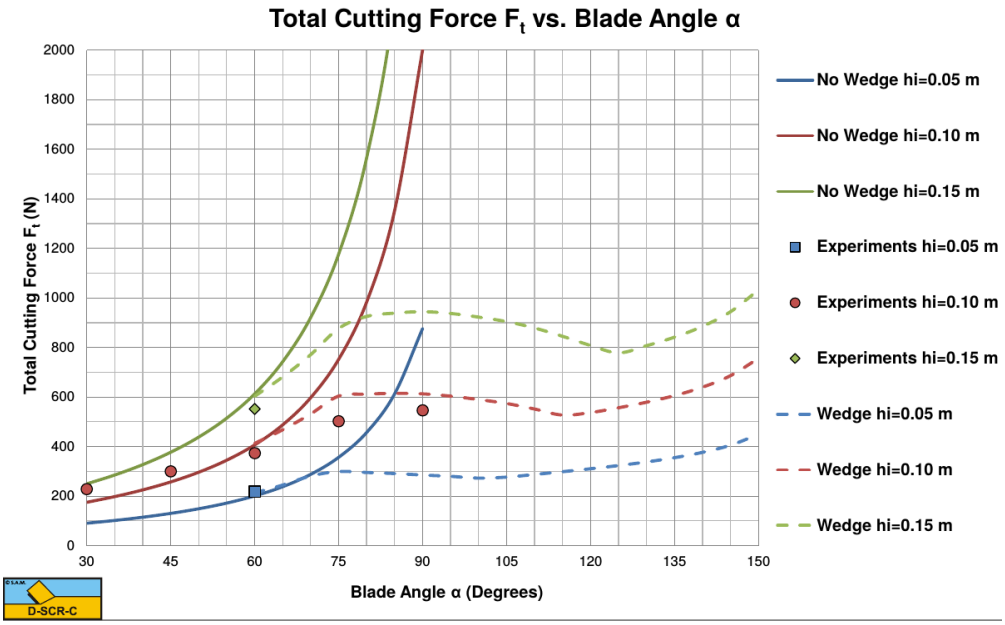

Figure 4.3: The Total Cutting Force vs. The Blade Angle. The lines show the theory according to Miedema (2014) for different cut layer thicknesses and the dots show the experimental results of Hatamura and Chjiiwa (1976b)

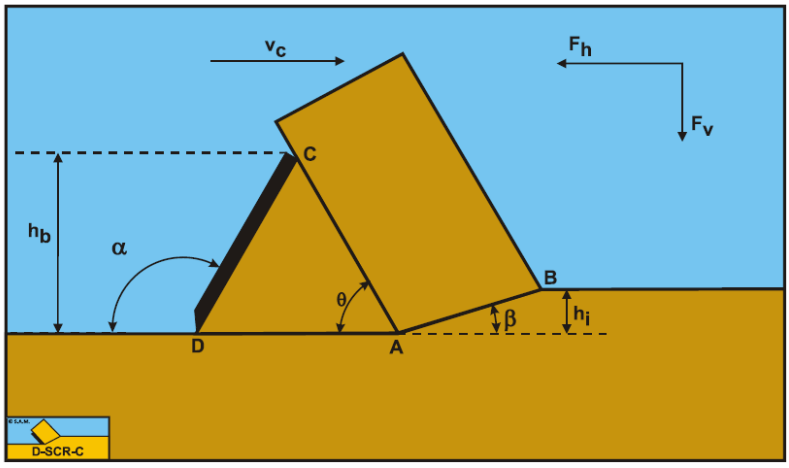

Figure 4.4: The wedge in the sand cutting process (source: Miedema (2014))

start to fall. After a while the particles settle down at the lower plate with an adequately low velocity. Then angles are measured by distinguishing the surface slopes of the sand piles both above the plates and below the plates (Fig. 4.6). To evaluate if the particles behave like real sand, the angles are shown in Fig. 4.7 and 4.8.

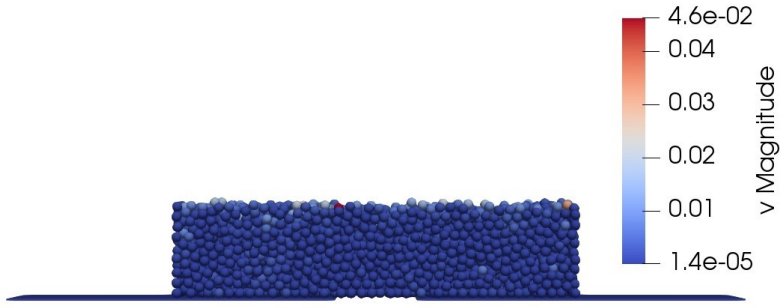

Figure 4.5: Particles are generated and settled on the plates

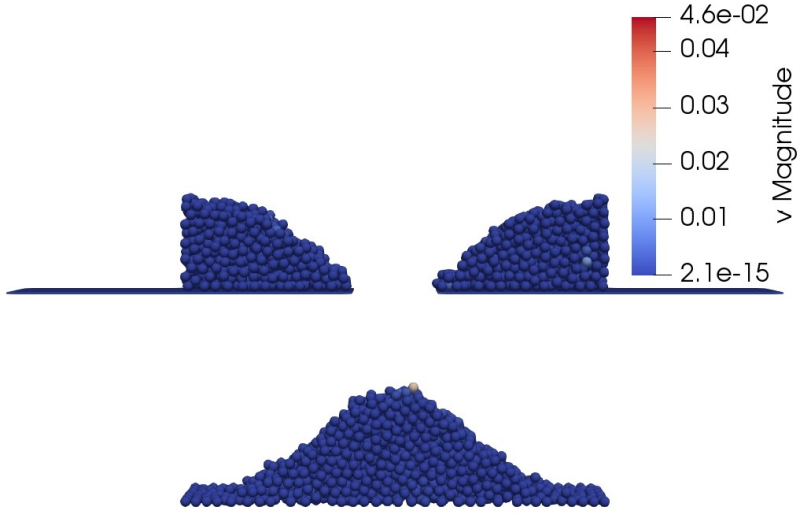

Figure 4.6: Particles fall through the gap between the plates and form up two piles at the top and one pile at the bottom

As shown by Fig. 4.7 and 4.8, the angles of the surface slopes of the upper and lower piles can be extracted within certain ranges. To ensure that the chosen angle of repose is representative enough, angles from both the left-side and right-side slopes on both the upper and lower piles are taken and examined. To calibrate the μ_r in Eq. (3.15), in total eleven tests are executed with varying rolling friction coefficients between 0 to 1 with 0.1 step size. The measured angles of repose from both the upper and bottom piles are plotted against the μ_r values, as depicted in Fig. 4.9. In Fig.

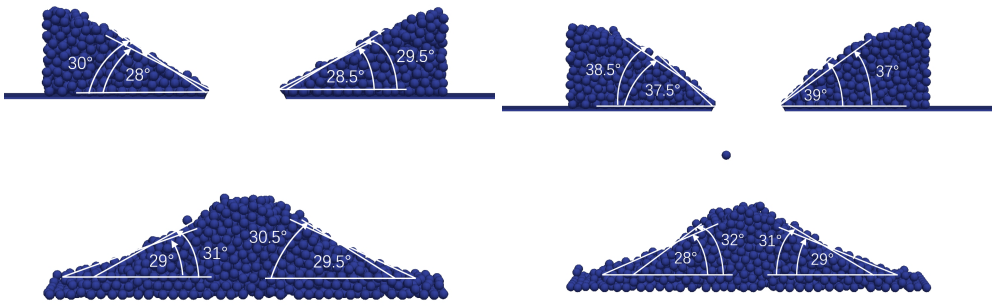

(a) Angle of repose with μ_r=0.1 (b) Angle of repose with μ_r=0.2

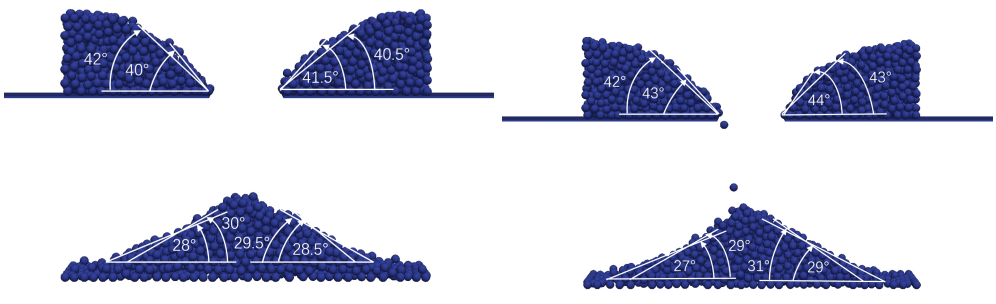

(c) Angle of repose with μ_r=0.3 (d) Angle of repose with μ_r=0.4

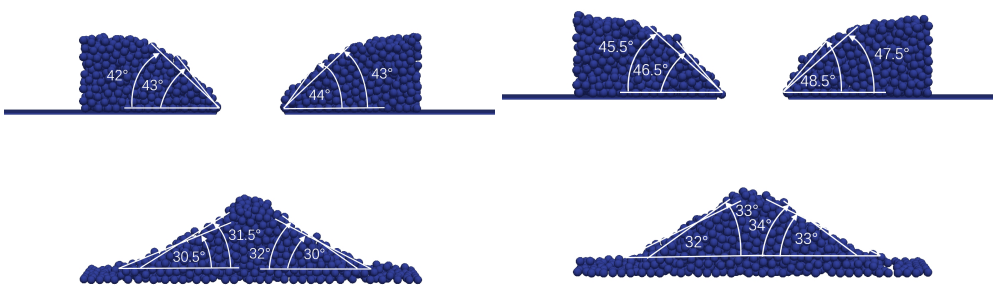

(e) Angle of repose with μ_r=0.5 (f) Angle of repose with μ_r=0.6

Figure 4.7: Angle of repose with varying rolling friction coefficients μ_r=0.1, 0.2, 0.3, 0.4, 0.5 and 0.6

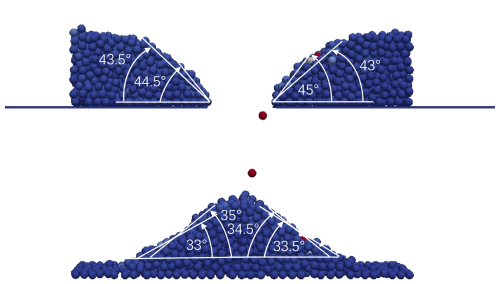

(a) Angle of repose with μ_r=0.7

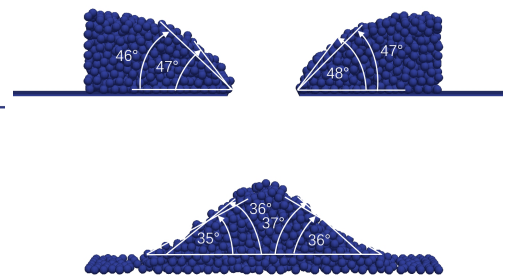

(b) Angle of repose with μ_r=0.8

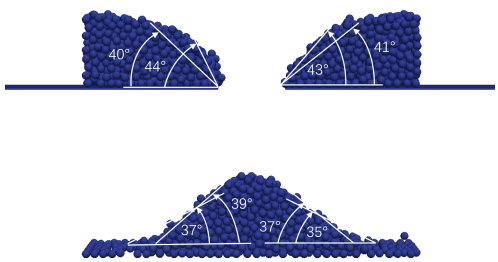

(c) Angle of repose with μ_r=0.9

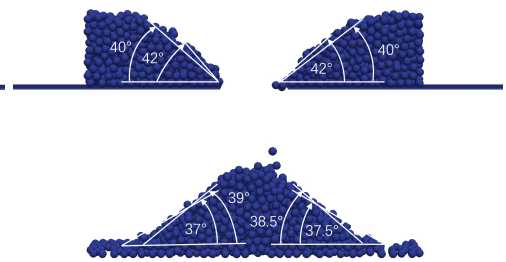

(d) Angle of repose with μ_r=1.0

Figure 4.8: Angle of repose with varying rolling friction coefficients μ_r=0.7, 0.8, 0.9, 1.0

4.9, the blue circles represent the average angle measured from the lower pile, the red circles represent the average angle measured from the upper piles. The vertical bars represent the bandwidths of variation on the measurement of these angles.

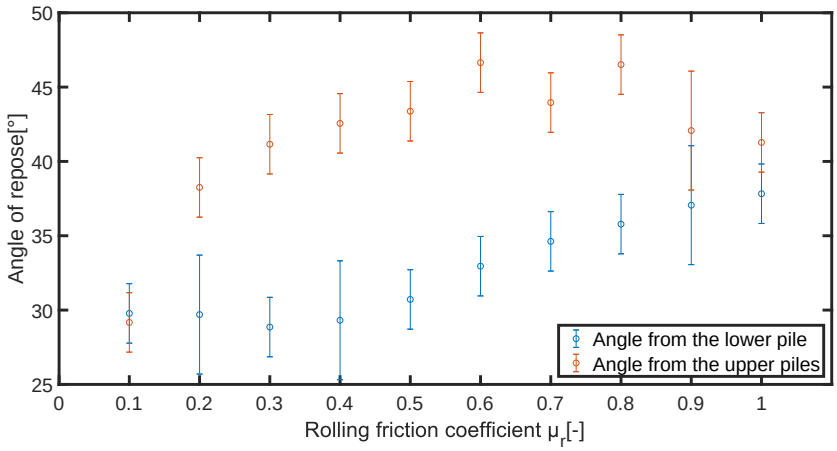

Figure 4.9: Angle of repose versus coefficient of rolling friction

The internal friction angle set as one of the most important input parameters for the DEM sand particles in these simulations is 30°. According to (Kim et al., 2018), the practical angle of repose for a sand pile is roughly 34°, slightly larger than the internal friction angle of sand because of the interlocking behaviour among sand particles in the pile.

As the rolling friction coefficient μ_r increasing from 0 to 1, larger counter torques are added to the particles to restrict their rotational motion. According to Fig. 4.9, when $\mu_r \leq 0.1$, the angle of repose from the lower pile is larger than that from the higher pile. This is because the number of the particles left on the upper plates is very low. Most particles roll and drop down readily since they are hardly restricted with rolling. However, when $\mu_r > 0.1$, the trend is different, the angle of repose from the lower pile is smaller. The reason is that the particles forming the lower pile are with higher kinetic energy than those on the upper plate. Thus these particle will travel a long distance before they stop, forming a smaller angle of repose than that above the plates. The angle of repose from the lower pile will be used for the determination of the appropriate rolling friction coefficient, since the tangent line of the sand pile surface is more stable and straight.

One can find in Fig. 4.9 the angle of repose of the lower pile increases from smaller than 30° to over 35° when rolling friction coefficient rises. It is about 34° when rolling friction coefficient μ_r is set to be 0.7, which matches the angle of repose of real sand. Therefore $\mu_r = 0.7$ is set in the rolling friction model for all the spherical DEM sand particles.

The angle of repose test has also been conducted on non-spherical DEM sand particles. As introduced in Chapter 3.2.3, the optimal shape for sand particle is Type 4, the 4-sphere combination, this type of particles are tested in the angle of repose test with a pre-defined internal friction angle of 30°. From Fig. 4.10, it can be seen that the angle of repose of the sand pile is also around 34°. As explained before this is reasonable because sand particles in reality are not spherical so they have the interlocking effect with each other, which ends up as the natural angle of repose is always slightly higher than the internal friction angle.

It is concluded that multi-spherical particles of type 4 and spherical particles with rolling friction coefficient $\mu_r = 0.7$ can both mimic the natural angle of repose of sand well. In this research project, sand cutting simulations in dry conditions are carried out using multispherical particles (type 4) because they can create the interlocking phenomenon more spontaneously in the solid structure. On the other hand, sand cutting simulations in underwater conditions are carried out by using spherical particles. The reason is that it has been discovered by testing that DEM-FVM coupling are much more stable when using spherical particles, while using multi-spherical particles the calculations for porosity and permeability are less accurate, leading to unstable results of the coupling.

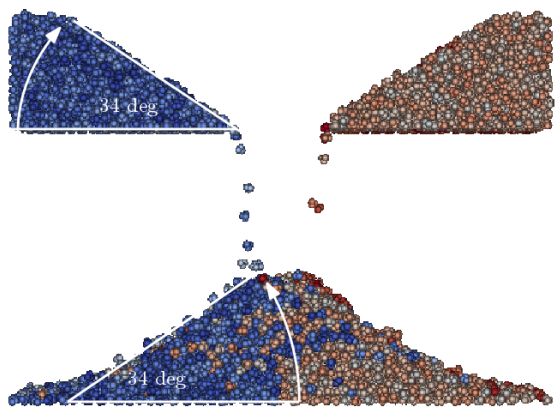

Figure 4.10: Angle of Repose test for multishpere particles

4.4. Simulations set-up of sand cutting in dry condition

To test the capacity and credibility of using DEM to simulate the sand cutting process, numerical simulations are carried out to make comparison with the experiment results from Hatamura & Chijiiwa. Or in other words, to use Hatamura & Chijiiwa's data to validate the numerical modelling of dry sand cutting.

4.4.1. Set-up of the numerical simulations

The **full-scale** simulation set-up equals to the set-up of the experiment done by Hatamura and Chijiiwa described in Chapter 4.1. The dimensions of the soil bin are $150cm$ in length by $33cm$ in width (Fig. 4.11). The height varies per simulation and can be respectively $5, 10$ or $15cm$.

However, there is a problem that occurs during this set-up. Simulating particles with the size of real sand particles (radius $= 0.2mm$) results in about 8~9 million particles. This amount of particles is with the existing available computation power of the computer not possible to simulate. A solution for this problem is to increase the radius of the particles to a workable radius of $1.25cm$, in this way a **full-scale** simulation can be done with the same size of Hatamura & Chijiiwa's experiments.

Another option is to scale down the dimensions of the set-up to a workable size where the amount of particles are within the computation capacity of the computer. The dimensions of the **small-scale** simulation are thus designed as $5.5cm$ in length, $0.47cm$ in width and the height varies per simulation and can be respectively $0.225cm$, $0.350cm$ or $0.475cm$, the radii of the particles used in the **small-scale** simulations are 0.2mm. For this research, both scales are tried and discussed.

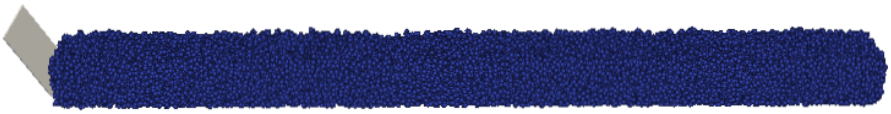

Figure 4.11: **Full-scale** simulation set-up with a layer thickness of 10 cm composed by multi-spherical particles (Type 4).

The full-scale simulation uses a blade made of steel to cut a layer of sand. The angle of the blade varies per simulation and can be 30°, 45° or 60° (Fig. 4.12). The dimensions of the blade are $33 \times 20 \times 0.1cm$. The speed of the blade are set as $5, 10$ or $14cm/s$ respectively. On the other hand, in the small-scale set-up, the dimensions of the blade are different, which are $0.5 \times 0.47 \times 0.01cm$ and moves with a reduced speed of $0.35cm/s$.

Material properties are also defined in DEM for the blade and the sand particles. Hatamura & Chijiiwa specified some of the sand properties. The blade is described as a 'smooth steel blade'. The properties which Hatamura & Chijiiwa described are taken as input values for the simulation, while the values that were unknown are estimated. Table 4.2 shows the properties of the materials and the contacts used in the simulation, where the coefficient of internal friction corresponds to an internal friction angle of 30° and the coefficient of external friction corresponds to an external friction angle of 20°.

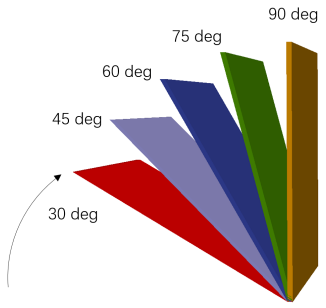

Figure 4.12: Blade angles used in the simulations of sand cutting process

Table 4.2: The material properties and contact parameters used in the sand cutting simulations in dry conditions

Material properties & contact parameters	Symbol	Value	Unit
Poisson' s ratio of the sand particle	ν_p	0.4	-
Material density of the sand particle	ρ_p	2670	kg/m^3
Poisson' s ratio of the blade (steel)	ν_{steel}	0.4	-
Coefficient of restitution (sand-sand)	ψ_p	0.0001	-
Coefficient of internal friction (sand-sand)	μ_p	0.577	-
Coefficient of restitution (sand-blade)	ψ_{pb}	0.0001	-
Coefficient of external friction (sand-blade)	μ_{pb}	0.364	-

4.4.2. Plan of the simulations for dry sand cutting

To check if the DEM model matches the experimental results of Hatamura and Chijiiwa. The following simulations are carried out for dry sand cutting process, as listed in Table 4.3, in which the **full-scale** simulations use the same dimensions as the experiments, while the **small-scale** simulations run on a scaled-down size.

Table 4.3: **Full-scale** and **Small-scale** simulations of dry sand cutting process

Test No.	Blade Angle	Cutting Speed	Layer Thickness		Test No.	Blade Angle	Cutting Speed	Layer Thickness
	[°]	$[cm/s]$	$[cm]$			[°]	$[cm/s]$	$[cm]$
Full-scale Simulations					**Small-scale** Simulations			
1.1	30°	5	10		1.8	30°	0.35	0.35
1.2	45°	5	10		1.9	45°	0.35	0.35
1.3	60°	5	5		1.10	60°	0.35	0.225
1.4	60°	5	10		1.11	60°	0.35	0.35
1.5	60°	10	10		1.12	60°	0.35	0.475
1.6	60°	14	10		1.13	75°	0.35	0.35
1.7	60°	5	15		1.14	90°	0.35	0.35

For the **full-scale** simulations, Test 1.1, 1.2 and 1.4 are designed for finding out the influence of the blade angle, Test 1.3, 1.4 and 1.7 are designed for investigating the influence of the cutting layer thickness, Test 1.4, 1.5 and 1.6 are for investigating the influence of the cutting speed.

For the **small-scale** simulations, Test 1.8, 1.9 and 1.11 are designed for finding out the influence of the blade angle, Test 1.13 and 1.14 are specially designed to check if the wedge theory validates in DEM simulations, and Test 1.10, 1.11 and 1.12 are designed for investigating the influence of the cutting layer thickness.

4.5. Results & validation of simulations of sand cutting in dry condition

This section shows the results of the numerical simulation for dry sand cutting where for both the **full-scale** and the **small-scale** simulations, the influences of the blade angle, the thickness of the cut layer and blade speed are discussed, which are also the effects studied in the experiments of Hatamura and Chijiiwa, as shown in Fig. 4.2.

Considering the fact that the set-up in the DEM simulations are not the exact duplication of the Haramura and Chijiiwa's experimental set-up, for example, in the **full-scale** simulations, the particle sizes are different from the experiments, in the **small-scale** simulations, the size of the whole set-up is much smaller than in the experiments, therefore it is decided that in order to make a fair comparison, the stresses, instead of the forces, on the surface of the blade, will be used as the main parameter

for validation, and that includes the stresses in the normal direction, the tangential direction and the total overall stress which is the value of the resultant force on the blade divided by the blade surface area.

4.5.1. Analysis of the results from the full-scale simulations

Validation of the shear angle in the shear zone

The failure mode for sand in cutting in dry environment, according to Miedema (2014), is the shear type. This means that a shear plane will develop and then be pushed onto the blade. When this occurs, a new shear plane appears ahead of the previous one. According to (Miedema, 2014), the shear angle can be calculated by taking the derivative of the horizontal force F_h (Eq. (4.1)) with respect to the shear angle β and making it equal to zero. Based on the experiment set-up of Hatamura and Chijiiwa, the theoretical value of the shear angles for those experiments are shown in Fig. 4.13.

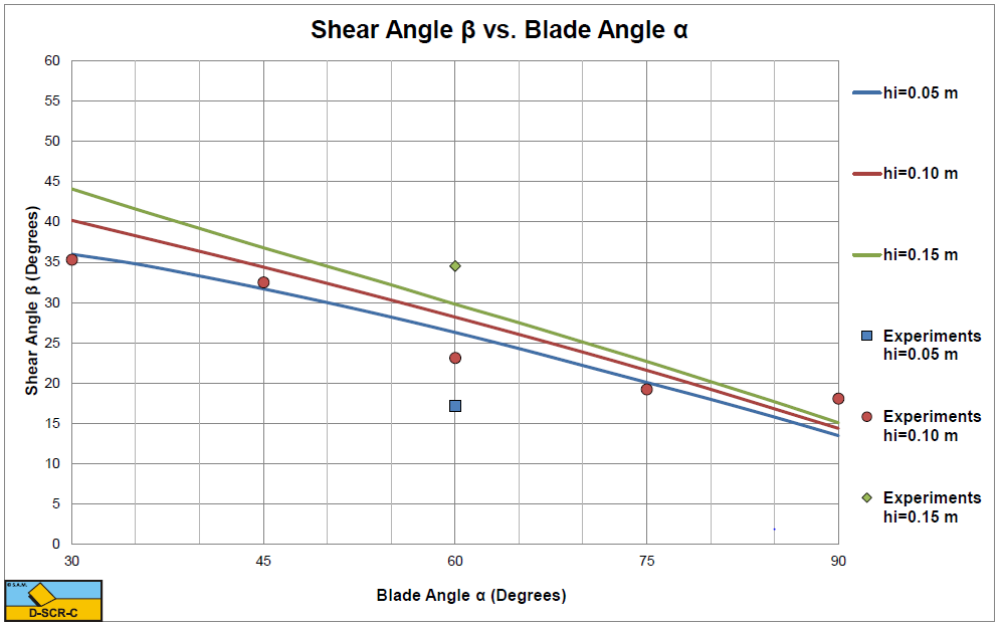

Figure 4.13: The shear angle β vs. the blade angle α: analytical results from (Miedema, 2014) (lines) & experimental results from (Hatamura and Chjiiwa, 1976b)

Fig. 4.13 shows that both the blade angle and cutting depth will impact the shear angle. The analytical solution of Miedema predicts the shear angle with changing blade angle within acceptable error margins, but predicts the shear angle very poorly when the cutting depth changes.

In Fig. 4.14 to 4.16 the shear plane of the **full-scale** DEM simulation is presented

for blade angles of respectively $30°, 45°$ and $60°$. The red particles are the ones which 'shear' over the blue ones. The red color shows particles which are moving above a velocity with a magnitude that equals the velocity of the particles at the tip of the blade. The blue particles are the ones which are below this critical velocity. To make a clear comparison, the shear angles recorded from the experiments of Hatamura & Chijiiwa are directly plotted in the figures, as indicated as the white lines, and the theoretical results from the analytical solution are also mentioned respectively.

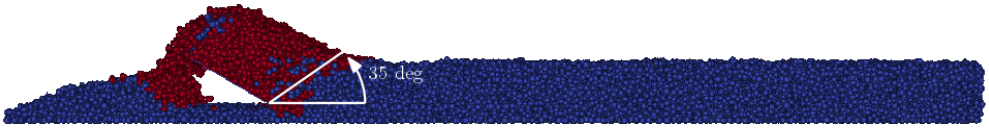

Figure 4.14: The shear plane in the DEM-simulation with a blade angle of $30°$, a blade speed of $5cm/s$ and a cutting depth of $10cm$ (Test 1.1). The analytical solution of Miedema for this shear angle is $40°$.

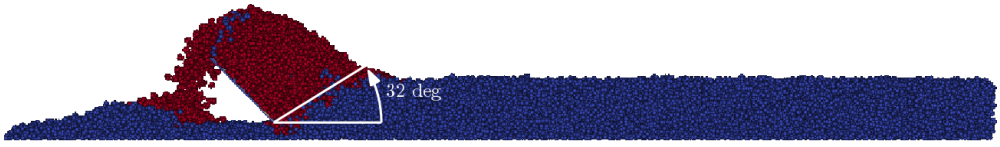

Figure 4.15: The shear plane in the DEM-simulation with a blade angle of $45°$, a blade speed of $5cm/s$ and a cutting depth of $10cm$ (Test 1.2). The analytical solution of Miedema for this shear angle is $34°$.

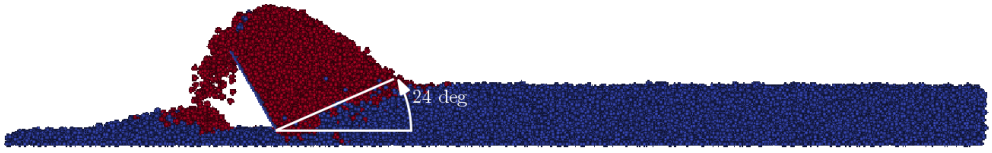

Figure 4.16: The shear plane in the DEM-simulation with a blade angle of $60°$, a blade speed of $5cm/s$ and a cutting depth of $10cm$ (Test 1.4). The analytical solution of Miedema for this shear angle is $28°$.

Not only the blade angle influences the shear angle but also the layer thickness of cut layer. The development of the shear plane is also depending on the ratio of the blade height over the layer thickness. A larger ratio results in a smaller shear angle. This trend can be found in Fig. 4.13. In Fig. 4.17, 4.18 and 4.19, the shear angle is shown for a $60°$ blade with a layer thickness of $5cm$, $10cm$ and $15cm$.

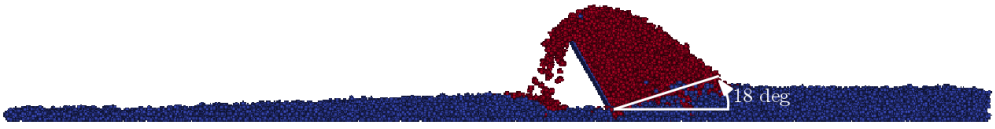

Figure 4.17: The shear plane in the DEM-simulation with a blade angle of $60°$, a blade speed of $5cm/s$ and a cutting depth of $5cm$ (Test 1.3). The analytical solution of Miedema for this shear angle is $26°$.

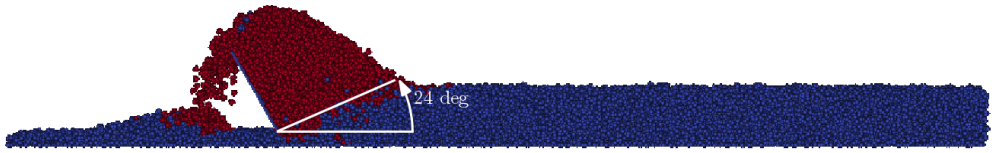

Figure 4.18: The shear plane in the DEM-simulation with a blade angle of $60°$, a blade speed of $5cm/s$ and a cutting depth of $10cm$ (Test 1.4). The analytical solution of Miedema for this shear angle is $28°$.

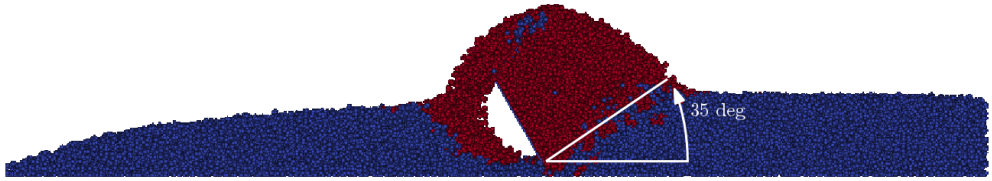

Figure 4.19: The shear plane in the DEM-simulation with a blade angle of $60°$, a blade speed of $5cm/s$ and a cutting depth of $15cm$ (Test 1.7). The analytical solution of Miedema for this shear angle is $30°$.

The shear planes in the DEM-simulation matches the shear planes observed by Hatamura and Chijiiwa well. Especially with changing cutting layer thickness, the simulated shear angles match the experimental results much better than the analytical solutions. Besides, after the shear plane forms it will be pushed over the blade and a new shear plane will form up, as illustrated in Fig. 4.20. This phenomenon has been clearly observed in the simulations.

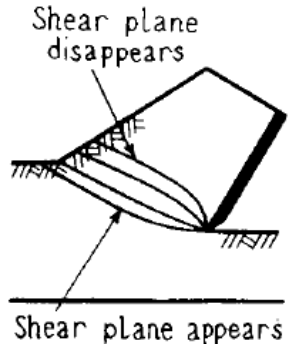

Figure 4.20: Appearance of shear plane produced by cutting, (Hatamura and Chjiiwa, 1976b)

The influence of blade angle

In Fig. 4.21, the developments of the total stress on the surface of the blade, which are recorded when the blade is cutting in the sand, are shown for all the three blade angles. The total/overall stress is calculated by using the resultant force, which is the combination of the normal and shear forces, to be divided by the surface area of the

blade. From the figure, it is clearly visible that the overall stress on the blade increases with increasing blade angle.

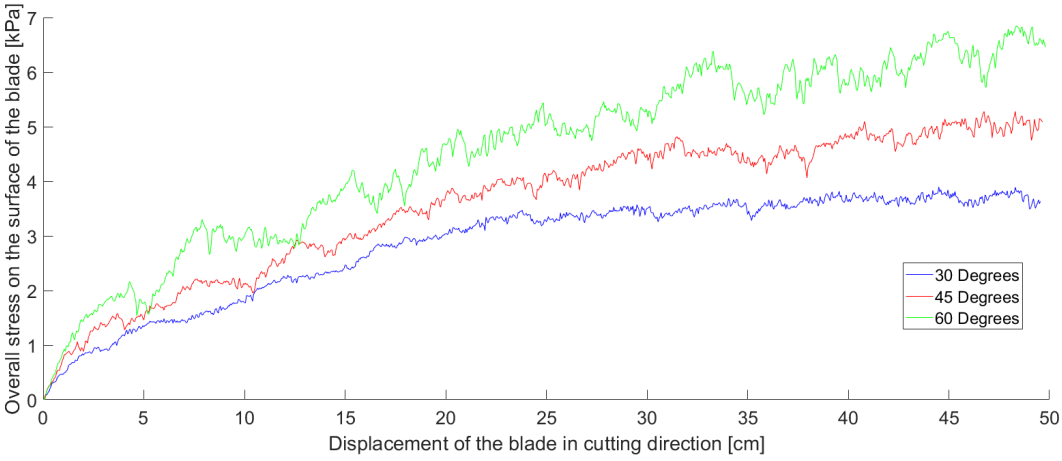

Figure 4.21: Effect of the cutting angle of the blade with a layer thickness of $10cm$ and a blade speed of $5cm/s$ (Test 1.1, 1.2 & 1.4).

The influence of the thickness of the cut layer

In Fig. 4.22 the developments of the total stress on the surface of the blade, which are recorded when the blade is cutting into the sand, are shown for all the three different cut layers thickness's. It can be found that the overall stress on the blade increases with increasing layer thickness.

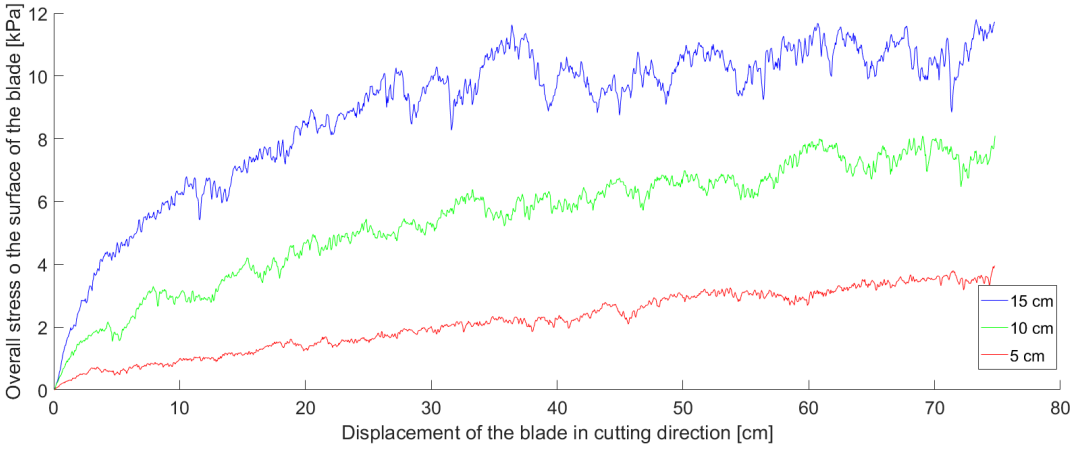

Figure 4.22: Effect of the depth of cut with a blade angle of $60°$ and a blade speed of $5cm/s$ (Test 1.3, 1.4 & 1.7).

The influence of the cutting speed

In Fig. 4.23 the simulation results for different cutting speeds are shown. The overall stresses on the blade do not change significantly with increasing cutting speed. This is reasonable because the cutting forces will increase due to the inertia effects only when the cutting speed is really high, while in the simulations conducted in this research, the maximum cutting speed reached is only $14cm/s$, not high enough to present an significant inertia effect.

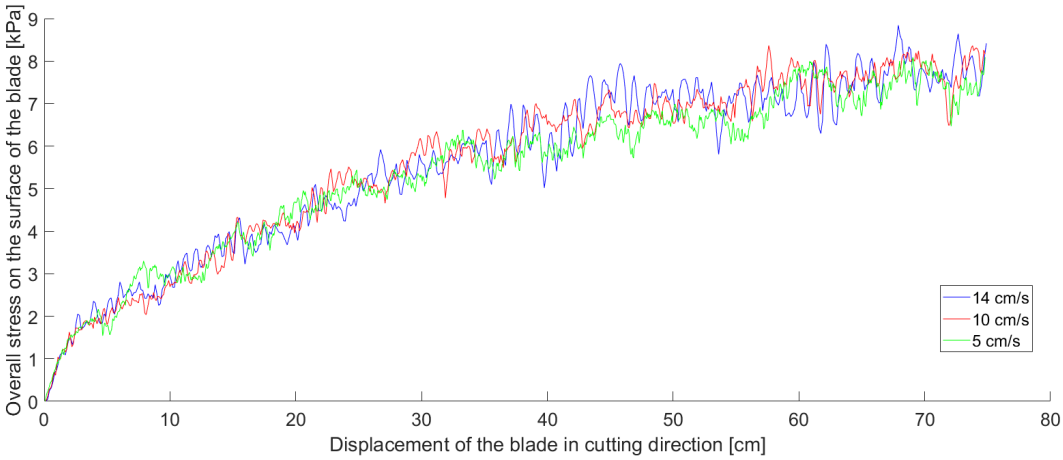

Figure 4.23: Effect of the cutting speed with a blade angle of $60°$ and a layer thickness of $10cm$ (Test 1.4, 1.5 & 1.6).

Validation of the cutting forces

The resulting normal, tangential and overall stresses on the blade from the experiments of Hatamura and Chijiiwa (the "H&C" column) and from the **full-scale** DEM simulations (the "DEM" column) are shown in Table 4.4. As introduced before, stresses are used to represent the cutting forces. Comparing the two results, it can be found that normal and overall stresses from the simulations in all scenarios are higher than the measurements from the experiments. The main reason for such a difference is that there is a difference in the porosities of the sand sample between the simulations and the experiments.

The particle density of the soil constituent is 2.67 g/cm^3 in the experiments of Hatamura and Chijiiwa and the soil bulk density is 1.46 g/cm^3. In the DEM simulations, the porosity is heavily influenced by the shape of the multisphere particles, and that results in a particle density of 2.67 g/cm^3 but with a soil bulk density of 1.602 g/cm^3, in other words, the sand sample in the DEM simulations has lower porosity than in the experiments.

Taking this difference into account, a calculation is made to slightly scale down the

cutting stresses from the simulation so that the simulations and the experiments are compared with the same soil bulk density, i.e., the ρ_s in Eq. (4.1) and (4.3). Since the forces are proportional with the soil bulk density, the stresses are also proportional with the soil bulk density. The adjusted simulation results are listed with column "DEM Scaled" in Table 4.4.

Table 4.4: Stresses on the blade from the experiments of (Hatamura and Chijiiwa, 1976b) (H&C) and the **full-scale** DEM simulations of dry sand cutting (DEM & DEM Scaled)

Blade Angle	Layer Thickness	Blade Speed	Normal Stress			Tangential Stress			Overall Stress		
[°]	[cm]	[cm/s]	[kPa]			[kPa]			[kPa]		
			H&C	DEM	DEM Scaled	H&C	DEM	DEM Scaled	H&C	DEM	DEM Scaled
30	10	5	3.0	3.5	3.1	1.7	1.3	1.2	3.5	3.7	3.4
45	10	5	4.0	5.0	4.3	2.2	1.8	1.6	4.6	5.3	4.6
60	5	5	3.1	5.1	3.1	1.2	1.8	1.0	3.3	5.4	3.2
60	10	5	5.1	7.2	5.6	2.4	2.4	1.8	5.7	7.7	5.9
60	10	10	5.2	7.3	5.9	2.4	2.5	1.9	5.8	7.7	6.2
60	10	14	5.5	7.3	5.8	2.9	2.5	2.0	6.2	7.8	6.2
60	15	5	7.6	10.2	9.3	3.5	3.3	3.0	8.4	10.8	9.8

In Figure 4.24, the cutting stresses of Hatamura & Chijiiwa are plotted against the adjusted results from the DEM simulations. Overall speaking, the simulation results resemble the experiments of Hatamura & Chijiiwa well.

The Tangential stresses of the DEM simulations show clear underestimations. This can be related to the roughness of the blade, The external friction coefficient between the particles and the blade is set to be 0.364, which is an empirical value. The actual external friction coefficient from Hatamura & Chijiiwa's experiments is unknown.

Furthermore the Total and Normal stresses recorded from the numerical simulations seem slightly higher than the experiments. Note that here the Total stress is the vectorial sum of the Normal and Tangential stresses. A potential reason for that is, it is questionable if Hatamura & Chijiiwa have obtained the completely steady state during their experiments. They obtained their values at the timing when the cutting blade was $20 \sim 25cm$ away from the starting point, because they assumed that the stresses/forces become more or less constant at that point. While in the DEM simulations, the results show that even after $25cm$, there are still a slight increase in the stresses. So that the steady state cutting forces recorded in the numerical modelling are slightly higher than the results from laboratory experiments.

4.5.2. Analysis of the results from the small-scale simulations

As explained before, in the **small-scale** simulations the dimensions of the blade ($0.5cm \times 0.47cm \times 0.01cm$) are different than the dimensions in the **full-scale** simulations and the experiments of Hatamura and Chijiiwa ($30cm \times 20cm \times 0.1cm$).

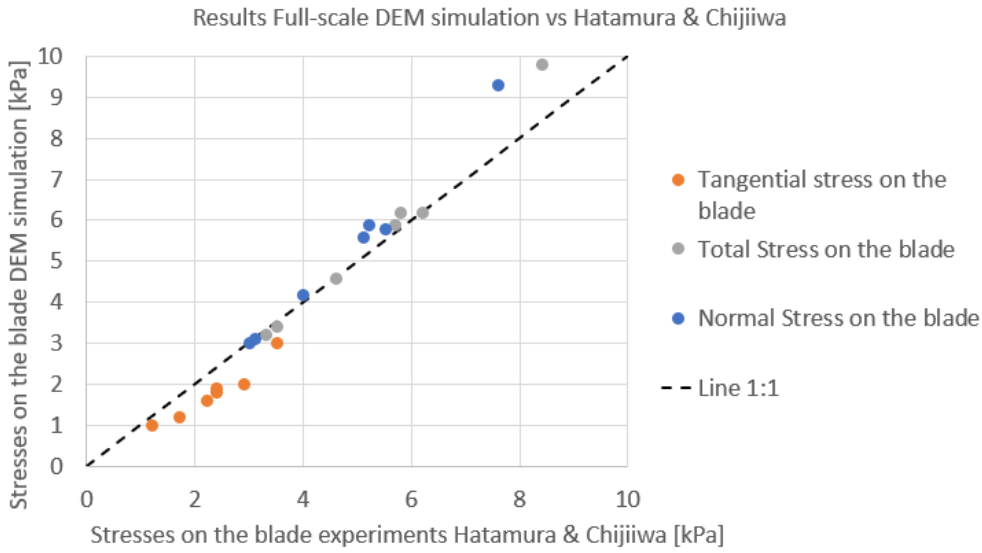

Figure 4.24: Stresses on the blade from the **full-scale** DEM simulations of dry sand cutting with adjusted bulk density vs. Stresses recorded from the experiments of Hatamura & Chijiiwa

The analysis on the results from the **small-scale** simulations focuses on the cutting forces.

Influence of the blade angle

Fig. 4.25 shows the development of the overall stress for different blade angles (Test 1.8, 1.9 & 1.11). It is again clearly visible that the stress on the blade increases with blade angles. The same pattern is observed as in the **full-scale** simulations. It is also observed that higher angle results in more scattering of the cutting forces.

Influence of the thickness of the cut layer

In Fig. 4.26 the development of the overall stress for three different cut layer thickness's are shown (Test 1.10, 1.11 & 1.12). It is clearly visible that the stress on the blade increases with the thickness of the cut layer. The same pattern is observed as in the **full-scale** simulations.

Validation of the cutting forces

The resulting normal, tangential and overall stresses on the blade from the experiments of Hatamura and Chijiiwa (the " H&C" column) and from the **small-scale** DEM simulations (the ¨DEM¨ column) are shown in Table 4.5. It is obvious that the stresses from the **small-scale** DEM simulation are much lower than the values

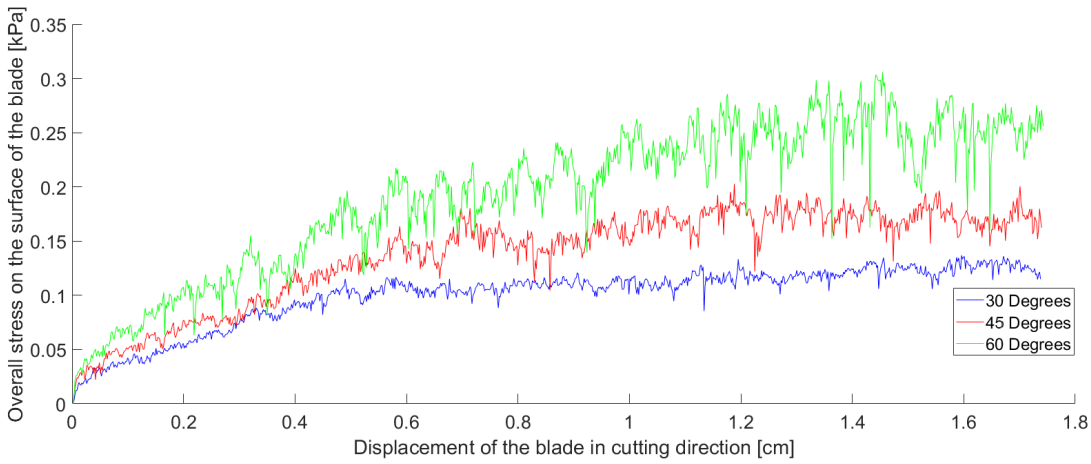

Figure 4.25: Effect of the blade cutting angle on the overall stress in the **small-scale** simulations with a layer thickness of $0.35cm$ and a blade speed of $0.35cm/s$ (Test 1.8, 1.9 & 1.11).

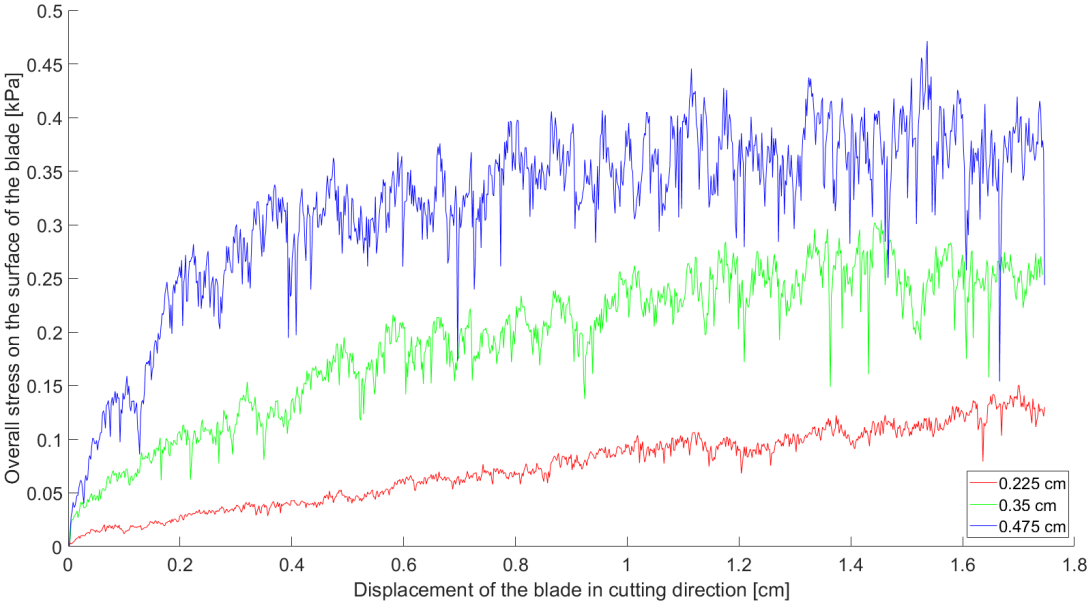

Figure 4.26: Effect of the cut layer thickness on the overall stress in the **small-scale** simulations with a blade angle of $60°$ and a blade speed of $0.35cm/s$ (Test 1.10, 1.11 & 1.12).

obtained from the lab experiments. This difference is mainly induced by the scaling effect.

To quickly estimate the scaling effect, a revisit is paid to Eq. (4.1), (4.2), (4.3) and (4.4). Based on the macro behaviour of the analytical model for dry sand cutting, it can be roughly accepted that $\alpha, \beta, \phi, \delta$ do not change from **small-scale** simulation to experiments. Besides, the h_b/h_i ratios are chosen to match the experiments (Table 4.3), so it is assumed that in Eq. (4.1) and (4.3), λ_{HD} and λ_{VD} stay the same.

In this way the cutting forces scale with the $(h_i^2 \cdot w)$ factor and the soil bulk density ρ_s. This factor is further divided by the surface area of the blade to find out the scaling factor for the cutting stresses. It is finally found out that the stresses on the blade is proportional with the layer thickness and the bulk density $(h_i \cdot \rho_s)$. In the **small-scale** simulations the layer thickness is 28.6 times smaller than in the experiments of Hatamura & Chijiiwa.

Furthermore the difference in the porosities of the DEM samples and the experimental samples are also considered to adjust the soil bulk density. Taking these two effects into account results in the the following values as ¨DEM Scaled¨ shown in Table 4.5 where the results are scaled with a factor 26.

It is found that the results of the **small-scale** DEM simulation after the scale-up, matches the experimental results from Hatamura & Chijiiwa well. In Fig. 4.27, the results of Hatamura & Chijiiwa are plotted against the scaled results of the **small-scale** DEM simulations. It is observed that DEM predicts the cutting forces much better at blade angle of 30° and 45° than at 60°. At 60°, there is an apparent overestimation on the normal stresses, leading to an overestimation on the overall stresses.

Table 4.5: Stresses on the blade from the experiments of (Hatamura and Chjiiwa, 1976b) (H&C) and the **small-scale** DEM simulations of dry sand cutting (DEM & DEM Scaled)

Test No.	Blade Angle [°]	Normal Stress [kPa]			Tangential Stress [kPa]			Overall Stress [kPa]		
		H&C	DEM	DEM Scaled	H&C	DEM	DEM Scaled	H&C	DEM	DEM Scaled
1.8	30	3.0	0.119	3.1	1.7	0.119	1.2	3.5	0.127	3.3
1.9	45	4.0	0.160	4.1	2.2	0.160	1.5	4.6	0.169	4.4
1.10	60	3.1	0.121	3.2	1.2	0.121	1.1	3.3	0.128	3.3
1.11	60	5.1	0.241	6.3	2.4	0.241	2.0	5.7	0.251	6.5
1.12	60	7.6	0.358	9.3	3.5	0.358	3.0	8.4	0.365	9.5

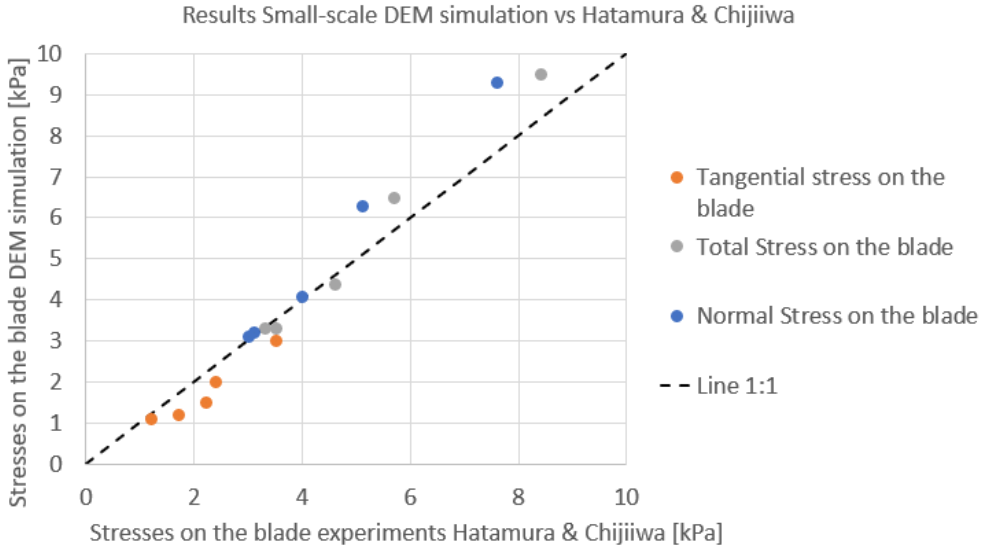

Figure 4.27: Stresses on the blade from the **small-scale** DEM simulations of dry sand cutting after scaling vs. Stresses recorded from the experiments of Hatamura & Chijiiwa

Validation of the wedge theory in dry sand cutting

Test 1.13 and 1.14 (Table 4.3) are specially carried out to exam the cutting forces with large cutting angles (75° & 90°). Miedema argued that when the blade angles is large, a wedge may occur in the sand cutting so that the cutting force cannot increase too fast. Based on the illustration of Fig. 4.4, he derived the analytical model for calculating the cutting forces when a wedge is present. This model can be found in (Miedema, 2017).

In this research project, the overall stresses on the blade from the experiments of Hatamura and Chiijiwa, the DEM simulations, the analytical model of Miedema with no wedge and the analytical model of Miedema with wedge, are listed in Table 4.6 and compared in the Fig. 4.28

Table 4.6: The overall stress on the blade from Miedema's analytical models (no wedge & wedge), Hatamura & Chiijiwa's experiments and DEM simulations

Blade angle	Analytical Model of Miedema		Experiments H&C	DEM Simulation Scaled
α_c [°]	No wedge [kPa]	Wedge [kPa]	[kPa]	[kPa]
30	3.79	3.79	3.5	3.30
45	5.69	5.69	4.6	4.40
60	9.39	9.39	5.7	6.50
75	17.88	13.33	11.8	11.11
90	42.42	14.39	13.3	14.78

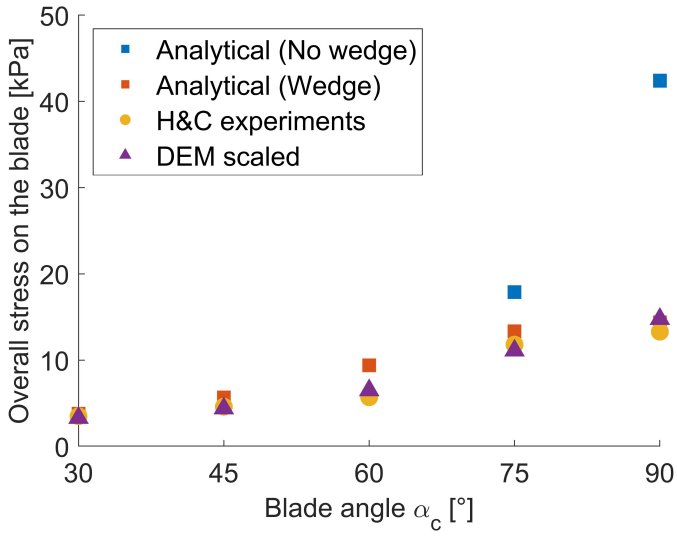

Figure 4.28: The overall stress on the blade with different blade angles from Miedema's analytical models (no wedge & wedge), Hatamura & Chiijiwa's experiments and DEM simulations

Fig. 4.28 illustrates the overall stresses on the blade with five blade angles from different methods. When the cutting angles are small (30°, 45° and 60°), both the no-wedge analytical model and the DEM results agree with the experimental results well. when the blade angle is over 60°, the no-wedge model significantly overestimates the cutting force, on the other hand, the wedge analytical model and the DEM results match the experiments well. It is thus concluded that DEM simulation can well predict the cutting force when a wedge occurs at high cutting angles.

4.6. Underwater sand cutting experiments from Miedema

Miedema carried out a series of underwater sand cutting experiments in the laboratory of Dredging Engineering (DE) of Delft University of Technology. The results of the experiments are published in (Miedema, 2017) and used as the validation data for DEM-FVM coupling simulations of underwater sand cutting process. A brief introduction of Miedema's experiments is given below.

4.6.1. Test of the hydraulic conductivity of sand samples

Before conducting the experiment of underwater sand cutting, a test on the hydraulic conductivity of the sand sample was carried out. For several sand samples that were used in the experiments, their porosities are tested and recorded. The velocity that water penetrates a sand sample was also recorded as the hydraulic conductivity

of that sample. The results are displayed in Table 4.7. With these measurements, Miedema established the relation between the hydraulic conductivity of the sand sample (K_{sand}) and the porosity of sand samples (n).

Table 4.7: The hydraulic conductivity vs. porosity from (Miedema, 2017)

Porosity	Hydraulic conductivity
n [-]	K_{sand} [m/s]
0.369	7.7×10^{-5}
0.385	1.65×10^{-4}
0.389	2.06×10^{-4}
0.399	2.4×10^{-4}
0.409	2.97×10^{-4}
0.418	3.07×10^{-4}
0.431	3.22×10^{-4}

4.6.2. Underwater sand cutting experiments

For the underwater sand cutting experiments, a tank of 30 m long, 2.5 m wide and 1.35 m high was used. This tank was filled with a sand layer of 0.5 m and a water layer of 0.6 m above it. The sand used is with a d_{50} of 200 μm. The main facilities in the laboratory are a carriage pulled by two steel cables, drums of a hydraulic winch and a squirrel-cage motor of 35 kW. The velocity of the carriage can be altered in a range between 0.05 m/s and 2.5 m/s and the pulling force is up to 6 kN. Fig. 4.29 shows a depiction of the experimental set-up.

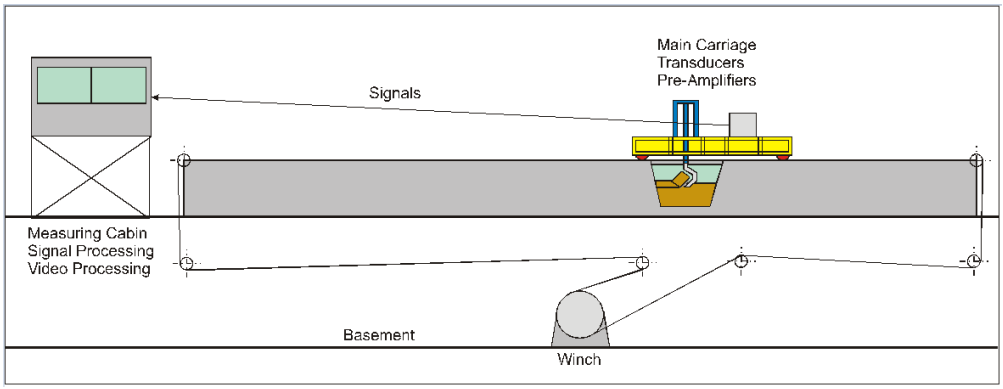

Figure 4.29: The side view of the laboratory for underwater sand cutting experiments

Two types of experiments were conducted, the experiments of **2D effect** and **3D effect**. The **2D effect** means that sand particles after cut can only fall from the top the blade, and they cannot fall from the transverse sides of the blade. The **3D effect**

means that sand particles after cut can fall not only from the top of the blade, but also from the transverse sides of the blade.

Only the cutting forces of the 2D effect experiments were well recorded and published, thus here only the 2D effect experiments are introduced. The cutting process of 2D effect is realized by using a middle blade and two side blades on both sides. The forces on the blade are measured by a dynamometer mounted on the middle blade, including the horizontal force, the vertical force, the transverse force and the bending moment. Similarly, the side blades are also equipped with dynamometers to measure the horizontal and vertical forces. To measure and record the pore pressure, there are four pore pressure transducers mounted on the middle blade. The set-up of the center blade is exhibited in Figure 4.30.

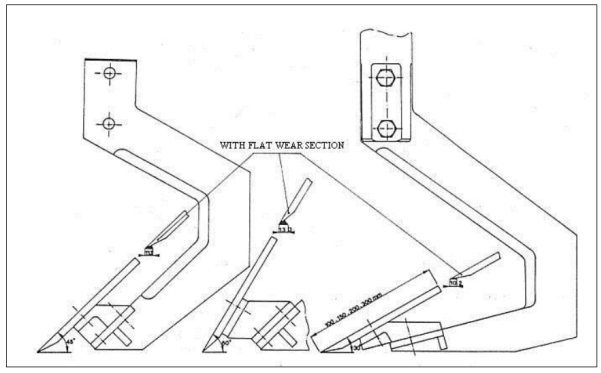

Figure 4.30: The side view of the center blade of 45°, 60° and 30° in the experiments of (Miedema, 2017)

The underwater sand cutting experiments were conducted with varying blade angles and blade heights. The experimental matrix is displayed in Table 4.8.

Table 4.8: Experiment matrix of underwater sand cutting with $200\mu m$ sand by Miedema

Blade angle	Blade height	Cutting layer thickness	h_b/h_i	Hydrostatic pressure
α_c [°]	h_b [mm]	h_i [mm]	[-]	p_h [kPa]
30	100	100	1	5.89
30	200	100	2	5.89
30	300	100	3	5.89
45	100	100	1	5.89
45	200	100	2	5.89
45	300	100	3	5.89
60	100	100	1	5.89
60	200	100	2	5.89
60	300	100	3	5.89

4.7. Simulations set-up of sand cutting in underwater condition

4.7.1. Test matrix for the underwater sand cutting simulations

As introduced in Chapter 4.3, spherical DEM particles with rolling friction are used in the underwater sand cutting simulations. Both the **2D effect** and **3D effect** simulations have been carried out. It should be noted that all the simulations are actually conducted in 3D domain. Among the two types, the simulations of 2D effect can be validated with the experiments of (Miedema, 2017).

In DEM, the simulations of 2D effect can be realized by setting the bounding walls in the transverse directions, which define the width of the sand sample, narrower than the width of the cutting blade. In this way, the particles can only move along the cutting blade and fall down from the top to the back of the blade, but they cannot fall down from the transverse sides of the blade, as shown by Fig. 4.32. The inverse set-up is arranged for the simulations of 3D effect so that the particles can fall down from both the blade top and arbitrarily the two transverse sides of cutting blade, as Fig. 4.33 shows.

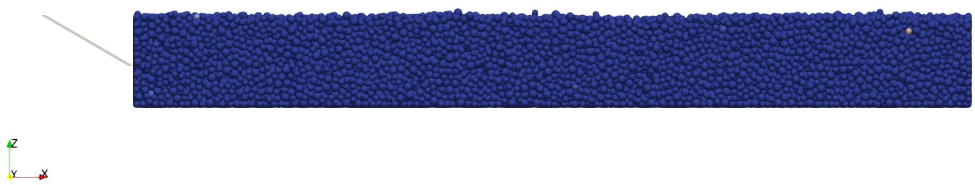

Figure 4.31: The side view of the blade and the sand sample

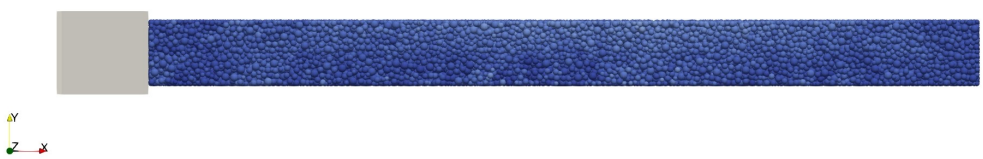

Figure 4.32: The plan view of the set-up for the width of the DEM sand sample and the blade in the simulation of **2D effect** underwater cutting

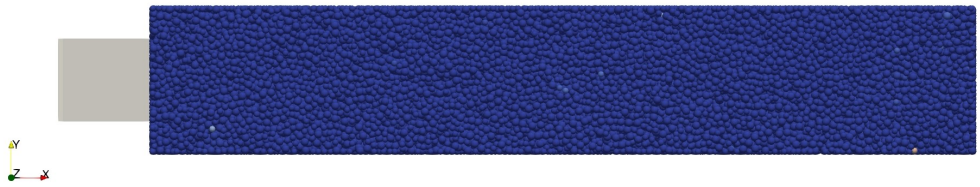

Figure 4.33: The plan view of the set-up for the widths of the DEM sand sample and the blade in the simulation of **3D effect** underwater cutting

Corresponding to the experimental matrix of Miedema's 2D effect tests (Table 4.8), the following test matrix is designed for the 2D effect simulations.

Table 4.9: Test protocol for the underwater sand cutting simulations of 2D effect ($d_{50} = 0.4mm$)

Test No.	Median diameter	Blade width	Blade angle	Blade height	Cutting layer thickness	$\frac{h_b}{h_i}$	Hydrostatic pressure	Cutting speed
	d_{50}	w	α_c	h_b	h_i		p_h	v_c
	[mm]	[mm]	[°]	[mm]	[mm]	[-]	[kPa]	[cm/s]
2.1	0.4	5	30	3	3	1	5.89	2
2.2	0.4	5	30	3	1.5	2	5.89	2
2.3	0.4	5	30	3	1	3	5.89	2
2.4	0.4	5	45	3	3	1	5.89	2
2.5	0.4	5	45	3	1.5	2	5.89	2
2.6	0.4	5	45	3	1	3	5.89	2
2.7	0.4	5	60	3	3	1	5.89	2
2.8	0.4	5	60	3	1.5	2	5.89	2
2.9	0.4	5	60	3	1	3	5.89	2
2.10	0.4	5	30	3	2.5	1.2	5.89	2
2.11	0.4	5	30	3	2	1.5	5.89	2

In Table 4.9, the initial hydrostatic pressure is set to 5.89 kPa to match the 0.6 m water depth. According to (Miedema, 2017), the variation of hydrostatic pressure along the depth of the sand sample can be neglected. Test 2.1 to 2.9 are designed to find out the influences of cutting angle α_c and the blade height over cutting depth ratio h_b/h_i on the cutting forces. Test 2.10 and 2.11 are added as intermediate cutting depths for purely checking the influence from the cutting depth h_i.

For the simulations of 3D effect, more tests are designed to check more parameters. As shown by Table 4.10, from Test 3.1 to 3.17, varying blade angle α_c and the varying blade height over cutting depth ratio h_b/h_i are implemented to check their influences on the cutting forces under 3D effect conditions. Apart from that, Test 3.1, 3.2 and 3.3

are designed to check the impact of hydrostatic pressure on the cutting process (0.6 m, 6 m and 60 m water depths), Test 3.12 to 3.17 are to validate if the wedge theory works in underwater 3D effect cutting simulations when the cutting angle is larger than 60°.

The median particle diameter in Test series 2 (Table 4.9) and Test series 3 (Table 4.10) is set to be the same as used in the **small-scale** simulations of dry sand cutting (Chapter 4.4), which is 0.4 mm. But it is also of interests to check if different particle size would show significant influence on the underwater cutting process. Thus Test series 4 is designed with $d_{50} = 1.2mm$, which is three times as large as in Test series 2 and 3.

As shown by the second half of Table 4.10, Test 4.1 to 4.10 are designed with big particles ($d_{50} = 1.2mm$) while the blade height is kept the same as in Test series 2 and 3 ($h_b = 3mm$), Test 4.11 to 4.18 are designed with big particles while the blade height is also increased to three times as the original blade height ($h_b = 9mm$). Although the cutting angle and hydrostatic pressure are fixed in this series of simulations, the influence of varying cutting speeds are specifically investigated with varying h_b/h_i ratio. In total six different cutting speeds are tried, 2 cm/s, 6 cm/s, 18 cm/s, 54 cm/s, 108 cm/s and 162 cm/s.

As illustrated by Fig. 4.32 and 4.33, the sizes of DEM sand samples used in 2D effect and 3D effect are different. Here below Table 4.11 shows the size of samples and number of particles used in each Test series. The particle size distribution (PSD) applied in these simulations are discrete distributions composed with three different diameters. The maximum diameter to minimum diameter ratio ($\frac{d_{max}}{d_{min}}$) is fixed to be 1.66. An illustration of the sand sample with a blade at its initial position is shown by Fig. reffig:l-w-h, in which the colors represent different particle diameters.

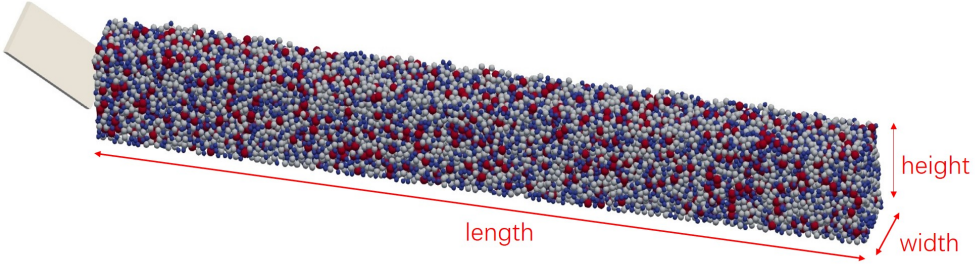

Figure 4.34: The length, width and height of the sand sample (The colors represent different particle sizes)

Table 4.10: Test protocol for the simulations of 3D effect. Test series 3 is with $d_{50} = 0.4mm$ and Test series 4 is with $d_{50} = 1.2mm$

Test No.	Median diameter	Blade width	Blade angle	Blade height	Cutting layer thickness	$\frac{h_b}{h_i}$	Hydrostatic pressure	Cutting speed
	d_{50}	w	α_c	h_b	h_i		p_h	v_c
	[mm]	[mm]	[°]	[mm]	[mm]	[-]	[kPa]	[cm/s]
3.1	0.4	5	30	3	3	1	5.89	2
3.2	0.4	5	30	3	3	1	58.86	2
3.3	0.4	5	30	3	3	1	588.60	2
3.4	0.4	5	30	3	1.5	2	5.89	2
3.5	0.4	5	30	3	1	3	5.89	2
3.6	0.4	5	45	3	3	1	5.89	2
3.7	0.4	5	45	3	1.5	2	5.89	2
3.8	0.4	5	45	3	1	3	5.89	2
3.9	0.4	5	60	3	3	1	5.89	2
3.10	0.4	5	60	3	1.5	2	5.89	2
3.11	0.4	5	60	3	1	3	5.89	2
3.12	0.4	5	75	3	3	1	5.89	2
3.13	0.4	5	75	3	1.5	2	5.89	2
3.14	0.4	5	75	3	1	3	5.89	2
3.15	0.4	5	90	3	3	1	5.89	2
3.16	0.4	5	90	3	1.5	2	5.89	2
3.17	0.4	5	90	3	1	3	5.89	2
4.1	1.2	15	30	3	3	1	5.89	2
4.2	1.2	15	30	3	1.5	2	5.89	2
4.3	1.2	15	30	3	1	3	5.89	2
4.4	1.2	15	30	3	3	1	5.89	6
4.5	1.2	15	30	3	1.5	2	5.89	6
4.6	1.2	15	30	3	1	3	5.89	6
4.7	1.2	15	30	3	3	1	5.89	18
4.8	1.2	15	30	3	3	1	5.89	54
4.9	1.2	15	30	3	3	1	5.89	108
4.10	1.2	15	30	3	3	1	5.89	162
4.11	1.2	15	30	9	9	1	5.89	2
4.12	1.2	15	30	9	4.5	2	5.89	2
4.13	1.2	15	30	9	3	3	5.89	2
4.14	1.2	15	30	9	9	1	5.89	6
4.15	1.2	15	30	9	9	1	5.89	18
4.16	1.2	15	30	9	9	1	5.89	54
4.17	1.2	15	30	9	9	1	5.89	108
4.18	1.2	15	30	9	9	1	5.89	162

Table 4.11: Particle size distribution and sand sample size in the simulations of 2D and 3D effect

Test group	Number of particles	Diameter [mm]	Weight percentage	$\frac{d_{max}}{d_{min}}$	Sand sample length [mm]	Sand sample width [mm]	Sand sample height [mm]
2D effect Series 2	19234	0.30	25%	1.66	50	4	5.3
		0.40	50%				
		0.52	25%				
3D effect Series 3	25735	0.30	25%	1.66	50	9	5.3
		0.40	50%				
		0.52	25%				
3D effect Series 4	24274	1.00	25%	1.66	150	27	16.7
		1.20	50%				
		1.66	25%				

4.7.2. Input parameters for the solid phase and fluid phase

For sand particles, (Miedema, 2017) did not make detailed description on the material properties for his underwater sand cutting experiments. However, he conducted the validation work by comparing the experimental results and the analytical solutions based on an angle of internal friction of 38° and a sand-steel angle of friction of 30°. Therefore these two angles are transferred to the coefficient of internal friction (sand-sand) and coefficient of external friction (sand-blade), and then applied into LIGGGHTS for DEM sand particles. They are 0.78 and 0.57 respectively.

As has been discussed in Chapter 4.3, the coefficient of rolling friction for the spherical particles in the underwater sand cutting simulations is set to be 0.7. All the other input parameters for DEM sand particles are the same as the material properties and contact parameters used in the sand cutting simulations in dry conditions, as listed in Table 4.2.

The fluid phase in simulated by OpenFoam. The mesh used in OpenFOAM for this research is three dimensional Cartesian mesh. As shown by Fig. 4.35, all the fluid cells are identical cubes, while the side length of the cube is around two times of the median diameter of the DEM sand particle.

Boundary conditions are very important in the OpenFOAM simulations. It is defined in the initial files. In OpenFoam, a boundary can be set as patch type or wall type. The patch type is a generic type without geometric or topological information about the mesh, such as an inlet or an outlet. The wall type is for a patch coinciding with a solid wall, like wall functions in turbulence modelling. In this research, the bottom boundary is set to be wall, while patch is applied to the other five boundaries as Fig. 4.35 shows. The boundary conditions chosen for the variables at the wall and the patches are exhibited in Table 4.12, where p is the kinematic pressure, U_f is the fluid velocity, U_s is the solid velocity, ρ_f is the fluid density, K_{sf} is the momentum exchange term, ϵ_f is the void fraction of fluid.

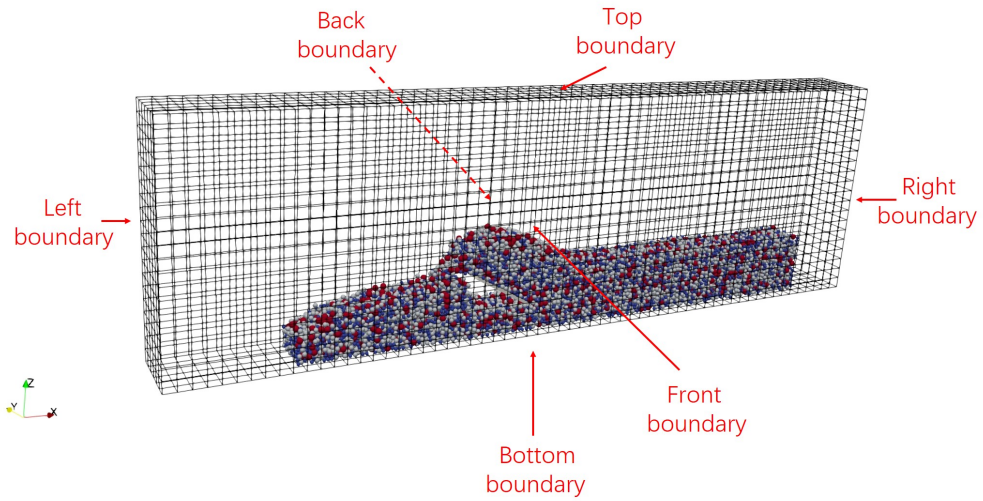

Figure 4.35: The boundaries of the mesh defined in OpenFOAM for underwater sand cutting simulations

Table 4.12: Fluid phase: mesh and boundaries set up in OpenFOAM

Boundary	Boundary condition			
	p	U_f	U_s , ρ_f , K_{sf}	ϵ_f
top	fixedValue	inletOutlet	zeroGradient	fixedValue
left	zeroGradient	inletOutlet	zeroGradient	zeroGradient
right	zeroGradient	inletOutlet	zeroGradient	zeroGradient
front	zeroGradient	inletOutlet	zeroGradient	zeroGradient
back	zeroGradient	inletOutlet	zeroGradient	zeroGradient
bottom	zeroGradient	noSlip	zeroGradient	zeroGradient

The viscosity of the fluid is set as $\nu_f = 1.787 \times 10^{-6}\ m^2/s$ and the gravitational acceleration is set as $g = -9.81\ m/s^2$. The initial conditions of the fluid are listed in Table 4.13.

Table 4.13: Initial properties used in OpenFOAM

Test No.	p_h [kPa]	ρ_f [kg/m^3]	U_f [m/s]	U_s [m/s]	K_{sf} [kg/(m^3·s)]	ϵ_f [-]
2.1-2.11	5.89	1000	(0 0 0)	(0 0 0)	0	1
3.1 & 3.4-3.17 & 4.1-4.18	5.89	1000	(0 0 0)	(0 0 0)	0	1
3.2	58.86	1000	(0 0 0)	(0 0 0)	0	1
3.3	588.60	1000	(0 0 0)	(0 0 0)	0	1

4.7.3. Coupling intervals in CFDEM for underwater cutting simulations

CFDEM coupling is sensitive to the coupling interval which is the ratio between FVM time step and DEM time step. In the simulations of this research, time step for DEM is smaller than for FVM. The following three criteria are considered when setting the time steps for DEM and FVM.

1) CFL condition (Courant–Friedrichs–Lewy) plays an important role in the stability of the numerical calculation in CFD. To fulfill the requirement of CFL condition, the CFL number should be lower than 1, which means the distance that the fluid travels within the mesh during one time step should be lower than the length of the mesh element (Courant et al., 1967). OpenFOAM conducts automatic check for this criterion.

2) The time step in DEM to detect the collision between neighbour particles should be lower than the time for the Rayleigh wave to transverse the smallest particle in the set (Ning and Ghadiri, 2006). Rayleigh wave is a surface acoustic wave travelling through the surface of solid (Telford et al., 1990). So the time step in DEM should be smaller than the Rayleigh time step as calculated by Eq. (4.5), where R_{min}, ρ_s, G_p and ν_p are the minimum radius, soild density, shear modulus and Poisson's ratio of the particles respectively.

$$\Delta t_r = \pi \cdot R_{min} \cdot \frac{\sqrt{\frac{\rho_s}{G_p}}}{0.1631\nu_p + 0.8766} \tag{4.5}$$

3) In the coupled scheme between DEM and FVM, the particle relaxation time is important to the stability of the simulation. Particle relaxation time (τ_p) defines the time for a particle to adjust its velocity to adapt for a new environment of forces.

Table 4.14: FVM(CFD) and DEM time steps and coupling intervals for the underwater sand cutting simulations

Test No.	d_{50} [mm]	v_c [cm/s]	FVM(CFD) time step [s]	DEM time step [s]	Coupling interval
2.1-2.11 & 3.1-3.17	0.4	2	2×10^{-5}	2×10^{-6}	10
3.1.1	0.4	2	1×10^{-5}	2×10^{-6}	5
4.1-4.3 & 4.11-4.13	1.2	2	2×10^{-5}	2×10^{-6}	10
4.4-4.6 & 4.14	1.2	6	2×10^{-5}	2×10^{-6}	10
4.7 & 4.15	1.2	18	1×10^{-5}	2×10^{-6}	5
4.8 & 4.16	1.2	54	1×10^{-5}	2×10^{-6}	5
4.9 & 4.17	1.2	108	2×10^{-6}	2×10^{-6}	1
4.10 & 4.18	1.2	162	2×10^{-6}	2×10^{-6}	1

Accordign to Hager (2014), the DEM time step has to be smaller than τ_p to reach the stability and the accuracy of the numerical simulation, and it is calculated as Eq. (4.6), where d_p is the diameter of the particle and μ_f is the dynamic viscosity of the fluid.

$$\tau_p = \frac{\rho_s \cdot {d_p}^2}{18 \cdot \mu_f} \tag{4.6}$$

In the underwater sand cutting simulations, to satisfy the constraints mentioned above, the DEM time step is set to 2×10^{-6} s. On the premises of not damaging the stability of the calculation or the accuracy of results, it is always wanted to set the time steps as large as possible to reduce the overall computational time. Thus several different FVM time steps have been tried out. Initially the FVM(CFD) time step was set as 2×10^{-4} s for the simulations using small particles ($d_{50} = 0.4\ mm$) and small cutting speed ($v_c = 2\ cm/s$), i.e., Test series 2 and 3. The results show that this coupling interval of 100 (FVM time step / DEM time step) is too large for the DEM sand particles to accept the updated fluid-solid interaction forces after each coupling step. The load on some of the particles is too high so that those particles are shot out.

Therefore, the FVM time steps of these simulations are gradually reduced to 2×10^{-5} s to realize the convergence. Thus a coupling interval of 10 is considered to be acceptable. Table 4.14 shows the FVM and DEM time steps and the corresponding CFDEM coupling intervals for all the simulations. Test 3.1.1 is specially designed to check if a reduced coupling interval from 10 to 5 will generate a difference on the cutting forces and fluid flow field in the simulation. All the input parameters of Test 3.1.1 are identical with Test 3.1 except for the FVM time step and the coupling interval. With relatively higher cutting velocities, 18 cm/s and 54 cm/s, the coupling interval is reduced to 5. When cutting with very high cutting speeds, 108 cm/s and 162 cm/s, the coupling interval is set to be 1 to make sure the information from the DEM side is sufficiently updated to the FVM side.

4.8. Calibration - permeability of DEM sand samples

As introduced in Chapter 3.5.4, the permeability κ of the sand sample can be calculated by Eq. (3.68). Chapter 4.6.1 has introduced the experimental results of Miedema on the relation between the porosity n and hydraulic conductivity K_{sand} of sand samples. The relation between K_{sand} and κ has been derived by Liu et al. (2019) analytically, as described by Eq. (4.7).

$$\kappa = \frac{K_{sand} \cdot \mu_f}{\rho_f \cdot g} \tag{4.7}$$

In the calculation of the permeability κ, the sphericity of the particles ϕ_s indicates the level that a particle shape is close to sphere. When ϕ_s is set to be 1, the particles are completely spheres, vice versa. Sand grains are not perfectly spheres in reality, then ϕ_s is chosen as the tuning factor for the correct permeability.

By substituting the median diameters of the DEM sand particles and the porosities measured by Miedema into Eq. (3.68), the permeabilities of the DEM sand samples are calculated. By applying Eq. (4.7), the hydraulic conductivity of the DEM sand samples can also be calculated. The results are shown in Table 4.15. Fig. 4.36 plots the hydraulic conductivities from both DEM simulations (K_{num}) and Miedema's experiments (K_{exp}) together versus the porosity.

Table 4.15: The comparison of the hydraulic conductivity from the simulation and the experiment

Porosity	DEM Simulation		Experiment
	Permeability κ [m^2]	Hydraulic conductivity K_{num} [m/s]	Hydraulic conductivity K_{exp} [m/s]
0.369	1.89×10^{-11}	1.04×10^{-4}	7.7×10^{-5}
0.385	2.27×10^{-11}	1.24×10^{-4}	1.65×10^{-4}
0.389	4.19×10^{-11}	2.3×10^{-4}	2.06×10^{-4}
0.399	4.68×10^{-11}	2.56×10^{-4}	2.4×10^{-4}
0.409	5.20×10^{-11}	2.85×10^{-4}	2.97×10^{-4}
0.418	5.75×10^{-11}	3.15×10^{-4}	3.07×10^{-4}
0.431	6.58×10^{-11}	3.61×10^{-4}	3.22×10^{-4}

Fig. 4.36 shows that the numerical hydraulic conductivity matches well with the experimental results. That means with the same porosity, the sand sample in the simulation holds similar permeability as a sand sample in nature to allow the fluid to flow through. The sphericity of the particles corresponding to different particle sizes are shown in Table 4.16.

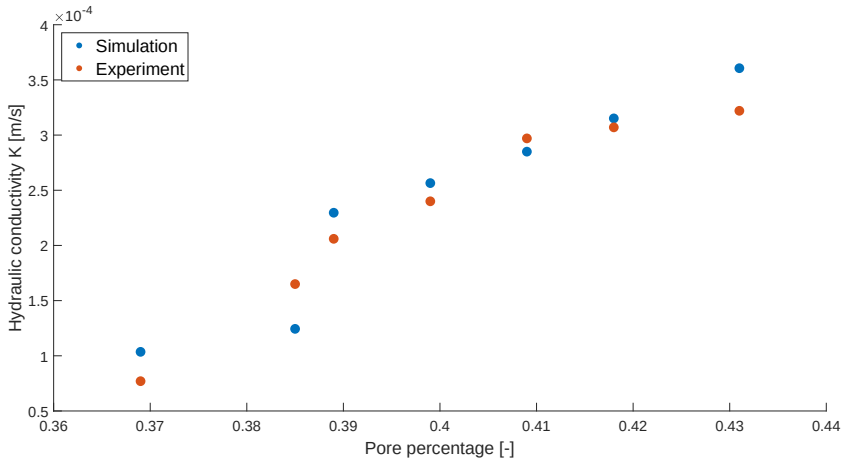

Figure 4.36: Validation of the hydraulic conductivities from the DEM simulations and Miedema's experiments

Table 4.16: The value of the sphericity of the particles versus the particle size

Median diameter d_{50} [mm]	ϕ_s [-]
0.4	0.411
1.2	0.137

4.9. Results & validations of simulations of sand cutting in underwater condition

In this section, the results from the DEM-FVM coupling simulations of underwater sand cutting process of both the 2D and 3D effects are discussed and validated against experimental results.

The simulation results from Test 4.1 to 4.10 are unstable and thus cannot be trusted. The reason is that the ratio between the blade height to the particle diameter in those simulations is too small, resulting in insufficient layers of particles on the blade surface. The blade height used in Test 4.1 to 4.10 is 3 mm, and the median particle diameter is 1.2 mm, so by average there are about 2.5 layers of particles in touch with the blade, not thick enough to perform the shear failure mechanism in sand cutting. Thus results of Test 4.1 to 4.10 will not be discussed in the following sections.

4.9.1. Validation of the shear angle from the 2D effect simulations

With the blade proceeding in the sand sample, a shear plane will appear due to the shearing between the particles in the sand pile. Therefore, an apparent

shear angle can be observed based on the velocity difference in the particles. Based on the observations from experiments, Miedema (2017) derived a semi-empirical and semi-analytical equation to calculate the shear angle for the underwater sand cutting process of 2D effect (Eq. (4.8)), which can be used to validate the simulation results.

$$\beta = 75^\circ - \frac{\alpha_c}{3} - \frac{\phi}{2} - \frac{\delta}{4} \tag{4.8}$$

This empirical equation is only valid when α_c is in the range of 15° to 60°, ϕ is between 30° and 45° and δ is close to two thirds of ϕ. The 2D effect simulations Test 2.1 to 2.11 fit in this scope. The shear angles from the simulations of 2D effect (Test 2.1-2.9) and the empirical solutions are displayed in Table 4.17.

Table 4.17: A comparison on the shear angle in underwater cutting between the numerical and empirical results

Blade angle α_c [°]	h_b/h_i [-]	Numerical shear angle β_{num} [°]	Empirical shear angle β_{emp}[°]
30	1	33.66	38.5
30	2	34.05	38.5
30	3	34.74	38.5
45	1	32.04	33.5
45	2	32.20	33.5
45	3	32.60	33.5
60	1	26.14	28.5
60	2	26.47	28.5
60	3	27.30	28.5

Table 4.17 shows the shear angles from DEM-FVM coupling simulations in all the cases are slightly smaller than the empirical solutions from Miedema, but the differences are still within acceptable error margin. Therefore it is considered that the 2D effect simulations have successfully performed the shear zone and shear angle in underwater sand cutting process.

Both in simulations and analytical calculations, the shear angle decreases when the blade angle α_c increases with constant internal friction angle ϕ and the external friction angle δ. The shear angles from the Test 2.1 to 2.9 are displayed in Fig. 4.37 to 4.45. The color of the particles indicating their velocities, ranging from blue for low velocity to red for high velocity. From the figures it is clear that shear angle β is negatively correlated to the blade angle α_c.

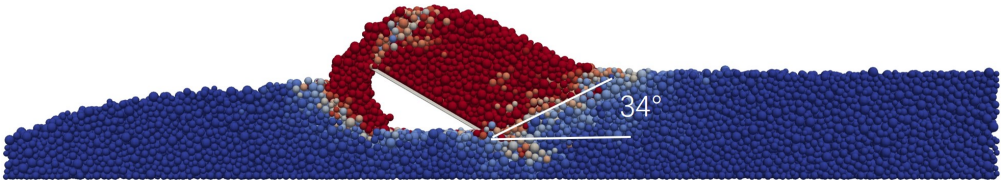

Figure 4.37: Shear angle with a blade angle α_c of 30°, h_b/h_i of 1 (Test 2.1)

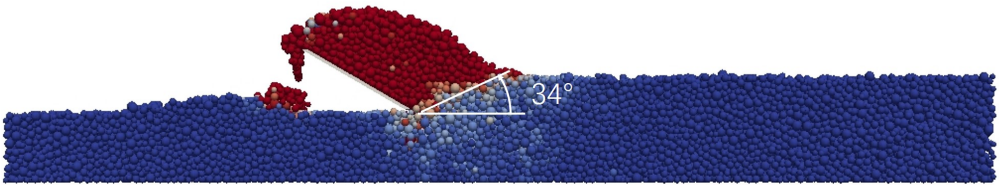

Figure 4.38: Shear angle with a blade angle α_c of 30°, h_b/h_i of 2 (Test 2.2)

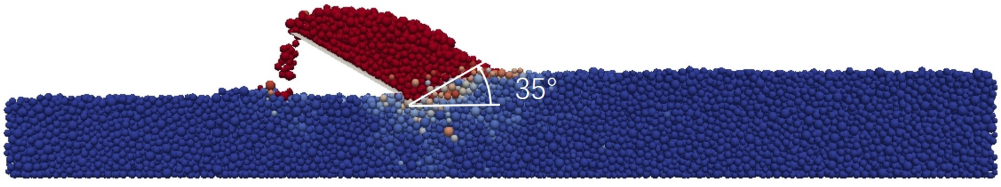

Figure 4.39: Shear angle with a blade angle α_c of 30°, h_b/h_i of 3 (Test 2.3)

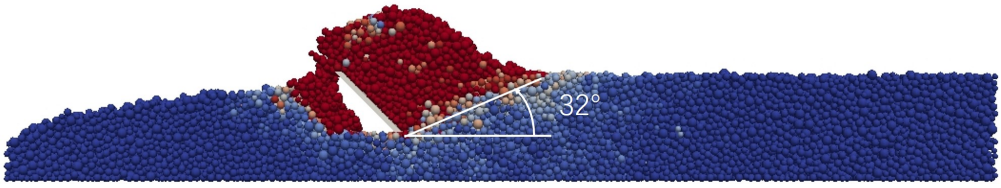

Figure 4.40: Shear angle with a blade angle α_c of 45°, h_b/h_i of 1 (Test 2.4)

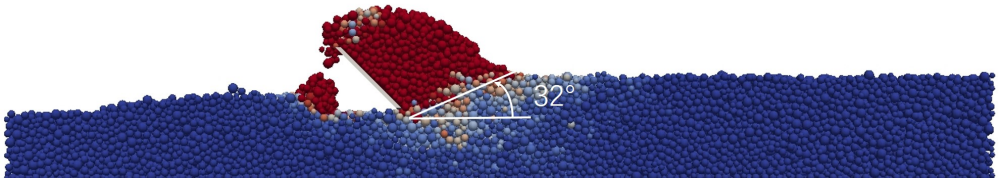

Figure 4.41: Shear angle with a blade angle α_c of 45°, h_b/h_i of 2 (Test 2.5)

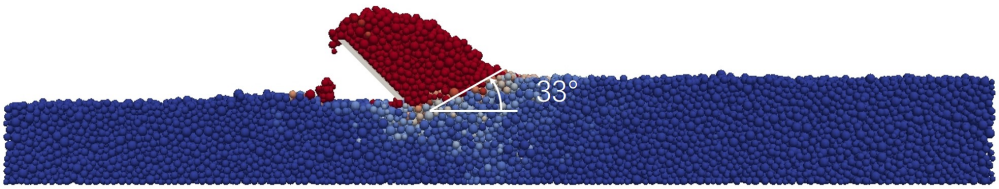

Figure 4.42: Shear angle with a blade angle α_c of 45°, h_b/h_i of 3 (Test 2.6)

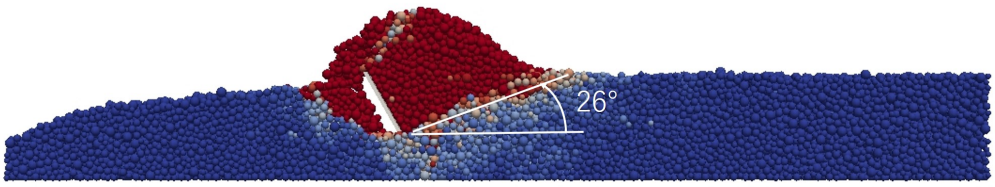

Figure 4.43: Shear angle with a blade angle α_c of 60°, h_b/h_i of 1 (Test 2.7)

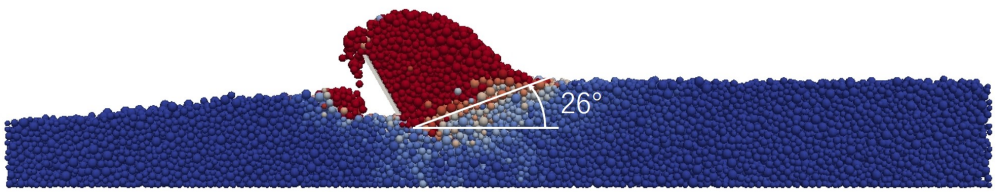

Figure 4.44: Shear angle with a blade angle α_c of 60°, h_b/h_i of 2 (Test 2.8)

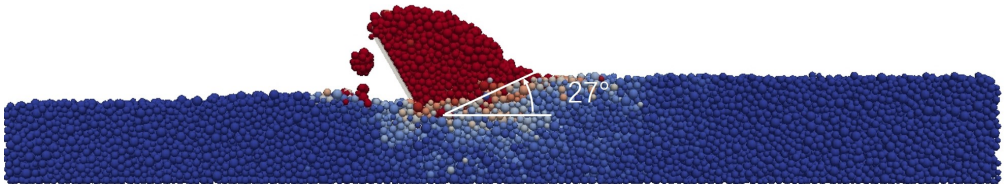

Figure 4.45: Shear angle with a blade angle α_c of 60°, h_b/h_i of 3 (Test 2.9)

4.9.2. Analysis of the cutting forces from the 2D effect simulations

The influence of the blade angle and cut layer thickness

For the underwater sand cutting simulations of 2D effect, the influence of the blade angle and the cutting layer thickness on the cutting force are evaluated by the overall stresses on the blade. Fig. 4.46 and 4.47 show the developments of the overall stress on the blade during the 2D effect underwater sand cutting simulations with different layer thickness h_i and blade angle α_c. In all the simulations, the overall stresses first increase when the blade is cutting into the sand pile, and then stay at a stable value when the cutting enters the steady state. The stresses in the steady state from all the simulations of 2D effect are calculated, including those in the horizontal direction, the transverse direction, the vertical direction and the overall ones. All the values are shown in Table 4.18.

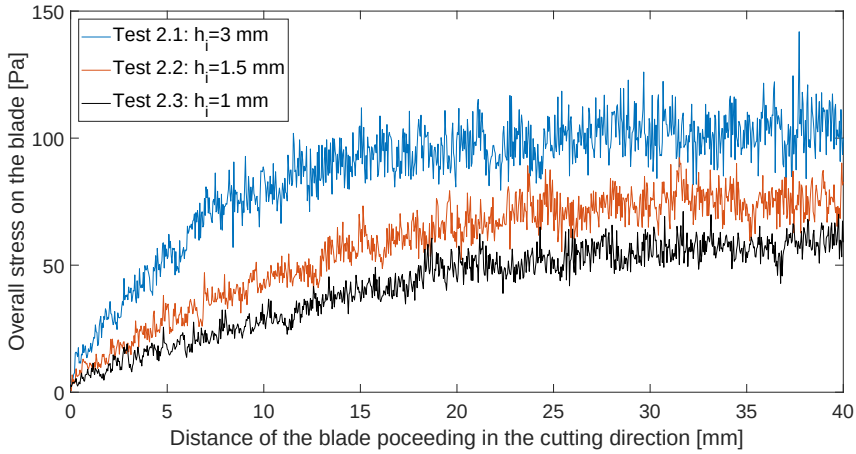

Figure 4.46: Development of the overall stress on the blade during the 2D effect underwater sand cutting simulations with different layer thickness h_i (Test 2.1, 2.2, 2.3: α_c=30°, p_h=5.89 kPa, v_c=2 cm/s)

Fig. 4.48(a) to 4.48(c) show that the correlations between the overall stress $S_{overall}$

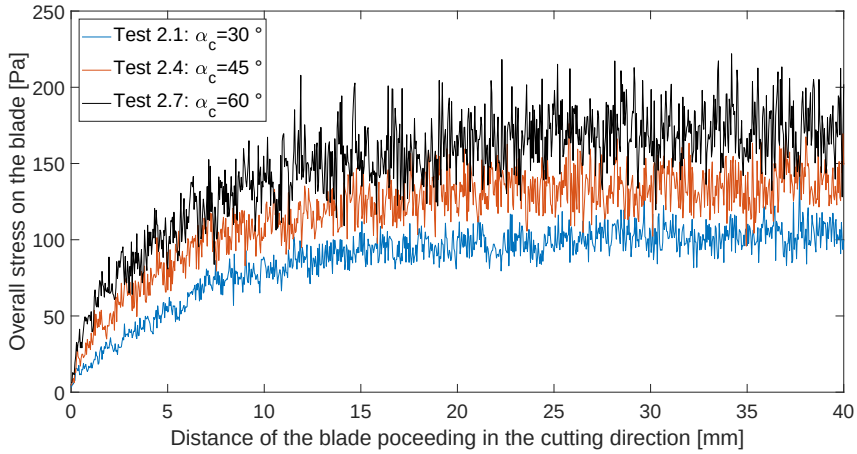

Figure 4.47: Development of the overall stress on the blade during the 2D effect underwater sand cutting simulations with different blade angle α_c (Test 2.1, 2.4, 2.7: h_i=3 mm, p_h=5.89 kPa, v_c=2 cm/s)

Table 4.18: Cutting stress in the steady state from the simulations of 2D effect

Test No.	Blade angle α_c [°]	h_b/h_i [-]	Horizontal stress S_h [Pa]	Transverse stress S_t [Pa]	Vertical stress S_v [Pa]	Overall stress [Pa] $S_{overall}$ [Pa]
2.1	30	1	80.51	0.27	60.83	101.27
2.2	30	2	57.99	0.68	44.22	73.25
2.3	30	3	43.51	0.34	33.38	55.10
2.4	45	1	122.54	0.86	55.28	134.93
2.5	45	2	85.34	0.32	38.38	93.98
2.6	45	3	63.96	0.78	27.10	69.82
2.7	60	1	164.63	-0.73	40.59	170.17
2.8	60	2	116.77	-0.91	26.65	120.31
2.9	60	3	86.00	-0.58	17.33	88.16
2.10	30	1.2	77.43	0.72	59.17	97.84
2.11	30	1.5	65.34	0.68	50.91	83.22

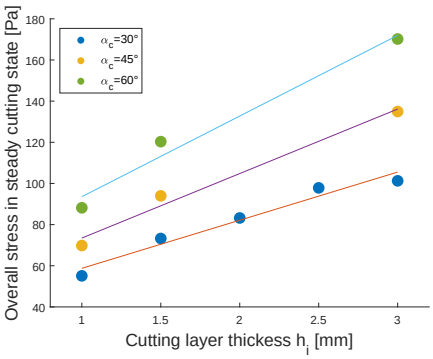

(a) Overall stress vs. h_i

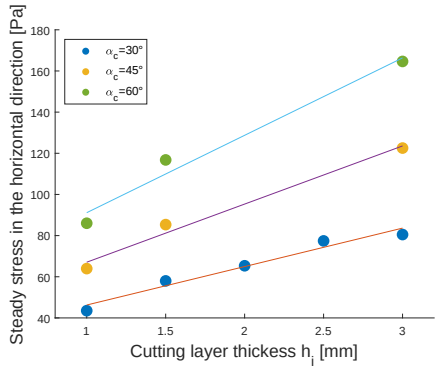

(b) Horizontal stress vs. h_i

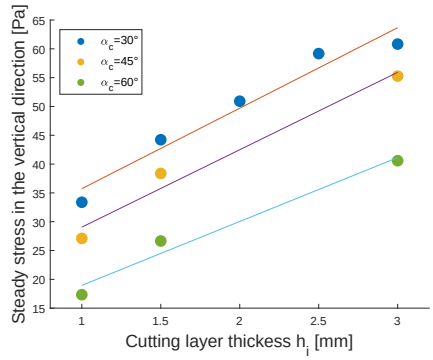

(c) Vertical stress vs. h_i

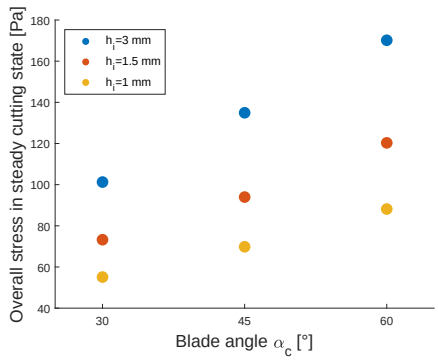

(d) Overall stress vs. α_c

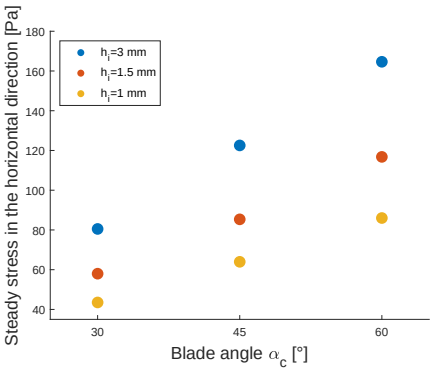

(e) Horizontal stress vs. α_c

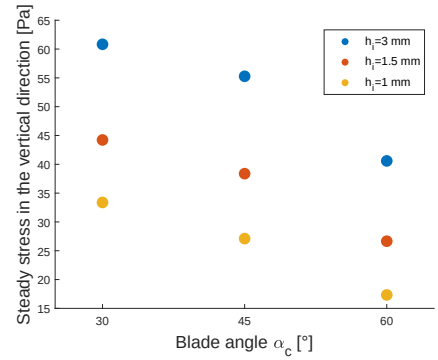

(f) Vertical stress vs. α_c

Figure 4.48: Steady stresses with different thicknesses of layer cut and blade angles from simulations of 2D effect (Test 2.1-2.11)

and the cutting layer thickness h_i is approaching a linear relation. The same pattern can also be found on the horizontal stress S_h and vertical stress S_v to the cutting layer thickness. Fig. 4.48(d) to 4.48(f) show that the overall stress $S_{overall}$ increases with the blade angle α_c. The horizontal steady stress S_h increases with blade angle α_c, while the vertical steady stress S_v shows an obvious decreasing tendency. But it can be found the values of the steady stresses in the vertical direction S_v are not as influential as those in the horizontal direction. Then the small contribution of the vertical stresses and the big contribution of the horizontal stresses lead to the positive correlation between the overall stress $S_{overall}$ and the blade angle α_c.

Validation of the cutting forces

From the experiments of Miedema (2017), only the cutting forces of the 2D effect tests are recorded and published, thus the validation for underwater sand cutting simulation is conducted with the simulation results of Test 2.1-2.9. Miedema has recorded all the results of cutting forces in the form of the dimensionless cutting force c_t, as calculated by Eq. (4.9). In Eq. (4.9), F_t is the overall cutting force, K_m is the weighted average hydraulic conductivity K of the sand package during the cutting process, ε is the average volume strain in the sand.

$$c_t = \frac{F_{ct} \cdot K_m}{\rho_f \cdot g \cdot v_c \cdot {h_i}^2 \cdot \varepsilon \cdot w} \tag{4.9}$$

K_m can be calculated by a weighted average function (Eq. (4.10) and (4.11)) of initial hydraulic conductivity of the sand package before cutting K_i and the maximum hydraulic conductivity of sand package appears in the dilatancy process K_{max}, while K_i and K_{max} are linked to permeability by Eq. (4.12) and (4.13), in which κ_i and κ_{max} refer to the initial and maximum intrinsic permeabilities respectively. The average volume strain ε in the sand can be calculated with the initial porosity (n_i) and the maximum porosity (n_{max}), as shown by Eq. (4.14).

$$K_m = a_1 \cdot K_i + a_2 \cdot K_{max} \tag{4.10}$$

$$a_1 + a_2 = 1 \tag{4.11}$$

$$K_i = \frac{\kappa_i \cdot \rho_f \cdot g}{\mu_f} \tag{4.12}$$

$$K_{max} = \frac{\kappa_{max} \cdot \rho_f \cdot g}{\mu_f} \tag{4.13}$$

$$\varepsilon = \frac{n_{max} - n_i}{1 - n_{max}} \tag{4.14}$$

c_t can also be determined analytically, Miedema (2017) derived the whole analytical solution and made comparison between the experimental and analytical results. He found that, in the experiments, the gravitational force of the layer cut on the blade was

included in the original vertical cutting force, while in the analytical solution it was not. To eliminate the effect of gravitational force, the original vertical cutting force is corrected by subtracting the gravitational force. The component of the gravitational force acting on the cutting blade is calculated by Eq. (4.15), and the corrected overall cutting force $F_{ct}{}'$ is calculated by Eq. (4.16), in which F_h and F_v are the horizontal and vertical cutting forces respectively.

$$G_v = (\rho_s - \rho_f) \cdot g \cdot h_i \cdot w \cdot \frac{sin(\alpha_c + \beta)}{sin(\beta)} \cdot \{\frac{h_b + h_i \cdot sin(\alpha_c)}{sin(\alpha_c)} + \frac{h_i \cdot cos(\alpha_c + \beta)}{2 \cdot sin(\beta)}\} \quad (4.15)$$

$$F_{ct}{}' = \sqrt{F_h^2 + (F_v - G_v)^2} \quad (4.16)$$

Once $F_{ct}{}'$ is obtained, the corrected dimensionless cutting force $c_t{}'$ can be calculated via Eq. (4.9), where F_{ct} should substituted by $F_{ct}{}'$. Two groups of dimensionless cutting forces are reported in Miedema's experiments, the non-corrected (original) and corrected ones. Correspondingly, the results from the 2D effect simulations are processed, resulting in two groups of dimensionless cutting forces, the non-corrected c_t and corrected $c_t{}'$. Simulation results from the 2D effect tests are listed in Table 4.19.

Table 4.19: All the results from the simulation of 2D effect for the validating the overall cutting forces

Test No.	α_c [°]	h_i [mm]	ε [-]	κ_i [m^2]	κ_{max} [m^2]	a_1 [-]	K_m [m/s]	Non-corrected c_t [-]	corrected $c_t{}'$[-]
2.1	30	3	0.31	2.16×10^{-11}	1.94×10^{-10}	0.506	5.9×10^{-4}	0.62	0.52
2.2	30	1.5	0.39	2.16×10^{-11}	7.59×10^{-11}	0.510	2.6×10^{-4}	0.62	0.54
2.3	30	1	0.52	2.16×10^{-11}	5.22×10^{-11}	0.514	2×10^{-4}	0.62	0.54
2.4	45	3	0.28	2.16×10^{-11}	1.54×10^{-10}	0.515	4.7×10^{-4}	0.51	0.51
2.5	45	1.5	0.55	2.16×10^{-11}	1.20×10^{-10}	0.540	3.7×10^{-4}	0.58	0.55
2.6	45	3	0.56	2.16×10^{-11}	6.79×10^{-11}	0.540	2.4×10^{-4}	0.60	0.56
2.7	60	3	0.31	2.16×10^{-11}	2.63×10^{-10}	0.505	7.7×10^{-4}	0.86	0.88
2.8	60	1.5	0.36	2.16×10^{-11}	1.11×10^{-10}	0.552	3.4×10^{-4}	0.86	0.86
2.9	60	1	0.50	2.16×10^{-11}	8.24×10^{-11}	0.564	2.6×10^{-4}	0.81	0.81

The non-corrected dimensionless cutting forces from the experiments and simulations, together with the analytical dimensionless cutting force, are plotted in Fig. 4.49. When α_c=30°, the simulated non-corrected dimensionless cutting forces are higher than both the experimental and analytical values. When ($\alpha_c = 45°$, $h_b/h_i = 1$) and ($\alpha_c = 60°$, $h_b/h_i = 1$), the simulated c_t shows significant underestimation comparing with the experimental value.

Fig. 4.50 shows the corrected dimensionless cutting forces $c_t{}'$ from the experiments, simulations and analytical calculations. The results match well with each other. In most scenarios, the simulated $c_t{}'$ slightly overestimate the experimental $c_t{}'$, but the difference is relatively small. The largest error margin appears at ($\alpha_c = 30°$, $h_b/h_i =$

2), the simulated c_t' is 17% higher than the experimental c_t'. It is considered still acceptable.

In conclusion, the underwater sand cutting simulations of 2D effect shows a successful validation against laboratory experiments on the dimensionless cutting forces. High accuracy can be reached by eliminating the gravitational force on the cut layer.

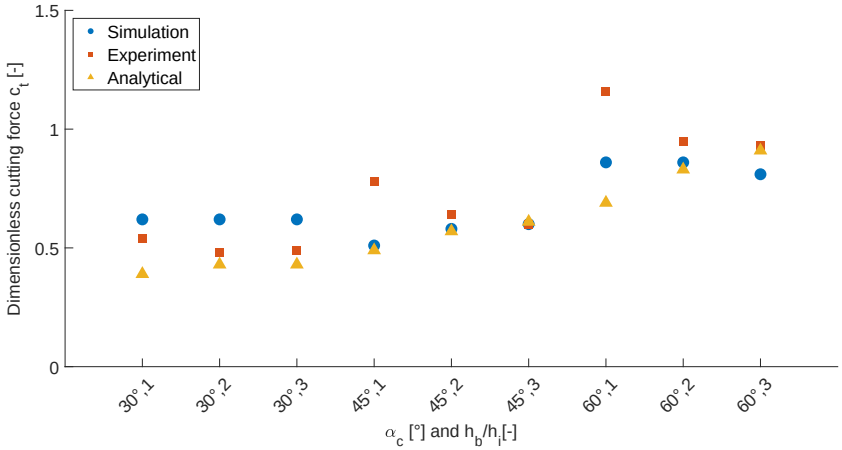

Figure 4.49: The dimensionless cutting forces from the simulation of 2D effect, the experiment and the analytical solutions (non-corrected) (Test 2.1-2.9)

4.9.3. Analysis of the cutting forces from the 3D effect simulations

The influence of the blade angle and cut layer thickness

For the underwater sand cutting simulations of 3D effect, the developments of horizontal, vertical and transverse stresses on the blade during cutting with different cutting depths are depicted by Fig. 4.51, Fig. 4.52 and Fig. 4.53

The horizontal and vertical cutting stresses show the same pattern as in the 2D effect simulations, the stresses increase when the blade starts cutting. They will finally fluctuate around stable values when the cutting enters steady state. For the transverse stress, the signs of the stress indicates its direction, it can be either positive or negative randomly. A positive sign means the stress is towards the right hand side of the blade and vice versa. This is because in the 3D effect cutting, the particles can fall down from both sides arbitrarily in the cutting process.

Cutting stresses recorded from Test 3.1 and 3.4 to 3.11 are listed out in Table 4.20. In Test 3.11, the vertical stress becomes negative, this is because with such a large cutting angle ($\alpha_c = 60°$) and shallow cutting depth ($h_b/h_i = 3$), the vertical force on

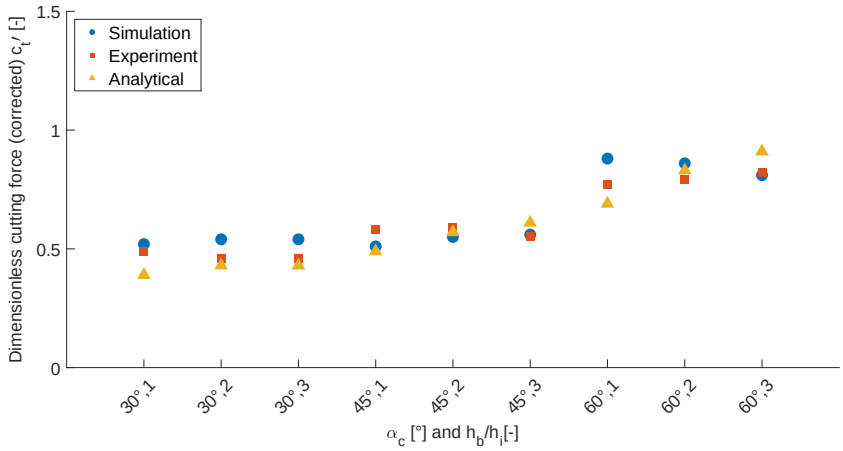

Figure 4.50: The dimensionless cutting forces from the simulation of 2D effect, the experiment and the analytical solutions (corrected for gravity effect) (Test 2.1-2.9)

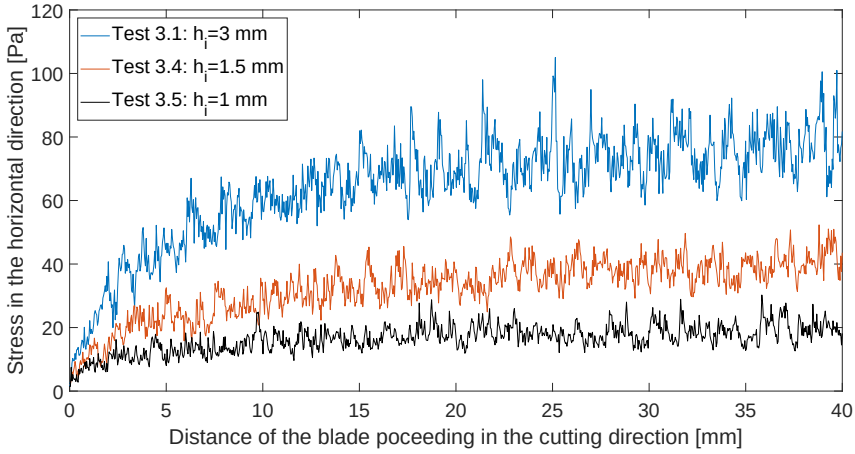

Figure 4.51: Effect of the cutting layer thickness on the cutting stress in the horizontal direction (Test 3.1, 3.4, 3.5: α_c=30°, p_h=5.89 kPa, v_c=2 cm/s)

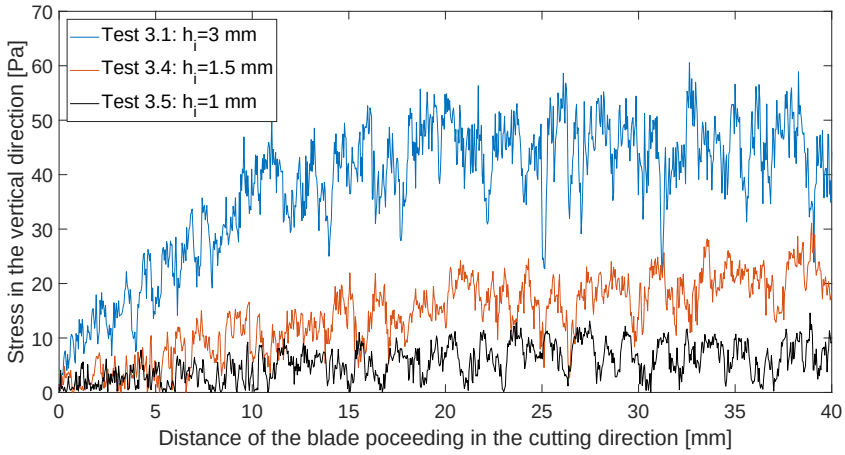

Figure 4.52: Effect of the cutting layer thickness on the cutting stress in the vertical direction (Test 3.1, 3.4, 3.5: α_c=30°, p_h=5.89 kPa, v_c=2 cm/s)

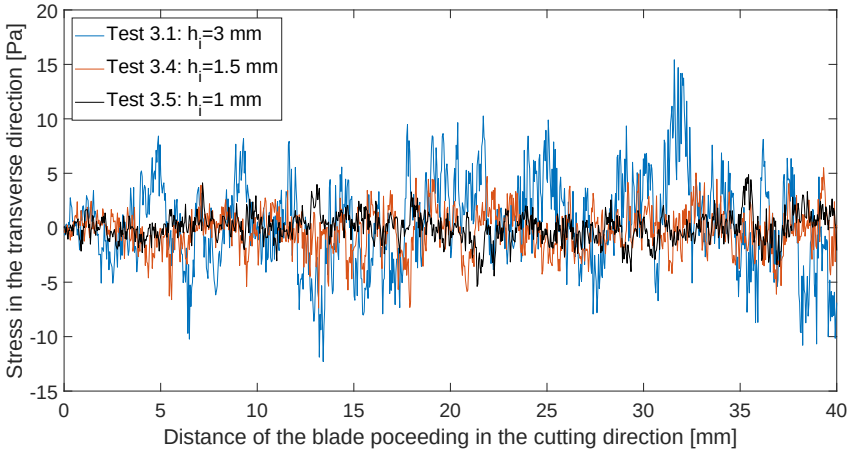

Figure 4.53: Effect of the cutting layer thickness on the cutting stress in the transverse direction (Test 3.1, 3.4, 3.5: α_c=30°, p_h=5.89 kPa, v_c=2 cm/s)

the blade is dominant by the external friction force, thus the resultant vertical force on the blade is almost zero or slightly upwards.

Fig. 4.54 plots the overall, horizontal and vertical cutting stresses versus different cutting depths and cutting angles. From Fig. 4.54(a) to 4.54(c) it is learned that all the three stresses show a more or less linear relation with the cutting depths. This correlation is the same as found in the 2D effect cutting simulations. Fig. 4.54(e) and 4.54(f) show that horizontal stress shows a positive correlation with the cutting angle while the vertical stress shows a negative correlation with the cutting angle. Because in all the scenarios, the horizontal stress is much larger than the vertical stress, thus the overall stress still shows a positive correlation with the cutting angle.

Table 4.20: Cutting stress in the steady state from the simulations of 3D effect with small particles (d_{50} = $0.4mm$)

Test No.	Blade angle α_c [°]	h_b/h_i [-]	Horizontal stress S_h [Pa]	Transverse stress S_t [Pa]	Vertical stress S_v [Pa]	Overall stress [Pa] $S_{overall}$ [Pa]
3.1	30	1	74.54	1.14	44.92	87.52
3.4	30	2	45.93	-0.34	22.62	51.55
3.5	30	3	31.12	-0.28	11.35	33.82
3.6	45	1	110.17	-0.26	37.86	117.04
3.7	45	2	69.75	-0.14	18.85	72.67
3.8	45	3	48.07	-0.43	4.73	49.05
3.9	60	1	142.22	-0.01	20.75	144.30
3.10	60	2	92.50	-1.47	8.08	93.45
3.11	60	3	62.1	-0.12	-0.32	62.89

The influence of the hydrostatic pressure

Results from Test 3.1 to 3.3 are used to evaluate the relation between the cutting force and the hydrostatic pressure. As introduced before, three hydrostatic pressures are applied for these simulations, 5.89 kPa, 58.86 kPa and 588.6 kPa. The overall stress development during the simulations are plotted in Fig. 4.55.

Fig. 4.55 shows that the overall stress on the blade is not influenced by the hydrostatic pressure when the cutting speed is low (v_c=2 cm/s). With a small cutting speed cavitation cannot be triggered, thus the hydrostatic pressure will not induce significant change on the cutting forces. The influence of the hydrostatic pressure on other aspects will be discussed in the later sections.

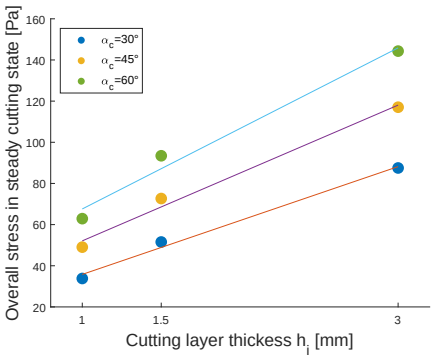

(a) Overall stress vs. h_i

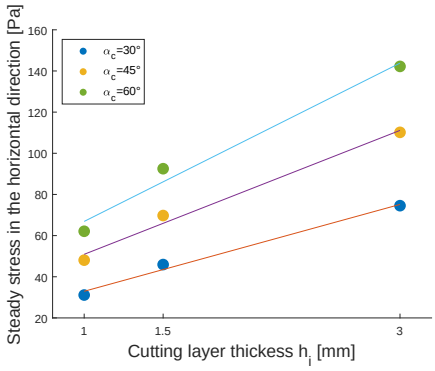

(b) Horizontal stress vs. h_i

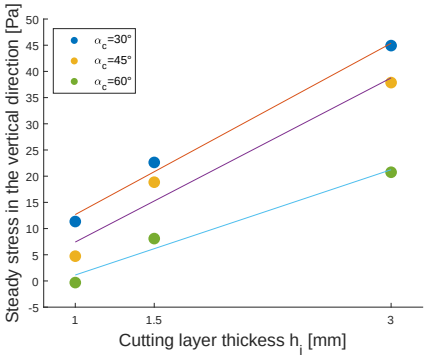

(c) Vertical stress vs. h_i

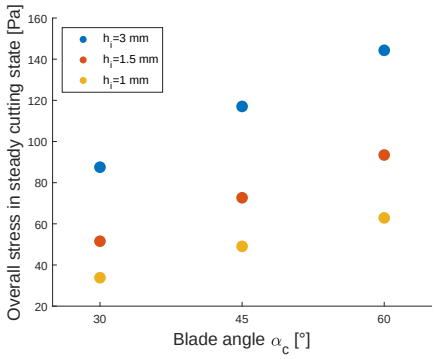

(d) Overall stress vs. α_c

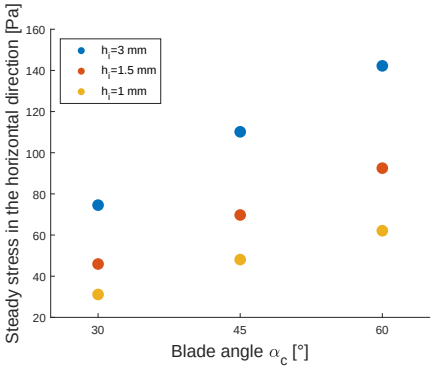

(e) Horizontal stress vs. α_c

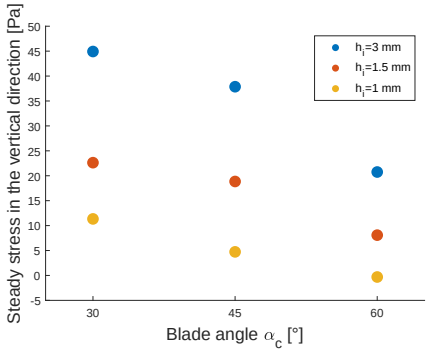

(f) Vertical stress vs. α_c

Figure 4.54: Steady cutting stresses with different thicknesses of layer cut and blade angles from simulations of 3D effect (Test 3.1-3.11)

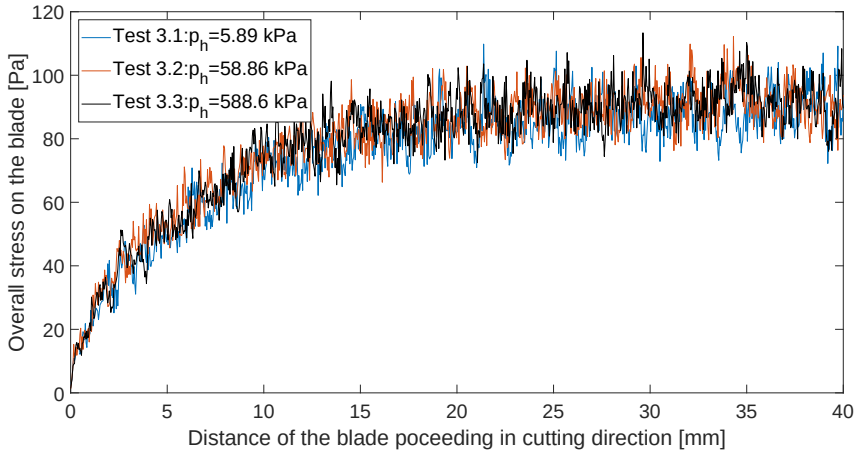

Figure 4.55: Effect of the hydrostatic pressure on the overall stress on the blade (Test 3.1, Test 3.2, Test 3.3: α_c=30°, h_i=3 mm, v_c=2 cm/s)

The influence of the DEM particle size

Results from Test 4.11 to 4.18 (d_{50}=1.2 mm) are compared with Test series 3 (d_{50}=0.4 mm) to analyze the influence of the DEM particle size. As mentioned before, results from Test 4.1-4.10 are abandoned because the blade can only cut roughly two layers of particles even with the largest h_i, making the cutting force unstable and unreliable.

The developments of the overall stresses on the blade in various tests are plotted in Fig. 4.56 to 4.58. As mentioned in Chapter 4.7.1, the sand sample in Test series 4 is 150 mm in length and in Test series 3 is 50 mm long. Therefore for making reasonable comparison, the horizontal axis in Fig. 4.56 to 4.58 is set to represent the fraction of sample length that the blade has cut to.

Fig. 4.59 shows the steady cutting state in Test 3.1 and 4.11, the sand samples are clipped from the middle, only the left half of the sand samples are displayed, in this way the position of the blade is visible. With $h_b/h_i = 1$, particles can climb over the blade, and also fall from the transverse sides of the blade. As shown by Fig. 4.56, the overall stresses in both tests increased at first, and then reached constant values in the steady state.

Fig. 4.57 shows that the overall stress in Test 3.4 has reached steady state, fluctuating around a stable value, on the contrary, the overall stress in Test 4.12 seems constantly increasing. It is thus necessary to check the cutting situations. Fig. 4.60 shows in Test 3.4, the cut layer has reached the top of the blade, and particles can fall from the top to the back of the blade, so the overall stress recorded is the steady state overall stress. In Fig. 4.61, it is found that the cut layer has not reached the top the blade even when the blade has cut a quite long distance into the DEM sand

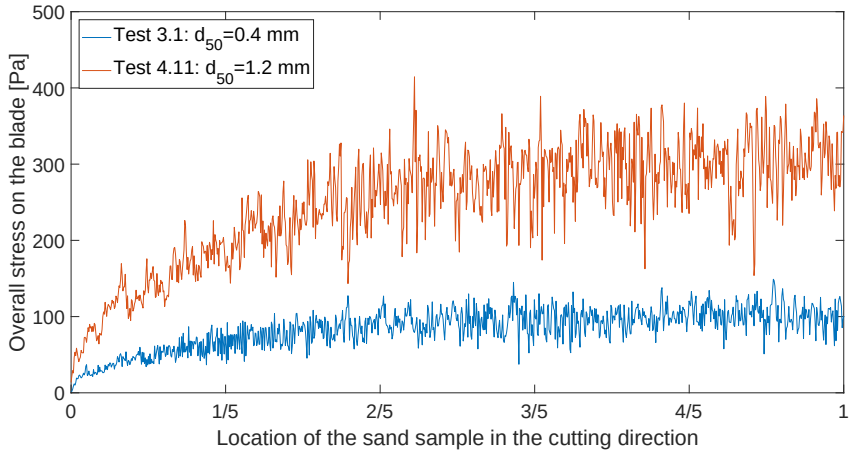

Figure 4.56: The developments of the overall stresses on the blade - effect of the median diameter on the overall stress on the blade (h_b/h_i=1, α_c=30°, p_h=5.89 kPa, v_c=2 cm/s. Blue line - Test 3.1: h_i=3 mm, h_b=3 mm; Red line - Test 4.11: h_i = 9 mm, h_b=9 mm)

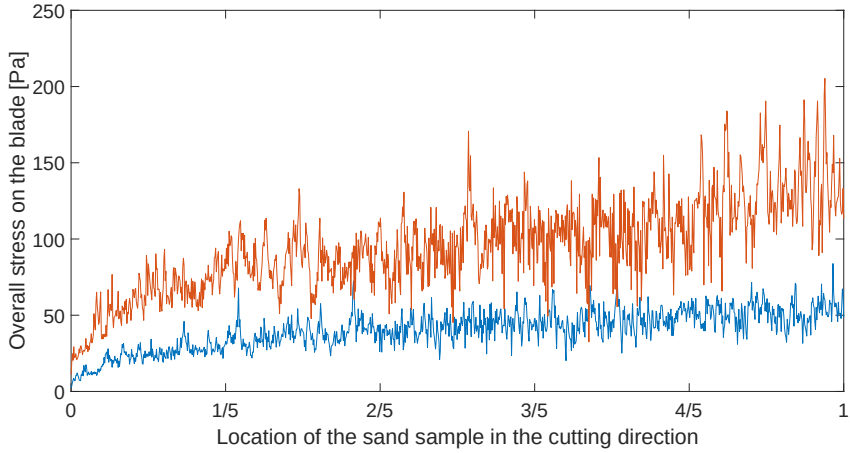

Figure 4.57: The developments of the overall stresses on the blade - effect of the median diameter on the overall stress on the blade (h_b/h_i=2, α_c=30°, p_h=5.89 kPa, v_c=2 cm/s. Blue line - Test 3.4: h_i = 1.5 mm, h_b=3 mm; Red line - Test 4.12: h_i = 4.5 mm, h_b=9 mm)

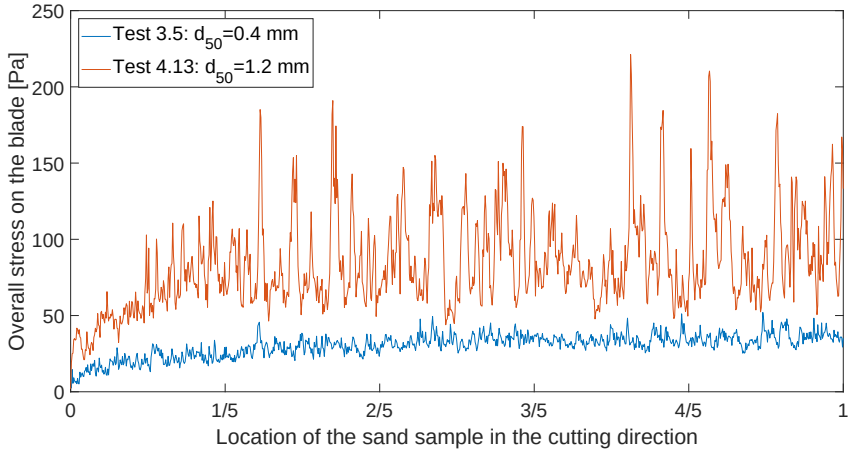

Figure 4.58: The developments of the overall stresses on the blade - effect of the median diameter on the overall stress on the blade (h_b/h_i=3, α_c=30°, p_h=5.89 kPa, v_c=2 cm/s. Blue line - Test 3.5: h_i = 1 mm, h_b=3 mm; Red line - Test 4.13: h_i = 3 mm, h_b=9 mm)

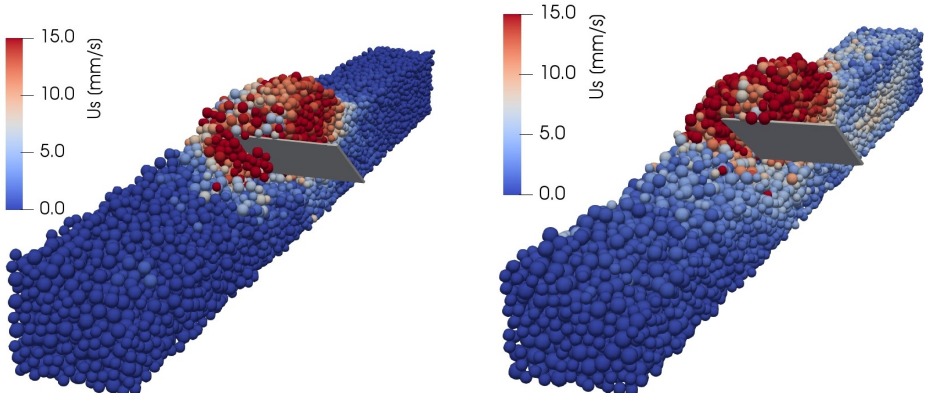

Figure 4.59: a):The steady state of the cutting process in Test 3.1 (clip section, particle size: d_{50}=0.4 mm, sand sample size: 50 mm×9 mm×5.3 mm, blade size: h_b=3 mm, w=5 mm, cutting depth: h_i=3 mm); b):The steady state of the cutting process in Test 4.11 (clip section, particle size: d_{50}=1.2 mm, sand sample size: 150 mm×27 mm×16.7 mm, blade size: h_b=9 mm, w=15 mm, cutting depth: h_i=9 mm)

sample, that is why the overall stress recorded has kept increasing, as shown in Fig. 4.57. However, in Test 4.12, it is observed that when the blade almost reached the end of the DEM sand sample, the cut layer has reached the top of the blade, and particles could fall from the top to the back of the blade. Thus in the stress record of Test 4.12 (Fig. 4.57), only the last 1/20 piece is considered as steady state. The h_b/h_i ratio for Test 3.4 and 4.12 is 2, it takes much longer time to enter the steady cutting state comparing with simulations with $h_b/h_i = 1$.

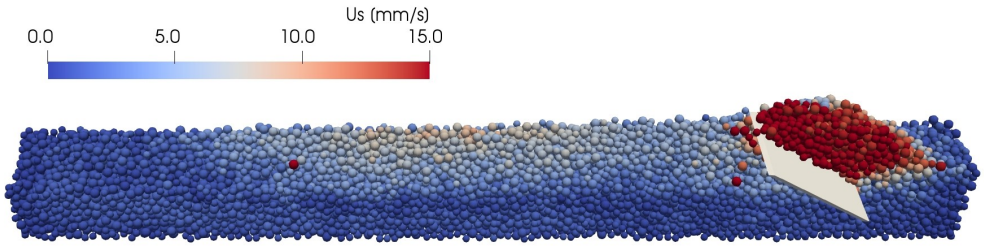

Figure 4.60: The state of the cutting process in Test 3.4 (clip section, particle size: d_{50}=0.4 mm, sand sample size: 50 mm×9 mm×5.3 mm, blade size: h_b=3 mm, w=5 mm, cutting depth: h_i=1.5 mm)

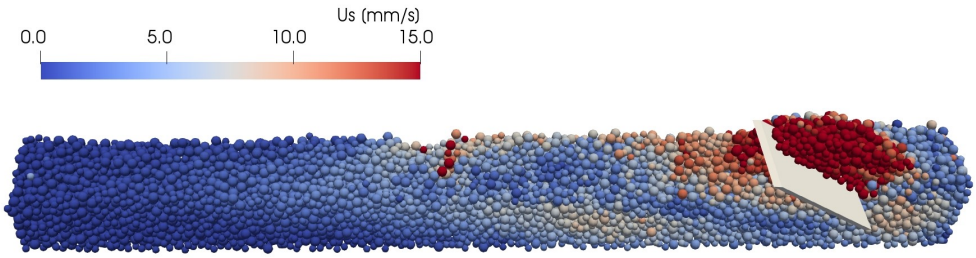

Figure 4.61: The state of the cutting process in Test 4.12 (clip section, particle size: d_{50}=1.2 mm, sand sample size: 150 mm×27 mm×16.7 mm, blade size: h_b=9 mm, w=15 mm, cutting depth: h_i=4.5 mm)

Fig. 4.58 shows the overall stress developments for Test 3.5 and 4.13. Large fluctuations are observed on the overall stress record of Test 4.13. Apart from that, the pattern of the overall stress development is similar to Fig. 4.56 (Test 3.1 and 4.11). Snapshots are taken from Test 3.5 and 4.13, as depicted by Fig. 4.62 and 4.63 respectively. The steady states of Test 3.5 and 4.13 are apparently different from the steady state of Test 3.1 and 4.11, the particles cannot form a sufficiently large pile on the blade to cover the whole blade surface, instead they can only fall from the transverse sides of the blade. With $h_b/h_i = 3$, they finally climbed to approximately half of the blade height and then keep steady in the later stage. Therefore, when calculating the overall stresses in Fig. 4.58, only half of the blade surface is considered. For Test 4.13, with smaller surface area of the blade covered by larger sand particles, larger fluctuations of the stress are generated. But the trends of the stress records are reasonable, so that

the average stresses in the steady cutting state are considered to be reliable.

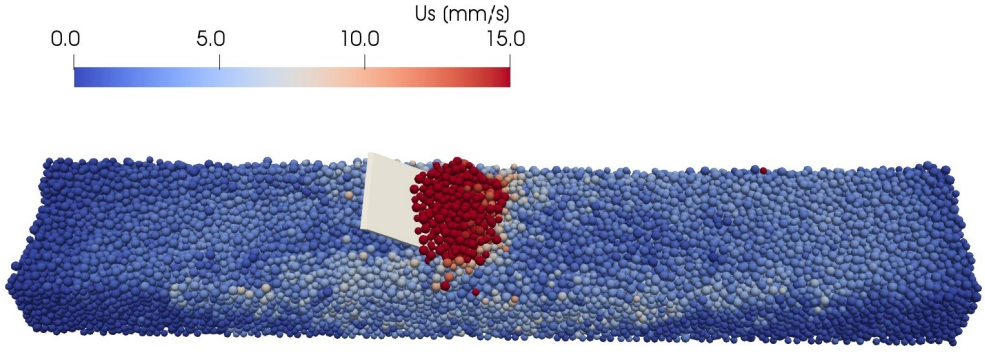

Figure 4.62: The steady state of the cutting process in Test 3.5 (particle size: d_{50}=0.4 mm, sand sample size: 50 mm×9 mm×5.3 mm, blade size: h_b=3 mm, w=5 mm, cutting depth: h_i=1 mm)

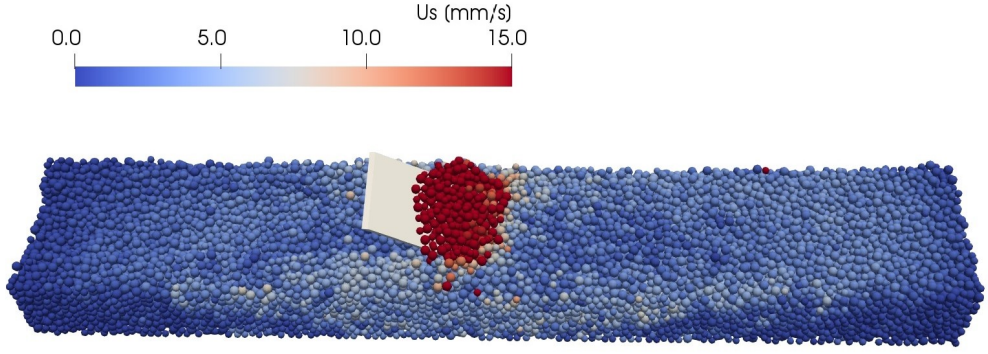

Figure 4.63: The steady state of the cutting process in Test 4.13 (particle size: d_{50}=1.2 mm, sand sample size: 150 mm×27 mm×16.7 mm, blade size: h_b=9 mm, w=15 mm, cutting depth: h_i=3 mm)

All the steady state overall stresses are listed out in Table 4.21. The ratio $(S_{1.2}/S_{0.4})$ between the overall stress using $d_{50} = 1.2mm$ particles is around 3 times to the overall stress with $d_{50} = 0.4mm$ particles. The ratio of cutting depths in each comparison group is also 3, i.e., 9 mm vs. 3 mm, 4.5 mm vs. 1.5 mm and 3 mm vs. 1 mm. As concluded in Chapter 4.9.3, in the cutting simulations of 3D effect, the overall cutting stress holds a positive linear correlation with the cutting depth. Therefore here it is considered that the ratio $S_{1.2}/S_{0.4} \approx 3$ is induced by different cutting depth. To further prove that, Test 3.1 $(d_{50} = 0.4mm)$ is compared with Test 4.13 $(d_{50} = 1.2mm)$, although the particle sizes are different, the h_b/h_i ratios are different, the cutting depths are the same $(h_i = 3mm)$. Results show that the overall cutting stresses are

almost the same (98.83 Pa vs. 99.56 Pa). Thus it is concluded that DEM particle size, within the tested range, does not influence the cutting stresses on the blade.

Table 4.21: Steady cutting stress from the simulations for analyzing the effect of particle size (Test 3.1, 3.4, 3.5 and Test 4.11, 4.12, 4.13)

Test No.	h_b/h_i [-]	h_i [mm]	d_{50} [mm]	$S_{overall}$ [Pa]	$S_{1.2}/S_{0.4}$ [-]
3.1	1	3	0.4	98.83	3.05
4.11		9	1.2	301.52	
3.4	2	1.5	0.4	50.55	2.91
4.12		4.5	1.2	146.9	
3.5	3	1	0.4	33.82	2.94
4.13		3	1.2	99.56	

The influence of the cutting speed

Input parameters for Test 4.11, 4.14, 4.15, 4.16, 4.17 and 4.18 are exactly the same except for the cutting speeds. The recorded cutting stresses from the simulations are listed in Table 4.22 and plotted in Fig. 4.64. Fig. 4.64 shows that both the horizontal and vertical cutting stresses increase with the cutting speed. The transverse stress, as listed in Table 4.22, is not linked with the cutting speed. According to Miedema (2017), the correlation between the cutting stress and cutting speed is approaching positively linear. In Fig. 4.64, linear regressions are plotted for all the stresses. The correlations are approaching linear, but not precisely linear. This is considered in agreement with Miedema's experimental observations.

It should be mentioned that even at 162 cm/s cutting speed (Test 4.18), cavitation did not occur. The reason is that the cutting depths in these simulations are only 9 mm. Thus even there is large pressure gradient present in the sand, the pore under pressure is not big enough to induce cavitation. The fluid pressure field will be analyzed later in Chapter 4.9.6.

Table 4.22: Cutting stresses in the steady state of the cutting process in different directions with respect to cutting speeds

Test No.	Cutting Speed	Horizontal stress	Transverse stress	Vertical stress	Overall stress
	v_c [cm/s]	S_h [Pa]	S_t [Pa]	S_v [Pa]	$S_{overall}$ [Pa]
4.11	2	263.97	-2.78	134.88	301.52
4.14	6	355.74	3.48	169.15	399.14
4.15	18	629.11	-12.19	220.53	676.62
4.16	54	1088.27	9.03	270.97	1137.46
4.17	108	2653.53	2.87	717.98	2792.47
4.18	162	4750.23	33.95	1292.02	4970.43

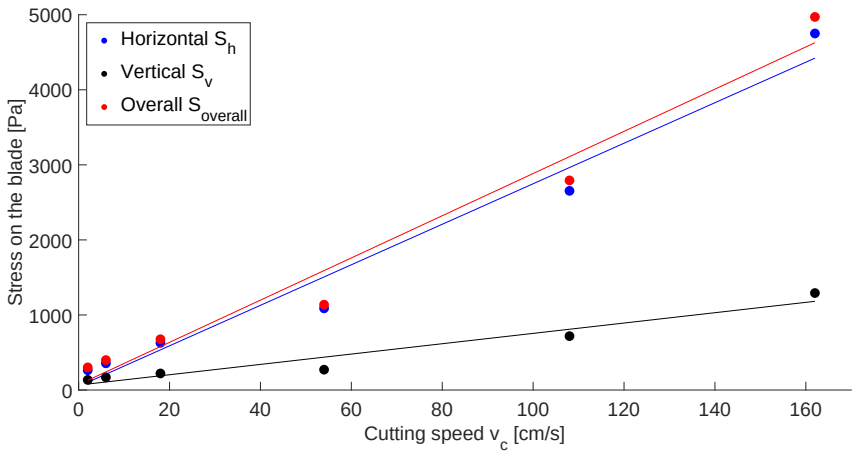

Figure 4.64: Stresses on the blade versus cutting speed (Test 4.11, 4.14-4.18)

The influence of the coupling interval

As introduced in Chapter 4.7.3, Test 3.1.1 is specially designed to check if smaller DEM-FVM coupling interval would induce significant difference in the cutting process. As listed in Table 4.23, coupling interval of Test 3.1 is 10 and in Test 3.1.1 is 5, all the other settings are the same. Fig. 4.65 shows the overall stress developments for both tests. The stress developments for the two tests are almost the same. The overall cutting stress in the steady state of Test 3.1.1, is slightly lower than in Test 3.1 (93 Pa vs. 98.93 Pa). This difference is considered acceptable. Therefore a DEM-FVM coupling interval of 10 is reliable at $v_c = 2$ cm/s cutting speed.

Table 4.23: Cutting stresses in the steady state of underwater sand cutting process with respect to coupling intervals

Test No.	Coupling interval steps [-]	Horizontal stress S_h [Pa]	Transverse stress S_t [Pa]	Vertical stress S_v [Pa]	Overall stress $S_{overall}$ [Pa]
3.1	10	87.82	-0.39	43.07	98.93
3.1.1	5	81.8	-1.28	44.15	93

Validation of the wedge theory in underwater sand cutting

As introduced before, the simulations of underwater sand cutting with α_c=75° and α_c=90° are conducted to analyze whether a wedge occurs with large blade angles in the underwater cutting process or not. The overall stresses on the blade from the simulations with these two groups are analyzed together with the results from the simulations with α_c=30°, 45° and 60°. All the results are shown in Fig. 4.66.

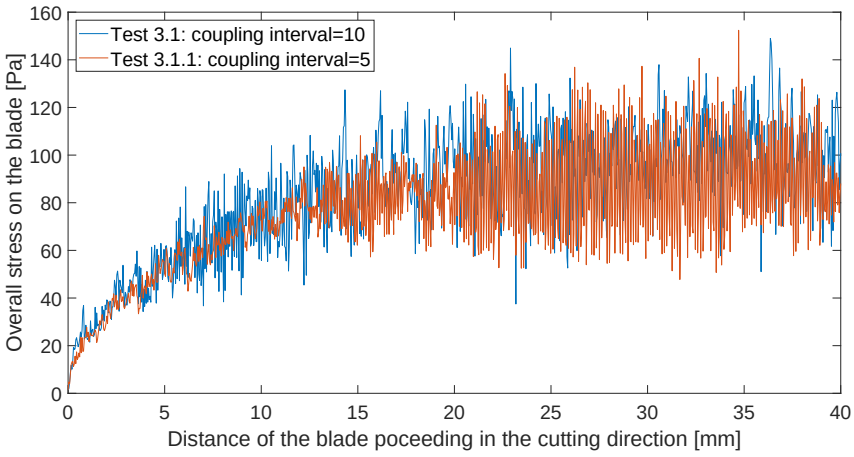

Figure 4.65: Overall Stress developments on the blade with different coupling intervals (Test 3.1, 3.1.1)

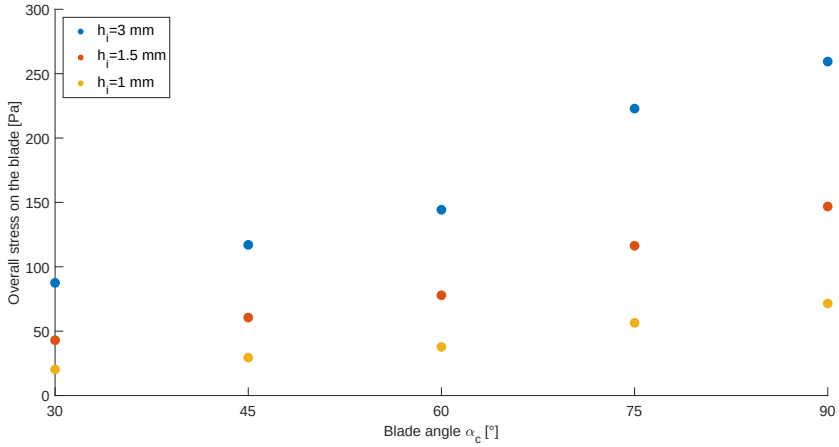

Figure 4.66: The overall stress on the blade with varying blade angles and cutting layer thicknesses in the simulations of underwater sand cutting (Test 3.1, Test 3.4-3.17: $v_c = 2$ cm/s)

Table 4.24: The overall stress on the blade with varying blade angles and cutting layer thicknesses in the simulations of underwater sand cutting (Test 3.9-3.17)

Test No.	h_i [mm]	Overall stress $S_{overall}$ [Pa]			Ratio of the stresses
		α_c=60°	α_c=75°	α_c=90°	
3.9 & 3.12 & 3.15	3	144.30	222.87	259.40	1:1.5:1.9
3.10 & 3.13 & 3.16	1.5	77.87	116.31	146.83	1:1.5:1.9
3.11 & 3.14 & 3.17	1	37.74	56.47	71.50	1:1.5:1.9

The trends in Fig. 4.66 shows that the increasing rate of the overall stresses with α_c over 60° is not significantly larger than that with α_c in the range of 30°-60°. According to Miedema (2017), this indicates the cutting mechanism changes with large blade angles.

He and Vlasblom (1998) carried out a series of experiments of underwater sand cutting with large blade angles in the laboratory of Dredging Engineering at Delft University of Technology. Few information can be found about the detailed input parameters for their experiments which are important for validation. But they reported that from their experiments the ratio between the cutting forces with blade angles of 60°, 75° and 90° is approximately 1:1.5:2, and they have observed wedge forming in the cutting. As shown by Table 4.24, the ratio of overall stresses with blade angles of 60°, 75° and 90° in the underwater sand cutting simulations is around 1:1.5:1.9. This is quite close to the ratio obtained from experiments. Therefore, it is concluded that DEM-FVM coupling model can simulate the underwater sand cutting with large cutting angles well.

If there is a wedge formed, only the particles in the layer cut move upwards along the front surface of the wedge, which is the "pseudo blade " in Miedema's words. The particles in the wedge move much slowly with respect to the blade in the vertical direction. To observe the wedge, the vertical velocity distribution of the particles near the blade in Test 3.15 with α_c=90° and h_i=3 mm is shown here in Fig. 4.67.

Although not very obvious, a wedge can be found between the blade and the layer cut from the vertical velocity distinction in Fig. 4.67. It can be seen the particles in the wedge have smaller velocities compared with the outer layer. The boundary line of the wedge to the shear layer is not very obvious. According to Miedema (2017), the wedge in underwater sand cutting is a dynamic wedge instead of a static wedge, meaning the grains in the wedge also move relative to the blade. In both reality and simulations, the surface between the wedge and the layer cut cannot be easily distinguished.

4.9.4. Analysis of the porosity change in the cutting zone

In this research, porosity represents the volume fraction of the fluid inside the soil. While the cutting blade proceeds in the sand, the porosity changes due to the movement of the sand. The main area of interest is the dilatation zone where the shearing happens.

Three locations, A, B and C, are chosen for analysing the porosity change during cutting process, as shown in Fig. 4.68. The locations of these three cells only differ in vertical direction. They are all at the centre location inside the sand package in the transverse direction. Location B is at the height of the blade tip, while Location A and C are one cell above and below the blade tip respectively.

The porosities at those three locations are monitored from the beginning to the moment that the blade passes Location A. Fig. 4.69 shows the porosity change at

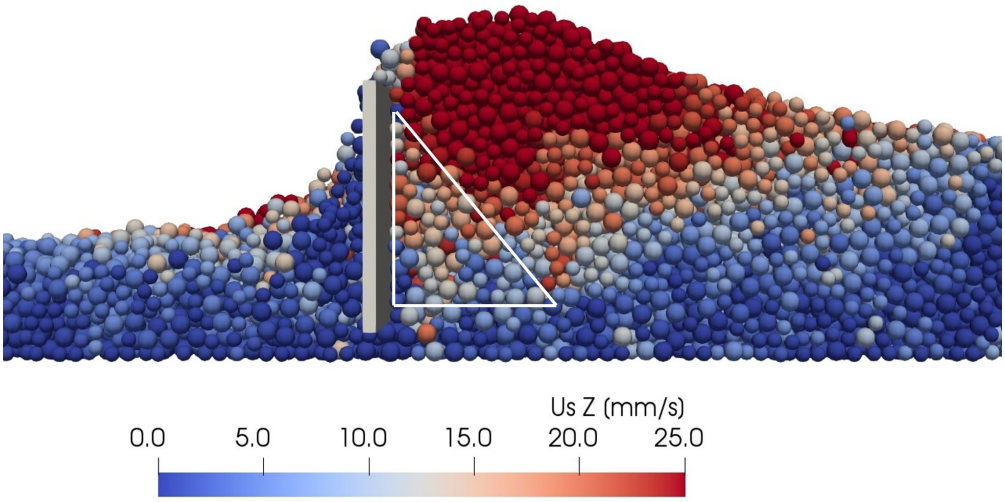

Figure 4.67: The wedge in the underwater cutting process - Test 3.15: α_c=90°, h_i=3 mm.

these three locations in this period in Test 3.1 (α_c=30°, h_i=3 mm, v_c=2 cm/s and p_h=5.89 kPa)

In Fig. 4.69, the porosities of the three locations remain undisturbed until around t=0.65 s, and then the porosity starts to change at the three locations. Later on, the porosities at Location B and C show fluctuations while that at Location A increases.

On one hand, the increase of the porosity is a phenomenon accompanied with dilatation, which means the pores increase in volume. On the other hand, the decrease of that indicates the particles are subject to some compression under the push of the proceeding blade. The fluctuation indicates alternation of the compression and dilatation.

From the porosity change, it is learned that particles at Location A experience the dilatation firstly and then some compression when they are on the surface of the blade. The particles at Location B experience the compression vigorously at first, and then compression and dilatation alternatively. The same trend is found at Location C, but the amplitude is much smaller. In general, the porosity at these three locations have all increased after 1.1 s.

To find out the quantitative difference of the porosities at the three locations, the initial, minimum and maximum values of the porosity (n_i, n_{min}, n_{max}) of different groups are calculated and listed in Table 4.25.

Comparing Test 3.1 and 4.11 in Table 4.25, it is found that the initial porosities of the sand samples with different particle sizes are similar to each other. The maximum

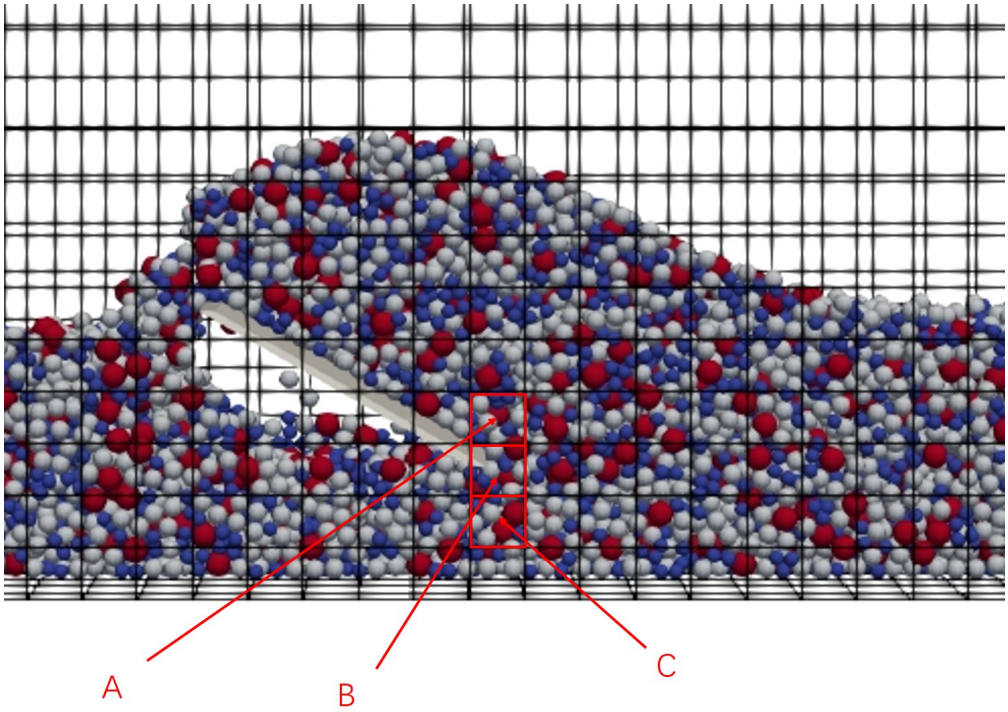

Figure 4.68: The location of the cells for analyzing the porosity change (Side view)

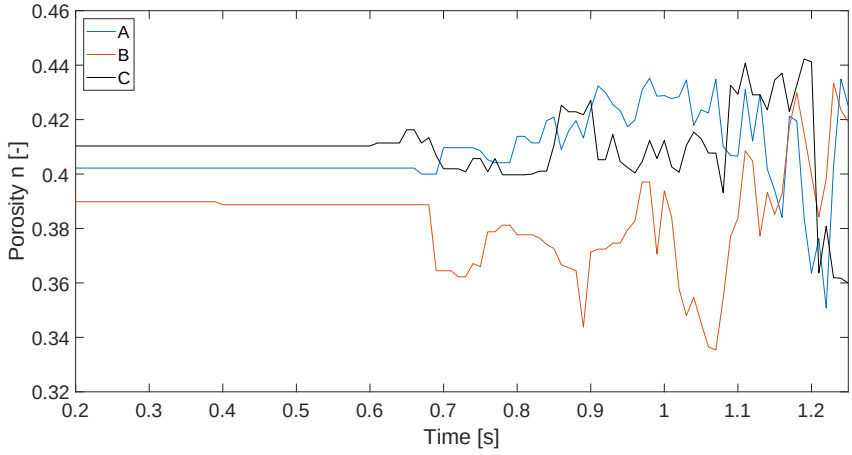

Figure 4.69: Porosity change during Test 3.1: α_c=30°, h_i=3 mm, p_h=5.89 kPa, v_c=2 cm/s

Table 4.25: The initial, minimum and maximum porosity at the three locations

Test No.	d_{50} [mm]	v_c [cm/s]	A			B			C		
			n_i	n_{min}	n_{max}	n_i	n_{min}	n_{max}	n_i	n_{min}	n_{max}
3.1	0.4	2	0.40	0.35	0.44	0.39	0.36	0.43	0.41	0.36	0.43
4.11	1.2	2	0.41	0.31	0.51	0.40	0.35	0.59	0.41	0.34	0.52
4.14	1.2	6	0.41	0.33	0.58	0.40	0.34	0.59	0.41	0.30	0.54
4.15	1.2	18	0.41	0.33	0.58	0.40	0.34	0.59	0.41	0.30	0.54
4.16	1.2	54	0.41	0.33	0.62	0.40	0.37	0.63	0.41	0.30	0.54
4.17	1.2	108	0.41	0.36	0.61	0.40	0.37	0.63	0.41	0.32	0.54
4.18	1.2	162	0.41	0.37	0.61	0.40	0.39	0.67	0.41	0.37	0.54

porosity is larger with larger particles (d_{50}=1.2 mm), while the minimum porosity is larger for smaller particles (d_{50}=0.4 mm).

In all the cases, dilatancy have been witnessed. But it should also be pointed out there is always a certain extent of compression has occurred before the final dilatancy. The level of compression $(n_i - n_{min})$ reduces when cutting velocity v_c increases. The possible reason for that is the sand samples used for the cutting simulations are not very dense. If a more wide PSD is applied, then it is believed that the level of compression will be much smaller. However, based on the trend observed in Fig. 4.69 and Table 4.25, it is reasonable to believe that, even with a much wider PSD, compression will still be an inevitable transient process before shear layer forms up.

4.9.5. Analysis of the fluid flow field

Fluid velocity is of importance to the underwater cutting process as it strongly influences the drag force on the particles. To evaluate the fluid velocity change in the cutting direction and the vertical direction, the same three cells used for the porosity change analysis are chosen as Fig. 4.68 shows. Fig. 4.70 and 4.71 show the horizontal and vertical fluid velocities of the three locations respectively for Test 3.1, from the beginning to the moment that the blade has passed Location A.

Fig. 4.70 and Fig. 4.71 show similar trends of the fluid velocities in the cutting and vertical directions at the three locations. Fluid velocities at Location A and B both increase but with different amplitudes when the blade approaches these locations. However, the fluid velocity at Location C shows some fluctuations, even turns negative at some moments.

Fig. 4.70 shows the fluid velocities in the cutting direction at Location A and B start to change at around t=0.7 s when the particles in the neighbourhood are mobilized by the blade. Then at about t=0.75 s, they both start to increase with some fluctuations. When the pore volume between the particles changes, fluid has to flow into the enlarged pores or out of the shrunken pores under the pressure gradient. The positive sign indicates that the direction of the fluid velocity is the same as that of the

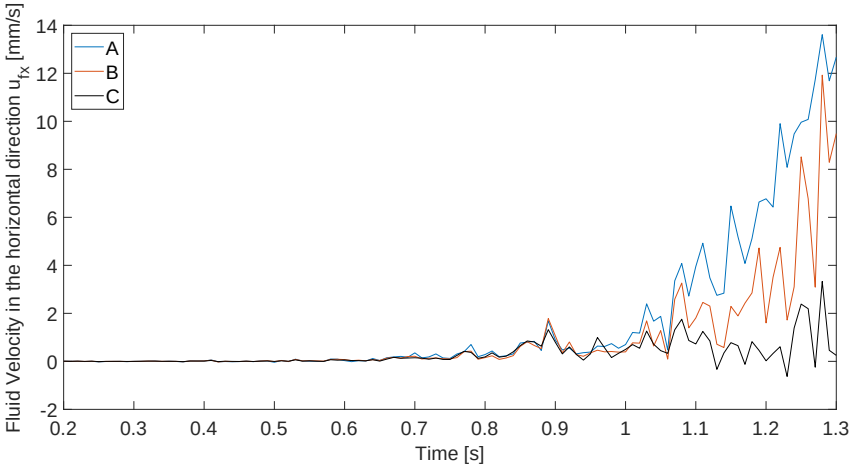

Figure 4.70: The fluid velocity in the cutting direction in Test 3.1: α_c=30°, h_i=3 mm, p_h=5.89 kPa, v_c=2 cm/s

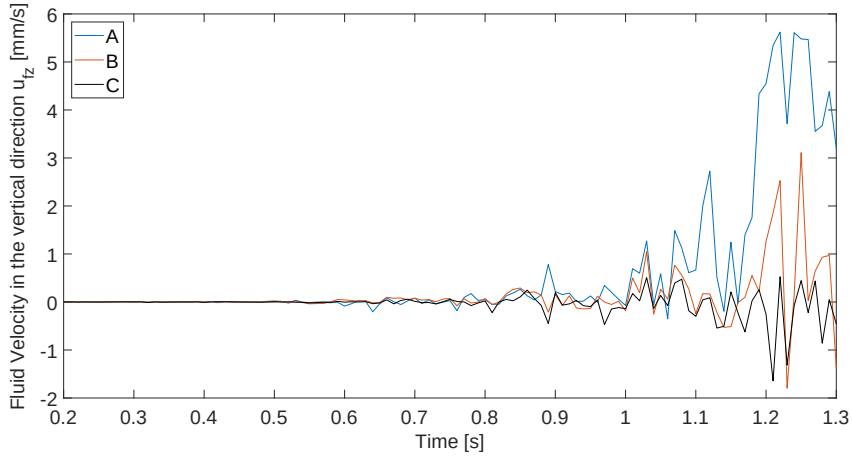

Figure 4.71: The fluid velocity in the vertical direction in Test 3.1: α_c=30°, h_i=3 mm, p_h=5.89 kPa, v_c=2 cm/s

blade. For the fluid velocity at Location C, there are always some fluctuations around 0 after t=0.7 s. This means the fluid below the height of the blade tip flows both in the positive and negative horizontal directions under the intervention of the blade movement.

In Fig. 4.71, the trend of the vertical velocity of fluid at Location A is similar to that in the horizontal direction, increasing with some fluctuation. But the situation is different for those at Location B and C. The fluid velocities at these two locations both show fluctuations around 0 after t=0.6 s. u_{fz} at Location C is mostly negative. This indicates the fluid below the blade tip mostly flows downwards penetrating the sand bed. The fluid at Location B flows upwards firstly while being compressed, but later upwards and downwards alternatively in the dilatation phase. This means a bifurcating tendency of the streamlines is present at this location.

Fluid velocity and pressure fields are visualized in Fig. 4.72 to 4.78 to show the change of the fluid flow field with different cutting velocities. The color of the arrows represents the magnitude of the fluid velocity and the direction of them stands for the velocity direction. The color of the background represents the fluid pressure. Fig. 4.72 is for Test 3.1, where small particles are used (d_{50}=0.4 mm). Fig. 4.73 to 4.78 are for Test 4.11 and 4.14-4.18, where big particles are used (d_{50}=1.2 mm), the cutting velocity ranges from 2 to 162 cm/s.

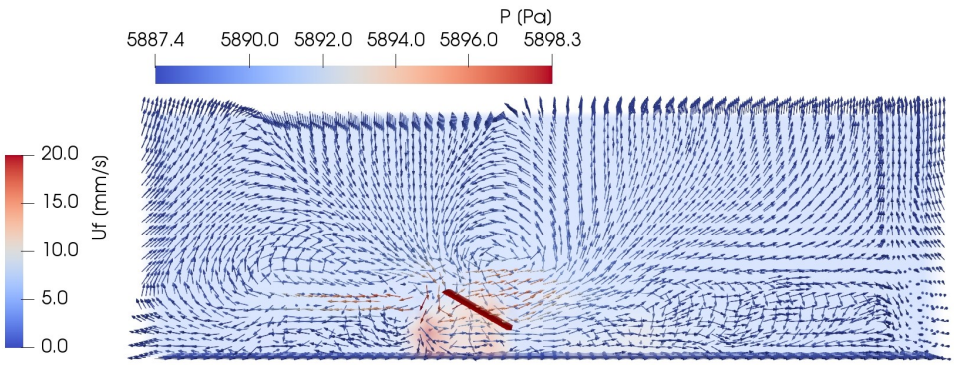

Figure 4.72: The fluid flow field of Test 3.1 (d_{50}=0.4 mm, α_c=30°, h_b=3 mm, h_i=3 mm, p_h=5.89 kPa, v_c=2 cm/s)

To distinguish the features of the fluid field corresponding to different cutting speeds, based on Fig. 4.72 to 4.78, the sketches of fluid velocity field with low, medium and high cutting speeds are made, as Fig. 4.79 to 4.81 show.

When the cutting speed is low, apparent large eddies can be found both in front of and behind the blade. The fluid velocities behind the blade are higher than other areas as displayed in Fig. 4.72 to 4.74. The particles fall down from the top of blade to the back of blade. The fluid near there is affected by the dropping particles. Meanwhile, the fluid behind the dropping particles flows away from the blade and goes up to join the eddy behind the blade. Hence, a part of the velocity vectors behind the blade

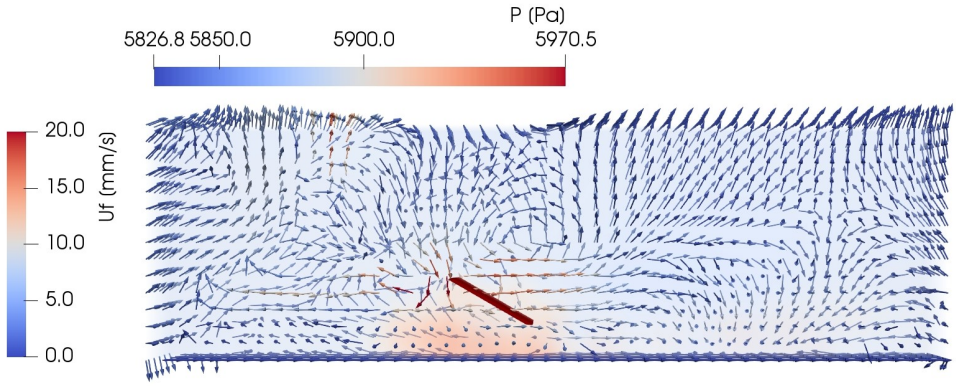

Figure 4.73: The fluid flow field of Test 4.11 (d_{50}=1.2 mm, α_c=30°, h_b=9 mm, h_i=9 mm, p_h=5.89 kPa, v_c=2 cm/s)

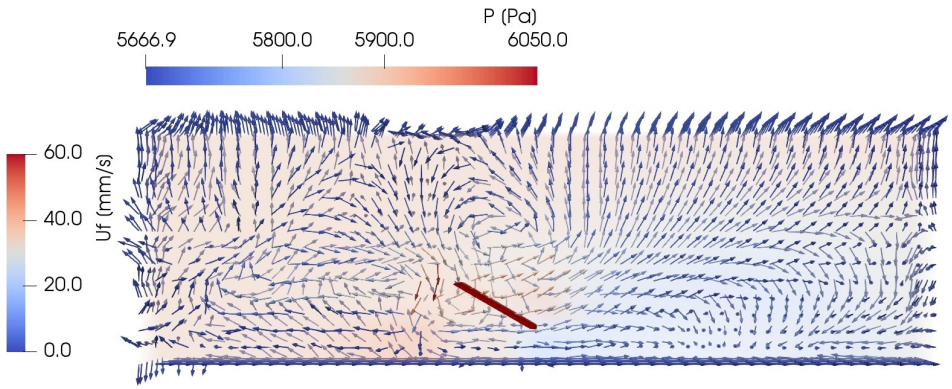

Figure 4.74: The fluid flow field of Test 4.14 (d_{50}=1.2 mm, α_c=30°, h_b=9 mm, h_i=9 mm, p_h=5.89 kPa, v_c=6 cm/s)

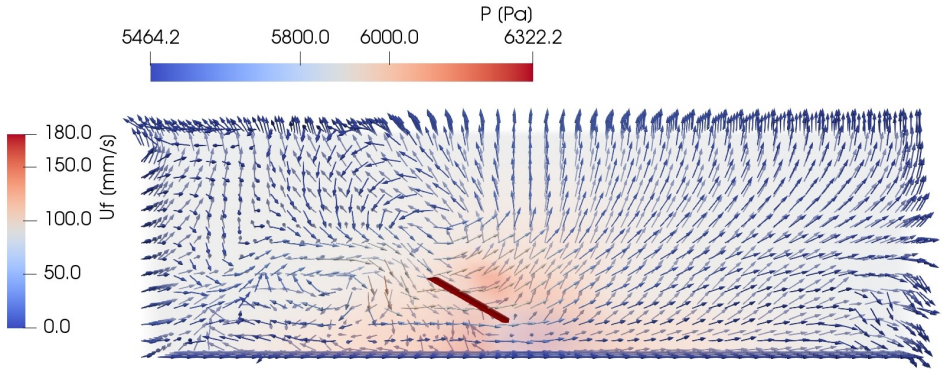

Figure 4.75: The fluid flow field of Test 4.15 (d_{50}=1.2 mm, α_c=30°, h_b=9 mm, h_i=9 mm, p_h=5.89 kPa, v_c=18 cm/s)

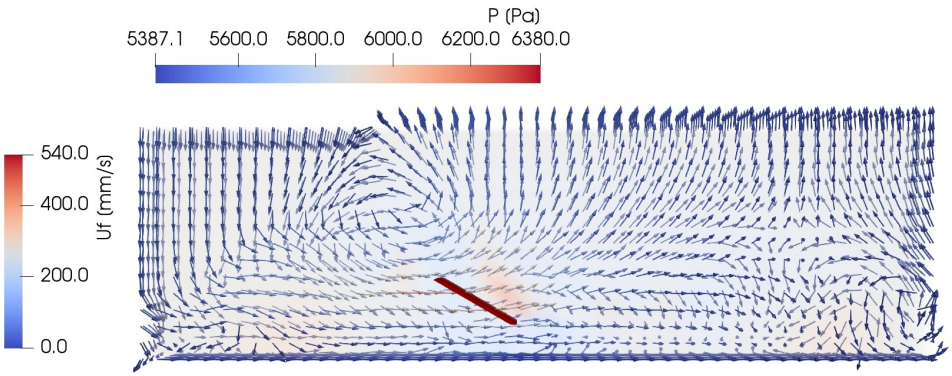

Figure 4.76: The fluid flow field of Test 4.16 (d_{50}=1.2 mm, α_c=30°, h_b=9 mm, h_i=9 mm, p_h=5.89 kPa, v_c=54 cm/s)

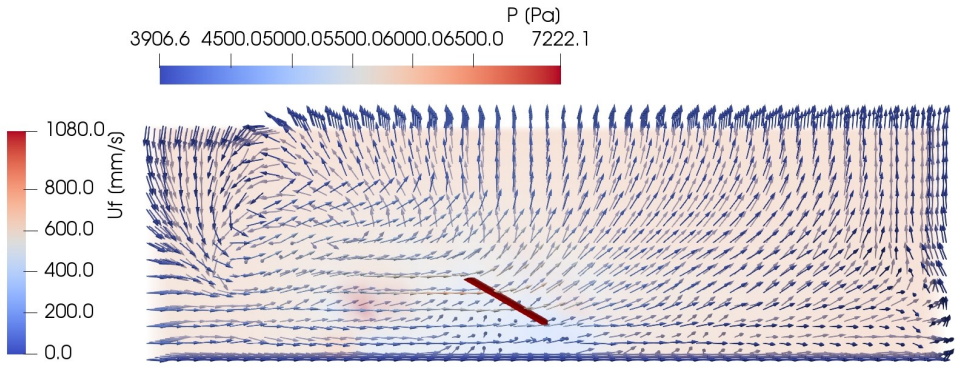

Figure 4.77: The fluid flow field of Test 4.17 (d_{50}=1.2 mm, α_c=30°, h_b=9 mm, h_i=9 mm, p_h=5.89 kPa, v_c=108 cm/s)

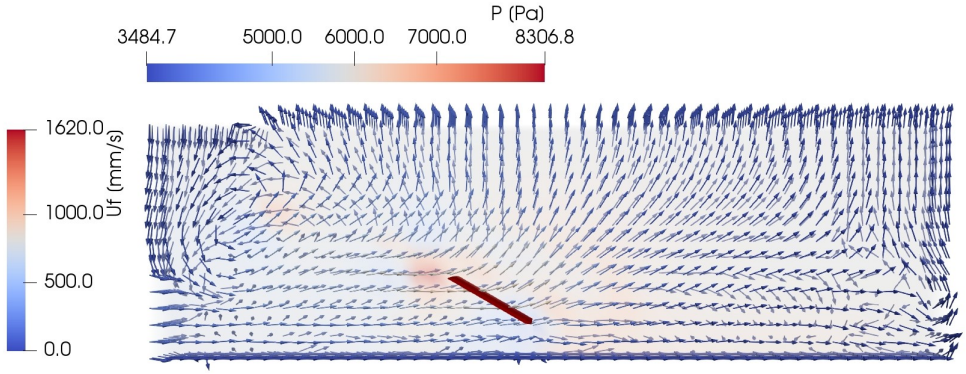

Figure 4.78: The fluid flow field of Test 4.18 (d_{50}=1.2 mm, α_c=30°, h_b=9 mm, h_i=9 mm, p_h=5.89 kPa, v_c=162 cm/s)

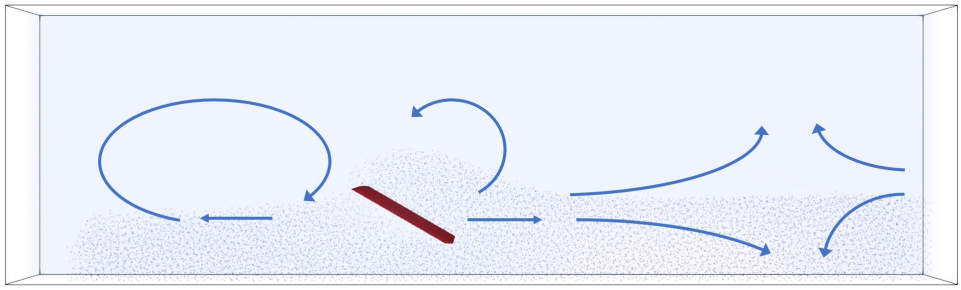

Figure 4.79: The sketch of the fluid flow field with low cutting speeds (v_c=2-6 cm/s)

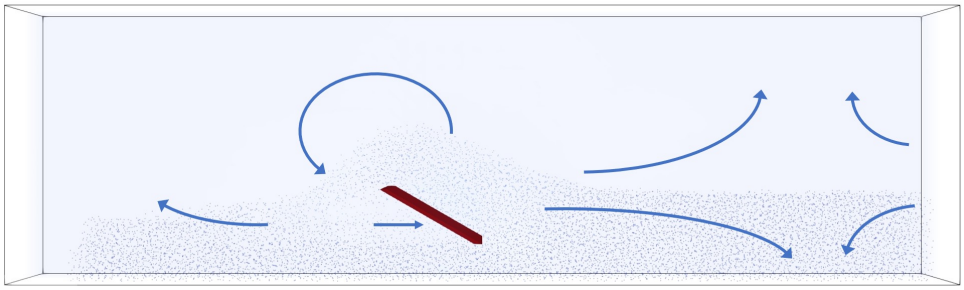

Figure 4.80: The sketch of the fluid flow field with medium cutting speeds (v_c=18-54 cm/s)

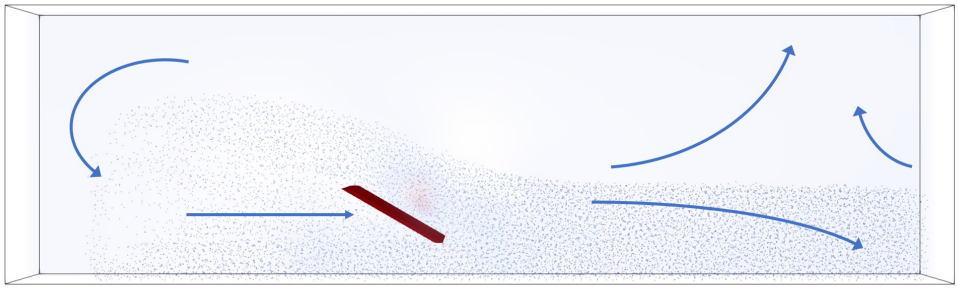

Figure 4.81: The sketch of the fluid flow field with high cutting speeds (v_c=108-162 cm/s)

are parallel to the horizontal direction. Under the push of the blade, the fluid in front of the blade and around the blade tip flows forward and the velocity vectors are almost horizontal. Near the right end of the sand sample, the velocity vectors near the free surface of the sand sample are split up into two groups and go upwards and downwards respectively. This is because the fluid above the free surface of the sand pile flows upwards under the disturbance of the moving blade, while the fluid in the lower layer of the sand pile flows downwards to penetrate the sand particles. The other two groups of velocity vectors coming from outside the right boundary encounter them and form a cavity around the free surface of the sand sample. A high pressure area is found behind the blade as the dropping particles gathering there.

Fig. 4.80 shows, when the cutting speed increases, the two large eddies near the blade gradually converge into one. The velocity vectors are parallel to the horizontal direction only behind the blade, while those in front of the blade start to direct upwards. The dropping particles start to move farther with a larger speed before settling on the seabed, making the void space between them and the blade larger. Then the fluid here flows towards the proceeding blade. The bifurcation of the velocity vectors and the cavity still exist far from the blade in the proceeding direction. The high pressure area behind the blade becomes farther from the blade.

Fig. 4.81 shows that the velocity vectors behind the blade are different when the cutting speed is even higher. They are influenced by the particle tail where the particles are moving at high speed. There is a large eddy caused by the settling particles near the left end of the sand sample. The fluid flow behind the blade follows the blade as the particles do not settle that rapidly due to their inertia. The velocity vectors in front of the blade are similar to the medium case. The furcation of the velocity vectors and the cavity are observed near the right end of the sand sample.

4.9.6. Analysis of the fluid pressure gradient distribution

Pressure gradient plays an important role in the momentum conservation for the fluid phase. The area of interest is the dilatation zone where the pore volume increases due to the shearing between the particles. The dilatation is reflected by the water pore under pressure. Fig. 4.82 indicates the fluid pressure in the shear zone is lower than that in the surrounding areas, as explained by the theory of underwater sand cutting (Miedema, 2017). This means the pores in the shear zone experience increase in volume due to the shear between particles.

Pressure gradient term also has a great effect on the forces acting on the particles. As Fig. 4.83 shows, the largest pressure gradient always appears in the dilatation zone, where the failure plane develops.

With varying cutting speeds, the strain rate in the solids changes, making the pressure gradient in the dilatation zone various in magnitudes. Table 4.26 lists out the cutting speeds and corresponding pressure gradients in the dilatation zone. Fig. 4.84 plots the pressure gradients for simulations using d_{50}= 1.2 mm particles.

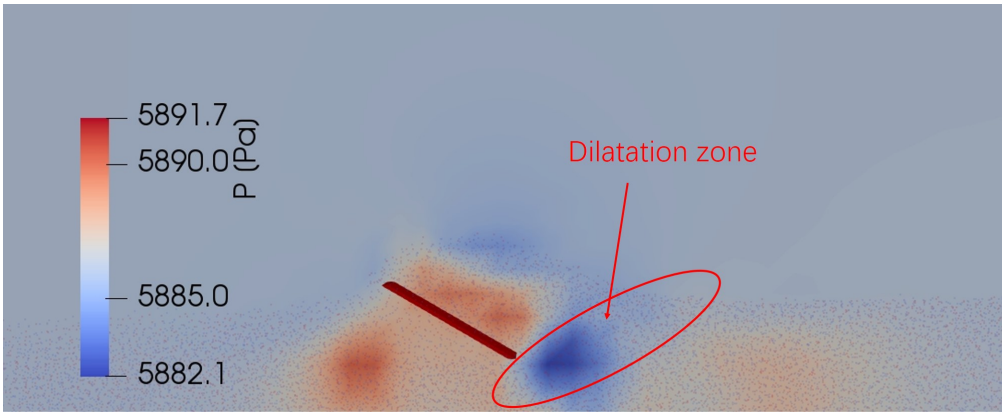

Figure 4.82: The low pressure in the dilatation zone (Test 3.1: α_c=30°, h_i=3 mm, v_c=2 cm/s, p_h=5.89 kPa)

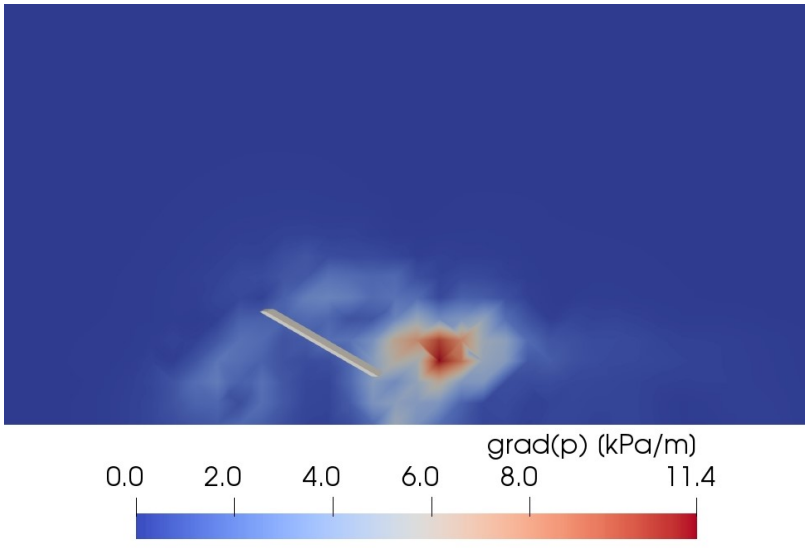

Figure 4.83: The pressure gradient "grad(p)" in the dilatation zone (Test 3.1: α_c=30°, h_i=3 mm, v_c=2 cm/s, p_h=5.89 kPa)

Table 4.26: Pressure gradient in the dilatation zone with different cutting speeds

Test No.	Median diameter d_{50} [mm]	Cutting speed v_c [cm/s]	Pressure gradient in the dilatation zone ∇p [kPa/m]
3.1	0.4	2	11.4
4.11	1.2	2	16.3
4.14	1.2	6	38.8
4.15	1.2	18	73.0
4.16	1.2	54	113.0
4.17	1.2	108	289.0
4.18	1.2	162	851.2

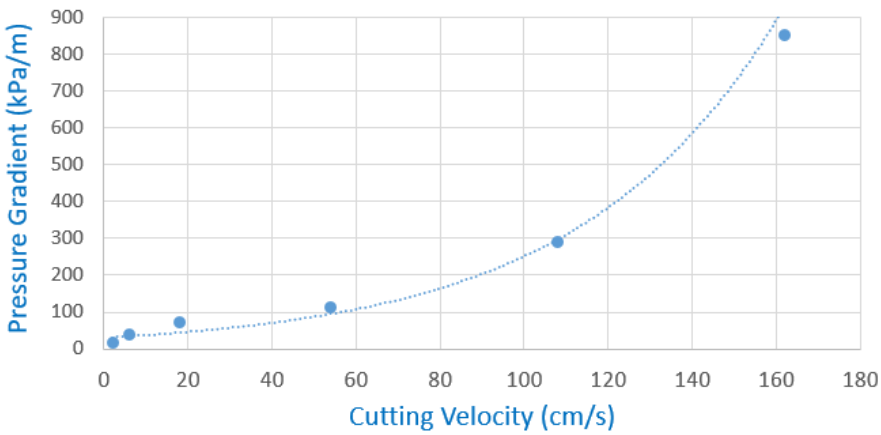

Figure 4.84: Pressure gradient with different cutting speeds, the dash line represents the curve fitting of an exponential relation

Table 4.26 and Fig. 4.84 show that the pressure gradient ∇p in the dilatation zone increases with the cutting speed v_c. A curve fitting based on an exponential relation is made in Fig. 4.84, which reveals that ∇p increases significantly faster with larger v_c. This tells that the resistance on the cutting blade will increase dramatically when cutting above 162 cm/s, because the pressure gradient also influences the particles in the form of a fluid-particle interaction force. This will be discussed in Chapter 4.9.7 in detail.

The pressure gradients in these simulations are not large enough to trigger cavitation. However, based on the pressure gradients obtained, it is deduced that if further increase the cutting speed to 200 cm/s above, then cavitation will occur.

4.9.7. Analysis of the fluid-solid interaction forces

The fluid-solid interaction forces applied are the Gidaspow drag force f_d, the pressure-gradient force $f_{\nabla p}$ and viscous force $f_{\nabla \cdot \tau}$. To study to how much extent these forces influence the cutting process of different cutting speeds or hydrostatic pressures, four areas of interest are specifically chosen from the fluid pressure distribution in the steady state, which are shown in Fig. 4.85.

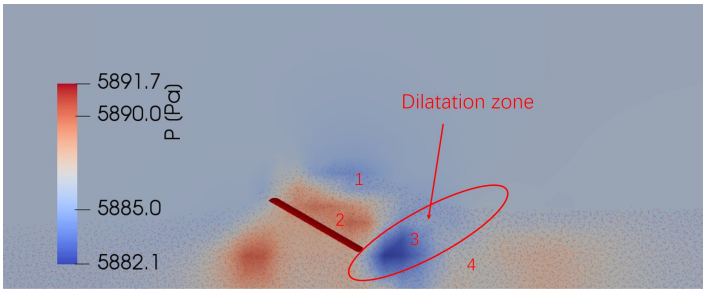

Figure 4.85: The four areas for studying the fluid-solid interaction forces (Test 3.1: α_c=30°, h_i=3 mm, v_c=2 cm/s, p_h=5.89 kPa)

The four areas of interest are the surface layer of the layer cut on the blade (Area 1), the inner layer of the layer cut (Area 2), the shear zone (Area 3) and the area in front of the shear zone (Area 4). In each area, the coupling forces acting on the particles are recorded. The average value of each coupling force is calculated by dividing the total coupling force in the area by the number of particles in the area. In this way, the three average coupling forces in each area are obtained, and then their contribution in the total fluid-solid interaction force can be examined.

The influence of the hydrostatic pressure

To study the influence of the hydrostatic pressure on the coupling forces, the results from Test 3.1-3.3 are listed out, as Table 4.27 shows. In all the cases, viscous forces are much smaller than the other two forces. Fig. 4.86 plots the change of the drag and

pressure gradient forces in all the four areas against the hydrostatic pressure p_h, where the solid lines stand for the magnitudes of the drag forces while the dashed lines are the magnitudes of the pressure gradient forces. The colours represent different areas.

Table 4.27: The fluid-solid interaction forces on the particles in different areas with different hydrostatic pressures

Test No.	d_{50} [mm]	v_c [cm/s]	p_h [kPa]	Area	Gidaspow drag force $\overline{f}_d$ [N]	Pressure-gradient force $\overline{f}_{\nabla p}$ [N]	Viscous force $\overline{f}_{\nabla\cdot\tau}$ [N]
3.1	0.4	2	5.89	1	5.02×10^{-7}	8.48×10^{-8}	4.10×10^{-10}
				2	5.45×10^{-7}	1.02×10^{-7}	3.86×10^{-10}
				3	5.84×10^{-7}	9.53×10^{-8}	1.78×10^{-10}
				4	3.83×10^{-8}	3.82×10^{-8}	4.77×10^{-11}
3.2	0.4	2	58.86	1	6.41×10^{-7}	1.32×10^{-7}	5.81×10^{-10}
				2	8.46×10^{-7}	1.24×10^{-7}	5.69×10^{-10}
				3	7.57×10^{-7}	1.24×10^{-7}	2.63×10^{-10}
				4	4.52×10^{-8}	3.64×10^{-8}	3.21×10^{-11}
3.3	0.4	2	588.6	1	7.53×10^{-7}	1.36×10^{-7}	6.93×10^{-10}
				2	8.08×10^{-7}	1.53×10^{-7}	6.74×10^{-10}
				3	8.99×10^{-7}	1.66×10^{-7}	3.70×10^{-10}
				4	1.25×10^{-7}	1.09×10^{-7}	9.11×10^{-11}

It can been seen from Fig. 4.86, in most of the cases, the forces increase with p_h, but there are also cases when the forces decrease or stay the same when p_h has increased to ten times larger. There is no fixed pattern to relate the coupling forces with the hydrostatic pressure. This is reasonable since cavitation did not occur in these simulations. A possible reason for the differences in the forces with different hydrostatic pressures is that each simulation is different, so different particles of different sizes appeared in the cells of those four specific areas in different test, and the coupling force is proportional to particle volume. Therefore the resulting coupling forces are different.

Fig. 4.86 also shows drag force in Area 4 is significantly smaller than in the other three areas. This is reasonable since Area 4 is the sand bed where water hardly flows there. To further understand which force dominates the coupling in each area, the influence fractions of theses forces are shown in a bar chart (Fig. 4.87) to display the general trend of the coupling forces with the increasing hydrostatic pressure.

In Fig. 4.87, the bars from left to right in a group denote the coupling force distribution in Area 1 to Area 4 respectively. It is clear that the viscous force $\overline{f}_{\nabla\cdot\tau}$ is so small that its contribution is negligible. Fig. 4.87 also implies that the Gidaspow drag force $\overline{f}_d$ always dominates in the four areas irrespective of different hydrostatic pressures at this low cutting speed (v_c=2 cm/s). The percentages of the forces do not change a lot in these cases. Hence it can be concluded that at this cutting speed,

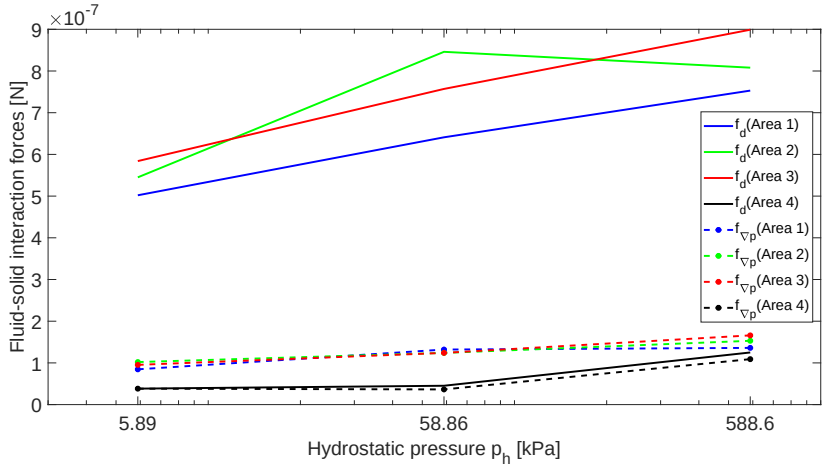

Figure 4.86: The drag forces and pressure gradient forces in different areas with different hydrostatic pressure

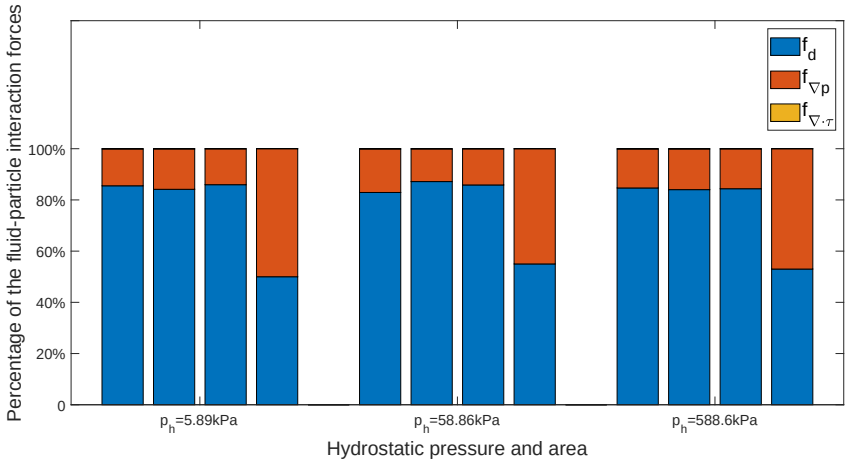

Figure 4.87: The percentage of different fluid-solid interaction forces in the four areas versus hydrostatic pressure, the bars from left to right in one group denote the coupling force distribution in Area 1 to Area 4 respectively. (v_c=2 cm/s, Test 3.1: p_h=5.89 kPa, Test 3.2: p_h=58.86 kPa, Test 3.3: p_h=588.6 kPa)

hydrostatic pressure does not significantly influence the coupling force distribution.

The influence of the cutting speed

Results from Test 4.11 and 4.14-4.18 are listed out in Table 4.28 to evaluate the effect of the cutting speed. Comparing with Table 4.27, one can find that the forces increase with particle size in general. This is because the forces are particle-based and related to the particle volume. It is again clear to see that the viscous force $\overline{f}_{\nabla\cdot\tau}$ is always the lowest force in all the cases. The drag force and the pressure gradient force are the governing forces for the interaction. Fig. 4.88 shows the change of drag and pressure gradient forces over the cutting speed, where the solid lines stand for the magnitudes of the drag forces while the dashed lines are the magnitudes of the pressure gradient forces. The colours represent different areas.

Table 4.28: The fluid-solid interaction forces on the particles in different areas with different cutting speeds

Test No.	d_{50} [mm]	v_c [cm/s]	p_h [kPa]	Area	Gidaspow drag force $\overline{f}_d$ [N]	Pressure-gradient force $\overline{f}_{\nabla p}$ [N]	Viscous force $\overline{f}_{\nabla\cdot\tau}$ [N]
4.11	1.2	2	5.89	1	1.61×10^{-5}	8.20×10^{-6}	3.73×10^{-9}
				2	2.06×10^{-5}	9.53×10^{-6}	3.07×10^{-9}
				3	4.85×10^{-5}	1.08×10^{-5}	1.63×10^{-9}
				4	1.07×10^{-5}	8.25×10^{-6}	1.62×10^{-9}
4.14	1.2	6	5.89	1	3.27×10^{-5}	7.09×10^{-6}	4.86×10^{-9}
				2	2.82×10^{-5}	1.54×10^{-5}	3.67×10^{-9}
				3	8.54×10^{-5}	1.85×10^{-5}	3.17×10^{-9}
				4	1.76×10^{-5}	1.25×10^{-5}	1.05×10^{-9}
4.15	1.2	18	5.89	1	5.01×10^{-5}	2.02×10^{-5}	1.23×10^{-8}
				2	5.16×10^{-5}	2.90×10^{-5}	5.65×10^{-9}
				3	1.52×10^{-4}	1.33×10^{-4}	9.63×10^{-9}
				4	1.07×10^{-4}	1.04×10^{-4}	7.96×10^{-9}
4.16	1.2	54	5.89	1	9.14×10^{-5}	6.58×10^{-5}	3.05×10^{-8}
				2	5.87×10^{-5}	5.93×10^{-5}	1.63×10^{-8}
				3	2.38×10^{-4}	2.26×10^{-4}	6.17×10^{-8}
				4	2.19×10^{-4}	1.41×10^{-4}	1.64×10^{-8}
4.17	1.2	108	5.89	1	2.08×10^{-4}	1.23×10^{-4}	5.94×10^{-8}
				2	1.69×10^{-4}	1.63×10^{-4}	3.89×10^{-8}
				3	2.57×10^{-4}	3.03×10^{-4}	3.28×10^{-8}
				4	2.27×10^{-4}	1.97×10^{-4}	2.25×10^{-8}
4.18	1.2	162	5.89	1	4.41×10^{-4}	2.20×10^{-4}	8.89×10^{-8}
				2	2.41×10^{-4}	2.37×10^{-4}	2.93×10^{-8}
				3	3.24×10^{-4}	4.58×10^{-4}	8.39×10^{-8}
				4	2.68×10^{-4}	2.67×10^{-4}	2.62×10^{-8}

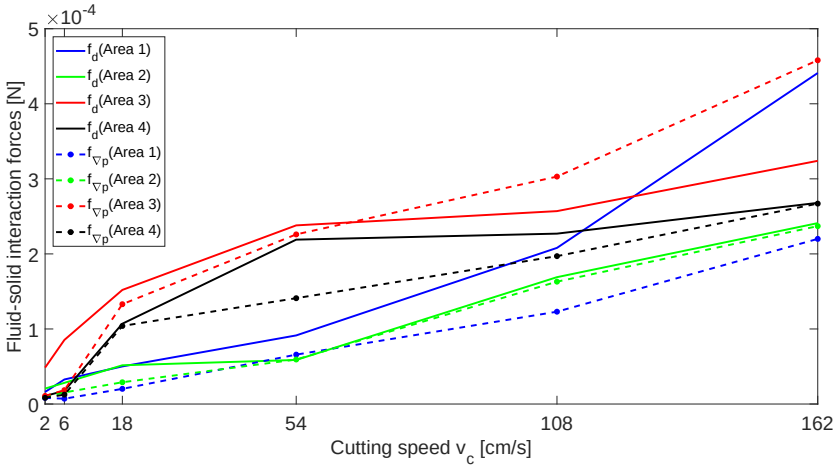

Figure 4.88: The drag forces and pressure gradient forces in different areas with different cutting speeds

Fig. 4.88 shows that, from low to high cutting speed, the drag force $\overline{f}_d$ and the pressure gradient force $\overline{f}_{\nabla p}$ both show increasing tendencies. In Area 1, $\overline{f}_d$ is always larger than $\overline{f}_{\nabla p}$. The gap between these two forces increases with v_c. The change in the rankings of $\overline{f}_d$ and $\overline{f}_{\nabla p}$ with v_c is quite remarkable in Area 3 where the dilatation happens. $\overline{f}_{\nabla p}$ surpasses $\overline{f}_d$ when v_c is over 54 cm/s and becomes the dominant force in the three coupling forces. To better review the influence fractions of theses forces, Fig. 4.89 is made to show the general trend of the coupling forces with the increasing cutting speed.

Fig. 4.89 indicates that the force dominance changes in the four areas with the cutting speed. One can find the Gidaspow drag force $\overline{f}_d$ is not always dominant among the three forces. When v_c is relatively low, $\overline{f}_d$ is the dominant force in all the four areas, but differs with its percentage. In the first two groups, $\overline{f}_d$ takes up more weight in Area 3. With a cutting speed over 18 cm/s, $\overline{f}_{\nabla p}$ starts to increase and takes over the dominant place in the last three groups. This phenomenon reflects the relation between the cutting speed and the pressure drop in the shear zone. With the blade proceeding faster, larger under pressure is created, resulting in large pressure gradient force.

Within Area 1 and 2, $\overline{f}_d$ occupies more in Area 1 than in Area 2 in most cases, as the particles in Area 1 are scoured by the fluid near the free surface of the sand sample. When v_c is over 54 cm/s, the portion of $\overline{f}_d$ increases in Area 1 but stays the same in Area 2. This means the influence of v_c on the fractions of the coupling forces is significant in Area 1 but not much in Area 2. The fractions of $\overline{f}_d$ and $\overline{f}_{\nabla p}$ in Area 4 are always similar in these cases, which means v_c poses little affect on the fluid-solid interaction in the undisturbed sand. Based on the trend found in Fig. 4.89,

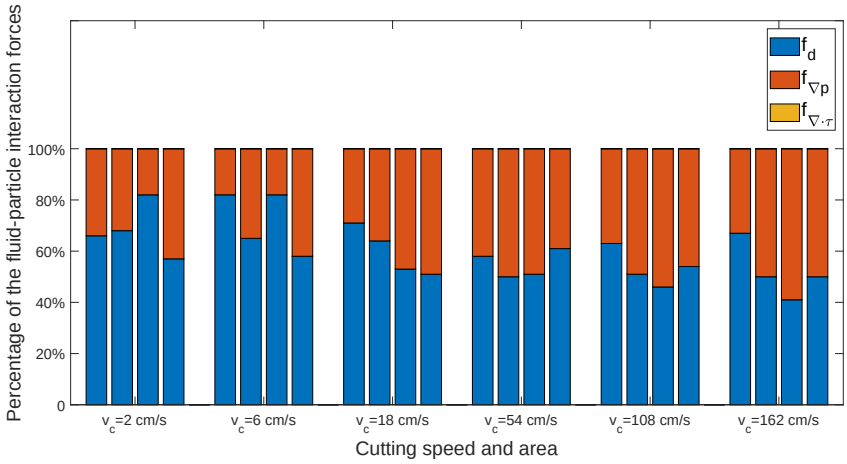

Figure 4.89: The percentage of different fluid-solid interaction forces in the four areas versus cutting speed, the bars from left to right in one group denote the coupling force distribution in Area 1 to Area 4 respectively. (p_h=5.89 kPa, Test 4.11: v_c=2 cm/s, Test 4.14: v_c=6 cm/s, Test 4.15: v_c=18 cm/s, Test 4.16: v_c=54 cm/s, Test 4.17: v_c=108 cm/s, Test 4.18: v_c=162 cm/s)

it is reasonable to believe, with further increased cutting speed, the pressure gradient force will become the most dominant force in Area 3, which is the shearing zone, and that would become the main resistance against cutting.

4.10. Conclusions and Recommendations

For numerical modelling of the dry sand cutting process.

1. In DEM, non-spherical particles based on a regular tetrahedron internal structure can well represent the mechanical behavior of natural sand. Phenomenons like interlocking, shearing and dilatation can occur spontaneously without any extra constitutive laws applied on macro scale. The porosity of a natural randomly packed particles sample is in the range of $0.36 \sim 0.41$, which is quite similar to real sand piles.
2. In the simulation of dry sand cutting, the mechanical properties of the particles can be chosen to match the values obtained from reality, e.g., engineering practice or lab experiments.
3. Adjustment is needed to overbridge the gap from the scale of the numerical simulation to the reality. The theory developed by (Miedema, 2017) can be applied to create the scaling relation. The cutting forces scale with the $(h_i^2 \cdot w \cdot \rho_s)$ factor, while the cutting stresses scale with the $(h_i \cdot \rho_s)$ factor.
4. The cutting speed in the simulation is relatively small, as a result the inertia effect is not investigated in this study, therefore the stresses are mainly induced

by gravity. The validation tests have proven that, the cutting forces on the blade, after scaling, resemble well with the experimental results from (Hatamura and Chjiiwa, 1976b).

5. The simulation results prove that, with large cutting angles (75° and 90°), the cutting force develop according to the wedge theory of Miedema (2017). However, the wedge is not static and thus cannot be easily visualized.

For numerical modelling of underwater sand cutting process.

1. The shear angles appeared in the underwater sand cutting simulations are slightly smaller than the empirical results. The differences are considered acceptable. Underwater sand cutting simulations have successfully presented the shear plane development, compression and dilatation processes.
2. In both the 2D and 3D effect simulations, the horizontal, vertical and overall cutting stresses increase near-linearly with cutting depth. The horizontal stress is positively correlated with the cutting angle, while the vertical stress shows the opposite. The horizontal stress is dominant, resulting in the overall stress is also positively correlated with the cutting angle.
3. Validation on the dimensionless cutting force for the 2D effect cutting process shows that, large errors appear at $h_b/h_i = 1$ when the results are not corrected for gravity effect. After the results are corrected for gravity effect, the numerical, experimental, and analytical dimensionless cutting forces agree with each other well.
4. Forces measured in 2D effect simulations are higher than in 3D effect simulations, because sand particles can fall from the transverse sides of the blade in the 3D effect simulations.
5. In non-cavitation cutting process, the cutting force does not change with hydrostatic pressure, besides, the horizontal, vertical and overall cutting forces all increase near-linearly with the cutting speed.
6. As long as there are sufficient layers of particles on the blade, the cutting stresses on the blade do not change with particle size.
7. Wedge also exists in underwater sand cutting with large cutting angles. The ratio of simulated overall cutting stresses of $\alpha_c = 60°$, 75° and 90° match well with experimental results.
8. The fluid flow pattern changes with the cutting velocity. On the hand, the largest water pore under pressure and pressure gradient, regardless of the change of cutting velocity, will always appear in the shear plane, in front of the tip of the blade. The largest pressure gradient increases exponentially with the cutting speed.
9. Viscous forces are negligibly small. In the shear plane, with low cutting speed (2 cm/s and 6 cm/s), drag force dominates the fluid-particle interaction, with

medium cutting speed (18 cm/s and 54 cm/s), drag force and pressure gradient force make more or less equal contributions in the fluid-particle interaction. When the cutting speed is high (108 cm/s and 162 cm/s), pressure gradient force becomes the dominant force in fluid-solid interaction.

In the simulations of dry sand cutting, the cutting speeds in these simulations are small, which leads to that the inertia force is negligible. However, in real-time engineering practice where the cutting speed is much higher, the inertia force plays an important role which cannot be neglected. Thus it is recommended that dry sand cutting simulations with higher cutting speeds should be carried out for investigating the influence of the inertia force.

For underwater sand cutting, it is recommended to conduct more simulations with higher cutting speed and deeper cutting depth. This is to trigger the occurrence of cavitation. It is necessary, especially for dredging applications, to investigate the performance of the DEM-FVM coupling when cavitation happens.

5

Numerical Modelling on the Cutting Process of Cohesive Soil

This chapter focuses on the numerical modelling on the cutting process of cohesive soil. First a series of calibration tests are conducted to determine the mechanical properties of the DEM soil sample, and then cutting simulations in both atmospheric and underwater conditions are carried out.

The experimental data from the (Hatamura and Chjiiwa, 1975, 1976a,b, 1977a,b) tests are used for the validation of cohesive soil cutting in atmospheric environment. The numerical results match with the experimental data within acceptable error margin. No experimental data is available for validating the underwater cohesive soil cutting simulations, hence the permeability of the DEM cohesive soil sample has not been properly calibrated. Therefore, the underwater simulations show drained cutting processes instead of undrained processes, which are expected in underwater cutting of clay.

Parts of this chapter have been published in Chen et al. (2014, 2015).

It has been introduced before that the goal of this research project is to establish a comprehensive framework for numerically modelling the underwater excavation process of sand, cohesive soil and rock. In Chapter 4 the DEM model for sand particles and the DEM-FVM coupling simulations for underwater sand cutting process have been elaborated. For the study on cohesive soil, this chapter will introduce the numerical modelling of material test of cohesive soil, and cohesive soil cutting process in the atmospheric and underwater conditions.

The experimental data from the (Hatamura and Chjiiwa, 1975, 1976a,b, 1977a,b) tests is used for the validation of cutting in atmospheric environment. Before conducting the cutting simulations, a series of calibration tests is designed so that the mechanical properties of the created cohesive soil sample in DEM can be determined.

A typical kind of cohesive soil encountered in nature is clay. The permeability of clay is usually in the range of $10^{-18} \sim 10^{-13}\ m^2$. However, it should be pointed out that (Hatamura and Chjiiwa, 1975, 1976a,b, 1977a,b) have not reported the permeability of the cohesive soil sample they used, thus in this research project the permeability of the DEM cohesive soil sample has not been properly calibrated. As a result, the simulations of underwater cutting process on cohesive soil in this research project do not resemble the underwater cutting process on natural clay.

Cohesive soil usually contains cohesion and adhesion forces. The formation of cohesion and adhesion forces can be very complicated, where the pore water pressure, the molecular attraction force (e.g., Van der Waals force), and the micro electrochemical reaction process could all play a role. For determining the cutting forces, only the mechanical properties are needed. It is thus decided for the calibration of DEM cohesive soil samples, only the apparent mechanical properties are investigated. They are the undrained shear strength, the cohesion, the adhesion and friction angles.

5.1. Calibration - the ring shear test

5.1.1. Types of cohesion

For determining the cohesion of cohesive soil, Yang et al. (2010) applied the triaxial tests under stationary load to find out the static cohesive strength c and also under cyclic load ($1HZ$) for finding out the dynamic cohesive strength c_d. A c_d/c ratio on the Haikou red clay ($c_d = 20kPa$) is recorded as 1.17. On the Shiroishi clay ($c_d = 52kPa$) this ratio is recorded as 1.86, and on the volcanic sedimentary sandy clay ($c_d = 51kPa$) is recorded as 1.59.

Here the question is raised up whether it is necessary to investigate the dynamic cohesion c_d in this research. For dredging applications, Miedema (2017) has derived a set of equations to calculate the cutting forces on the blade in both horizontal and vertical directions in clay cutting process, as shown below in Eq. (5.1), (5.2) and (5.3). F_h is the horizontal cutting force which is aligned with the direction of the cutting blade $[N]$ while F_v is the vertical cutting force $[N]$, α is the cutting angle [-], β is the

angle of the shear plane to the direction of the cutting velocity [-], λ is the velocity strengthening factor representing that when the cutting velocity increases, clay soil gets stronger. c is the static cohesive strength $[Pa]$ while a is the static adhesive stress $[Pa]$, h_i is the cutting depth $[m]$ and h_b is the blade height $[m]$, w is the width of the blade $[m]$, r_{ac} is the ratio between adhesion and cohesion [-] and α_{ac} the adhesion coefficient defined as $\frac{a}{c}$ [-].

$$F_h = \lambda \cdot c \cdot h_i \cdot w \cdot \frac{\frac{sin(\alpha)}{sin(\beta)} + r_{ac} \cdot \frac{sin(\beta)}{sin(\alpha)}}{sin(\alpha + \beta)} \tag{5.1}$$

$$F_v = \lambda \cdot c \cdot h_i \cdot w \cdot \frac{\frac{cos(\alpha)}{sin(\beta)} - r_{ac} \cdot \frac{cos(\beta)}{sin(\alpha)}}{sin(\alpha + \beta)} \tag{5.2}$$

$$r_{ac} = \frac{a \cdot h_b}{c \cdot h_i} = \alpha_{ac} \cdot \frac{h_b}{h_i} \tag{5.3}$$

In Eq. (5.1) to (5.3), Miedema assumes that there is no internal or external friction for clay soil, in this way c forms up the whole undrained shear strength and a forms up the whole external shear strength. This assumption, often referred as the "$\phi = 0°$" concept, is taken by many dredging engineers. The reason behind is that dredging engineers consider the underwater clay cutting process to be undrained due to the high cutting speed and low permeability. However, in other application fields, e.g., dike and embankment constructions, the consolidation period is much longer and the strength of the clay layer increases when being loaded. Hence this assumption does not apply.

Via the mineralogy study in the experiments of Chen et al. (2019a), it is discovered that cohesive soil often contains a certain amount of quartz, which people usually refer as the sand content. This makes the cohesive soil also has internal and external friction angles. For example, in the cohesive soil of Chen et al. (2019a), the internal friction angle found can be up to 20°, and external friction angle can be up to 27°. In this research, the term "cohesive soil" is used instead of "clay", because cohesive soil could be a mixture of clay and sand, not pure clay. For cohesive soil, the term c in Eq. (5.1) to (5.3) should be replaced by s_u, which is the undrained shear strength of the soil.

From Eq. (5.1) to (5.3), it is learned that, when dealing with high excavation speed, dredging engineers tend to use a velocity strengthening factor λ rather than using a pre-determined c_d. c_d is typically used in the assessment of seismic properties of the soil for protection against earthquakes. On the contrary, the undrained shear strength s_u used in dredging practice is measured by the quasi-static shear test, not by fast cyclic loading. Thus it is determined in this research, a series of ring shear simulations will be undertaken to find out the undrained shear strength and static cohesion of the DEM cohesive soil samples.

5.1.2. Simulation set-up

The principle of the direct shear tests follows the ASTM D-6773 standard (2015), in which the Schulze ring shear test device has been introduced. The standard Schulze ring has a inner radius of 0.05 m and outer radius of 0.1 m. However, as introduced in Chapter 3.3, in this research, big particles are used to form up cohesive soil samples, so the ring shear test device is also set to a larger size to contain the DEM cohesive soil sample. Table 5.1 lists out the input parameters for the simulation.

In total five different particle radii are tested, 1.85, 2.2, 2.5, 2.8 and 3 cm, to find out the relation between particles' size and the cohesion. The cohesion energy density K is another key parameter in determining the cohesion strength of cohesive DEM soil samples. In this research project, cohesive DEM soil sample with a cohesion of 15~20 kPa is expected, because the plastic loam in the experiments of Hatamura and Chjiiwa (1976b) has a cohesion of about 15.7 kPa. Pachón-Morales et al. (2019) have conducted a series of calibration tests with different K values. Based on their research output, the cohesion energy density K in this research project is fixed at $K = 300\ kPa$.

The ring shear device is shown by Fig. 5.1, the inner circle has a radius of 0.5 m, the outer circle 1 m. The walls are modelled as steel. On the inner surfaces of the ring, to prevent the soil sample from sliding on the top and bottom surfaces, there are in total 16 fins installed, 8 on the top lid and 8 on the bottom ring. The shear test is undertaken in the following steps:

1. In the generation and settling phases, the ring is filled with cohesive DEM particles. The particles then settle naturally due to gravity. A gravitational acceleration of -9.81 m/s^2 is applied to all the particles in this period.
2. After all the particles are settled down. The gravitational acceleration is removed. A compression force is then applied by the top ring to the DEM sample vertically downwards, the compression stress is maintained at a constant level by a servomechanism during the shear test.
3. Shearing is commenced by rotating the bottom ring at a rotational speed of $\omega = 3\ rad/min$ until a constant torque T_c is reached. The shear stress can be approximated according to Eq. (5.4), where τ is the shear stress $[kPa]$, T_c the torque $[Nm]$, r_{mean} the average radius of the machine $[m]$ and A_{ring} the contact surface between the rings and the soil $[m^2]$.

$$\tau \approx \frac{T_c}{r_{mean} \cdot A_{ring}} \tag{5.4}$$

5.1.3. Results of ring shear simulations

A snapshot of the cohesive DEM sample during the steady state of the ring shear test is shown in Fig. 5.2, where the colors of the particles represent the particle

Table 5.1: The input parameters for the numerical ring shear simulations

Parameters for the ring shear test device	Symbol	Value	Unit
Inner radius	r_{inner}	0.5	[m]
Outer radius	r_{outer}	1	[m]
Height	h_{ring}	0.38	[m]
Young's modulus of steel	E_{steel}	160	[GPa]
Coefficient of internal friction (steel-steel)	μ_{steel}	0.1	[-]
Poisson' s ratio of the steel	ν_{steel}	0.4	[-]
No. of fins on the lid	-	8	[-]
No. of fins on the bottom	-	8	[-]
Rotation speed	ω	3	[rad/min]
Normal stress on the lid	σ	55.1, 110.2, 220.5	[kPa]
Parameters for cohesive soil particles			
Density	ρ_p	2710	[kg/m^3]
Cohesion energy density	K	300	[kPa]
Radius	r_p	1.85, 2.2, 2.5, 2.8, 3	[cm]
Young's modulus of the soil particle	E_p	30	[MPa]
Poisson' s ratio of the soil particle	ν_p	0.4	[-]
Coefficient of internal friction (soil-soil)	μ_p	0.35	[-]
Coefficient of external friction (soil-steel)	μ_e	0.15	[-]

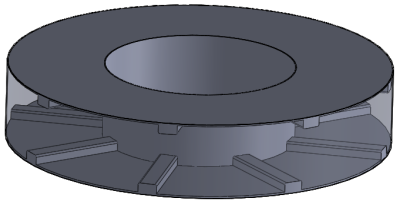

Figure 5.1: The ring shear test device used to obtain the cohesive properties of the cohesive DEM soil sample.

velocity. Blue represents the low velocities 0m/s, and dark red represents the highest velocity of 0.05m/s.

The shear stress development in the ring shear simulations when using the 1.85 cm radius particles, under the three different compressive normal stresses (55.1 kPa, 110.2 kPa and 220.5 kPa), are depicted in Fig. 5.3. Fig. 5.3 shows that the bigger the applied normal stress is, the longer it takes to reach the steady state. In the steady state, even there are fluctuations in the signal, the shear stress does not have an apparent increasing or decreasing trend any more. Besides, it should be mentioned

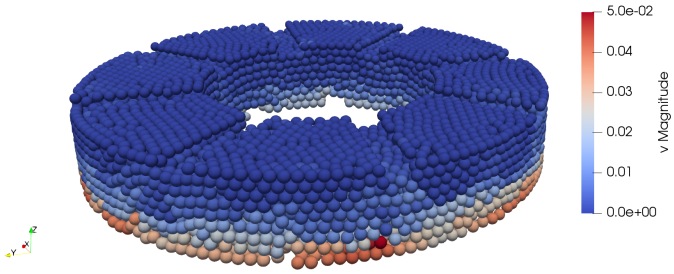

Figure 5.2: A snapshot of the cohesive DEM sample during the steady state of the ring shearing test, where the colors of the particles represent the particle velocity. Blue represents the low velocity 0m/s, and dark red represents the highest velocity 0.05m/s

that the ring shear simulations are conducted only by DEM, without the coupling with FVM, so the external loads are all burdened by the particles. From the perspective of soil mechanics, it is a drained process.

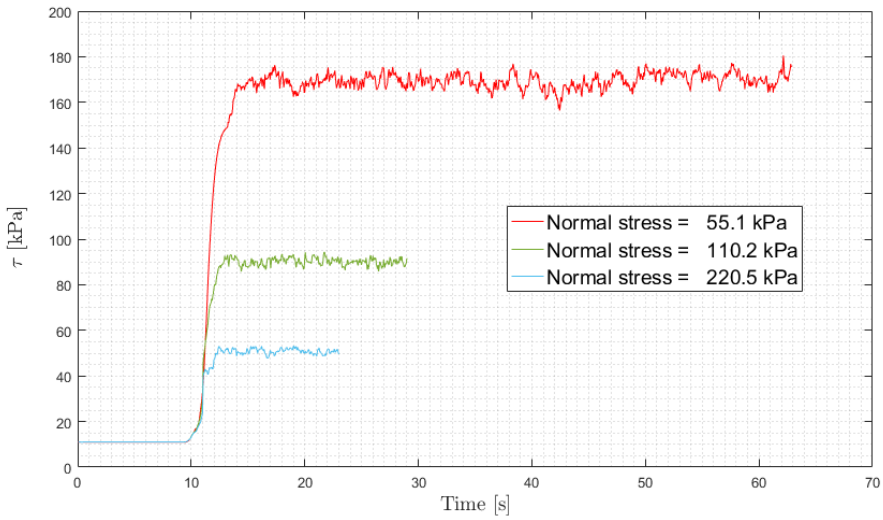

Figure 5.3: Shear stress developments from the numerical ring shearing tests under three normal stresses ($r_p = 1.85$ cm).

The steady-state shear stresses for this group of tests, are plotted versus the applied normal stresses, together with the Mohr-Coulomb failure criterion, in Fig. 5.4. By taking the intersection point of the failure line and the τ axis, the cohesion of the cohesive DEM soil sample is obtained. For this sample, $c = 20.5\ kPa$. The internal friction angle can also be obtained by calculating the steepness of the failure line. For

this sample, $\phi = 31°$.

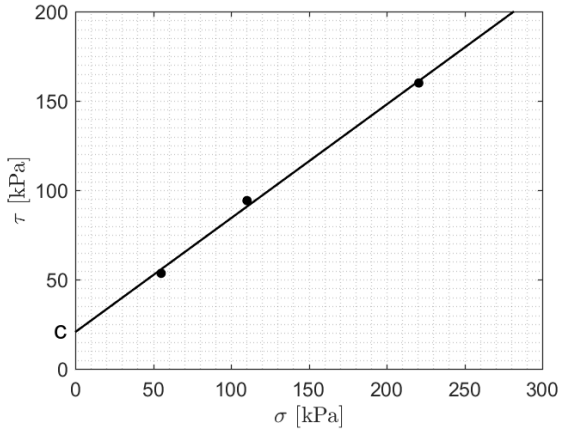

Figure 5.4: Results from the ring shearing simulations with the Mohr-Coulomb failure line

As introduced in Chapter 3.3, the global cohesive strength can be increased by increasing the particles radii. In this research project, five particle radii, from 0.0185m to 0.03m (1.85 ~ 3 cm), have been tested while the cohesion energy density K is fixed at 300 kPa. By the same post-processing steps as described above, the cohesion (c) of all the five samples are obtained and plotted in Fig. 5.5, where the correlation between the cohesion and the particle radius is almost linear. Finally it is found that with the particle radius of 0.0185m (1.85 cm), an macroscopic cohesion of approximately 20.5 kPa can be obtained. This sample will be later used for the cutting tests.

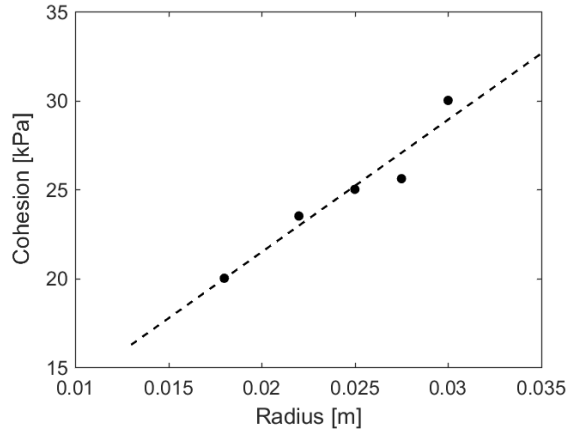

Figure 5.5: The computed internal shear strengths or cohesion for a range of radii are depicted as black points. The dashed straight line represents a linear fit through the computed values

The internal friction angle observed from Fig. 5.4 is 31°. If it is a cohesive soil in nature, it usually means there is a significant amount of quartz in the soil, because this angle is higher than commonly encountered in clay. This relatively large friction angle is induced by: 1) the input parameters in the particle contact model, especially the μ_p in Table 5.1; 2) the "interlocking" effect of spherical DEM particles in the sample, while in nature the platelet structures that form real clay can slide more easily. It is recommended that in future research projects, to conduct more calibration simulations, so that the cohesion and friction of the cohesive DEM soil sample can reach the expected values at the same time.

5.2. Calibration - the blade pull out test

5.2.1. Simulation set-up

The adhesion, i.e., the adhesive shear strength, of the cohesive DEM soil sample is also investigated. The horizontal blade pull-out simulations are set up to test the adhesion of the numerical sample. As shown by Fig. 5.6, a steel blade is located in the middle of the cohesive DEM soil sample and will be horizontally pulled out, and the shear stress on the blade is recorded. The input parameters for the blade pull-out simulation are listed in Table 5.2. The particle size is the same as in the ring shear simulations, each particle has a radius of 1.85 cm. The blade pull-out test is undertaken in the following steps:

1. In the generation and settling phases, two bounded spaces are filled with cohesive DEM particles. The top bounded space is bounded by the top wall, the four side walls and the blade. The bottom bounded space is bounded by the bottom wall, the four side walls and the blade. The particles then settle naturally due to gravity. A gravitational acceleration of -9.81 m/s^2 is applied to all the particles in this period.
2. After all the particles are settled down. The gravitational acceleration is removed. A very small compression force is then applied by the top and bottom walls to the DEM sample vertically, the compression stress is maintained at a constant level by a servomechanism during the shear test.
3. Shearing is commenced by pulling out the blade until a constant shear stress on the blade τ is reached. Since the compression stress is very small (0.001 kPa) and there is no gravity, the shear stress on the blade in the steady state can be considered as the adhesion of the cohesive DEM soil sample.

In Table 5.2, the adhesion energy density is set at $K_a = 0.75 \cdot K = 225kPa$. In (Chen et al., 2019a), it is reported that the adhesion factor α_{ac} for cohesive soil with an undrained shear strength s_u around 20 kPa, is about 0.75. The adhesion factor is defined as the ratio of adhesion versus the undrained shear strength of cohesive soils. In this research project, the reported cohesion of the cohesive DEM soil sample is 20.5 kPa. When no external compression stress or gravitational acceleration is applied, this

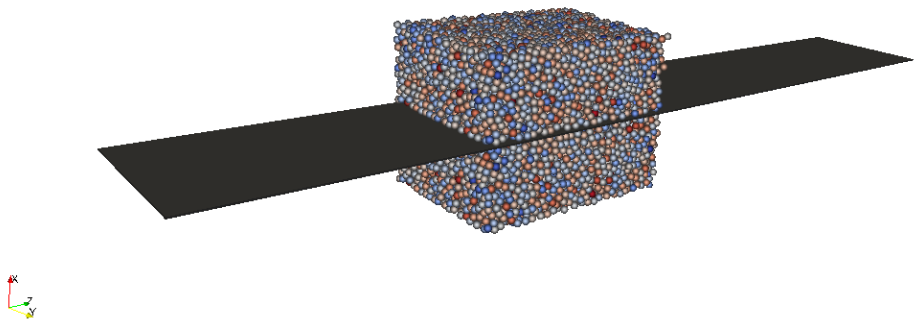

Figure 5.6: Numerical blade pull-out test. The particles and the blade are displayed in the graph, while the top wall, the bottom wall and the four sides walls are made invisible. The walls are used to keep the DEM soil sample inside.

Table 5.2: Input parameters for the blade pull-out simulation

Parameters for the blade and walls	Symbol	Value	Unit
Blade width	w	0.5	[m]
Blade length	l_b	5	[m]
Young's modulus of steel (blade & walls)	E_{steel}	160	[GPa]
Coefficient of internal friction for blade and walls (steel-steel)	μ_{steel}	0.1	[-]
Coefficient of external friction (blade-soil)	μ_{pb}	0.15	[-]
Coefficient of external friction (wall-soil)	μ_{pw}	0	[-]
Poisson' s ratio of the steel (blade & walls)	ν_{steel}	0.4	[-]
Blade pull-out speed	$V_{pullout}$	0.5	[m/s]
Normal stress on top and bottom walls	σ	0.001	[kPa]
Parameters for cohesive soil sample			
Sample width	w_s	0.5	[m]
Sample length	l_s	0.8	[m]
Sample height of bottom half	h_{bs}	0.3	[m]
Sample height of top half	h_{ts}	0.3	[m]
Density of particle	ρ_p	2710	$[kg/m^3]$
Cohesion energy density (soil-soil)	K	300	[kPa]
Adhesion energy density (soil-steel)	K_a	225	[kPa]
Particle radius	r_p	1.85	[cm]
Young's modulus of the soil particle	E_p	30	[MPa]
Poisson' s ratio of the soil particle	ν_p	0.4	[-]
Coefficient of internal friction (soil-soil)	μ_p	0.35	[-]

cohesion is considered roughly equals the undrained shear strength, $c \approx s_u$. Although the ratio between the adhesion and cohesion energy densities does not necessarily equals the adhesion factor of a cohesive DEM soil sample, it is still considered reasonable to use the adhesion factor for estimating the adhesion energy density.

5.2.2. Results of the blade pull-out test

The recorded external shear stress τ_a has been plotted in Fig. 5.7. The external shear strength of the numerical sample in the steady state is approximately 7.1 kPa. This can be considered as the adhesion of the sample. However it is much smaller than the 75 % of cohesion of the sample.

The reason behind is that the contact force is calculated based on the overlap distance, while the allowed overlap distance between the stiff DEM particles and the DEM metal surface is much smaller than the overlap distance between two DEM particles, since the metal blade has a much higher stiffness than the soil particles. The relation between the internal and external shear strengths of the cohesive DEM soil samples could be studied in the further follow-up research.

As mentioned in the beginning of this chapter, the experimental data from the (Hatamura and Chjiiwa, 1976b) tests will be used for the validation of cutting cohesive soil. However, (Hatamura and Chjiiwa, 1976b) did not state the adhesive strength of the cohesive soil they used in the experiments, thus it is decided the cohesive DEM soil sample ($c = 20.5kPa$ & $a = 7.1kPa$) can be used for the simulation of the cutting process.

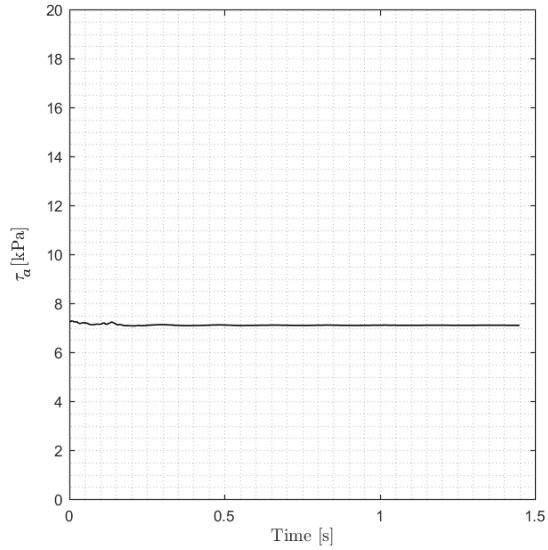

Figure 5.7: Development of the external shear stress on the blade during the blade pull-out simulation

5.3. Simulation set-up of cohesive soil cutting in atmospheric condition

Hatamura and Chijiiwa have conducted cutting experiments on clay and plastic loam. But they have only reported force measurements on the cutting of plastic loam, while no cutting force is recorded in their clay cutting experiments. Therefore, the experimental data of cutting plastic loam is used for validation of numerical simulations.

It should be clarified that their experiments were carried out in atmospheric condition, that means it is a dry environment outside of the plastic loam sample. Under this circumstance, the internal pores of the soil sample are still filled with pore water to a certain percentage depending on the saturation level, but the surface of the soil is not fully saturated. On the contrary, underwater clay cutting test means the whole soil sample is submerged in water, and the surface of the soil is also fully saturated.

In the experiments of plastic loam cutting, Hatamura and Chijiiwa have tried various cutting angles, cutting depths and speeds to investigate their effects on the cutting forces. Loam is soil composed mostly of sand (particle size $> 63\ \mu m$), silt (particle size $> 2\ \mu m$), and a smaller amount of clay (particle size $< 2\ \mu m$). By weight, its mineral composition is about 40–40–20% concentration of sand–silt–clay, respectively (Kaufmann and Cleveland, 2008). The results Hatamura and Chijiiwa have obtained are shown in Fig. 5.8.

To validate the DEM model for cohesive soil cutting, the Hatamura and Chjiiwa experiments with blade angles of 30°, 45° and 60° are selected out as the focus of the study.

As introduced in Chapter 5.1 and 5.4, big DEM particles are used for creating enough macro cohesive strength of the clay sample. Thus a much bigger numerical soil sample is generated compared with the dimensions of the soil samples used by (Hatamura and Chjiiwa, 1976b), as shown in Table 5.3. Although the blade size and cutting depth are larger in the simulations than in the experiments, the ratio of the blade height over the cutting depth h_b/h_i are kept the same as in the experiments. The material properties of the particles and the blade are set the same as the particles and blade used in the blade pull-out simulations (Table 5.2).

Due to the differences on the dimensions of the soil sample and the blade size, the comparison for validation will be made on the cutting stresses instead of cutting forces. The DEM soil sample and the numerical cutting blades used in the simulations are shown in Fig. 5.9.

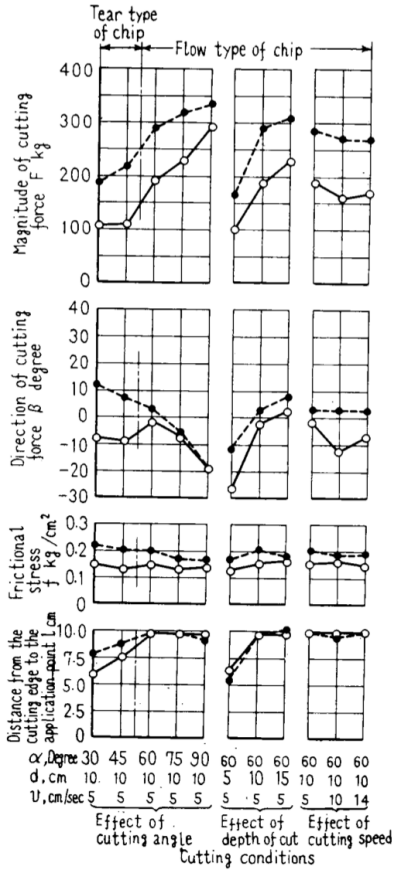

Figure 5.8: Experimental results from the plastic loam cutting tests of (Hatamura and Chjiiwa, 1975, 1976a,b), the solid lines represent the final results.

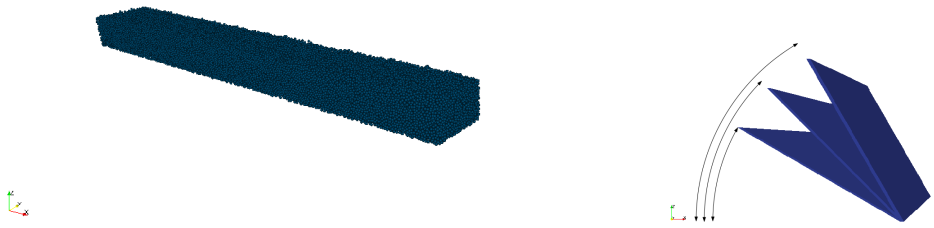

(a) (b)

Figure 5.9: The cuboid cohesive DEM soil sample (a) and the cutting blades with angles of 30°, 45° and 60° (b) used in the simulations

Table 5.3: Parameters used in the setup of Hatamura & Chijiiwa experiments and the numerical simulations for cohesive soil cutting

	Parameter	Symbol	Hatamura & Chijiiwa	Numerical Simulation	Units
Soil sample	thickness	t_s	0.25	0.6	[m]
	width	w_s	0.33	0.94	[m]
	length	l_s	1.5	11	[m]
	cohesion	c	15.7	20.5	[kPa]
	adhesion	a	-	7.1	[kPa]
Blade	length	l_b	0.2	1	[m]
	width	w	0.33	0.94	[m]
	angle	α_c	30°, 45°, 60°	30°,45°,60°	[-]
	cutting speed	v_c	0.05	0.05	[m/s]
	cutting depth	h_i	0.1	0.5	[m]
	h_b/h_i		1, 1.41, 1.73	1, 1.41, 1.73	[-]
Particles	medium radius	r_{50}	0.002	1.85	[cm]

5.4. Results & validation of simulations of cohesive soil cutting in atmospheric condition

5.4.1. Validation of the shear angle in the shear zone

In sand cutting, a clear shear plane is visible during the numerical simulations, as shown in Fig. 4.14, 4.15 and 4.16. However it is not the case in cohesive soil cutting simulations, the shear zone in cohesive soil cutting is much thicker, which makes it harder to identify a clear shear angle in the cutting zone. It is recommended by (Hatamura and Chjiiwa, 1976b) that one can connect all the most apparent deformation points to define the shear plane for cutting cohesive soil.

To find out the shear angles in the simulations of cohesive soil cutting process, Fig. 5.10, 5.11 and 5.12 depict the cutting patterns observed in the DEM simulations. These simulations are conducted with cutting depth of 0.5 m and the cutting speed of 0.05 m/s, and three blade angles of 30°, 45° and 60° respectively. In Fig. 5.10 to 5.12, the brighter color of the particles indicates higher velocities where the most remarkable deformation occurs. For comparison, the shear angles observed in the (Hatamura and Chjiiwa, 1976b) experiments with the same cutting angles have also been plotted out using the orange lines in the same graphs. (Hatamura and Chjiiwa, 1976b) concluded that shearing is the dominant failure mode in their clay cutting experiments, for which illustrations can be found in Fig. 2.8. They also claimed that the appearance of the cutting zone may insignificantly differ when the cutting angle changes: with lower cutting angles 30° and 45°, there are tearing occurred under the blade, while from the 60° cutting angle the failure completely follow the flow type, which is plastic.

From Fig. 5.10, 5.11 and 5.12, it can be witnessed that the shear lines observed in the DEM simulations approach the shear lines from the experiments. As the same as

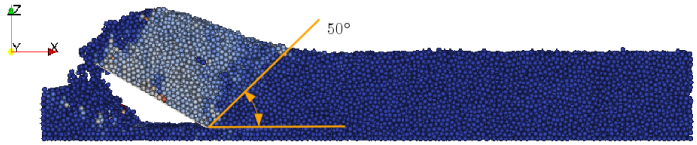

Figure 5.10: Cutting pattern observed in the DEM-simulation for a blade angle of $30°$, a blade speed of $0.05m/s$ and a cutting depth of $0.5m$. The orange line depicts the direction of the shear plane observed by (Hatamura and Chjiiwa, 1976a) when using the same cutting angle $(30°)$

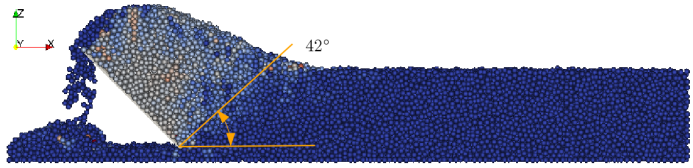

Figure 5.11: Cutting pattern observed in the DEM-simulation for a blade angle of $45°$, a blade speed of $0.05m/s$ and a cutting depth of $0.5m$. The orange line depicts the direction of the shear plane observed by (Hatamura and Chjiiwa, 1976a) when using the same cutting angle $(45°)$

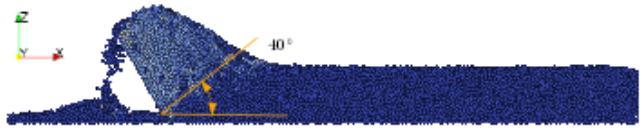

Figure 5.12: Cutting pattern observed in the DEM-simulation for a blade angle of $60°$, a blade speed of $0.05m/s$ and a cutting depth of $0.5m$. The orange line depicts the direction of the shear plane observed by (Hatamura and Chjiiwa, 1976a) when using the same cutting angle $(60°)$

the shear planes observed by Hatamura and Chijiiwa, the shear planes in the simulation stay in a constant position relative to the cutting blade irrespective of its proceedings. In Fig. 5.12, the shear line in the DEM simulation is not so obvious simply because of the high thickness of the shear zone.

It is noted that there is no clear tensile crack found in the simulations. Regarding this, (Hatamura and Chjiiwa, 1975) argued that the occurrence of the tear type in cohesive soil cutting is determined by the relation between the tensile strength σ_t and the cohesive shear strength c, only when $c > |\sigma_t|$, e.g., the compacted loam tested in their experiments, the cohesive soil can be cut in tear type.

However, in their own experiments for cutting of plastic loam where $c < |\sigma_t|$, tensile cracks have been witnessed underneath the blade, that is because the lower cutting angle makes the process more "penetrating" than "pushing" as in the case of higher cutting angle, and this offers significant help for the bifurcation of tensile cracks. On the contrary, when cutting clay with larger cutting angles, correspondingly there will be higher vertical compressive stress caused by adhesion in the soil. This compensates for the tensile stress, that is why no tensile crack can develop when cutting clay with big cutting angles.

So overall speaking, the occurrence of the tear type in clay cutting is not just determined by the material property or the blade angle. It is a combination of both the material properties ($c/|\sigma_t|$ ratio) and the geometry (blade angle, cutting depth and soil thickness) of the cutting zone. Based on this consideration, it is recognized that for developing the tear crack in clay cutting, there should be still a thick layer of soil underneath the blade, e.g., in the experiments of Hatamura and Chjiiwa. In DEM simulations, it will make the computation much heavier if an extra thick layer of particles is added at the bottom, besides, an extra bottom layer does not contribute to the cutting forces on the blade. Therefore, there is no extra bottom layer in the conducted simulations, and the blade has almost reached the bottom of the DEM soil sample. As a result, the tear crack can hardly develop.

5.4.2. Validation of the cutting forces

Besides the shear angles, the cutting forces on the surface of the blade are compared in the manner of stresses. The development for the normal cutting stresses on the blade obtained from the DEM simulations are depicted in Fig. 5.13.

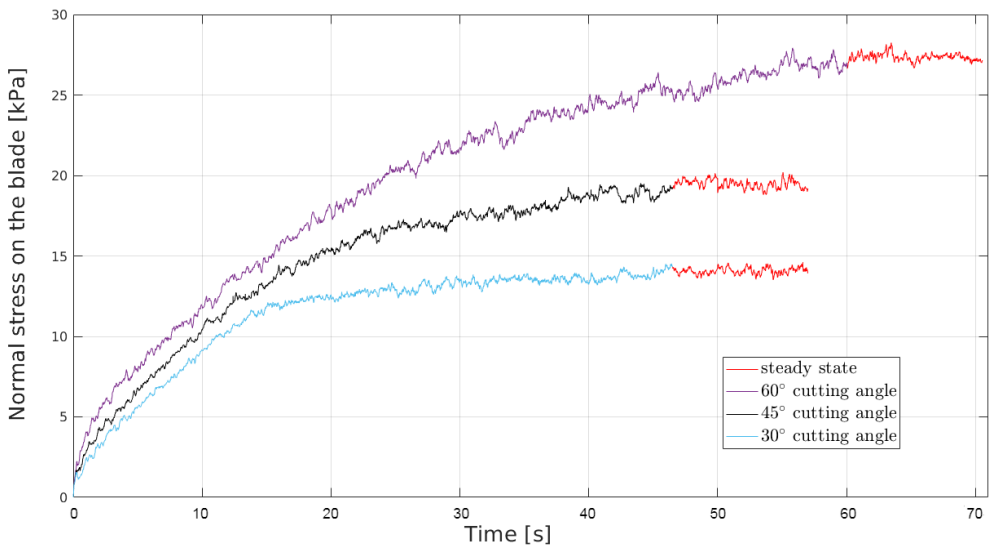

Figure 5.13: The measured normal stress on blade versus the cutting time as obtained from simulations. The blue line depicts the normal stress for a blade angle of 30°, the black line for a blade angle of 45° and the purple line for a blade angle of 60°. The highlighted red parts represent the steady states used in calculating the steady state blade stress.

A scaling relation based on Eq. (5.1) and (5.2) for the normal and shear stresses on the surface of the blade are derived. It is known that the h_b/h_i ratio and the α angle are set the same in both the experiment and the simulation. With the following assumptions:

1. the shear angle β in the simulation is the same as in the experiment (Fig. 5.10 to Fig. 5.12).
2. the adhesion factor α_{ac} in the Hatamura and Chjiiwa experiment is unknown, but it is assumed equal to the α_{ac} in the simulation.
3. the strengthening factor λ in the simulation is the same as in the experiment since cutting velocities are the same.
4. the ratio between the undrained shear strengths of the Hatamura & Chiijiwa plastic loam sample and the cohesive DEM soil sample $\frac{s_{u,H\&C}}{s_{u,DEM}}$ can be approximated by the ratio of cohesions of the two samples $\frac{c_{H\&C}}{c_{DEM}}$.

A simple scaling law can be established as Eq. (5.5). Using the scaling law, the overall stresses, the normal stresses and the shear stresses on the blade surface in all the DEM simulations have been scaled to the experiment scale and compared with the measurements from the (Hatamura and Chjiiwa, 1976b) experiments. The results are listed out in Table 5.4 and plotted in Fig. 5.14.

$$\frac{S_{H\&C}}{S_{DEM}} = \frac{s_{u,H\&C}}{s_{u,DEM}} \approx \frac{c_{H\&C}}{c_{DEM}} \tag{5.5}$$

Table 5.4: An overview of stresses on the blade for blade angles of $30°$, $45°$ and $60°$ at a cutting depth of $0.1m$ and blade speed of $0.05m/s$ obtained by (Hatamura and Chjiiwa, 1976b), and the scaled results obtained from the DEM-simulations.

	Hatamura & Chijiiwa Measurements			Scaled Results of DEM Simulations			Units
Blade angles	30	45	60	30	45	60	[°]
Normal stress S_n	10.2	14.2	25.2	10.8	14.9	20.9	[kPa]
Shear stress S_s	11.7	10.7	12.8	12.4	11.2	10.6	[kPa]
Overall stress $S_{overall}$	15.6	17.8	28.2	16.5	18.7	23.5	[kPa]
Error				5.7	5.1	-16.7	[%]

Fig. 5.13 shows the steady state cutting force is reached sooner for the $30°$ and $45°$ blades than for the blade with an angle of $60°$. Two reasons are behind this phenomenon:

- Although the blade length is the same, higher cutting angle does come with a higher cutting height, which makes it longer for the shear layer to climb over the blade when there is gravity present.
- For the $30°$ and $45°$ blades, the cutting is more like "penetrating" into the soil which makes the cohesive soil torn in chunks before the particles flow over the blade. While in the case of $60°$ blade, the soil is first pushed and compressed until a certain layer thickness is reached and then this layer thickness stays constant

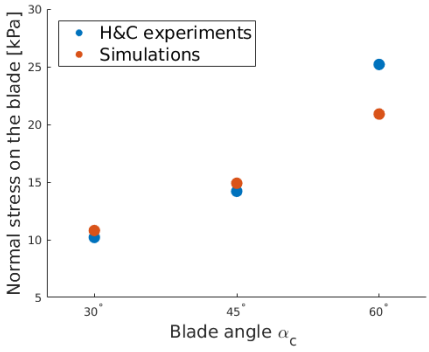

(a) Normal stress vs. α_c

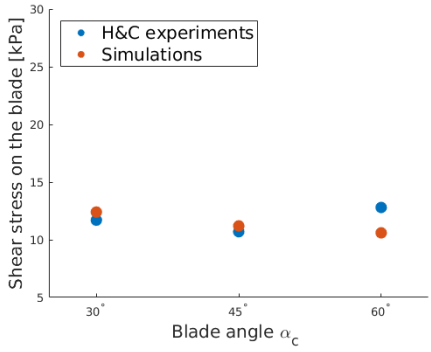

(b) Shear stress vs. α_c

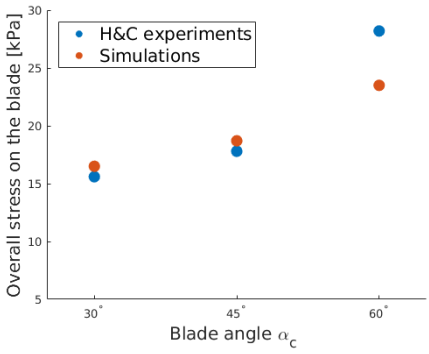

(c) Overall stress vs. α_c

Figure 5.14: Cutting stresses on the blade in the steady state measured from the Hatamura & Chiijiwa experiments versus the record from simulations

when the particles later climb over the blade. This leads to higher resistance force from the soil and also much longer time to reach the steady state.

From Table 5.4 it can be seen that in the cases of 30° and 45° cutting, the numerical cutting forces are 5 ∼ 6% higher than the experimental results, which could be seen as an acceptable error margins. At a blade angle of 60°, a 16.7% lower cutting force is measured from the numerical simulations than in the experiments, which indicates that the numerical model did not predict the cutting force successfully in this case.

The differences are possibly induced by the unknown adhesive strength of the plastic loam in the experiments. In (Chen et al., 2019a), a list of adhesion factors (α_{ac}) is reported based on many measurements, and a Linear-Exponential Correlation has been concluded by curve fitting the measurements of adhesion factor (α_{ac}) on undrained shear strength (s_u). The result shows that the lower the undrained shear strength (s_u) is, the higher the adhesion factor (α_{ac}) will be. In the (Hatamura and Chjiiwa,

1976b) experiments, the cohesion (c) of the plastic loam is 15.7 kPa, the undrained shear strength (s_u) is expected to be slightly higher than this value but should still be within 20 kPa. The reason is simply that there is a small internal friction angle detected by Hatamura & Chiijiwa in the plastic loam.

When the cohesive shear strength is below 20 kPa, the adhesion factor α_{ac} is very high, approaching 1. In the reports of Hatamura and Chjiiwa, they did not mention the adhesion factor of the tested plastic loam, but an educated guess can be made that its adhesion factor should be approaching to 1. So the adhesive shear strength of the plastic loam is expected to be around 15 kPa.

On the other hand, the cohesive shear strength of the numerical clay sample used in the DEM simulation is 20.5 kPa, according to the same assumption, the undrained shear strength of the numerical clay sample should then be slightly higher than 20.5 kPa. In this way, the adhesion factor for the cohesive DEM soil sample is around $7.1 \div 20.5 = 0.35$, so there is a high chance that the adhesion factor in the DEM simulation is much lower than that of the experiments.

In Eq. (5.1) and (5.1), with a lower α_{ac}, F_h will be smaller while F_v will be larger. When cutting with 30° and 45° blade angles, the two effects more or less cancels each other out. However, when cutting with 60° blade angle, the horizontal cutting force F_h becomes much more dominant in the overall force $F_{overall}$, so an underestimation of F_h in this circumstance leads to an underestimation of $F_{overall}$. As a result, $s_{overall}$ in the simulation is lower than in the experiments when cutting with 60° blade angle.

It is a pity that due to the lack of the information on the adhesive strength of the plastic loam used in (Hatamura and Chjiiwa, 1976b) experiments, the validation tests are not fully precise. However, the numerical results for the blade forces are still in the same order of magnitude as found in the experiments by Hatamura and Chijiiwa, and the tendencies of the blade forces versus the increasing cutting angles also match very well. Overall it can be concluded that the developed DEM model gives a good approximation of the total cutting forces on the blade in plastic loam cutting for at least small cutting angles.

5.5. Simulation set-up of cohesive soil cutting in underwater condition

Because there is insufficient data available for submerged cohesive soil cutting, either laboratory test or field test, it is decided to investigate fully saturated underwater cohesive soil cutting under typical conditions encountered in dredging operations. In modern day dredging, this means a blade angle between $50° \sim 55°$ at a dredging depth of $10 \sim 30m$ and high cutting speeds in the range of $1.5m/s$ up to $5m/s$.

For the simulations in the submerged condition, i.e., the fully saturated underwater environment, a new DEM clay sample is generated. The material properties are set

to be the same as used in the atmospheric cutting simulations, while the size of the sample is reduced to $11 \times 0.5 \times 1m$ so the thickness of the sample is now 0.5 m instead of 0.6 m, which was the case in Chapter 5.4. This change is made simply because the bottom 0.1 m does not contribute much to the cutting force but it needs a lot of computational effort to calculate the particles in that part. The input parameters can be found in Table 5.5.

Table 5.5: Parameters used in the setup of DEM simulations for underwater cohesive soil cutting

	Parameter	Symbol	Value	Units
Soil sample	thickness	t_s	0.5	[m]
	width	w_s	0.94	[m]
	length	l_s	11	[m]
	cohesion	c	20.5	[kPa]
	adhesion	a	7.1	[kPa]
	porosity	n	0.362	[-]
	permeability	κ	8.6×10^{-7}	$[m^2]$
Blade	length	l_b	1	[m]
	width	w	0.94	[m]
	angle	α_c	51.5°	[-]
	cutting speed	v_c	1.5, 3, 5	[m/s]
	cutting depth	h_i	0.5	[m]
	h_b/h_i		1.57	[-]
Particles	medium radius	r_{50}	1.85	[cm]
	minimum radius	r_{min}	2.2	[cm]
	maximum radius	r_{max}	1.5	[cm]

As shown by Table 5.5, a uniform PSD is applied with the minimum radius $r_{min} = 1.5cm$, the maximum radius $r_{max} = 2.2cm$ and the medium radius $r_{50} = 1.85cm$. Since there is no experimental data to make comparison, thus the sphericity coefficient ϕ_s is set as default, 1. The resultant permeability is $8.6 \times 10^{-7}\ m^2$. The simulations are performed at relatively high cutting speeds of $1.5m/s$, $3m/s$ and $5m/s$ respectively.

For the fluid phase, the viscosity of the fluid is set as $\nu_f = 1.787 \times 10^{-6}\ m^2/s$ and the gravitational acceleration is set as $g = -9.81\ m/s^2$. In the simulation domain, a hydrostatic pressure of $300kPa$ is present to simulate a dredging operation depth around 20 m. The initial conditions of the fluid are listed in Table 5.6. The boundary conditions of the fluid domain is set the same as Table 4.12.

Table 5.6: Initial properties used in OpenFOAM for underwater cutting simulations on cohesive soil

p_h	ρ_f	U_f	U_s	K_{sf}	ϵ_f
[kPa]	[kg/m^3]	[m/s]	[m/s]	[kg/(m^3·s)]	[-]
300	1000	(0 0 0)	(0 0 0)	0	1

5.6. Results & analysis of simulations of cohesive soil cutting in underwater condition

5.6.1. Analysis of the fluid flow field

The results of the submerged, i.e., fully underwater cohesive soil cutting simulations are discussed below. The fluid velocity field and the fluid pressure field found from the numerical simulation at a blade speed of $5m/s$ and a hydrostatic pressure of $300kPa$ are shown in Fig. 5.15 and 5.16 respectively. The many black dots represent the locations of the DEM soil particles. The background color in Fig. 5.15 represents the fluid velocity field, the range of the magnitude of the fluid velocity is indicated by dark blue for $0m/s$ to dark red for $5m/s$. The background color in Fig. 5.16 represents the fluid pressure field, the pressure range is indicated by dark blue for $290kPa$ to dark red for $340kPa$.

In Fig. 5.15 it can be found that the cutting mechanism is the flow type, which is expected at this cutting angle and such high cutting speed, and it is clear that the velocity of the fluid is at its highest magnitude near the cutting blade and gets smaller towards the top of the soil cut. This is a clear indication that the soil particles are sheared due to the high strain rates imposed by the cutting blade on the soil skeleton.

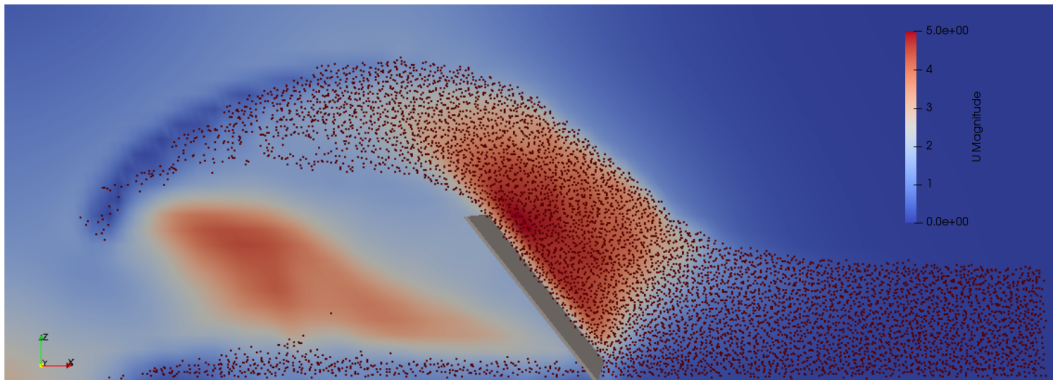

Figure 5.15: The fluid velocity field in saturated clay cutting with a 5 m/s blade at a hydrostatic pressure of $300kPa$. The range of the magnitude of the fluid velocity is indicated by dark blue for very low velocities ($0m/s$) and dark red for high velocities ($5m/s$).

Fig. 5.16 displays the fluid pressure field in the submerged cohesive soil cutting simulation at a cutting speed of $5m/s$ and a hydrostatic pressure of $300kPa$. The hydrostatic pressure is indicated in grey, low pressure zones in blue and high pressure zones in red. As the blade passes, the surrounding fluid is affected by the blade and gets a velocity unequal to 0. According to the Bernoulli's equation, this higher speed results in a lower static pressure behind the blade; hence the blue color in the zone behind the blade.

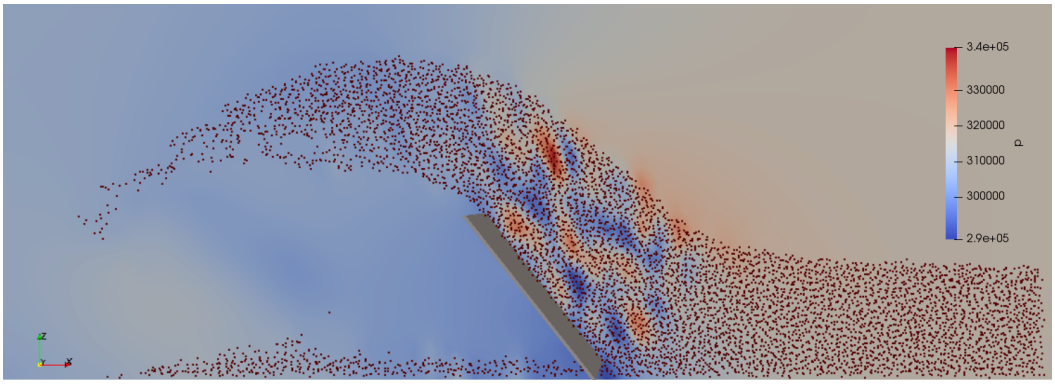

Figure 5.16: The fluid pressure field in saturated clay cutting with a 5 m/s blade at a hydrostatic pressure of $300kPa$. The pressure range is indicated by dark blue for very low value ($290kPa$) and dark red for high value ($340kPa$).

It has already been mentioned when analyzing the velocity field (Fig. 5.15) that the major shear plane develops between the shear layer and the virgin soil, apart from that in Fig. 5.16 it is found that in the shear layer (the cut part attached to the blade) there are also several smaller layers. The physical process is, during the shearing between the soil particles, the pore volume may increase due to dilatation or decreases due to compaction. This leads to pockets of water under pressure or water over pressure in the pores. With very high external loading rates, the fluid may not have enough time to flow into or out of the pores to reach the pressure equilibrium. Pressure gradients thus form up between in and out of the pores, combining with the hydrostatic pressure, a confining pressure is imposed on the soil, increasing the force required to cut. In this case (Fig. 5.16), the highest pressure gradient witnessed is $\nabla p = 340kPa/m$, which helps the DEM soil particles to resist against the deformation of the solid skeleton.

5.6.2. Analysis on the influence of the cutting speed on the cutting force

Fig. 5.17, 5.18 and 5.19 show the results for the normal stress development on the blade measured from the $1.5m/s$, $3m/s$ and $5m/s$ cutting simulations. The cutting forces are presented with stresses because the surface area of the blade has already been taken into consideration. The red line depicts the normal stress for cutting at atmospheric conditions and the black line for submerged cutting at a hydrostatic pressure of $300kPa$.

The values of the normal stresses in the steady cutting state have been recorded in Table 5.7, in which the ratios between the normal stress on the blade from the submerged simulations versus the atmospheric simulations are also listed out.

Fig. 5.17 shows the stress development at the lowest cutting speeds of $1.5m/s$, initially the normal stress recorded on the blade in submerged cutting is higher than

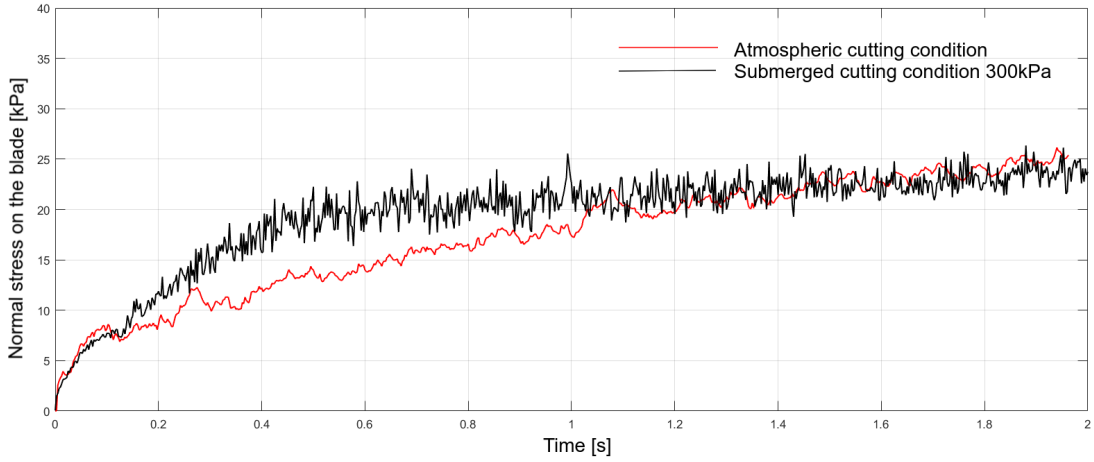

Figure 5.17: The normal stress on the blade recorded for cutting speed of $1.5m/s$. The red line depicts the normal blade stress for cutting at the atmospheric condition and the black line for the underwater condition at a hydrostatic pressure of $300kPa$.

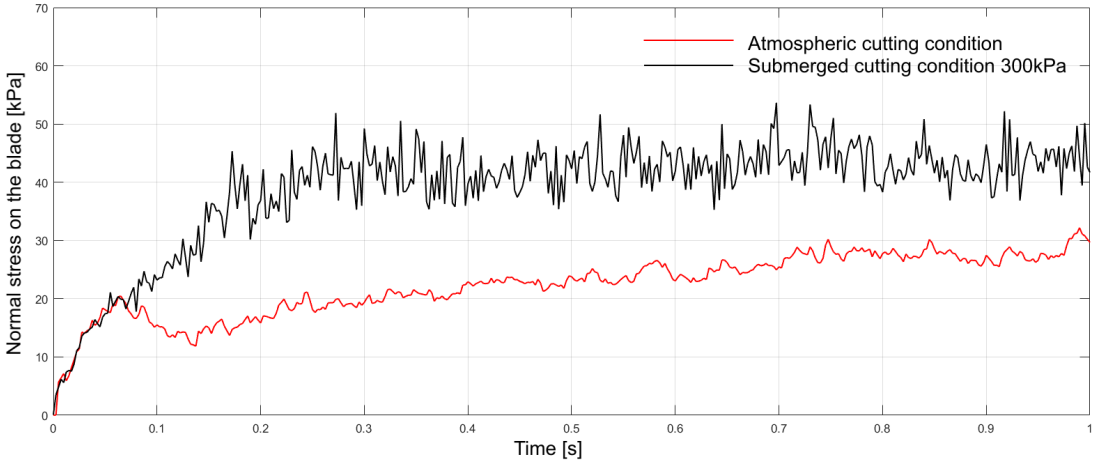

Figure 5.18: The normal stress on the blade recorded for cutting speed of $3m/s$. The red line depicts the normal blade stress for cutting at the atmospheric condition and the black line for the underwater condition at a hydrostatic pressure of $300kPa$.

that in atmospheric condition. But after 1.1 second both records reach the same value (23.5 kPa) in the steady state. The difference in the beginning is induced by a slightly underwater dilantancy hardening effect, where the pressure gradient force acting on the particles from the water makes the submerged DEM soil sample more difficult to excavate. Later in the steady state, since the cutting speed is not very high, it becomes a drained cutting process on loosened soil, hence the normal stress in submerged condition is equal to the normal force in atmospheric condition.

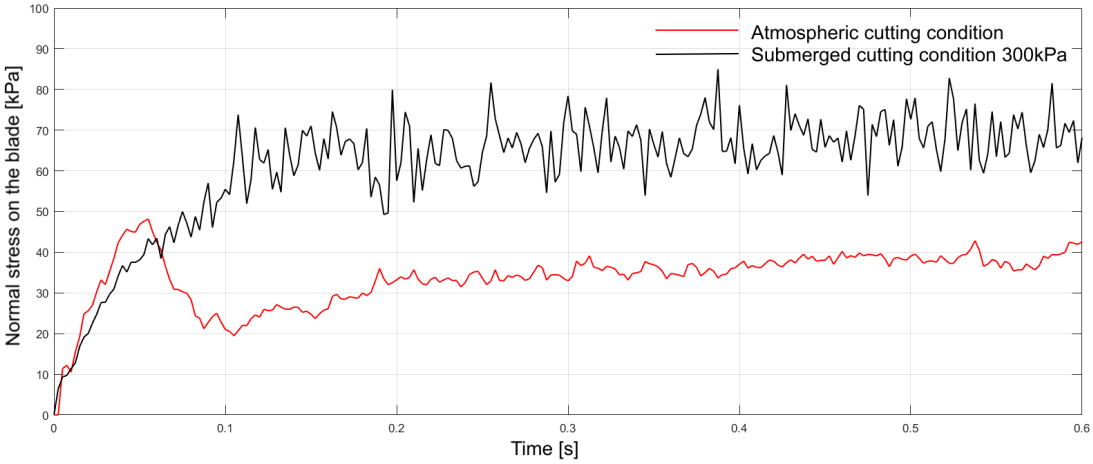

Figure 5.19: The normal stress on the blade recorded for cutting speed of $5m/s$. The red line depicts the normal blade stress for cutting at the atmospheric condition and the black line for the underwater condition at a hydrostatic pressure of $300kPa$.

Table 5.7: The normal stresses recorded on the blade in the steady cutting state from the simulations of atmospheric and submerged cohesive soil cutting, the S/A ratio is the ratio between the submerged measured stresses versus the atmospheric ones.

	Normal Stress on the Blade		
Cutting Speed	Atmospheric	Submerged	S/A Ratio
1.5 m/s	24.5 kPa	24.5 kPa	1
3 m/s	28.5 kPa	45 kPa	1.58
5 m/s	39 kPa	70 kPa	1.79

Fig. 5.18 depicts the normal stresses on the blade for cutting at a speed of $3m/s$ for both at the atmospheric and submerged conditions. The difference in this scenario is obvious. As introduced in Table 5.5, the porosity of the DEM soil sample is 0.362, indicating that initially the sample is quite compacted. Therefore, in the beginning of the cutting, the blade needs to loosen the interlocking in the soil sample to enable the shearing to occur. This process leads to the build-up of the dilatancy stress (particle-particle). This mechanism works both for the atmospheric and submerged conditions till 0.067 second (Fig. 5.18). After that, there are two story-lines developed, as discussed below.

1. In the atmospheric cutting, since there is no surrounding water to provide the confinement, this dilatancy stress (particle-particle) is dissipated, as it can be seen that from 0.067 to 0.133 second there is a decrease in the atmospheric cutting force (the red line). After 0.133 second the atmospheric cutting force gradually increases, approaching a stable value (27.5 kPa). The start point of the steady state is marked as the moment when DEM particles have climbed over the top of the blade and falling down to the back of the blade.

2. In submerged cutting the process is different. Unlike in the $1.5m/s$ cutting test, this time the cutting speed is higher, $3m/s$. This high cutting speed makes the cutting an undrained process. The difference lies in that when shearing occurs, the pore volume tends to increase, and that has different consequences in different cutting scenarios:

   - If it is an atmospheric cutting, the particles will just be loosened;
   - If it is submerged cutting but with relatively small cutting speed ($1.5m/s$), then the surrounding water has enough time to flow into the pores in the cut layer, so that the pressure equilibrium can be quickly rebuilt, and that can be considered as the drained cutting process;
   - If the cutting speed is rather high, like in this scenario ($3m/s$), the surrounding water does not have enough time to fill the pores, resulting in a much higher pressure gradient force from the surrounding water towards the cut layer. Hence although the layer on the blade has already been cut, it still remains compacted.

In conclusion, the pressure gradient force (fluid-particle) and the dilatancy stress (particle-particle) which cannot be dissipated, make the cutting force in submerged condition much larger than in atmospheric condition. The ratio between the submerged and the atmospheric cutting stresses is 1.58.

Fig. 5.19 depicts the normal stress developments on the blade for cutting at a speed of $5m/s$, where the same principle applies. In the atmospheric condition, a first build-up and then dispersion of the dilatancy stress (particle-particle) have again been witnessed. The recorded stress in the beginning (till 0.067 s) is even higher than in the submerged condition. The reason is very simple. In atmospheric cutting, there is only particle-particle contacts in the soil, so this is a fully drained process. Correspondingly the effective stress is higher, thus the resistance force on the blade is higher. On the contrary, in underwater condition, parts of the external loads are borne by the water pore pressure, thus the effective stress is lower, resulting in lower resistance force on the blade.

In the submerged cutting simulations, because of the higher loading rates at $5m/s$ compared to $3m/s$, the pressure gradient between the environment and the cut layer is even higher. As mentioned before, the observed pressure gradient in the shear zone is in the order of $10^{-1} - 10^{0} MPa/m$, resulting in significant increase in the normal force and thus in the total force on the blade. This pressure gradient force helps to keep the cut layer in a densely compacted form so that the build-up dilatancy stress cannot be dispersed. These factors result in a bigger difference between the cutting forces at atmospheric conditions and saturated conditions. The detected force ratio is 1.79 in this case.

The simulation results are also plotted in Fig. 5.20, and curve fittings have been plotted together with the measurements.

Clay is the most representative cohesive soil. According to Van der Schrieck (2012),

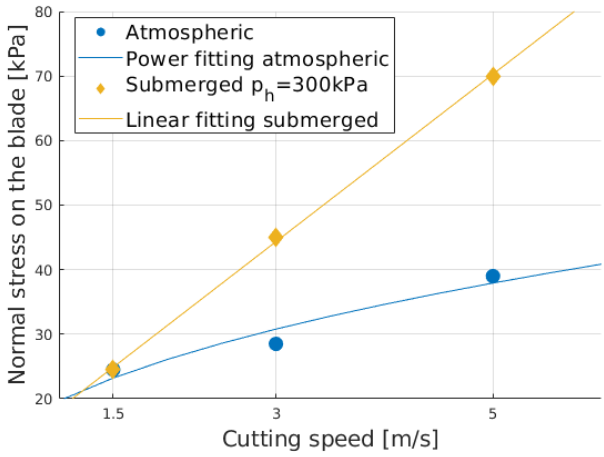

Figure 5.20: The normal stresses recorded on the blade in the steady cutting state from the simulations of atmospheric and submerged cohesive soil cutting. The straight line represents the linear regression on the submerged cutting measurements, while the curve line represents the power regression on the atmospheric cutting measurements.

in the dredging industry an empirical relation exists between the clay cutting force and cutting speed, as shown below:

$$F_{clay} \propto v_c^b \quad with \quad b = 0.1 \; - \; 0.3 \tag{5.6}$$

In Fig. 5.20, for submerged cutting simulations, this relation is almost linear ($F_{clay} \propto v_c^1$). The cutting force increases much faster with the cutting speed in comparison with Eq. 5.6. This 'cutting force - cutting speed' relation from the simulations does not resemble clay cutting behavior. It actually resembles sand cutting behavior (Fig. 4.64). The main reason is that the permeability of the cohesive DEM soil sample is too high ($8.6 \times 10^{-7}\ m^2$). While in nature clay's permeability is usually in the range of $10^{-18} - 10^{-13}\ m^2$. As mentioned before, there is no experimental data available to validate the submerged cohesive soil cutting simulation, yet from the atmospheric cutting experiments of (Hatamura and Chjiiwa, 1976b) there is no information on the permeability of plastic loam they used, so the permeability of the numerical sample has not been tuned beforehand.

With such a high permeability, the underwater dilatancy hardening effect, plays an important role in the overall resistance against cutting. In cutting process with high cutting speeds (3 and 5 m/s), the pressure gradient force (fluid-particle) makes the submerged cutting forces much larger than the atmospheric cutting forces. While at a low cutting speed (1.5 m/s), the cutting forces of atmospheric and submerged cutting simulations are the same simply because this is a fully drained process.

In Fig. 5.20, for atmospheric cutting simulations, $F_{clay} \propto v_c^{0.4}$, the b value is slightly higher than in Eq. 5.6. It indicates that, without the influence of the fluid flow, the

"cutting force - cutting speed" relation on the cohesive DEM soil sample is actually quite close to real clay.

It has also been mentioned that a dissipation of the dilatancy stress may occur in atmospheric cutting process. In Fig. 5.13 it is noticed that at very low cutting speed (0.25 m/s), there is no dissipation. At 1.5 m/s cutting speed (Fig. 5.17), a slight dissipation can be observed at around 0.1 second when the atmospheric cutting force drops from above the submerged cutting force to below the submerged cutting force. At even higher cutting speeds (3 and 5 m/s), the dissipation of the dilatancy stress is very obvious (Fig. 5.18 and 5.19).

5.7. Conclusions and recommendations

Cohesive DEM soil sample can be created by using the Simplified Johnson-Kendall-Roberts (SJKR) cohesion model. The internal shear strength of the sample can be calibrated by the direct shear tests using the ring shear device, and the external shear strength can be tested by the blade pull-out tests. The results of these tests show a clear cohesion, a clear internal friction angle, a clear adhesion and a clear external friction angle. It proves that these two tests satisfy the need for calibrating the major mechanical properties of the cohesive DEM soil sample.

The developed DEM model is validated using the cutting experiments conducted on plastic loam by (Hatamura and Chjiiwa, 1976b). Although the created cohesive DEM soil sample does not precisely match the mechanical properties of the plastic loam, via using the scaling law, the results obtained by the developed DEM model match with the results found by Hatamura and Chijiiwa within acceptable error margins. The difference is mainly induced by the mismatch of the unknown adhesion of the plastic loam in the Hatamura and Chjiiwa (1976b) experiments and the adhesion obtained from the numerical samples.

Comparisons are made between atmospheric and submerged cutting simulations with various cutting speeds. The "cutting force - cutting speed" relation obtained from atmospheric cutting simulations approaches the empirical relation from clay cutting practice. It is also concluded from the atmospheric cutting simulations that a first build-up and then dissipation process of the particle-particle dilatancy stress can occur when certain cutting speed is reached (around 1.5 m/s) and the initial soil body is densely compacted.

On the contrary, the "cutting force - cutting speed" relation obtained from submerged cutting simulations shows a large difference from the empirical relation. The story behind is that, because there is no experimental data available for validating the submerged cutting process on cohesive soil, the permeability of the cohesive DEM soil sample has not been calibrated in advance, so the permeability of the cohesive DEM soil sample is much higher than that of natural clay. As a result, high pressure gradient force appears with high cutting speed, leading to much higher cutting force, compared with the cutting force from empirical equation (Eq. (5.6)).

It should be mentioned that very big particles compared to real soil grains are used to reach the desired order of magnitude for the undrained shear strength and cohesion of the cohesive DEM soil sample, it is recommended in further research to investigate the influence of the cohesive energy density K on the global cohesion, to enable the usage of millimeter level DEM particles.

It is also a pity that the validation of atmospheric cutting process is not complete due to the fact that there is no information available on the adhesion of the plastic loam cut in the (Hatamura and Chjiiwa, 1976b) experiments, it is thus recommended in the future to conduct cohesive soil cutting experiments on the premise that all the mechanical properties of the soil sample are known, so that more comprehensive validation can be carried out.

There is no validation on submerged cutting process of cohesive soil due to the lack of experimental data. It is recommended in future research, to conduct submerged cohesive soil cutting experiments where all the necessary mechanical properties are measured in advance (permeability, cohesion, adhesion, undrained shear strength and etc.). After that, numerical modelling can be carried out with proper calibrations.

Overall speaking, it is believed that via proper calibration tests, the DEM-FVM coupling model for cohesive soil can be applied for predicting the cutting force and describing the physics in both atmospheric and submerged cutting processs.

6

General Applicability and Scaling Tests on DEM Rock Samples

This chapter first discusses on the general applicability of using DEM to create rock samples, and then the relevant scaling laws between the input parameters on the micro scale (particle size) to the output mechanical properties on the macro scale (samples' size), which forms up the calibration work of DEM rock samples. For testing the general applicability, three types of rock samples, weak, medium strength and strong, are created respectively and compared with real rock mechanical properties.

For developing the scaling law, the methodology introduced in Chapter 3.4.3 is implemented. The correlation between the particle bond strengths ($\bar{k}_n$, $\bar{k}_s$), the particle bond Young's Modulus $\bar{E}_c$ and the apparent macroscopic compressive and tensile strengths (σ_c, σ_t), are established.

6.1. Selection between the static and dynamic DEM rock sample generation methods

In Chapter 3.4.2, both the static and dynamic generation methods for DEM rock sample have been introduced. For conducting the scaling tests for rock properties, representative 3D DEM samples are the premises. In this section, simple uni-axial compression tests are carried out to make a selection between the static method, i.e., the Lozano method (Lozano et al., 2016), and the dynamic method, i.e., the Potyondy method (Potyondy and Cundall, 2004). The aim is to create a rock sample by DEM with a similar porosity as described in (Grima et al., 2015).

The designated porosity is 37.9%. The test samples are created to be cylinders with the height 63.4mm and the diameter of the cross-section 31.7mm, simply because it is the size used in (Potyondy and Cundall, 2004). The results show that, using the Potyondy method, this designated porosity can be reached. On the contrary, using the Lozano method, the designated porosity cannot be reached.

With the Lozano method, initially d_{max}/d_{min} was set to 1.66, which is the same as set in (Potyondy and Cundall, 2004), in this way the smallest porosity obtained is 44%. To reach a smaller porosity, d_{max}/d_{min} is then set to 2.0, thereafter the porosity obtained is 42%. It is not reasonable to try even bigger d_{max}/d_{min}, otherwise there will be too many small particles in the sample so that the integrity of the sample is damaged. With the sample of a 42% porosity, a good coordination number, 6, was achieved. This sample, generated by the Lozano method, is tested in the UCS test, the result turns out to be disappointing. As shown in Fig. 6.1, the particles just run away when the top plate is loading downwards. The reasons are:

1. the sample is too loose and there is too much space inside the structure for compression, thus the sample cannot hold enough resistance against the external loads;

2. unlike in the Potyondy method, the particles in the Lozano method have no overlap with each other, i.e., there is no pre-stress existing in the sample, that results in the particles tend to slip over each other instead of shearing when the plate is loading from the top side.

In conclusion, the question from Chapter 3.4.2, "*which generation method to use?*", is answered here. The static generation method from Lozano et al. (2016) cannot be used for creating rock samples though it is relatively faster. The dynamic generation method from Potyondy and Cundall (2004) is chosen for creating rock samples in this research. In the rest of the chapter, all the DEM rock samples tested are created with the dynamic generation method.

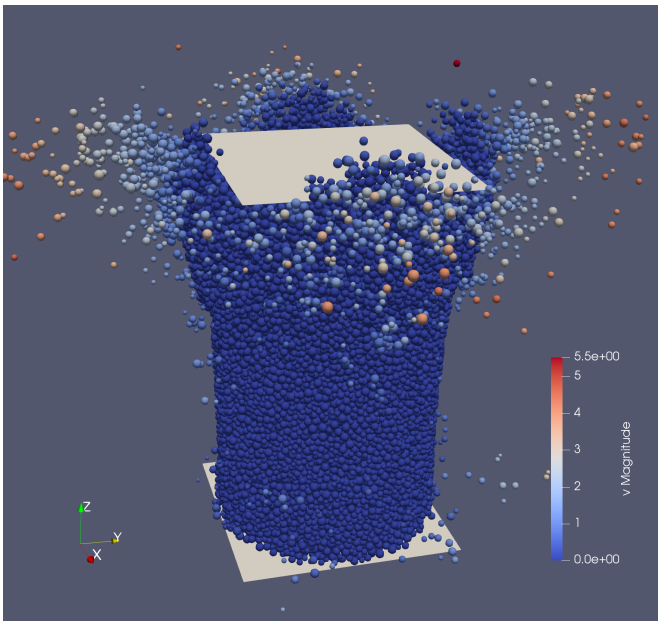

Figure 6.1: Uniaxial compression test on the rock sample generated by the Lozano method

6.2. General applicability of using DEM for rocks

In (Potyondy and Cundall, 2004), the parallel bond model (PBM) has been applied to both 2D and 3D simulations to test the mechanical properties of rock samples. In recent years, the application of PBM in 2D simulations has been reported in a variety of literature. For example, (Shi et al., 2015), (Yin and Yang, 2019) and etc. However, there are few publications available about the performance of PBM in 3D simulations of UCS and BTS tests on rock. Potyondy and Cundall (2004) simulated the compression test of the Lac du Bonnet granite, a very strong rock with the UCS of 200 MPa. In this research, as the starting point of testing the implementation of the PBM into LIGGGHTS, it is decided that the general applicability of the model should be tested via trying rock samples with different strength ranges. Because rocks with big difference in strengths frequently also come with different ductility number/brittleness index. For example the Lac du Bonnet granite recorded by Potyondy and Cundall (2004) has a brittleness index of 21.5, while a much weaker rock, the Savonnieres limestone recorded by Grima et al. (2015) only holds a brittleness index of 9. Therefore it brings the question if the PBM is also capable of simulating more ductile rock mechanical behaviour.

Hence three rock samples are picked out from the literature, the Savonnieres limestone from Grima et al. (2015) representing the weak/low strength rock (UCS = 7.92 MPa), the oil shale from Shen et al. (2018) representing medium strength rock (UCS = 21 MPa) and the Lac du Bonnet granite from Potyondy and Cundall (2004) representing the strong/high strength rock (UCS = 200±22 MPa). The mechanical properties

Table 6.1: Rock properties recorded by Grima et al. (2015), Shen et al. (2018) and Potyondy and Cundall (2004)

Rock	UCS σ_c [MPa]	BTS σ_t [MPa]	Young's Modulus E_c [GPa]	Poisson's Ratio ν	Porosity n
Low strength Limestone	7.92	0.88	5.95	0.31	37.86%
Medium strength Oil shale	21	1.1	12.6	0.21	unknown
High strength Granite	200	9.3	72	0.26	unknown

of the rock can be found in Table 6.1. Correspondingly, the input parameters used in the DEM simulations are listed out in Table 6.2.

In Table 6.2, the number of particles of the UCS and the BTS samples are not fixed, it is because for each test, there are three samples used. Due to the randomness and the uncertainty of the generation process, as introduced in Chapter 3.4.2, the final number of particles in the sample may have some small variations, even the procedure and input parameter do not change.

Fig. 6.2a shows one of the samples used for conducting the compression test and Fig. 6.2b shows one of the samples in the Brazilian tensile test, in which the color of the particle indicates its radius. When the radii of the particles increase, the colour ranges gradually from blue to red. Besides, the plates used as the loading body and the fixed bottom are both square surfaces with triangular meshes. They are used to track the force and stress evolutions, as shown in Fig. 6.3.

Each test is conducted three times, and the average of the three is recorded and shown below in Table 6.3. The simulations have described the rock failure behaviour very realistically and spontaneously. In the compression tests, the downward moving plate applies force to the rock sample, due to the irregularity inside the solid structure, the propagation of the force is not evenly distributed. The loading goes through the rock sample in the manner of the force/stress wave. By grading the particles´ colour with its velocity magnitude, the frontier of the force wave can be clearly seen. It is also found that the stress concentration happens from time to time. If locally there is a stress concentration, then in the following timesteps, a force/stress wave will spread from this concentration spot and the concentration will gradually fade out until it disappears. Some snapshots are obtained from the simulation to help illustrate the process. In Fig. 6.4, a stress concentration can be witnessed near the bottom of the sample, the process of initiation, expansion, decay and disappearance is tracked.

According to Table 6.3, in general the simulated UCS values are within acceptable ranges compared to the real rock samples. Concerning the other simulated mechanical

Table 6.2: Input Parameters for the UCS simulations to test the general applicability on three different-strength rock samples

Parameters	Symbol [Units]	Weak	Medium	Hard
UCS test sample height	L [mm]	64	64	64
UCS test sample diameter	D [mm]	32	32	32
BTS test sample thickness	L_1 [mm]	16	16	16
BTS test sample diameter	D_1 [mm]	32	32	32
UCS test sample number of particles	n_p	44918~ 45033	44918~ 45033	44918~ 45033
BTS test sample number of particles	n_{p1}	12437~ 12541	12437~ 12541	12437~ 12541
Sample porosity	n	35%	35%	35%
Maximum particle diameter	d_{max} [mm]	1.33	1.33	1.33
Minimum particle diameter	d_{min} [mm]	0.8	0.8	0.8
Mean particle diameter	d_{avg} [mm]	1.06	1.06	1.06
PSD ratio	d_{max}/d_{min}	1.66	1.66	1.66
Particle density	ρ_p $[kg/m^3]$	2780	2100	2630
Contact & Bond Young's modulus	E_c, $\bar{E}_c$ [GPa]	5.95	12.6	72
Particle stiffness' s ratio	k_n/k_s, $\bar{k}_n/\bar{k}_s$	3.1	3.1	3.1
Internal friction coefficient (particle-particle)	μ_p	0.57	0.57	0.57
External friction coefficient (particle-wall)	μ_e	0.36	0.36	0.36
Loading speed	v [mm/s]	5	5	5
Simulation time step	Δt [s]	10^{-7}	10^{-7}	10^{-7}
Size of the loading & bottom plates	A_{plate} $[mm^2]$	32×32	32×32	32×32
Bond strength in normal direction	T_n [MPa]	7.92	21	200
Bond strength in shear direction	T_s [MPa]	7.92	21	200

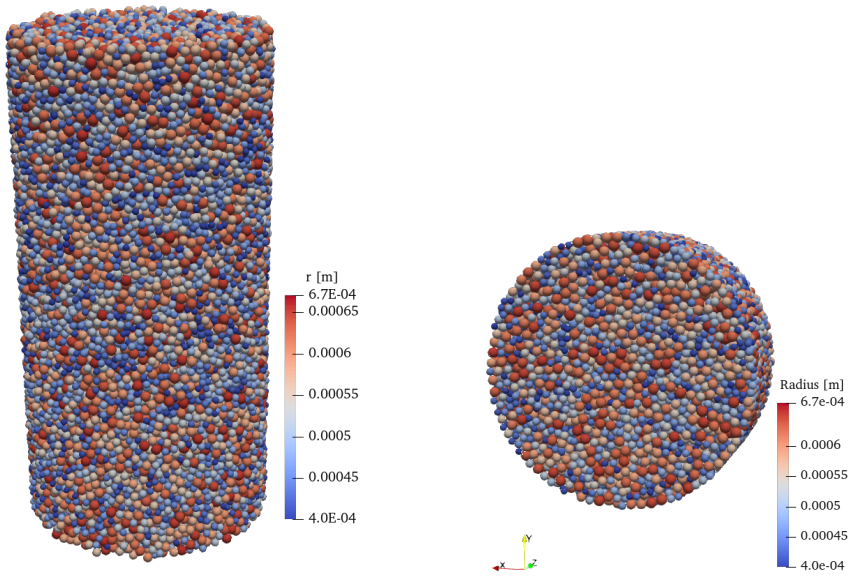

Figure 6.2: Cylindrical Rock Sample in DEM for the UCS (a) and BTS (b) tests (Colour profile shows different particle radii).

properties, the BTS values match well for weak and medium rock, but show a significant overestimation for the hard rock, besides the Young's Modulus and the Poisson's ratio are not matching very well, but they are still within reasonable ranges. So it can be concluded that the Parallel Bond Method (PBM) has the general applicability so that it can be used for modelling the mechanical behaviour of rocks with various strengths.

6.3. Scaling between the Young's modulus - bond strength ratio and the rock samples' strengths

In the previous section, the general applicability of DEM in simulating rock behaviour has been proven. The next step is to develop the scaling law, where a series of UCS and BTS tests are conducted. Again the three types of rocks from the literature, the Savonnieres limestone from Grima et al. (2015) representing the weak/low strength rock (UCS = 7.92 MPa), the oil shale from Shen et al. (2018) representing medium strength rock (UCS = 21 MPa) and the Lac du Bonnet granite from Potyondy and Cundall (2004) representing the strong/high strength rock (UCS = 200 MPa), are used as the reference materials. The general methodology has been explained in Chapter 3.4.3, several input parameters are determined beforehand, the friction coefficient between particles is set to be $\mu_p = 0.57$ ($\phi = 30°$). The average particle diameter is set to be

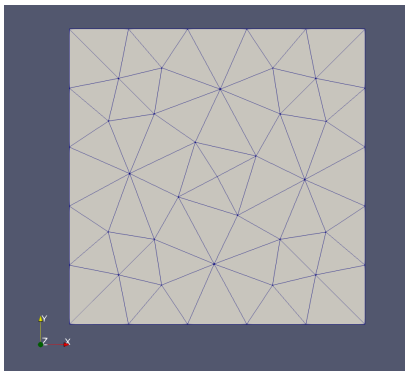

Figure 6.3: Loading Plate used in the Simulations of the UCS and the BTS tests

Table 6.3: UCS and BTS tests results on weak, medium and hard rocks in DEM simulations

		σ_c [MPa]	σ_t [MPa]	E_c [GPa]	ν
Weak	Original	7.92	0.88	5.95	0.31
	Simulated	7.3	0.72	3.4	0.10
Medium	Original	21	1.1	12.6	0.21
	Simulated	20.2	0.9	16.7	0.13
Hard	Original	200	9.3	72	0.26
	Simulated	194.4	15.85	85	0.18

$1/30$ of the diameter of the rock sample, $D_{avg} = D/30$. Apart from that, important relations are pending to be established between the micro-input and the macro-output. In (Potyondy and Cundall, 2004) it is set that for the DEM particles, $E_c = \bar{E}_c =$ *the measured Young's modulus*, and bond strengths $T_n = T_s =$ *the expected UCS*. However, from their simulation results, the obtained tensile strength of the DEM sample, σ_t, is much larger than the BTS of the real rock sample, which indicates that the T_n is set too high. To figure out the relation, in this research, the following equation is generated,

$$T_n = T_s = \bar{E}_c/(\frac{\bar{E}_c}{T_n}) \tag{6.1}$$

The $\frac{\bar{E}_c}{T_n}$ ratio, is used as one of the tuning factors to build up the scaling law from micro to macro scale. As mentioned before in Chapter 3.4.3, this section focuses on the $\{\frac{\bar{E}_c}{T_n}, \frac{\sigma_c}{T_n}\}$ and the $\{\frac{\bar{E}_c}{T_n}, \frac{\sigma_t}{T_n}\}$ scaling relation. The following values are tested for the $\frac{\bar{E}_c}{T_n}$ ratio: 100, 250, 500, 750, 1000 and 1250. The input parameters from Table 6.2 are inherited excerpt for the bond strengths in the normal and shear directions.

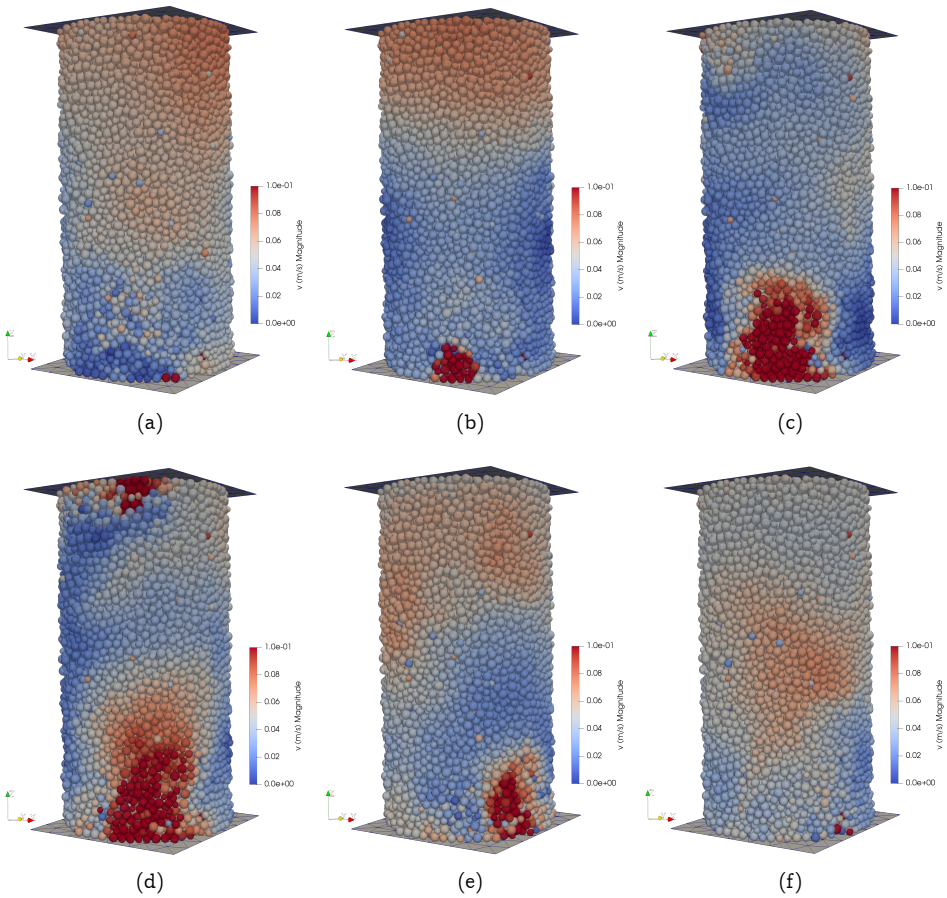

Figure 6.4: Stress concentration in the weak rock simulation and force/stress wave propagation (time sequence: from top to bottom, from left to right)

Table 6.4: Peak stresses from the plates

$\bar{E}_c/T_n$	Top plate SL (MPa)	Bottom plate SL (MPa)	Top plate DL (MPa)	Bottom plate DL (MPa)
300	11.273	11.241	11.279	11.259
550	9.753	9.740	9.789	9.794
800	7.220	7.183	7.240	7.260
1050	5.150	5.140	5.160	5.180

However, before testing for the scaling laws, two special UCS simulations on the weak rock samples are made to test the homogeneity of the generated rock sample. That is: one simulation is conducted by only letting the top plate moving downwards with 5mm/s, referred as single loading (SL), the other simulation is carried out by letting the top plate moving downwards with 2.5mm/s and the bottom plate moving upwards also with 2.5mm/s, referred as double loading (DL). If the samples have good homogeneity in the vertical direction, then the results from these two simulations should be the same or very close to each other. Because the purpose is to test the homogeneity of the rock sample, some special $\frac{\bar{E}_c}{T_n}$ ratio, other than the ones mentioned in the previous section, are adopted. They are 300, 550, 800 and 1050.

The peak stresses from the top and bottom plates when major breakage occurs have been recorded for both the single loading scenario and the double loading scenario in Table 6.4. It can been seen that with a fixed $\frac{\bar{E}_c}{T_n}$ ratio, the peak stresses from the top and bottom plates, no matter it is in single or double loading scenario, are almost identical. The registered σ_{peak} in the double loading scenario are all slightly higher than in the single loading scenario. In the single loading scenario, the top plate always holds higher σ_{peak} than the bottom plate, while in the double loading scenario there is no fixed pattern. Overall speaking, the difference between the single loading and the double loading scenarios are negligible. It indicates that the Potyondy method does have the advantage over the gravitational deposition method (DEM Solutions, 2016) since it keeps the homogeneity of the DEM sample in the vertical direction.

Since the differences between the σ_{peak} obtained from the single and the double loading scenarios are insignificant, thus it is determined that using the single loading method, is valid for obtaining the UCS and BTS values of the DEM rock samples. A series of UCS and BTS simulations have been carried out with various $\bar{E}_c/T_n$ values, afterwards, by averaging the σ_{peak} between the top and bottom plates, the UCS value σ_c and the BTS value σ_t for each sample are obtained and displayed in Table 6.5.

In Fig. 6.5 and 6.6, the σ_c obtained from the numerical simulations (scattered marks) is plotted together with the a polynomial fitting curve (solid line), and the laboratory measurements (dotted line). Correspondingly, the $\{\frac{\bar{E}_c}{T_n}, \frac{\sigma_c}{T_n}\}$ relation is plotted in Fig. 6.6, together with a power regression fitting curve. The polynomial fitting for

Table 6.5: Results of the UCS and BTS simulations on three sets of rock samples under various $\bar{E}_c/T_n$ ratios

	E_c / T_n	100	250	300	360	500	550	600	750	800	1000	1050	1250
Weak rock	E_c [GPa]	5.95	5.95	5.95		5.95	5.95		5.95	5.95	5.95	5.95	5.95
	T_n [MPa]	59.5	23.8	19.8		11.9	10.8		7.92	7.44	5.95	5.67	4.74
	σ_c [MPa]	6.5	9	11.26		10.55	9.8		7.3	7.2	5.45	5.15	4.5
	σ_t [MPa]	2.46	2.25	1.27		1.14	0.75		0.72	0.55	0.51	0.33	0.32
	σ_c/σ_t	2.64	4	8.87		9.25	13.07		10.18	13.09	10.69	15.85	14.06
	σ_c/T_n	0.11	0.38	0.57		0.89	0.91		0.92	0.97	0.92	0.91	0.95
	σ_t/T_n	0.04	0.09	0.06		0.1	0.07		0.09	0.07	0.09	0.06	0.07
Medium rock	E_c [GPa]	12.6	12.6			12.6		12.6	12.6		12.6		12.6
	T_n [MPa]	126	50.4			25.2		21	16.8		12.6		10.08
	σ_c [MPa]	18.7	24.1			21.4		20.2	17.5		15.9		14.3
	σ_t [MPa]	3.8	1.56			1		0.9	0.675		0.56		0.42
	σ_c/σ_t	4.92	15.4			21.6		22.4	25.9		28.4		34
	σ_c/T_n	0.15	0.48			0.85		0.96	1.04		1.26		1.42
	σ_t/T_n	0.03	0.031			0.039		0.042	0.042		0.044		0.042
Hard rock	E_c [GPa]	72	72		72	72			72		72		72
	T_n [MPa]	720	288		200	144			96		72		57.6
	σ_c [MPa]	103.7	163.8		194.4	224			179.9		144		91.2
	σ_t [MPa]	26	21.6		15.85	9.35			8.15		4.9		3.1
	σ_c/σ_t	4	7.6		12.3	24			22.1		29.4		29.4
	σ_c/T_n	0.14	0.57		0.97	1.56			1.87		2		1.58
	σ_t/T_n	0.036	0.075		0.08	0.065			0.085		0.068		0.054

σ_c and the power regression fitting for $\frac{\sigma_c}{T_n}$ are given by Eq. (6.2) and (6.3) respectively.

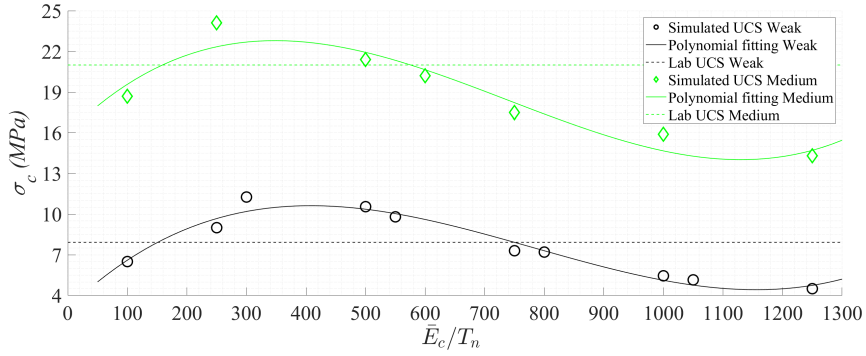

(a)

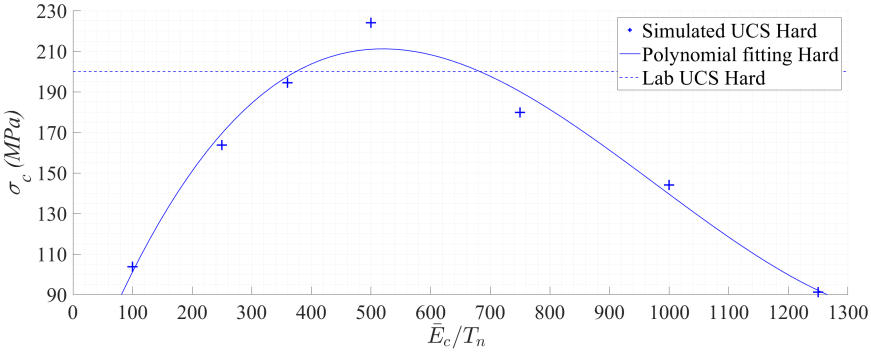

(b)

Figure 6.5: Unconfined compressive strength σ_c obtained from the simulations, the curve fittings and the laboratory experiments vs. the $\bar{E}_c/T_n$ ratio, a) the weak and medium rocks, b) the hard rocks

$$\sigma_c\ [MPa] = \begin{cases} 2.96 \cdot 10^{-8} \cdot (\frac{\bar{E}_c}{T_n})^3 - 6.95 \cdot 10^{-5} \cdot (\frac{\bar{E}_c}{T_n})^2 + 0.04 \cdot (\frac{\bar{E}_c}{T_n}) + 3.08, & \text{for weak rocks} \\ 3.68 \cdot 10^{-8} \cdot (\frac{\bar{E}_c}{T_n})^3 - 8.12 \cdot 10^{-5} \cdot (\frac{\bar{E}_c}{T_n})^2 + 0.04 \cdot (\frac{\bar{E}_c}{T_n}) + 16, & \text{for medium rocks} \\ 3.49 \cdot 10^{-7} \cdot (\frac{\bar{E}_c}{T_n})^3 - 10^{-3} \cdot (\frac{\bar{E}_c}{T_n})^2 + 0.78 \cdot (\frac{\bar{E}_c}{T_n}) + 33.2, & \text{for hard rocks} \end{cases} \quad (6.2)$$

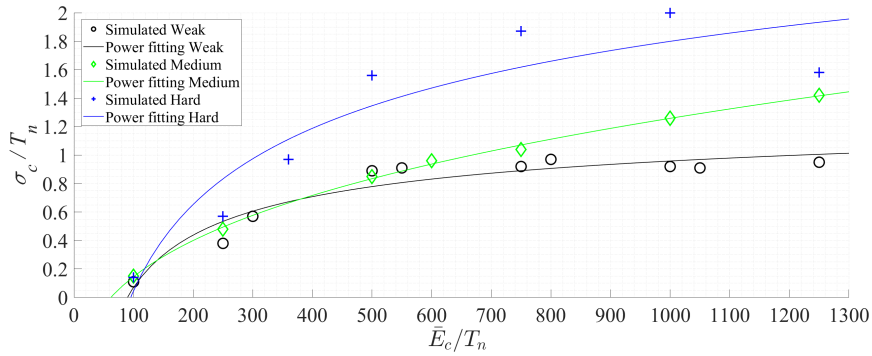

Figure 6.6: the $\{\frac{\bar{E}_c}{T_n}, \frac{\sigma_c}{T_n}\}$ relations with curve fittings

$$\frac{\sigma_c}{T_n} = \begin{cases} -10.69 \cdot (\frac{\bar{E}_c}{T_n})^{-0.44} + 1.46, & \text{for weak rocks} \\ 0.24 \cdot (\frac{\bar{E}_c}{T_n})^{0.32} - 0.88, & \text{for medium rocks} \\ -11.83 \cdot (\frac{\bar{E}_c}{T_n})^{-0.18} + 5.18, & \text{for hard rocks} \end{cases} \tag{6.3}$$

No matter for weak, medium, or hard rock, with the increase of the $\frac{\bar{E}_c}{T_n}$ value, the σ_c shows the trend of first increase and then decrease. Here below the reasons are analysed. When the $\frac{\bar{E}_c}{T_n}$ ratio is very small, e.g. < 300, the bond strengths T_n and T_s are very high, that makes the bonds too strong to be broken, then what happened is, instead of generating major fractures and breaking the rock into big chips, where stress concentration inside the body is needed, the forces from the external loading are just transmitted downwards and to the lateral side. Later it can be found that the bottom part of the rock sample get expanded and some shear bond breaks happened horizontally among the particles at the bottom, and then those particles just flee away, which also makes the sample to sink while the main body of the sample is still intact, resulting in a low maximum compressive stress when the recording is finished. The bond network of the rock sample right before the bottom is crushed can be found in Fig. 6.7. The reason the bond network is displayed here instead of the particles is that in this case the bond network can show the phenomenon with a more clear vision.

When the $\frac{\bar{E}_c}{T_n}$ ratio further increases. Major shear plane can be developed and the rock is broken into big chips. Fig. 6.8 shows the snapshots of different time steps around the structural failure moment for weak rock when $\frac{\bar{E}_c}{T_n} = 750$. The color of

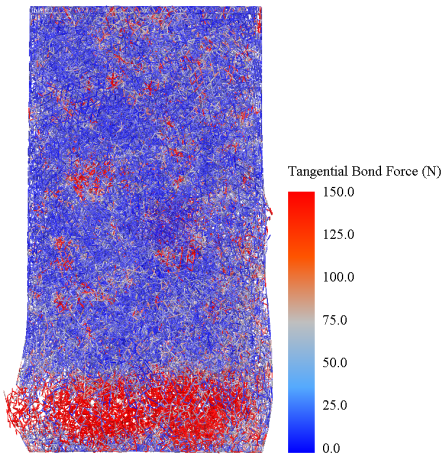

Figure 6.7: The bond network of weak rock right before the breakage at the bottom when $\frac{\bar{E}_c}{T_n} = 100$, the color indicates the magnitude of the shear force in the bond

the particles indicates their velocity magnitude, it can be surprisingly discovered that when the sample is about to fail, all the particles will reach a higher mobility level simultaneously. The solid structure at this time would adjust itself to the maximum ability to avoid a major break. Then then maximum stress is reached along the shear plane and major failure is initiated. Finally full shear plane is developed, as shown in Fig. 6.8d, the sample is broken into two parts and the lower part is pushed apart to the right from the original body. The macroscopic shear angle is about 52°, as shown in Fig. 6.8c and 6.8d, while the analytical value of the shear angle calculated from the Mohr-Coulomb failure criterion (Eq. (6.4)) is 60°. The macroscopic shear angle from the simulations does not agree precisely with the analytical solution. But it should be noted that the analytical shear angle is calculated based on purely homogeneous and isotropic material, while the DEM rock samples created in this research cannot be perfectly homogeneous, thus certain deviations exist in the macroscopic shear angle. In general, 52° is still a quite realistic value and within acceptable ranges.

$$\beta_{UCS} = 45° + \phi/2 = 45° + 15° = 60° \tag{6.4}$$

When the $\frac{\bar{E}_c}{T_n}$ ratio is increased to much higher values, i.e., 900-1300, the bond strengths become so small that the rocks are weakened, that is why a decrease of σ_c is witnessed at the tail of the curve.

The $\{\frac{\bar{E}_c}{T_n}, \frac{\sigma_c}{T_n}\}$ correlation is expressed by Eq. (6.3). The trend can be summarized as a sharp increase in the beginning and then level off to a stable value. For relatively weak rock (UCS $<$ 10 MPa), the stable value would be around 1. For medium strength

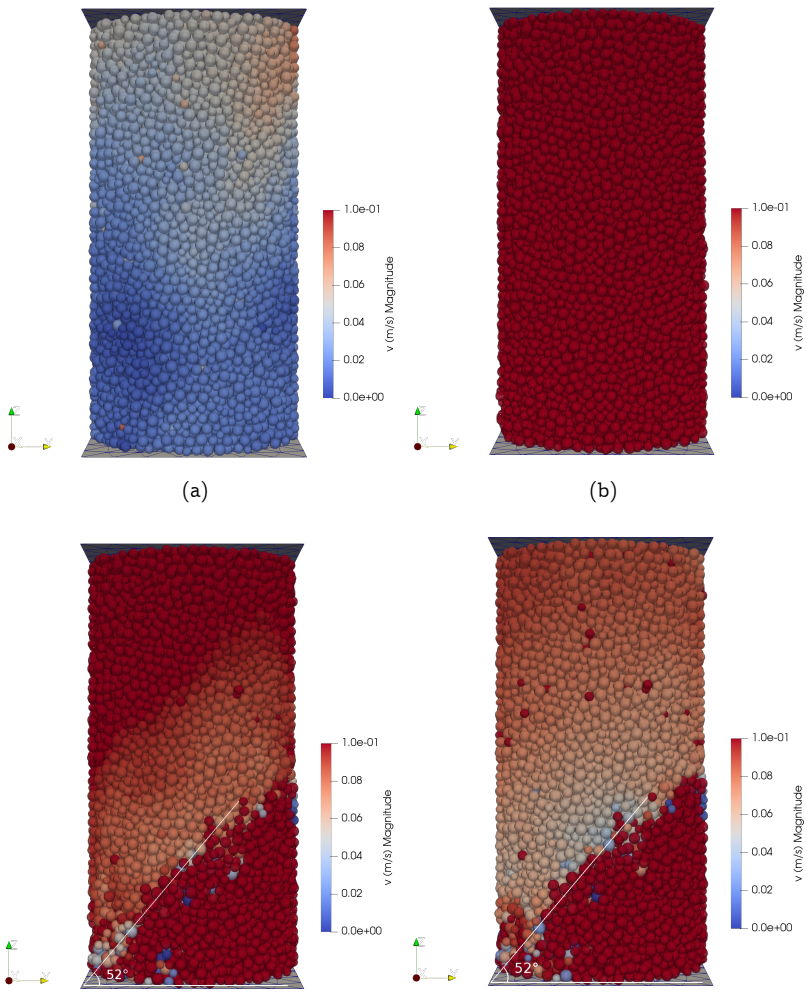

Figure 6.8: Development of the main shear plane in weak rock when $\frac{\bar{E}_c}{T_n} = 750$, time sequence: from left to right and top to bottom. a) before failure; b) all particles are motivated to resist breaking; c) shear plane appears; d) shear plane fully developed

rock (UCS ≈ 20-30 MPa), the $\frac{\sigma_c}{T_n}$ ratio keeps increasing when $\frac{\bar{E}_c}{T_n}$ is swelling. Although it is not clear if a steady value will appear with even bigger $\frac{\bar{E}_c}{T_n}$ ratio, when T_n is set to be equal to the UCS measured from laboratory, the σ_c is quite approaching T_n ($\frac{\sigma_c}{T_n} = 0.96$), which indicates that slightly bigger $\frac{\bar{E}_c}{T_n}$ ratio can be tested to create medium-strength rock sample with the expected UCS. For very hard rock (UCS ≈ 200 MPa), the steady value for $\frac{\sigma_c}{T_n}$ is around 2, but it should be noticed $\frac{\sigma_c}{T_n}$ reaches 1 when $\frac{\bar{E}_c}{T_n}$ is between 350-400.

In Fig. 6.8, the shear plane occurs near the bottom of the weak DEM rock sample. For medium and hard rocks, the situations are different. For the medium strength rock, as shown in Fig. 6.9(a), the shear plane occurs near the center of the rock sample. For the hard rock, not just shear plane, but also a vertically downwards tensile crack has been witnessed in the simulation, as shown by Fig. 6.9(b). By analyzing the footage of the simulation, it is discovered that the vertical tensile crack is developed first, and then shear planes are initiated in each half chip. This phenomenon in nature typically exists among very stiff and brittle rocks. Considering the fact that the hard DEM rock sample in this simulation holds a brittleness index of 22.1 and the particle Young's modulus of 72 GPa, the behavior of the simulation is deemed reasonable and realistic.

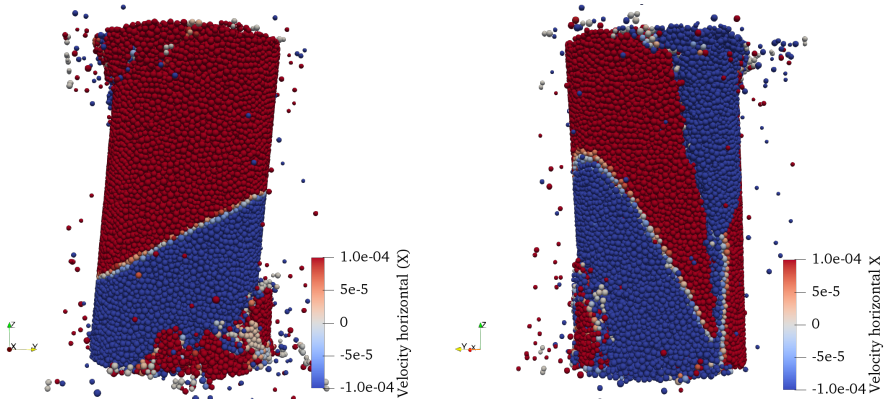

(a) (b)

Figure 6.9: Development of the main failure plane in UCS simulations of medium and hard rocks. The color indicates the particles' velocity in horizontal direction. a) Test on medium rock with $\frac{\bar{E}_c}{T_n} = 750$, where a main shear plane is witnessed near the center of the rock sample. b) Test on hard rock with $\frac{\bar{E}_c}{T_n} = 750$, in which both shear and tensile cracks are observed.

In numerical simulations, it is hard to determine the moment of failure for the solid structure in advance, so sometimes the loading plate continues to move downwards

after the failure of the sample until a pre-described time. After that pre-described time, the plate stops moving and the sample does not have contact with the plate any more. The relation between the stress σ on the plate and the axial strain ϵ of the rock sample has been studied, it is found that the major structure failures happen at $\epsilon = 0.69\% - 0.91\%$ in these UCS simulations. These are quite reasonable results comparing with the UCS experiments in the laboratory.

On the other hand, the results from the BTS simulations are also plotted. In Fig. 6.10 and 6.11, the σ_t obtained from the numerical simulations (scattered marks) is plotted together with the a power regression fitting curve (solid line), and the laboratory measurements (dotted line). Correspondingly, the $\{\frac{\bar{E}_c}{T_n}, \frac{\sigma_t}{T_n}\}$ relation is plotted in Fig. 6.11, together with a non-linear power regression fitting curve. The non-linear power regression fitting for σ_t and $\frac{\sigma_t}{T_n}$ are given by Eq. (6.5) and (6.6) respectively.

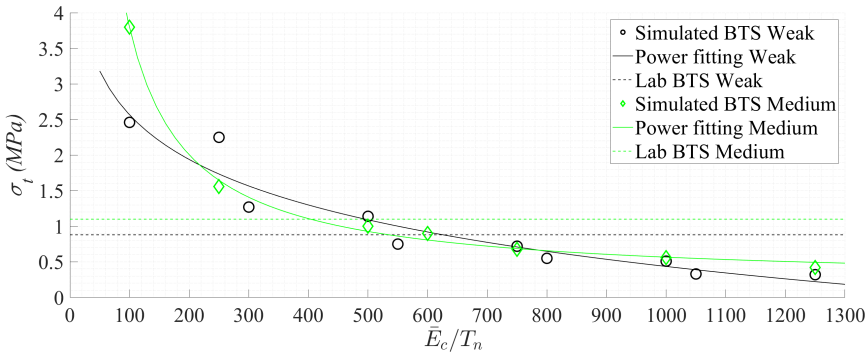

(a)

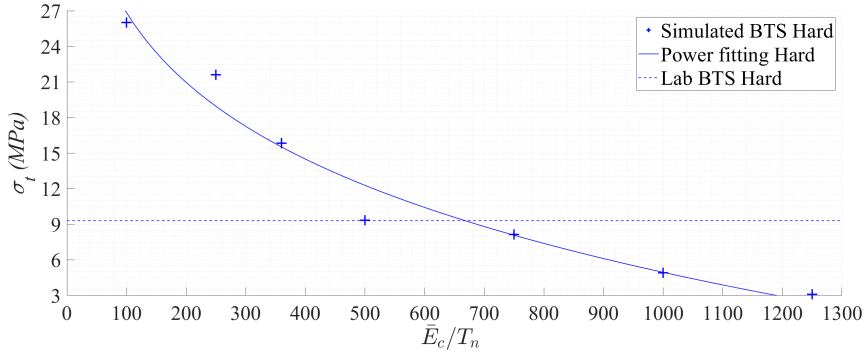

(b)

Figure 6.10: Brazilian tensile strength σ_t obtained from the simulations, the curve fittings and the laboratory experiments vs. the $\bar{E}_c/T_n$ ratio, a) the weak and medium rocks, b) the hard rocks

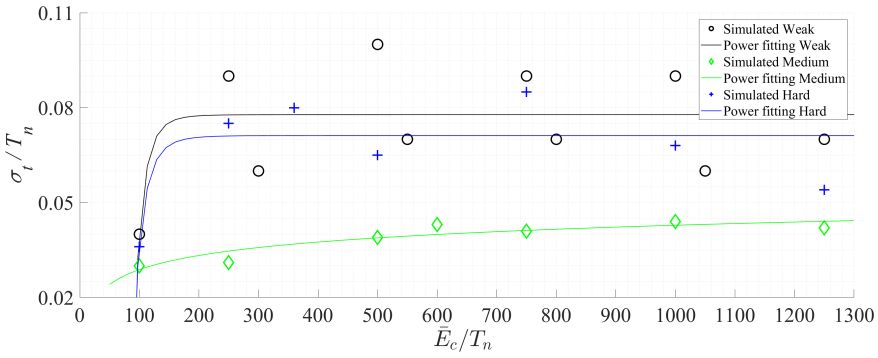

Figure 6.11: the $\{\frac{\bar{E}_c}{T_n}, \frac{\sigma_t}{T_n}\}$ relation from simulations with power curve fittings

$$\sigma_t \ [MPa] = \begin{cases} -29.44 \cdot (\frac{\bar{E}_c}{T_n})^{-0.027} + 35.89, & \text{for weak rocks} \\ 344.8 \cdot (\frac{\bar{E}_c}{T_n})^{-0.99} + 0.2, & \text{for medium rocks} \\ -31.36 \cdot (\frac{\bar{E}_c}{T_n})^{0.14} + 85.8, & \text{for hard rocks} \end{cases} \tag{6.5}$$

$$\frac{\sigma_t}{T_n} = \begin{cases} -1.12 \cdot 10^{12} \cdot (\frac{\bar{E}_c}{T_n})^{-6.74} + 0.08, & \text{for weak rocks} \\ -0.13 \cdot (\frac{\bar{E}_c}{T_n})^{-0.07} + 0.12, & \text{for medium rocks} \\ -3.67 \cdot 10^{10} \cdot (\frac{\bar{E}_c}{T_n})^{-6} + 0.07, & \text{for hard rocks} \end{cases} \tag{6.6}$$

It can be seen from Fig. 6.10 and 6.11 the simulated BTS value σ_t keeps decreasing with a rising $\frac{\bar{E}_c}{T_n}$. The reason behind is simply the bond strengths are getting lower and it has reduced the tensile strength of the rock. The failure modes for all the rocks are the same, which is a main tensile crack in the middle of the rock cylinder, meanwhile at the top and sometimes also at the bottom where the rock is directly in contact with the loading plate there are crushed zones. A typical failure mode can be found in Fig. 6.12.

Eq. 6.6 has revealed the correlation between $\frac{\bar{E}_c}{T_n}$ and $\frac{\sigma_t}{T_n}$. With the amplifying $\frac{\bar{E}_c}{T_n}$, the $\frac{\sigma_t}{T_n}$ ratio will rapidly grow in the beginning and then approaching a steady value. The steady values are 0.08, 0.04 and 0.07 for weak, medium and hard rocks.

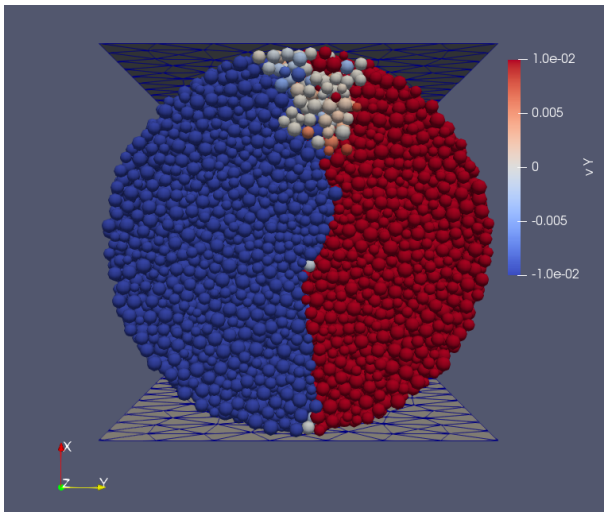

Figure 6.12: The failure moment of the rock sample of medium strength with $\frac{\bar{E}_c}{T_n} = 600$ in the BTS simulations, color of the particles indicates the horizontal velocities, with blue to the left and red to the right

However, it is discovered, with various $\frac{\bar{E}_c}{T_n}$ ratios, the time of the tensile crack changes. The higher the ratio, the sooner the rock will break. Fig. 6.13 has taken snapshots of the BTS simulation of the weak rock samples with $\frac{\bar{E}_c}{T_n} = 300, 550, 800, 1050$. What can be witnessed is at the same time step, the $\frac{\bar{E}_c}{T_n} = 1050$ rock sample already has fully developed tensile crack, and the $\frac{\bar{E}_c}{T_n} = 800$ rock sample has almost finished the crack development, on the contrary, the tensile crack of the $\frac{\bar{E}_c}{T_n} = 550$ rock has only been developed by less than 50% while the $\frac{\bar{E}_c}{T_n} = 300$ rock has not developed any apparent tensile crack yet.

The ductility number / brittleness index is calculated by Eq. (2.5), which can be represented by the $\frac{\sigma_c}{\sigma_t}$ ratio in DEM simulation. From the simulation results, the relation between the ductility number / brittleness index and the $\frac{\bar{E}_c}{T_n}$ ratio is plotted in Fig. 6.14. Polynomial regression fittings are drawn as solid lines in the Figure. The polynomial relations are given by Eq. (6.7).

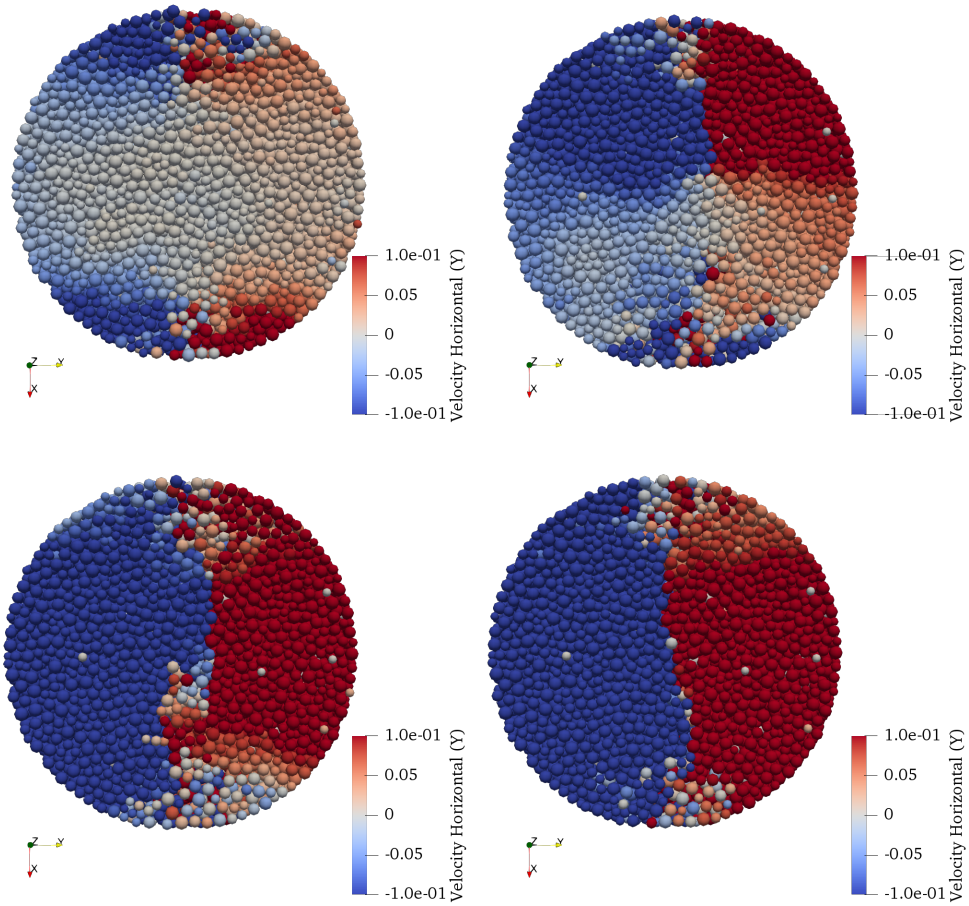

Figure 6.13: Snapshots at the same time step of the BTS simulation of weak rock with $\frac{\tilde{E}_c}{T_n} = 300, 550, 800, 1050$ (from top to bottom and left to right)

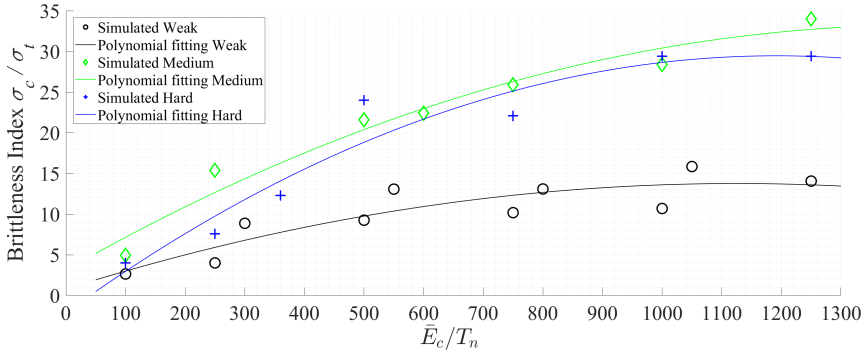

Figure 6.14: the $\{\frac{\bar{E}_c}{T_n}, \frac{\sigma_c}{\sigma_t}\}$ relation from the simulations with polynomial curve fittings

$$\frac{\sigma_c}{\sigma_t} = \begin{cases} -1.02 \cdot 10^{-5} \cdot (\frac{\bar{E}_c}{T_n})^2 + 0.02 \cdot (\frac{\bar{E}_c}{T_n}) + 0.8, & \text{for weak rocks} \\ -1.45 \cdot 10^{-5} \cdot (\frac{\bar{E}_c}{T_n})^2 + 0.04 \cdot (\frac{\bar{E}_c}{T_n}) + 3.1, & \text{for medium rocks} \\ -2.22 \cdot 10^{-5} \cdot (\frac{\bar{E}_c}{T_n})^2 + 0.05 \cdot (\frac{\bar{E}_c}{T_n}) - 2.1, & \text{for hard rocks} \end{cases} \tag{6.7}$$

The correlation shows a polynomial proportion, under which a brittleness index can be estimated by a given $\frac{\bar{E}_c}{T_n}$. Medium and hard rocks show very similar brittleness, while the weak rock has lower brittleness index indicating it is the most ductile material among the three. The brittleness index can be estimated with known $\frac{\bar{E}_c}{T_n}$ ratio and the UCS, but can hardly be accurately predicted since more scaling simulations are required to cover a complete range of the rock strengths.

6.4. Scaling of the bonds' stiffness ratio and the ductility number

In (Potyondy and Cundall, 2004), the ratio between the normal stiffness and the shear stiffness, $\frac{\bar{k}_n}{\bar{k}_s}$, is simply set to match the Poisson's ratio ν. What interesting is, the Poisson's ratio of the Lac du Bonnet granite which Potyondy and Cundall (2004) used as the reference material is around 0.26, while the $\frac{\bar{k}_n}{\bar{k}_s}$ ratio they applied in the DEM simulation as input parameter is 2.5, in the paper there is no explanation about the link between this 2.5 to the 0.26. Since it is not clear, then it is decided to try a

certain range of $\frac{\bar{k}_n}{\bar{k}_s}$ to observe the change in the macro behaviour.

The $\frac{\bar{k}_n}{\bar{k}_s}$ ratio plays an important role in determining the bonds' tendency to break in tensile or shear direction, thus would also influence the ductility/brittleness of the whole rock sample. The UCS and BTS of the rock samples with various $\frac{\bar{k}_n}{\bar{k}_s}$ ratios are tested. The input parameters of the simulations are still the same as in Table 6.2 except for the $\frac{\bar{k}_n}{\bar{k}_s}$ ratio. The $\frac{\bar{k}_n}{\bar{k}_s}$ ratio are tested with the following values: 0.5, 1.0, 1.5, 2.0, 2.5, 2.8, 3.1, 3.5 and 4.0, so that a scaling relation $\{\frac{\bar{k}_n}{\bar{k}_s}, \frac{\sigma_c}{\sigma_t}\}$ can be built up.

The UCS value σ_c and the BTS value σ_t for each sample are obtained and displayed in Table 6.6.

Table 6.6: Results of the UCS and BTS simulations on three sets of rock samples under various $\frac{\bar{k}_n}{\bar{k}_s}$ ratios

	$\bar{k}_n$ / $\bar{k}_s$	0.5	1	1.5	2	2.5	2.8	3.1	3.5	4
Weak rock	σ_c [MPa]	3.06	4.21	5.1	5.7	6.03	6.8	7.3	8.8	7.73
	σ_t [MPa]	0.4	0.51	0.59	0.6	0.66	0.67	0.72	0.79	0.86
	σ_c/σ_t	7.7	8.3	8.7	9.5	9.2	10.1	10.1	11.2	9
Medium rock	σ_c [MPa]	6.85	10.52	14.16	20.58		27	20.2	17.38	15.28
	σ_t [MPa]	0.596	0.61	0.88	1.18		1.26	0.9	0.79	0.69
	σ_c/σ_t	11.5	17.2	16.1	17.4		21.4	22.4	22	22.1
Hard rock	σ_c [MPa]	34	88.4	124	157.5		217.8	194.4	184.9	162.9
	σ_t [MPa]	4.35	5.9	6.5	8.4		12.78	15.85	12.6	8.7
	σ_c/σ_t	7.8	15	19.1	18.8		17	12.3	14.7	18.7

In Fig. 6.15, the σ_c obtained from the numerical simulations (scattered marks) is plotted together with the a polynomial fitting curve (solid line), and the laboratory measurements (dotted line). The polynomial fitting for σ_c is given by Eq. (6.8).

$$\sigma_c\ [MPa] = \begin{cases} -0.09 \cdot (\frac{\bar{k}_n}{\bar{k}_s})^3 + 0.47 \cdot (\frac{\bar{k}_n}{\bar{k}_s})^2 + 0.95 \cdot (\frac{\bar{k}_n}{\bar{k}_s}) + 2.66, & \text{for weak rocks} \\ -0.98 \cdot (\frac{\bar{k}_n}{\bar{k}_s})^3 + 2.97 \cdot (\frac{\bar{k}_n}{\bar{k}_s})^2 + 6.74 \cdot (\frac{\bar{k}_n}{\bar{k}_s}) + 2.27, & \text{for medium rocks} \\ -5.66 \cdot (\frac{\bar{k}_n}{\bar{k}_s})^3 + 11.4 \cdot (\frac{\bar{k}_n}{\bar{k}_s})^2 + 87.35 \cdot (\frac{\bar{k}_n}{\bar{k}_s}) - 10.28, & \text{for hard rocks} \end{cases} \tag{6.8}$$

In Fig. 6.15, no matter weak, medium or hard rocks, σ_c always shows a trend of first

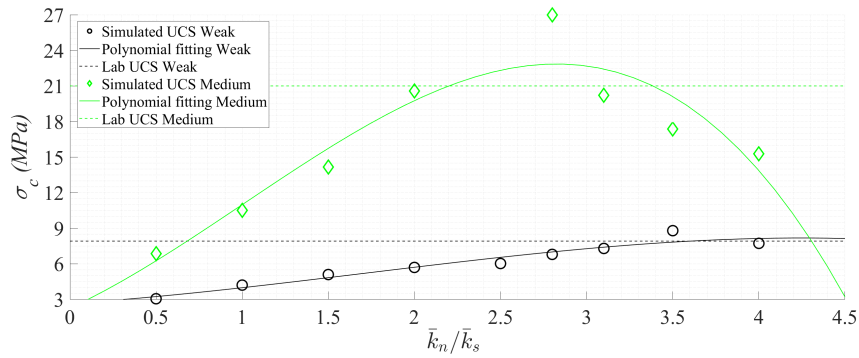

(a)

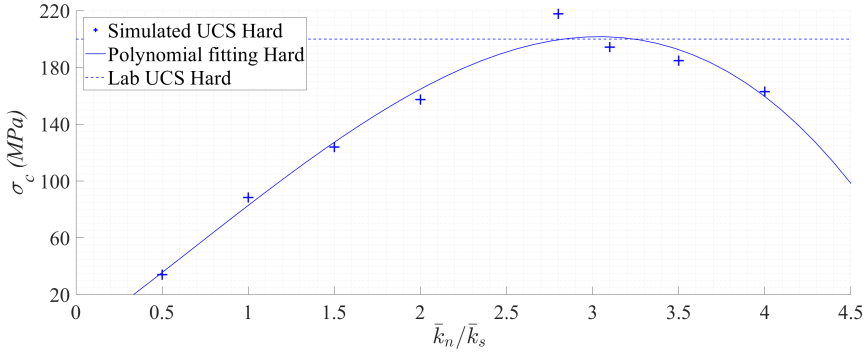

(b)

Figure 6.15: Unconfined compressive strength σ_c obtained from the simulations, the curve fittings and the laboratory experiments vs. the $\bar{k}_n$ / $\bar{k}_s$ ratio, a) the weak and medium rocks, b) the hard rocks

increasing and then decreasing. For the weak rock the trend is less obvious but there is a peak observed at $\frac{\bar{k}_n}{\bar{k}_s} = 3.5$. To understand this trend, effort has been made to analyse these stages. When $\frac{\bar{k}_n}{\bar{k}_s}$ is rather small and $\bar{k}_n$ is constant, the $\bar{k}_s$ value becomes very high. This results in the situation that a bond can break in shear failure with much smaller shear displacement, meanwhile not only one, but several shear cracks can be developed simultaneously which further damages the integrity of the rock before the structural failure. So the major structure failure would happen with much less axial strain, i.e., the top plate has only descended a very small distance. As mentioned before, the Young's Modulus $\bar{E}_c$ are fixed in this part of the scaling testing, thus the overall measured force when the rock breaks is comparably small.

If the $\frac{\bar{k}_n}{\bar{k}_s}$ ratio increases, the shear stiffness of the bond $\bar{k}_s$ is diminished, thus the rock can endure more vertical loading from the top plate before breakage, in this way the compressive strength rises up. But it is not a infinite process, when the $\frac{\bar{k}_n}{\bar{k}_s}$ value boosts too much, the shear stiffness gets so small that naturally resulting in much lower strengths of the rock sample.

However, even the trends of the weak, medium and hard rock are the same according to Fig. 6.15, their failure patterns are not always the same. The weak and medium rocks tend to fail in mainly shear planes. The shear planes for the weak rock are closer to the bottom, and depends on the $\frac{\bar{k}_n}{\bar{k}_s}$ ratio, more than one big shear cracks can be developed. For instance, Fig. 6.16a shows more than one shear cracks have occurred on the bottom left part of the rock with $\frac{\bar{k}_n}{\bar{k}_s} = 0.5$, and Fig. 6.16b displays the shear cracks also near the bottom of the rock with $\frac{\bar{k}_n}{\bar{k}_s} = 1$, meanwhile it is interesting to see a big chip breaks out on the top right part of the rock, which is quite often seen in laboratory experiments, too.

On the contrast, shear cracks on the medium-strength rocks usually occur around the central part of the rock samples. The bond network is displayed in Fig. 6.17 with the horizontal bond forces, where a black solid line is drawn to indicate the shear plane since it was not very obvious in the bond network.

From the simulation results, it is observed that the failure mode for the hard rock is quite different. Instead of big shear planes, in the hard rock simulations, there are either one or several vertically downwards penetrating cracks developed, and often accompanied by sheared chips at the bottom or top. Demonstrations of this type of failure can be found in Fig. 6.18. Fig. 6.18a shows the breakage of the hard rock with $\frac{\bar{k}_n}{\bar{k}_s} = 2$, where the red and blue colors of the particles indicating the sample is

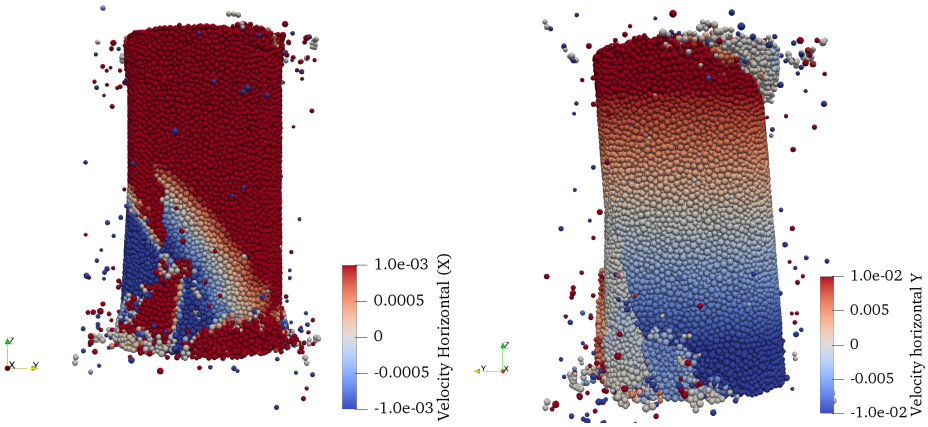

Figure 6.16: UCS simulations of weak rocks, on which shear cracks occurs more closer to the bottom. The color indicates the particles' velocity in horizontal direction. a) $\frac{\bar{k}_n}{\bar{k}_s} = 0.5$, in which more than one shear cracks are observed; b) $\frac{\bar{k}_n}{\bar{k}_s} = 1$, not only shear cracks occurs at the bottom left part, but also a big chip bursts out on the top right part of the rock sample

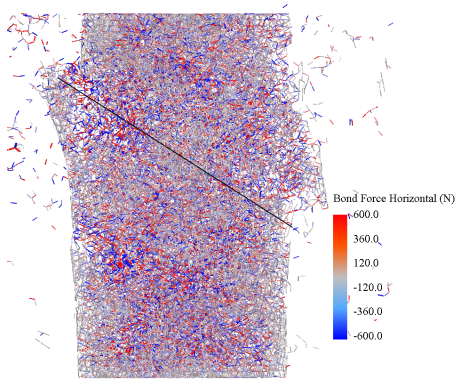

Figure 6.17: The bond network of medium-strength rock at breakage when $\frac{\bar{k}_n}{\bar{k}_s} = 2$, the color indicates the horizontal force in the bond and a black solid line is drawn to indicate the shear plane

splitting apart by a penetrating tensile crack. What is interesting to see is that in the blue half of the rock, a shear crack has been developed, which is actually induced by relatively big shear stiffness of the bond $\bar{k}_s$. On the left corner of the rock, a sheared chip is generated and leaving the body. Fig. 6.18b shows the breakage of hard rock with $\frac{\bar{k}_n}{\bar{k}_s} = 2.8$, again a penetrating vertical crack is observed and a sheared chip is generated at the back bottom of the sample. As already been mentioned earlier when interpreting Fig. 6.9, these behaviours observed in Fig. 6.18 are quite realistic for very hard, especially very brittle rocks. After examining all the failure patterns, it is concluded that if, for a rock sample, its brittleness index is larger than 17 and the UCS larger than 150 MPa, most probably in the UCS tests the failure pattern will be tensile dominant plus some secondary shear planes.

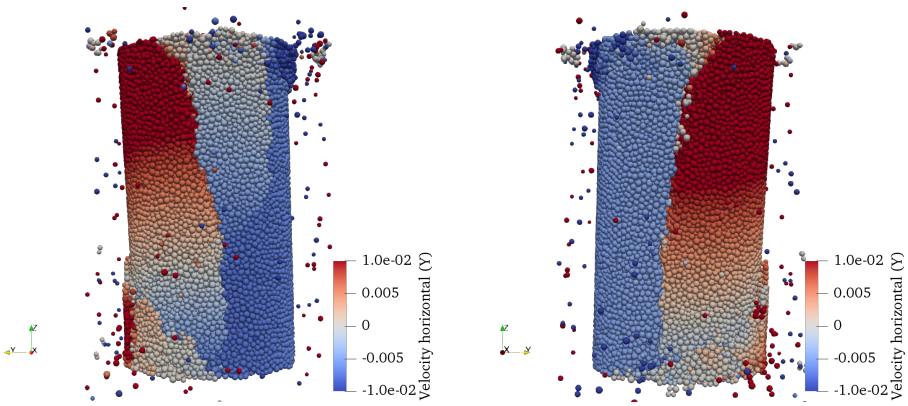

Figure 6.18: UCS simulations of hard rocks, on which one or more downwards penetrating cracks are developed. The color indicates the particles' velocity in horizontal direction. a) $\frac{\bar{k}_n}{\bar{k}_s} = 2$, in which a downwards penetrating tensile crack has split the sample into two halves, and then in the right half there is a shear crack can be spotted, besides a visible sheared chip has been developed at the left bottom of the rock; b) $\frac{\bar{k}_n}{\bar{k}_s} = 2.8$, a downwards penetrating tensile crack is developed in the rock

Via conducting all the simulations, it is discovered that for UCS tests, a range of 2-3.5 would be appropriate for the $\frac{\bar{k}_n}{\bar{k}_s}$ ratio. When the ratio gets too big, some unrealistic behaviour emerges. Fig. 6.19 shows the breakage of medium rock with $\frac{\bar{k}_n}{\bar{k}_s} = 4.0$, it can be witnessed that two big chips from the top are generated due to shearing while the rest of the rock stays intact. This is quite unusual in the rock UCS experiments. So $\frac{\bar{k}_n}{\bar{k}_s} > 3.5$ is not recommended.

On the other hand, the results from the BTS simulations are also plotted. In Fig. 6.20, the σ_t obtained from the numerical simulations (scattered marks) is plotted

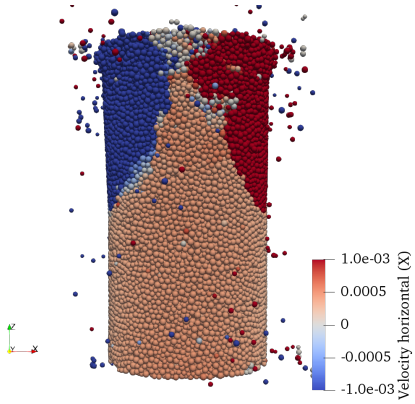

Figure 6.19: UCS simulation of medium rock sample with $\frac{\bar{k}_n}{\bar{k}_s} = 4.0$, two chips from the top are generated due to shearing while the rest of the rock stays intact

together with the a polynomial fitting curve (solid line), and the laboratory measurements (dotted line). Correspondingly, the polynomial fitting for σ_t is given by Eq. (6.9).

$$\sigma_t \ [MPa] = \begin{cases} 0.12 \cdot (\frac{\bar{k}_n}{\bar{k}_s}) + 0.37, & \text{for weak rocks} \\ -0.03 \cdot (\frac{\bar{k}_n}{\bar{k}_s})^3 + 0.001 \cdot (\frac{\bar{k}_n}{\bar{k}_s})^2 + 0.49 \cdot (\frac{\bar{k}_n}{\bar{k}_s}) + 0.28, & \text{for medium rocks} \\ -1.53 \cdot (\frac{\bar{k}_n}{\bar{k}_s})^3 + 9 \cdot (\frac{\bar{k}_n}{\bar{k}_s})^2 - 11.41 \cdot (\frac{\bar{k}_n}{\bar{k}_s}) + 8.58, & \text{for hard rocks} \end{cases} \tag{6.9}$$

In the BTS tests, there are always a crushed zones formed up at the top of the sample since this part directly suffers from the compression of the moving plate. As shown in Fig. 6.12, a major tensile crack split the rock sample into two parts, the blue part tends to move leftwards while the red part rightwards, the crushed zone on the top is the reason of the occurrence of this major crack. With fixed $\bar{k}_n$, a bigger $\frac{\bar{k}_n}{\bar{k}_s}$ ratio literally means a smaller $\bar{k}_s$, thus the shear failure between bonded particles will be postponed, so the crushed zone is larger when the sample breaks. Considering the fact that the Young's Modulus during the elastic deformation of the sample does not change with different $\frac{\bar{k}_n}{\bar{k}_s}$ ratio, so a higher $\frac{\bar{k}_n}{\bar{k}_s}$ ratio will make the sample fail at higher external load, resulting in higher apparent tensile strength. That is why in Fig. 6.20 it is witnessed the BTS value increases with increasing $\frac{\bar{k}_n}{\bar{k}_s}$ ratio. Another phenomenon

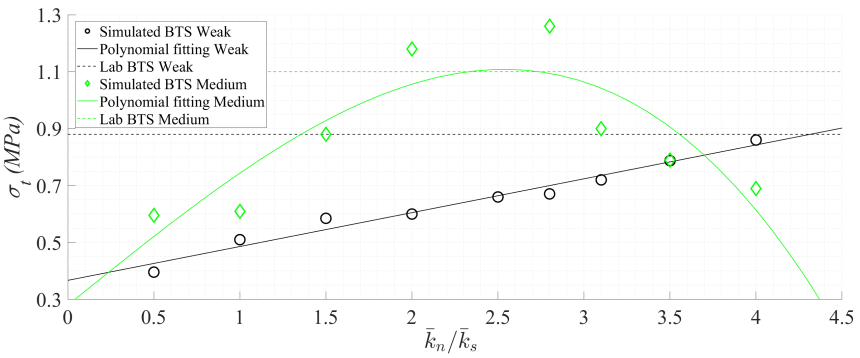

(a)

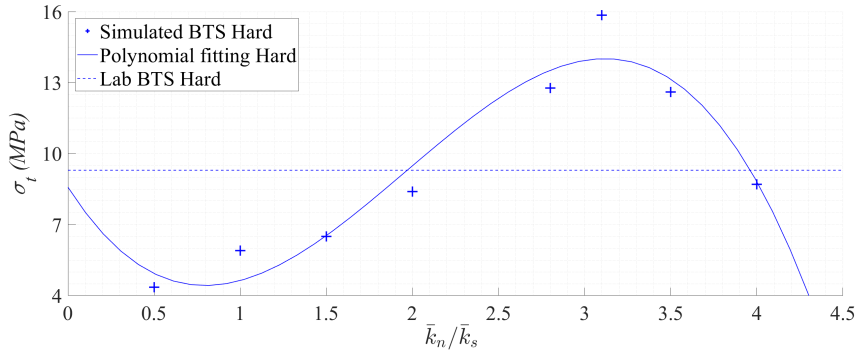

(b)

Figure 6.20: Brazilian tensile strength σ_t obtained from the simulations, the curve fittings and the laboratory experiments vs. the $\bar{k}_n$ / $\bar{k}_s$ ratio, a) the weak and medium rocks, b) the hard rocks

observed is, extra shear cracks occurred when the $\frac{\bar{k}_n}{\bar{k}_s}$ ratio is very low, as shown in Fig. 6.21, in the BTS simulation of weak rock sample with $\frac{\bar{k}_n}{\bar{k}_s} = 0.5$, big crushed zones are found both at the top and the bottom of the samples, and a big shear crack is witnessed in the blue part of the rock in parallel with the tensile crack. This behaviour exactly fits the theory mentioned above. $\bar{k}_s$ is too big when the $\frac{\bar{k}_n}{\bar{k}_s}$ ratio is only 0.5, so the shear force builds up too fast in the bond, resulting the bond breaks in shear with very small tangential displacement. These shear cracks significantly damage the integrity of the rock sample, resulting in much smaller BTS values from the simulations.

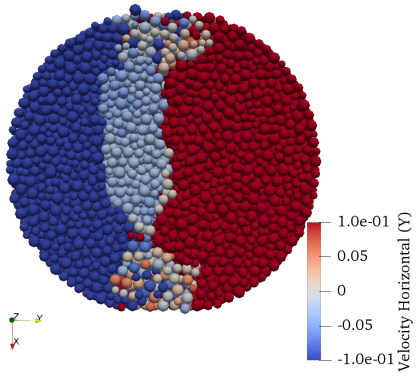

Figure 6.21: BTS simulation of weak rock sample with $\frac{\bar{k}_n}{\bar{k}_s} = 0.5$, big crushed zones are found both at the top and the bottom of the samples, a big shear crack is witnessed in the blue part of the rock in parallel with the tensile crack. The color of the particles represent their horizontal velocities

But it should be noted that the increase of σ_t is not an infinite process, when the $\frac{\bar{k}_n}{\bar{k}_s}$ ratio gets too big, the $\bar{k}_s$ becomes very small, which weakens the rock sample. That is why an decrease of σ_t is observed when $\frac{\bar{k}_n}{\bar{k}_s} > 3.1$ for the medium and hard rocks. For the weak rock, the decrease trend has not appeared in the tested range. It is not clear if a decrease trend will occur for the weak rock if the $\frac{\bar{k}_n}{\bar{k}_s}$ ratio is further increased.

After examining the strengths of the rock samples with varying $\frac{\bar{k}_n}{\bar{k}_s}$ ratio, it is now the time to check the impact of the $\frac{\bar{k}_n}{\bar{k}_s}$ ratio on the ductility number, in other words, the brittleness index, which can be calculated by Eq. (2.5). From the simulation results, the relation between the ductility number / brittleness index and the $\bar{k}_n$ / $\bar{k}_s$

ratio is plotted in Fig. 6.22. Polynomial regression fittings are drawn as solid lines in the Figure. The polynomial relations are given by Eq. (6.10).

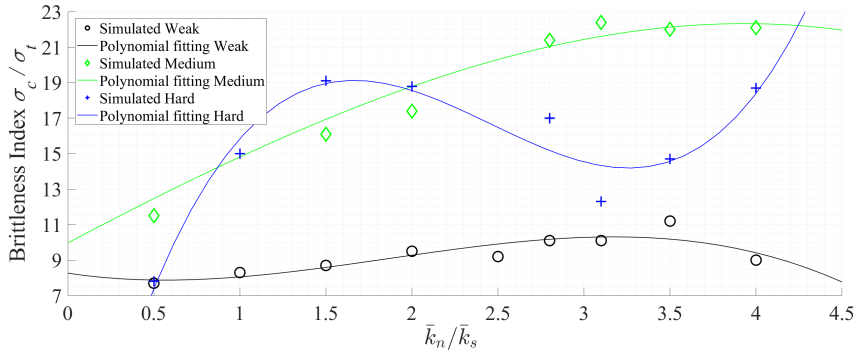

Figure 6.22: the $\{\frac{\bar{k}_n}{\bar{k}_s}, \frac{\sigma_c}{\sigma_t}\}$ relation from simulations with polynomial curve fittings

$$\frac{\sigma_c}{\sigma_t} = \begin{cases} -0.28 \cdot (\frac{\bar{k}_n}{\bar{k}_s})^3 + 1.54 \cdot (\frac{\bar{k}_n}{\bar{k}_s})^2 - 1.48 \cdot (\frac{\bar{k}_n}{\bar{k}_s}) + 8.26, & \text{for weak rocks} \\ -0.07 \cdot (\frac{\bar{k}_n}{\bar{k}_s})^3 - 0.21 \cdot (\frac{\bar{k}_n}{\bar{k}_s})^2 + 5.13 \cdot (\frac{\bar{k}_n}{\bar{k}_s}) + 9.97, & \text{for medium rocks} \\ 2.44 \cdot (\frac{\bar{k}_n}{\bar{k}_s})^3 - 18 \cdot (\frac{\bar{k}_n}{\bar{k}_s})^2 + 39.7 \cdot (\frac{\bar{k}_n}{\bar{k}_s}) - 8.24, & \text{for hard rocks} \end{cases} \quad (6.10)$$

It is assumed that the $\frac{\bar{k}_n}{\bar{k}_s}$ ratio would have a significant impact on the brittleness of the rock because it determines the tendency of a bond's failure in the shear or the tensile failure mode. From Fig. 6.22 it can be observed that indeed the ductility number varies a lot with the $\frac{\bar{k}_n}{\bar{k}_s}$ ratio, but there is no unified pattern. For the weak rock, it is learned that the variation of $\frac{\bar{k}_n}{\bar{k}_s}$ does not change the ductility of the sample significantly. The ductility number / brittleness index is in the range of $8 < m < 11$. For medium rock, a stable increasing trend is found on the ductility number. In the future this polynomial relation could be used for calibrating the rock samples when needed. On the contrary, the trend on the hard rock is much more complicated, a "increase - decrease - increase" trend is observed. It is not clear how this trend can be explained.

6.5. Conclusions and Recommendations

Some conclusions can be drawn based on the studies in this chapter.

1. For generating the DEM rock sample, the static generation method from Lozano et al. (2016) cannot be used for creating rock samples, though it is relatively faster. The dynamic generation method from Potyondy and Cundall (2004) is able to produce good DEM rock samples, although the process takes longer time. This method is also better than the gravitational deposition method since it can keep the homogeneity in the vertical direction.
2. The parallel bond method (PBM) has the general applicability to be used for modelling the mechanical behaviour of the rocks with various strengths, from very weak rock (UCS $<$ 10 MPa) to very hard rock (UCS $\sim$ 200 MPa). From the simulations carried out, the UCS values are within acceptable ranges compared to real rocks while the BTS values match well for weak and medium rock, but show a significant overestimation for the hard rock. Overall speaking, the performance confirms the advantage of PBM over the point contact bond method on performing very hard rock behaviour.
3. PBM can display the shock wave propagation and the stress concentration during the loading process on the DEM rock sample. PBM can also distinguish the breaking patterns for different rocks. For relatively weak and in the brittle-ductile transition rock, a clear shear plane can be witnessed in the UCS test. For very hard and brittle rock, vertical cracks occurs in the UCS test. For the BTS test, clear vertical cracks can be observed at failure. These performances are all spontaneous and intuitive, without the help of any special constitutive laws.
4. The $\{\frac{\bar{E}_c}{T_n}, \frac{\sigma_c}{T_n}\}$ correlation can be summarised as a sharp increase in the beginning and then level off to a stable value. For relatively weak rock (UCS $<$ 10 MPa), the stable value would be around 1. For medium strength rock (UCS $\approx$ 20-30 MPa), the $\frac{\sigma_c}{T_n}$ ratio keeps increasing although it is not clear if a steady value will appear with even bigger $\frac{\bar{E}_c}{T_n}$ ratio. For hard rock (UCS $\approx$ 200 MPa), the steady value for $\frac{\sigma_c}{T_n}$ is around 2.
5. The $\{\frac{\bar{E}_c}{T_n}, \frac{\sigma_t}{T_n}\}$ correlation can be concluded as, with the amplifying $\frac{\bar{E}_c}{T_n}$, the $\frac{\sigma_t}{T_n}$ ratio will rapidly grow in the beginning and then approaching a steady value. The steady values are 0.08, 0.04 and 0.07 for weak, medium and hard rocks.
6. Extra shear cracks could be developed both in the UCS and BTS simulations when the the $\frac{\bar{k}_n}{\bar{k}_s}$ ratio is too small. The $\{\frac{\bar{k}_n}{\bar{k}_s}, \frac{\sigma_c}{\sigma_t}\}$ ratio can be concluded as, for the weak rock, the ductility number of the sample only varies in a small range $8 < m < 11$, which reflects the mechanical property of the real rock well. For medium rock, a stable increasing trend is found on the ductility number. But the trend on the hard rock is much more complicated, a "increase - decrease -

increase" trend is observed. It is not clear how this trend can be explained.

The study in this chapter makes it convincing that the PBM is indeed superior to other numerical methods in terms of describing very detailed and dynamic mechanical behaviour of rocks. It is by no doubt recommended to conduct material test simulations with more ranges of rock strengths. In this chapter, only three rocks are targeted (UCS = 7.92 MPa, 21 MPa and 200 MPa), the gaps in-between are too big. This makes it impossible to find out where the transition of the failure patterns and the transition of the trends of the correlations mentioned above happen. To build up a sound scaling law, which in the future can be used as the references for creating the desired DEM rock sample, much more simulations should be conducted, so that a database can be established. This can significantly increase the convenience for applying PBM in scientific research and engineering practice.

7

Conclusions and Recommendations

In this chapter the overall conclusions and recommendations of this research project are presented.

7.1. Conclusions

7.1.1. Numerical modelling of sand cutting process

In DEM, non-spherical particle based on a tetrahedron internal structure can well represent the mechanical behavior of natural sand. Phenomenons like interlocking, shearing and dilatation can occur spontaneously without any extra constitutive laws applied on macro scale. Non-spherical particles are used in dry sand cutting simulations, and the results are validated by comparing with the experimental results of Hatamura and Chjiiwa (1975, 1976a,b). The validation tests show that, the cutting forces on the blade, after scaling, agree well with the experimental results.

Spherical DEM particles can be used to model sand only when the rotational movement is significantly damped. With a rolling friction coefficient $\mu_r = 0.7$, the correct angle of repose can appear in the calibration tests. Underwater sand cutting simulations are carried out and validated by comparing with the experiments of Miedema (2017). Validation on the dimensionless cutting force for the 2D effect underwater cutting process shows that, large errors appear at $h_b/h_i = 1$ when the results are not corrected for gravity effect. After the results are corrected for gravity effect, the numerical, experimental, and analytical dimensionless cutting forces agree with each other well.

The simulation results from both the dry and underwater sand cutting simulations prove that, with large cutting angles (75° and 90°), the cutting force develop according to the wedge theory of Miedema (2017). However, the wedge is not static and thus cannot be easily visualized.

7.1.2. Numerical modelling of cohesive soil cutting process

Cohesive DEM soil sample can be created by using the Simplified Johnson-Kendall-Roberts (SJKR) cohesion model. The internal shear strength of the sample can be calibrated by the direct shear tests using the ring shear device, and the external shear strength can be tested by the blade pull-out tests. The results of these tests show a clear cohesion, a clear internal friction angle, a clear adhesion and a clear external friction angle. It proves that these two tests satisfy the need for calibrating the major mechanical properties of the cohesive DEM soil sample.

The developed DEM model for atmospheric cohesive soil cutting process is validated using the cutting experiments conducted on plastic loam by (Hatamura and Chjiiwa, 1976b). Although the created cohesive DEM soil sample does not precisely match the mechanical properties of the plastic loam, via applying the scaling law, the results obtained by the developed DEM model match with the results found by Hatamura and Chijiiwa within acceptable error margins. The difference is mainly induced by the mismatch of the unknown adhesion of the plastic loam in the Hatamura and Chjiiwa (1976b) experiments and the adhesion obtained from the numerical samples.

Submerged cohesive soil cutting simulations are performed with 300 kPa hydrostatic pressure and various cutting speeds. Unfortunately there is no experimental data available for validation. The "cutting force - cutting speed" relation obtained from the simulations is compared with an empirical relation on clay cutting. The comparison shows that the increase of cutting force when cutting with higher cutting speed has been significantly overestimated in the simulations. The reason is that permeability of the cohesive DEM soil sample has not been tuned to the level of that of natural clay. As a result, higher pressure gradient force appears with higher cutting speed, leading to much higher cutting force.

7.1.3. General applicability and scaling tests on DEM rock samples

The parallel bond method (PBM) has the general applicability for modelling the mechanical behaviour of the rocks with various strengths, from very weak rock (UCS $<$ 10 MPa) to very hard rock (UCS $\approx$ 200 MPa). It confirms the advantage of PBM over the point contact bond method on performing very hard rock behaviour.

The $\{\frac{\bar{E}_c}{T_n}, \frac{\sigma_c}{T_n}\}$ correlation can be summarised as a sharp increase in the beginning and then level off to a stable value. The $\{\frac{\bar{E}_c}{T_n}, \frac{\sigma_t}{T_n}\}$ correlation can be concluded as, with the amplifying $\frac{\bar{E}_c}{T_n}$, the $\frac{\sigma_t}{T_n}$ ratio will rapidly grow in the beginning and then approaching a steady value.

The $\{\frac{\bar{k}_n}{\bar{k}_s}, \frac{\sigma_c}{\sigma_t}\}$ ratio can be concluded as, for the weak rock, the ductility number of the sample only varies in a small range $8 < m < 11$, which reflects the mechanical property of the real rock well. For medium rock, a stable increasing trend is found on the ductility number. But the trend on the hard rock is much more complicated, a "increase - decrease - increase" trend is observed. It is not clear how this trend can be explained.

7.1.4. Other conclusions

A 3D dynamic numerical modelling framework has been established for simulating the underwater excavation process. This model enables the observation on the internal structure of the soil and the transient/instant behaviour during cutting. Phenomenons like underwater dilatancy, crack formation and shear layer formation, which are quite difficult to observe and measure in lab experiments, can now emerge spontaneously in the simulations.

It should be pointed out that particle based numerical models contain a certain amount of stochasticity in their simulation results. A number of repetitions on the

calibration and cutting simulations are the common practices to improve the accuracy of numerical results. In recent years, more meticulous calibration procedures on the mechanical properties of materials in DEM have been reported by Derakhshani et al. (2015), Katterfeld et al. (2019) and Mohajeri et al. (2020).

In this research project, it is not feasible to carefully calibrate every parameter in the model or conduct many repetitions due to the limitation of time. The calibration simulations on sand and cohesive soil in this thesis have been carried out twice and the average results are presented. This also applies to the UCS and BTS simulations on weak rock sample. The other simulations have been carried out only once, and experimental results are introduced for validation purposes. For excavation simulations, it remains unknown that the bandwidth of variation of the simulations results if a sufficient number of repetitions are carried out.

7.2. Recommendations

7.2.1. Numerical modelling of sand cutting process

Although forces measured from the dry sand cutting simulations match the experimental results well, it should be pointed out that the cutting speeds in these simulations are small, so the inertia forces have been neglected. It is recommended that simulations with higher cutting speeds should be carried out for investigating the influence of the inertia force in dry sand cutting.

For the simulations of underwater sand cutting process, the cutting speeds are not high enough to trigger the occurrence of cavitation. Therefore it is also recommended in future research, to simulate underwater sand cutting with higher cutting speed, to investigate if the DEM-FVM coupling model can well incorporate the cavitation phenomenon.

7.2.2. Numerical modelling of cohesive soil cutting process

The validation of atmospheric cutting process is not complete due to the fact that there is no information available on the adhesion of the plastic loam cut in the (Hatamura and Chjiiwa, 1976b) experiments, it is thus recommended in the future to conduct cohesive soil cutting experiments on the premise that all the necessary mechanical properties of the soil sample are known, so that more comprehensive validation can be carried out.

There is no validation on submerged cutting process of cohesive soil due to the lack of experimental data. It is recommended in future research, to conduct submerged cohesive soil cutting experiments where all the necessary mechanical properties are measured in advance (permeability, cohesion, adhesion, undrained shear strength and etc.). After that, numerical modelling can be carried out with proper calibrations.

7.2.3. General applicability and scaling tests on DEM rock samples

It is recommended to conduct material test simulations with more ranges of rock strengths. In this chapter, only three rocks are targeted (UCS = 7.92 MPa, 21 MPa and 200 MPa), the gaps in-between are too big. This makes it impossible to find out where the transition of the failure patterns and of the trends of the correlations mentioned above happens. To build up a sound scaling law, which in the future can be used as the references for creating the desired DEM rock sample, much more simulations should be conducted, so that a database can be established. This can significantly increase the convenience for applying PBM in scientific research and engineering practice.

7.2.4. Other recommendations

As mentioned before, due to the limitation of time, it is not possible to carry out a sufficient number of repetitions on each simulation within this research project. Therefore, it is recommended in future research projects, to conduct more calibration and excavation simulations with a sufficient number of repetitions. This will help the numerical model to a better stability, accuracy and reproducibility.

In summary, experimental study gives people the ability to observe the physics from outside, while DEM-FVM coupling gives people the ability to observe the physics from the microscopic level, i.e., the inside. It is thus believed that DEM-FVM coupling provides with a bright future for researchers to understand more and more physics.

Bibliography

Abdeli, M., Miedema, S., van Rhee, C., Schott, D., and Alvarez Grima, M. (2010). Discrete element method modelling of sand cutting. *WODCON XIX, September*, pages 12–14.

Adema, A. T., Yang, Y., and Boom, R. (2010). Discrete element method-computational fluid dynamic simulation of the materials flow in an iron-making blast furnace. *ISIJ international*, 50(7):954–961.

Ahnert, A. and Borowski, C. (2000). Environmental risk assessment of anthropogenic activity in the deep-sea. *Journal of Aquatic Ecosystem Stress and Recovery*, 7(4):299–315.

Ai, J., Chen, J.-F., Rotter, J. M., and Ooi, J. Y. (2011). Assessment of rolling resistance models in discrete element simulations. *Powder Technology*, 206(3):269–282.

Akgiray, Ö. and Saatçı, A. M. (2001). A new look at filter backwash hydraulics. *Water Science and Technology: Water Supply*, 1(2):65–72.

Alassi, H. T. (2008). Modeling reservoir geomechanicsusing discrete element method: Application to reservoirmonitoring.

Alonso, E., Yerro, A., and Pinyol, N. (2015). Recent developments of the material point method for the simulation of landslides. *IOP Conference Series: Earth and Environmental Science*, 26(1):012003.

Bagi, K. (1993). A quasi-static numerical model for micro-level analysis of granular assemblies. *Mechanics of materials*, 16(1-2):101–110.

Bagi, K. (2005). An algorithm to generate random dense arrangements for discrete element simulations of granular assemblies. *Granular Matter*, 7(1):31–43.

Bandara, S. and Soga, K. (2015). Coupling of soil deformation and pore fluid flow using material point method. *Computers and Geotechnics*, 63:199–214.

Biarez, J. and Gourvès, R. (1989). *Powders and grains: proceedings of the International Conference on Micr omechanics of Granular Media, Clermont-Ferrand, 4-8 September 1989*. Balkema.

Boskalis (2017). Cutter suction dredger helios. https://boskalis.com/download-center/download/eyJmaWxlVWlkIjoxNDk1NywicmVmZXJlbmNlVWlkIjowfQ%3D%3D/957954afbdd64a1cce50008c16be719a6c9319ac.html.

Bouillard, J., Lyczkowski, R., and Gidaspow, D. (1989). Porosity distributions in a fluidized bed with an immersed obstacle. *AIChE Journal*, 35(6):908–922.

Brace, W. and Martin Iii, R. (1968). A test of the law of effective stress for crystalline rocks of low porosity. In *International Journal of Rock Mechanics and Mining Sciences & Geomechanics Abstracts*, volume 5, pages 415–426. Elsevier.

Brilliantov, N. V., Spahn, F., Hertzsch, J.-M., and Pöschel, T. (1996). Model for collisions in granular gases. *Physical review E*, 53(5):5382.

Carman, P. (1937a). Fluid flow through granular beds. *Chemical Engineering Research and Design*, 75:S32 – S48.

Carman, P. C. (1937b). Fluid flow through granular beds. *Trans. Inst. Chem. Eng.*, 15:150–166.

Carman, P. C. (1956a). *Flow of gases through porous media*. Academic press.

Carman, P. C. P. C. (1956b). *Flow of gases through porous media*. London : Butterworths Scientific. Includes bibliographical references and index.

Ceccato, F. (2015). *Study of large deformation geomechanical problems with the Material Point Method*. PhD thesis, Università degli Studi di Padova.

CFDEM, C.-O. S. C. (2018). Dem and cfd. *URL: http://www. cfdem. com*.

Chen, F., Drumm, E. C., and Guiochon, G. (2011). Coupled discrete element and finite volume solution of two classical soil mechanics problems. *Computers and Geotechnics*, 38(5):638–647.

Chen, X. and Miedema, S. (2013). Porosity calculation in discrete element modeling of sand cutting process. In *WODCON XX: "The Art of Dredging"*. World Dredging Association.

Chen, X., Miedema, S., and Van Rhee, C. (2015). Numerical modeling of excavation process in dredging engineering. *Procedia engineering*, 102:804–814.

Chen, X., Miedema, S. A., and van Rhee, C. (2013). Influence of particle geometry on the simulation of sand cutting process. In *ASME 2013 32nd International Conference on Ocean, Offshore and Arctic Engineering*, pages V006T10A008–V006T10A008. American Society of Mechanical Engineers.

Chen, X., Miedema, S. A., and van Rhee, C. (2014). Numerical methods for modeling the rock cutting process in deep sea mining. In *ASME 2014 33rd International Conference on Ocean, Offshore and Arctic Engineering*, pages V003T10A002–V003T10A002. American Society of Mechanical Engineers.

Chen, X., van den Broecke, J., Liu, G., Hong, G., and Miedema, S. (2019a). Experimental analysis of the cohesion-adhesion relation of cohesive soil. In *WODA 2019 22nd World Dredging Congress & Expositions*. World Organization of Dredging Associations.

Chen, X., van den Broecke, J., Liu, G., Hong, G., and Miedema, S. (2019b). A study on the clay adhesion factor. In *The Dredging Summit & Expo ' 19*. Western Dredging Association (WEDA).

Chung, J. S. et al. (1996). Deep-ocean mining: technologies for manganese nodules and crusts. *International Journal of Offshore and Polar Engineering*, 6(04).

Cleary, P. W. and Prakash, M. (2004). Discrete-element modelling and smoothed particle hydrodynamics: potential in the environmental sciences. *Philosophical Transactions-Royal Society Of London Series A Mathematical Physical And Engineering Sciences*, 362:2003–2030.

Courant, R., Friedrichs, K., and Lewy, H. (1967). On the partial difference equations of mathematical physics. *IBM journal of Research and Development*, 11(2):215–234.

Cui, L. and O' Sullivan, C. (2003). Analysis of a triangulation based approach for specimen generation for discrete element simulations. *Granular Matter*, 5:135–145.

Cundall, P. A. (1971a). A computer model for simulating progressive, large scale movement in blocky rock systems. In *Symp. ISRM, Nancy, France, Proc.*, volume 2, pages 129–136.

Cundall, P. A. (1971b). The measurement and analysis of accelerations in rock slopes. *PhD Thesis, Imperial College of Science & Technology*.

Cundall, P. A. and Strack, O. D. (1979). A discrete numerical model for granular assemblies. *geotechnique*, 29(1):47–65.

Darcy, H. P. G. (1856). *Les Fontaines publiques de la ville de Dijon. Exposition et application des principes à suivre et des formules à employer dans les questions de distribution d'eau, etc.* V. Dalamont.

DCS Computing Gmbh (2018a). The cdt model. https://www.cfdem.com/media/DEM/docu/gran_rolling_friction_cdt.html.

DCS Computing Gmbh (2018b). The herzian model. https://www.cfdem.com/media/DEM/docu/gran_model_hertz.html.

Del Cid, L. I. (2015). *A discrete element methodology for the analysis of cohesive granular bulk solid materials*. Colorado School of Mines.

DEM Solutions (2016). Edem 2017 user guide, edinburgh, uk. *DEM Solutions Ltd*.

Derakhshani, S. M., Schott, D. L., and Lodewijks, G. (2015). Micro–macro properties of quartz sand: experimental investigation and dem simulation. *Powder Technology*, 269:127–138.

Duda, M. and Renner, J. (2012). The weakening effect of water on the brittle failure strength of sandstone. *Geophysical Journal International*, 192(3):1091–1108.

Ebrahimi, M., Gupta, P., Robinson, M., Crapper, M., Ramaioli, M., and Ooi, J. Y. (2013). Comparison of coupled dem-cfd and sph-dem methods in single and multiple particle sedimentation test cases. In *3rd International conference on particle-based methods-fundamentals and applications (PARTICLES 2013)*.

Enwald, H., Peirano, E., and Almstedt, A.-E. (1996). Eulerian two-phase flow theory applied to fluidization. *International Journal of Multiphase Flow*, 22:21–66.

Ergun, S. (1952). Fluid flow through packed columns. *Chem. Eng. Prog.*, 48:89–94.

Evans, I. (1965). The force required to cut coal with blunt wedges. *International Journal of Rock Mechanics and Mining Sciences & Geomechanics Abstracts*, 2(1):1 – 12.

Evans, I. and Pomeroy, C. (1966). *The strength, fracture and workability of coal*. Pergamon.

Evans, J. W. (1993). Random and cooperative sequential adsorption. *Reviews of modern physics*, 65(4):1281.

Fakhimi, A. and Lanari, M. (2014). Dem–sph simulation of rock blasting. *Computers and Geotechnics*, 55:158–164.

Feng, Y., Han, K., and Owen, D. (2003). Filling domains with disks: an advancing front approach. *International Journal for Numerical Methods in Engineering*, 56(5):699–713.

Fielke, J. M. (1999). Finite element modelling of the interaction of the cutting edge of tillage implements with soil. *Journal of Agricultural Engineering Research*, 74(1):91–101.

Flores, P. and Lankarani, H. M. (2016). *Contact force models for multibody dynamics*, volume 226. Springer.

Fountaine, E. (1954). Investigations into the mechanism of soil adhesion. *Journal of soil science*, 5(2):251–263.

Gehle, C. and Kutter, H. (2003). Breakage and shear behaviour of intermittent rock joints. *International Journal of Rock Mechanics and Mining Sciences*, 40(5):687–700.

Gidaspow, D. (1994). *Multiphase flow and fluidization: continuum and kinetic theory descriptions*. Academic press.

Gidaspow, D., Bezburuah, R., and Ding, J. (1991). Hydrodynamics of circulating fluidized beds: kinetic theory approach. Technical report, Illinois Inst. of Tech., Chicago, IL (United States). Dept. of Chemical Engineering.

Goeree, J. C., Keetels, G. H., Munts, E. A., Bugdayci, H. H., and van Rhee, C. (2016). Concentration and velocity profiles of sediment-water mixtures using the drift flux model. *The Canadian Journal of Chemical Engineering*, 94(6):1048–1058.

Goniva, C., Kloss, C., Hager, A., and Pirker, S. (2010). An open source cfd-dem perspective. In *Proceedings of OpenFOAM Workshop, Göteborg*, pages 22–24.

Goniva, C., Kloss, C., and Pirker, S. (2009). Towards fast parallel cfd-dem: An open-source perspective. In *Open Source CFD International Conference*, volume 2009.

Grima, M. A., Miedema, S., van de Ketterij, R., Yenigül, N., and van Rhee, C. (2015). Effect of high hyperbaric pressure on rock cutting process. *Engineering Geology*, 196:24–36.

Gwyther, D. (2008). Environmental impact statement, solwara 1 project. *Nautilus Minerals Niugini Limited, Main Report Coffey Natural Systems, Brisbane*.

Hærvig, J. (2017). *On the Adhesive Behaviour of Micron-sized Particles in Turbulent Flow: A Numerical Study Coupling the Discrete Element Method and Large Eddy Simulations*. PhD thesis, Aalborg Universitetsforlag.

Hager, A. (2014). Cfd-dem on multiple scales: An extensive investigation of particle–fluid interactions. *Johannes Kepler University Linz, Linz*.

Hager, A., Kloss, C., Pirker, S., and Goniva, C. (2013). Parallel open source cfd-dem for resolved particle-fluid interaction. *Journal of Energy and Power Engineering*, 7(9):1705.

Hastings, W. K. (1970). Monte carlo sampling methods using markov chains and their applications. *Biometrika*, 57(1):97–109.

Hatamura, Y. and Chjiiwa, K. (1975). Analysis of the mechanism of soil: 1st report. cutting patterns of soils. *Bulletin of JSME*, 18(120):619–626.

Hatamura, Y. and Chjiiwa, K. (1976a). Analysis of the mechanism of soil cutting: 2nd report. deformation and internal stress of soil in cutting. *Bulletin of JSME*, 19(131):555–563.

Hatamura, Y. and Chjiiwa, K. (1976b). Analysis of the mechanism of soil cutting: 3rd report. distribution of stresses on cutting blade and cutting force. *Bulletin of JSME*, 19(137):1376–1384.

Hatamura, Y. and Chjiiwa, K. (1977a). Analysis of the mechanism of soil cutting: 4th report, properties of soils related to cutting. *Bulletin of JSME*, 20(139):130–137.

Hatamura, Y. and Chjiiwa, K. (1977b). Analysis of the mechanism of soil cutting: 5th report, cutting theories of soils. *Bulletin of JSME*, 20(141):388–395.

He, J. and Vlasblom, W. (1998). Modelling of saturated sand cutting with large rake angle. In Randall, R., editor, *Proceedings 15th world dredging congress, Las Vegas, Nevada, USA, June 28-July 2, 1998: dredging into the 21st century*, pages 905–919. WEDA.

Helmons, R. (2017). *Excavation of hard deposits and rocks: On the cutting of saturated rock*. PhD thesis, Delft University of Technology.

Helmons, R., Miedema, S., Grima, M. A., and van Rhee, C. (2016a). Modeling fluid pressure effects when cutting saturated rock. *Engineering Geology*, 211:50–60.

Helmons, R., Miedema, S., and van Rhee, C. (2016b). Simulating hydro mechanical effects in rock deformation by combination of the discrete element method and the smoothed particle method. *International Journal of Rock Mechanics and Mining Sciences*, 86:224–234.

Hertz, H. R. (1882). Uber die beruhrung fester elastischer korper und uber die harte. *Verhandlung des Vereins zur Beforderung des GewerbefleiBes, Berlin*, page 449.

Hoek, E., Carranza-Torres, C., and Corkum, B. (2002). Hoek-brown failure criterion-2002 edition. *Proceedings of NARMS-Tac*, 1(1):267–273.

Huang, H. (1999). *Discrete element modeling of tool-rock interaction*. PhD thesis, University of Minnesota.

Huang, H. and Detournay, E. (2013). Discrete element modeling of tool-rock interaction ii: rock indentation. *International Journal for Numerical and Analytical Methods in Geomechanics*, 37(13):1930–1947.

Huang, H., Detournay, E., and Bellier, B. (1999). Discrete element modelling of rock cutting. *Rock Mechanics for Industry*, 1(1):123–130.

Huang, H., Lecampion, B., and Detournay, E. (2013). Discrete element modeling of tool-rock interaction i: rock cutting. *International Journal for Numerical and Analytical Methods in Geomechanics*, 37(13):1913–1929.

Huang, S., Su, X., and Qiu, G. (2015). Transient numerical simulation for solid-liquid flow in a centrifugal pump by dem-cfd coupling. *Engineering Applications of Computational Fluid Mechanics*, 9(1):411–418.

International Association of Dredging Companies (IADC) (2019). Dredging in figures 2018. https://iadc-dredging.com/wp-content/uploads/2019/10/dredging-in-figures-2018.pdf.

International Seabed Authority (ISA) (2014). Polymetallic nodules exploration areas in the clarion-clipperton fracture zone.

Ishii, M. and Hibiki, T. (2005). *Thermo-fluid dynamics of two-phase flow*. Springer Science+ Business Media.

Jaime, M. C., Zhou, Y., Lin, J.-S., and Gamwo, I. K. (2015). Finite element modeling of rock cutting and its fragmentation process. *International Journal of Rock Mechanics and Mining Sciences*, 80:137–146.

Jodrey, W. and Tory, E. (1985). Computer simulation of close random packing of equal spheres. *Physical review A*, 32(4):2347.

Kaitkay, P. and Lei, S. (2005). Experimental study of rock cutting under external hydrostatic pressure. *Journal of Materials Processing Technology*, 159(2):206–213.

Katterfeld, A., Coetzee, C., Donohue, T., Fottner, A. J., Grima, A., Gomez, A. R., Ilic, D., Kačianauskas, R., Necas, J., Ostrava, T., et al. (2019). Calibration of dem parameters for cohesionless bulk materials under rapid flow conditions and low consolidation. *Powder Technol.*

Kaufmann, R. K. and Cleveland, C. J. (2008). *Environmental science*. McGraw-Hill College.

Kim, K. S., Yu, S., and Ahn, I.-H. (2018). Simulation of solid particle sedimentation by using moving particle semi-implicit method. *Journal of the Korean Society of Marine Environment & Safety*, 24(1):119–125.

Kozeny, J. (1927a). Uber kapillare leitung der wasser in boden. *Royal Academy of Science, Vienna, Proc. Class I*, 136:271–306.

Kozeny, J. (1927b). Ueber kapillare leitung des wassers. *Boden sitzungsberichte wiener akademie*, 136:271–306.

Kuiper, R. J., Miedema, S. A., Frumau, J. C., et al. (2013). Influence of the hyperbaric effect on apparent material strength of fully saturated porous rock for low strain rates. In *Offshore Technology Conference*. Offshore Technology Conference.

Labra, C., Rojek, J., Oñate, E., and Zarate, F. (2008). Advances in discrete element modelling of underground excavations. *Acta Geotechnica*, 3(4):317–322.

Lal, R. (2006). *Encyclopedia of soil science*, volume 2. CRC Press.

Lei, S. and Kaitkay, P. (2003). Distinct element modeling of rock cutting under hydrostatic pressure. In *Key Engineering Materials*, volume 250, pages 110–117. Trans Tech Publ.

Liu, M., Suo, S., Wu, J., Gan, Y., Hanaor, D. A., and Chen, C. (2019). Tailoring porous media for controllable capillary flow. *Journal of colloid and interface science*, 539:379–387.

Lopez, A. (2014). Lpt for erosion modeling in openfoam. www.tfd.chalmers.se/~hani/kurser/OS_CFD_2013/AlejandroLopez/LPT_for_erosionModelling_report.pdf.

Lozano, E., Roehl, D., Celes, W., and Gattass, M. (2016). An efficient algorithm to generate random sphere packs in arbitrary domains. *Computers & Mathematics with Applications*, 71(8):1586–1601.

Luding, S., Lätzel, M., Volk, W., Diebels, S., and Herrmann, H. (2001). From discrete element simulations to a continuum model. *Computer methods in applied mechanics and engineering*, 191(1):21–28.

Luo, J. (2015). *Dynamics of Flexible Risers for Deep Sea Mining Applications*. Msc thesis, Delft University of Technology.

Mahabadi, O., Lisjak, A., Grasselli, G., Lukas, T., and Munjiza, A. (2010). Numerical modelling of a triaxial test of homogeneous rocks using the combined finite-discrete element method. In *Proc. European Rock Mechanics Symp.(EUROCK2010), Lausanne, Switzerland*, pages 173–176.

Mahdavimanesh, M., Noghrehabadi, A., Behbahaninejad, M., Ahmadi, G., and Dehghanian, M. (2013). Lagrangian particle tracking: model development. *Life Science Journal*, 10(8s):34–41.

MARUM (2010). Marine minerals - nodules, crusts and vents. http://worldoceanreview.com/wp-content/uploads/2010/10/7_5-smoker_01.jpg.

Meester, R. et al. (1996). Nearest neighbor and hard sphere models in continuum percolation. *Random structures and algorithms*, 9(3):295–315.

Mehta, A. and Barker, G. (1994). The dynamics of sand. *Reports on Progress in Physics*, 57(4):383.

Merchant, M. E. (1944). Basic mechanics of the metal-cutting process. *ASME J. of Applied Mechanics*, 11:A168.

Merchant, M. E. (1945a). Mechanics of the metal cutting process. i. orthogonal cutting and a type 2 chip. *Journal of applied physics*, 16(5):267–275.

Merchant, M. E. (1945b). Mechanics of the metal cutting process. ii. plasticity conditions in orthogonal cutting. *Journal of applied physics*, 16(6):318–324.

Metrikine, A., Delft University of Technology, F. o. C. E., and of structural mechanics, G. S. (2006). *Dynamics, Slender Structures and an Introduction to Continuum Mechanics: CT4145*. TU Delft.

Metropolis, N., Rosenbluth, A. W., Rosenbluth, M. N., Teller, A. H., and Teller, E. (1953). Equation of state calculations by fast computing machines. *The journal of chemical physics*, 21(6):1087–1092.

Miedema, S. A. (1987). Calculation of the cutting forces when cutting water saturated sand. *Doctor thesis, Delft, Netherlands*.

Miedema, S. A. (2011). Soil cutting processes: The cutting of water saturated sand. In *ASME 2011 30th International Conference on Ocean, Offshore and Arctic Engineering*, pages 841–853. American Society of Mechanical Engineers.

Miedema, S. A. (2014). *The Delft Sand, Clay and Rock Cutting Model*. IOS Press.

Miedema, S. A. (2017). *The Delft Sand, Clay & Rock Cutting Model 3rd Edition B*. IOS Press BV, Delft, 3 edition.

Miedema, S. A. and Zijsling, D. (2012). Hyperbaric rock cutting. In *ASME 2012 31st International Conference on Ocean, Offshore and Arctic Engineering*, pages 103–116. American Society of Mechanical Engineers.

Mitchell, W. F. (1881). Hms challenger. https://commons.wikimedia.org/wiki/File:HMS_challenger_William_Frederick_Mitchell.jpg.

Mohajeri, M. J., Helmons, R. L., van Rhee, C., and Schott, D. L. (2020). A hybrid particle-geometric scaling approach for elasto-plastic adhesive dem contact models. *Powder Technology*, 369:72–87.

Munjiza, A. A. (2004). *The combined finite-discrete element method*. John Wiley & Sons.

Mustoe, G., Henriksen, M., Huttelmaier, H., and eds. (1989). Proc., 1st us conf. on discrete element methods.

Nautilus Minerals (2016). Seafloor production tools. http://www.nautilusminerals.com/irm/content/seafloor-production-tools.aspx?RID=333.

Nguyen, D. H., Levy, F., Van Bang, D. P., Guillou, S., Nguyen, K. D., and Chauchat, J. (2012). Simulation of dredged sediment releases into homogeneous water using a two-phase model. *Advances in water resources*, 48:102–112.

Nguyen, K. D., Guillou, S., Chauchat, J., and Barbry, N. (2009). A two-phase numerical model for suspended-sediment transport in estuaries. *Advances in Water Resources*, 32(8):1187–1196.

Ning, Z. and Ghadiri, M. (2006). Distinct element analysis of attrition of granular solids under shear deformation. *Chemical engineering science*, 61(18):5991–6001.

Nishimatsu, Y. (1972). The mechanics of rock cutting. In *International Journal of Rock Mechanics and Mining Sciences & Geomechanics Abstracts*, volume 9, pages 261–270. Elsevier.

Obermayr, M., Dressler, K., Vrettos, C., and Eberhard, P. (2013). A bonded-particle model for cemented sand. *Computers and Geotechnics*, 49:299–313.

Oñate, E., Celigueta, M. A., Idelsohn, S. R., Salazar, F., and Suárez, B. (2011). Possibilities of the particle finite element method for fluid–soil–structure interaction problems. *Computational Mechanics*, 48(3):307.

Ozturgut, E., Lavelle, J., and Burns, R. (1981). Impacts of manganese nodule mining on the environment: results from pilot-scale mining tests in the north equatorial pacific. *Elsevier Oceanography Series*, 27:437–474.

Pachón-Morales, J., Do, H., Colin, J., Puel, F., Perre, P., and Schott, D. (2019). Dem modelling for flow of cohesive lignocellulosic biomass powders: Model calibration using bulk tests. *Advanced Powder Technology*, 30(4):732–750.

Padan, J. (1990). Commercial recovery of deep seabed manganese nodules: Twenty years of accomplishments. *Mar. Min.*, 9(1):87–103.

Potyondy, D. and Cundall, P. (2004). A bonded-particle model for rock. *International journal of rock mechanics and mining sciences*, 41(8):1329–1364.

Potyondy, D., Cundall, P., Lee, C., et al. (1996). Modelling rock using bonded assemblies of circular particles. In *2nd North American Rock Mechanics symposium*. American Rock Mechanics Association.

Procházka, P. (2004). Application of discrete element methods to fracture mechanics of rock bursts. *Engineering Fracture Mechanics*, 71(4):601–618.

Rabobank International (2013). Dredging, profit margins expected to remain fairly healthy until 2018. http://www.dredging.org/media/ceda/org/documents/resources/othersonline/rabobank-outlook_dredging_september_2013.pdf.

Radjaï, F. and Dubois, F. (2011). *Discrete-element modeling of granular materials*. Wiley-Iste.

Rahman, M., Abdeli, M., Miedema, S., and Schott, D. (2011). Simulation of passive soil failure and cutting processes in sand. In *ASME 2011 30th International Conference on Ocean, Offshore and Arctic Engineering*, pages 809–823. American Society of Mechanical Engineers.

Rahman, M., Katterfeld, A., Schott, D., and Lodewijks, G. (2010). Influence of the software on the calibration process of dem simulations. *Bulk Solids Europe*, pages 9–10.

Rojek, J. (2007). Discrete element modelling of rock cutting. *Computer Methods in Materials Science*, 7(2):224–230.

Rojek, J., Karlis, G., Malinowski, L., and Beer, G. (2013). Setting up virgin stress conditions in discrete element models. *Computers and geotechnics*, 48:228–248.

Rojek, J. and Oñate, E. (2007). Multiscale analysis using a coupled discrete/finite element model. *Interaction and Multiscale Mechanics*, 1(1):1–31.

Rojek, J., Oñate, E., Kargl, H., Labra, C., Akerman, J., Restner, U., Lammer, E., and Zarate, F. (2008). Prediction of wear of roadheader picks using numerical simulations. *Geomechanics and Tunnelling*, 1(1):47–54.

Rojek, J., Oñate, E., Labra, C., and Kargl, H. (2011). Discrete element modelling of rock cutting. In *Particle-based methods*, pages 247–267. Springer.

Rona, P. and Scott, S. (1993). Aspecialissueonsea-floorhydrothermalmineralization, newperspecitive. *EconomicGeology*, 88(8):1935–2294.

Rona, P. A. (2008). The changing vision of marine minerals. *Ore Geology Reviews*, 33(3):618–666.

Roxborough, F. F. (1987). The role of some basic rock properties in assessing cuttability. In *Seminar on Tunnels: Wholly Engineered Structures*.

Roxborough, F. F. and Phillips, H. R. (1975). Rock excavation by disc cutter. In *International Journal of Rock Mechanics and Mining Sciences & Geomechanics Abstracts*, volume 12, pages 361–366. Elsevier.

Satake, M. and Jenkins, J. T. (2013). *Micromechanics of Granular Materials: Proceedings of the US/Japan Seminar on the Micromechanics of Granular Materials, Sendai-Zao, Japan, October 26-30, 1987*, volume 20. Elsevier.

Savage, S. (1983). Mechanics of granular materials: new models and constitutive relations. *Studies in Applied Mechanics*, 7:261–282.

Schmeeckle, M. W. (2014). Numerical simulation of turbulence and sediment transport of medium sand. *Journal of Geophysical Research: Earth Surface*, 119(6):1240–1262.

Scholtès, L. and Donzé, F.-V. (2012). Modelling progressive failure in fractured rock masses using a 3d discrete element method. *International Journal of Rock Mechanics and Mining Sciences*, 52:18–30.

Sepp, S. (2011). Rounded and fine-grained eolian sand sample from the gobi desert. https://commons.wikimedia.org/wiki/File:Sand_from_Gobi_Desert.jpg.

Shen, G., Chen, C., Gao, S., Zhang, H., Chen, Y., and Zhang, Y. (2018). Research on wangqing oil shale physical and mechanical properties and hydraulic fracturing pressure. *Exploration Engineering (Rock & Soil Drilling and Tunneling)*, 45:1–4.

Shi, Z., Jiang, T., Jiang, M., Liu, F., and Zhang, N. (2015). Dem investigation of weathered rocks using a novel bond contact model. *Journal of Rock Mechanics and Geotechnical Engineering*, 7(3):327–336.

Shimizu, H., Koyama, T., Ishida, T., Chijimatsu, M., Fujita, T., and Nakama, S. (2010). Distinct element analysis for class ii behavior of rocks under uniaxial compression. *International Journal of Rock Mechanics and Mining Sciences*, 47(2):323–333.

Shimizu, H., Murata, S., and Ishida, T. (2011). The distinct element analysis for hydraulic fracturing in hard rock considering fluid viscosity and particle size distribution. *International Journal of Rock Mechanics and Mining Sciences*, 48(5):712–727.

Siriwardane, H. and Zaman, M. (1994). Computer methods and advances in geomecahnics. In *Proc. 8 th. Int. Conf. of Computer Met. And Advances in Geomech., Morgantown, USA*.

Standard, A. (2015). D6773: Standard shear test method for bulk solids using the schulze ring shear tester.

Stienen, J. (1982). *Die Vergroeberung von Karbiden in reinen Eisen-Kohlenstoff-Staehlen*. RWTH Aachen.

Stoyan, D. (2002). Random systems of hard particles: models and statistics. *Chinese journal of stereology and image analysis*, 7(1).

Suzuki, K. (2013). Discovery and distribution of mud containing very high concentrations of rare earth elements and yttrium around minami-torishima island. *Japan Agency for Marine-Earth Science and Technology*.

Telford, W. M., Telford, W., Geldart, L., Sheriff, R. E., and Sheriff, R. (1990). *Applied geophysics*. Cambridge university press.

Thiel, H., Weikert, H., and Karbe, L. (1986). Risk assessment for mining metalliferous muds in the deep red sea. *Ambio (Sweden)*.

Thornton, C. (1993). Powders and grains 93. *Balkema, Rotterdam*.

Vallier, A., Revstedt, J., and Nilsson, H. (2011). Procedure for the break-up of cavitation sheet. In *4-th International Meeting on Cavitation and Dynamic Problems in Hydraulic Machinery and Systems, October, 26-28, 2011, Belgrade, Serbia*, pages 77–85.

Van der Schrieck, G. (2009). Dredging technology. *Lecture notes Delft University of Technology, Delft*.

Van der Schrieck, G. (2012). Lecture notes dredging technology. *Delft University of Technology*.

van Grunsven, F., Keetels, G., and van Rhee, C. (2016). Modeling offshore mining turbidity sources. *WODCON XXI: Innovations in dredging*.

van Kesteren, W. (1995). Numerical simulations of crack bifurcation in the chip forming cutting process in rock. *Fracture of Brittle Disordered Materials: Concrete, Rock and Ceramics*, pages 505–524.

Van Wachem, B. and Almstedt, A.-E. (2003). Methods for multiphase computational fluid dynamics. *Chemical Engineering Journal*, 96(1):81–98.

van Wijk, J. (2016). *Vertical hydraulic transport for deep sea mining: A study into flow assurance*. PhD thesis, Delft University of Technology.

Verhoef, P. N. W. (1997). Wear of rock cutting tools: Implications for the site investigation of rock dredging projects.

Verruijt, A. and Broere, W. (2011). *Grondmechanica*. VSSD.

Verruijt, A. and van Baars, S. (2005). *Grondmechanica*. VSSD.

Vlasblom, W. (2007). Cutting of rock. *Lecture Book Dredging Processes*.

VOSTA LMG (2020). The t-cutter head. https://www.vostalmg.com/components/cutting-systems/cutter-head.

Weij, D., Keetels, G. H., Goeree, J., and van Rhee, C. (2016). An extension of the drift-flux model for submarine granular flows. *International Journal of Computational Methods and Experimental Measurements*, 4(4):444–453.

Wen, C.-Y. and Yu, Y.-H. (1966). Mechanics of fluidization. In *Chem. Eng. Prog. Symp. Ser.*, volume 62, pages 100–111.

Wikipedia (2005). Palm jumeirah. https://en.wikipedia.org/wiki/Palm_Jumeirah.

Wikipedia (2010). Ductility. https://en.wikipedia.org/wiki/Ductility.

Williams, J., Mustoe, G., and eds. (1993). Proc., 2nd int. conf. on discrete element methods.

Wright, I. (2006). Marine minerals - nodules, crusts and vents. http://www.TeAra.govt.nz/en/photograph/5513/polymetallic-nodules.

Xia, K. (2017). *Experimental study of Air-lift system in application of vertical transportation*. Msc thesis, Delft University of Technology.

Yamazaki, T. (2004). Geotechnical characteristics of deep-ocean sediments for design of mining systems. In *Proc. Int. Symp. on Eng. Practice and Performance of Soft Deposits*, pages 81–86.

Yang, Q., Wang, M., Luan, M.-t., et al. (2010). Experimental research of correlation on static and dynamic strength of unsaturated silty clay. *Rock Soil Mech*, 31(1):71–75.

Yeom, S. B., Ha, E.-S., Kim, M.-S., Jeong, S. H., Hwang, S.-J., and Choi, D. H. (2019). Application of the discrete element method for manufacturing process simulation in the pharmaceutical industry. *Pharmaceutics*, 11(8):414.

Yin, P.-F. and Yang, S.-Q. (2019). Discrete element modeling of strength and failure behavior of transversely isotropic rock under uniaxial compression. *Journal of the Geological Society of India*, 93(2):235–246.

Zhou, Z., Kuang, S., Chu, K., and Yu, A. (2010). Discrete particle simulation of particle–fluid flow: model formulations and their applicability. *Journal of Fluid Mechanics*, 661:482–510.

List of Publications

JOURNAL PUBLICATIONS

8. **Echaroj, S., Ong, H.C., Chen, X.**, *Simulation of Mixing Intensity Profile for Bioethanol Production via Two-Step Fermentation in an Unbaffled Agitator Reactor*, Energies, 13, 5457 (2020).

7. **Xiong, T., Miedema, S. A., Chen, X.**(correspondent author), *Comparative analysis between CFD model and DHLLDV model in fully-suspended slurry flow*, Ocean Engineering 181, 29-42 (2019).

6. **Xiong, T., Zhang, X., Miedema, S. A., Chen, X.**(correspondent author), *Study of the characteristics of the flow regimes and dynamics of coarse particles in pipeline transportation*, Powder Technology, 347, 148-158 (2019).

5. **Chen, X., Miedema, S. A., van Rhee, C.**, *Numerical modelling of excavation process in dredging engineering*, Procedia Engineering, 102, 804-814 (2015).

4. **Miedema, S.A., Nieuwboer, B.J., Chen, X.**, *An analytical Spillage Model for Cutter Head in Dredging Sand or Gravel*, WEDA Journal of Dredging, **[Submitted]**, (2019).

3. **Chen, X., Miedema, S.A., van Rhee, C.**, *Discrete Element Modelling for Unconfined Compression Test on Rock*, WEDA Journal of Dredging, **[Submitted]**, (2019).

2. **Wang, Y., Chen, X., Miedema, S.A., Yang Q., Fang Z.**, *Numerical Investigation of the Flow Field and Mass Transfer Characteristics in a Jet Slurry Pump*, Journal of Hydrodynamics, **[Submitted]**, (2020).

1. **Liang, X., Liu, G., Hong, G., Chen, X., Xie, L., Li W.**, *Study on rock cutting failure mechanism of large-scale cutting model tests*, Frontiers in Earth Science, **[Submitted]**, (2020).

CONFERENCES

16. **Ermolaeva, N. S., Yu, Y., Chen, X., & Ren, H.** , *Measurements vs. estimation of nominal and local strain in a tubular K-joint of a stinger*, Tubular Structures XIV, 195-202 (2012).

15. **Chen, X., Miedema, S. A.**, *Porosity calculation in discrete element modelling of sand cutting process*, WODCON 2013 World Dredging Congress, The Art of Dredging, 3-7 June, 2013, Brussels, Belgium (2013).

14. **Chen, X., Miedema, S.A., van Rhee, C.**, *Influence of Particle Geometry on the Simulation of Sand Cutting Process*, ASME 2013 International Conference on Ocean, Offshore and Arctic Engineering, OMAE 2013, 9-14 June, 2013, Nantes, France (2013).

13. **Chen, X., Miedema, S.A., van Rhee, C.**, *Numerical Methods for Modeling the Rock Cutting Process in Deep Sea Mining* , ASME 2014 International Conference on Ocean, Offshore and Arctic Engineering, OMAE 2014, 8-13 June, 2014, San Francisco, USA (2014).

12. **Chen, X., Miedema, S.A., van Rhee, C.**, *Sensitivity Study of Bond Radius and Energy Dissipation in Parallel Bond Method*, Crossroads of Particle Science and Technology - Joint Conference of 5th UK-China and 13th UK Particle Technology Forum, 12-15 July, 2015, Leeds, UK (2015).

11. **Kuiper, R.J., Chen, X., Frumau, C.L., & Miedema, S.A.**, *Reduction of Energy Consumption When Using a Grab for Deep-Sea Mining Operations*, Offshore Technology Conference, 2-5 May, 2016, Houston, Texas, USA (2016).

10. **Chen, X., Miedema, S.A., van Rhee, C.**, *Application of Parallel Bond Method in Rock Compression Simulation*, The 5th International Dredging Technology Development Conference, 27-29 November, 2017, Beijing, China, (2017).

9. **de Ridder, J.K., de Vreede, M.A., Wang, F., Talmon, A.M., & Chen, X.**, *Preliminary results on the influence of large diameter pipeline for hydraulic transport in laboratory conditions*, The 5th International Dredging Technology Development Conference, 27-29 November, 2017, Beijing, China, (2017).

8. **Miedema, S.A., Chen, X.**, *Criterion for the transition of heterogeneous flow to fully stratified flow in slurry transport*, The First International Water Environment Ecological Construction Development Conference - Harmony with Nature, 17-19 October, 2018, Wuhan, China (2018).

7. **Xiong, T., Zhang, X., Miedema, S. A., Chen, X.**, *Characteristics Research on Coarse Particles in Pipeline Transportation based on CFD-DEM*, The 22nd World Dredging Congress & Exposition, WODCON XXII, 22-26 April 2019, Shanghai, China (2019).

6. **Chen, X., van den Broecke, J.W., Liu, G., Hong, G., & Miedema, S.A.**, *Experimental Analysis of the Cohesion-Adhesion Relation of Cohesive Soil*, The 22nd World Dredging Congress & Exposition, WODCON XXII, 22-26 April 2019, Shanghai, China (2019).

5. **Chen, X., Xiong, T., Zhang, X., & Miedema, S.A.**, *Numerical Modelling of Slurry Transport for Coarse Particles*, WEDA Dredging Summit and Expo '19, 4-7 June, 2019, Chicago, USA (2019).

4. **Chen, X., van den Broecke, J.W., Liu, G., Hong, G., & Miedema, S.A.**, *A Study on the Clay Adhesion Factor*, WEDA Dredging Summit and Expo '19, 4-7 June, 2019, Chicago, USA (2019).

3. **Rutten, T., Chen, X., Liu, G., Hong, G., & Miedema, S.A.**, *Experimental study on rock cutting with a pickpoint*, CEDA Dredging Days 2019, 7-8 November 2019, Rotterdam, The Netherlands (2019).

2. **Chen, X., Rutten, T.,Liu, G., Hong, G. & Miedema, S.A.**, *A 3D analytical model for linear rock cutting process*, Proceedings of the Western Dredging Association Dredging Summit & Expo '20, Houston, TX, USA, June 9-12, 2020.

1. **Miedema, S.A., Wang, F., Hong, G. & Chen, X.**, *Dominating Factors in slurry transport in inclined pipes*, Proceedings of the Western Dredging Association Dredging Summit & Expo '20, Houston, TX, USA, June 9-12, 2020.

MAGAZINES

13. **Chen, X., Miedema, S.A., van Rhee, C.**, *Introduction to Deep Sea Mining and the Relevance to Dredging Engineering I*, China Dredging, **29**, 49-52 (2017).

12. **Chen, X., Miedema, S.A., van Rhee, C.**, *Introduction to Deep Sea Mining and the Relevance to Dredging Engineering II*, China Dredging, **30**, 49-51 (2017).

11. **Chen, X., Miedema, S.A., van Rhee, C.**, *Introduction to Deep Sea Mining and the Relevance to Dredging Engineering III*, China Dredging, **32**, 50-53 (2017).

10. **Ye, Q., Chen, X., Aarninkhof, S.G.J., 概论环境友好的疏浚工程: 基于"与自然共建"(BwN) 理念的 *Delft* 技术路线**, China Dredging, **32**, 45-49 (2017).

9. **van Grunsven, F., Chen, X.**, *Introduction to Deep Sea Mining and the Relevance to Dredging Engineering IV*, China Dredging, **33**, 47-52 (2017).

8. **Chen, X., 聚焦生态疏浚新理念, 开发疏浚前沿新技术**, China Dredging, **34**, 19-20 (2017).

7. **Xiong, T., Chen. X.**, *Overview of the Works of the AMORAS Sediment Processing Facility in Belgium*, China Dredging, **37**, 25-28 (2018).

6. **Chen. X.**, *Building with Nature: Dynamic Integration of "Hard Engineering" and "Soft Engineering"*, China Dredging, **37**, 31-34 (2018).

5. **Chen, X., Miedema, S.A., van Rhee, C., 并行粘合模型在岩石压缩模拟中的应用**, China Dredging, **38**, 79-84 (2018).

4. **Miedema, S.A., Chen, X., 泥浆输送中非均匀流转向完全层流的判据**, China Dredging, **39**, 51-58 (2018).

3. **Miedema, S.A., Chen, X.**, *Production Estimation of Water Jets and Cutting Blades in Dragheads*, China Dredging, **41**, 27-38 (2019).

2. **Chen, X., Wang, X., Miedema, S.A., van Rhee, C.**, *Introduction to Deep Sea Mining and the Relevance to Dredging Engineering V: The Cutting Process*, China Dredging, **48**, 22-33 (2020).

1. **Miedema, S.A., Chen, X., Nieuwboer, B.J.**, *Cutter Head Spillage When Dredging Sand or Gravel*, China Dredging, **48**, 34-44 (2020).

AWARDS

2. Excellent Paper Award, The 5th International Dredging Technology Development Conference, 27-29 November, 2017, Beijing, China, (2017).

1. Excellent Paper Award, The First International Water Environment Ecological Construction Development Conference - Harmony with Nature, 17-19 October, 2018, Wuhan, China (2018).

Acknowledgements

It has been a long journey, but I must say this PhD is by no doubt the most wonderful experience that has ever happened in my professional life. I feel so much appreciation for all the kind help I have received.

To begin with, Cees, you taught me the knowledge from both the scientific world and the industrial world. I feel so lucky that I can work with you for these years, because you have so much knowledge that you can explain each dredging matter in the most scientific way. Through all the talks, presentations and lectures I received from you, I build up the framework of dredging knowledge. You enabled me to solve a dredging problem in a scientific but still quite practical manner. Besides, you give me the freedom to develop all the other skills. When I discuss with you the work I did besides my PhD, for example, supervising master students, setting up joint-research program, organizing conferences and symposiums, and promoting the communication in WODA, you give me guidance and support, you explain me the context and allow me to develop. I really appreciate for these helps, you encouraged me to know and get myself known to the international dredging community.

To Sape, oh where should I start. I started following you since the first day I arrived in this country. Sometimes you tell a joke with a very serious face expression, and I start thinking: it sounds absurd, but he is my supervisor, a well-known scientist, so it must be true. Then you start laughing. For all these years, you really cared about me, you constantly ask me if I need any help. And whenever I asked for help from you, no matter if it is a research problem, an administrative problem, or even some personal matters, you always contribute as much as possible. I always want to discuss every little detail with you, the PhD work, the other works, and personal life. Apart from that, you stimulated my passion for writing. You write many papers by yourself and you also set the requirement on me to publish at least two papers annually. After several years it has also become my habit and I enjoy the writing a lot.

To both of you, Cees and Sape, there are two things I want to express my appreciation for: 1) I love dredging because of you. From knowing almost nothing to reaching the current knowledge level, I become more and more attracted by dredging. I do not feel like I am working in the office, it is more like a adventure to satisfy my own curiosity. Your guidance and teaching are the driving force for my enthusiasm. 2) You supported me during the bottom of my life. When my life was chaotic, you held patience on me, you did not give up on me. You wait until I got recovered. Thank you very much gentlemen!

When conducting the research projects in this thesis, I had the luck to work together

with some of our excellent master students in the dredging engineering group, I worked with Rick Bekkers and Xiuqi Wang on the sand study, with Jan van den Broecke on the clay study, with Tom Rutten and Maarten de Jonge on the rock study. Much appreciation for all those hard-working but also very nice days, I wish you all have successful engineer career. For slurry transport research, I worked together with Ting Xiong, we wrote papers together, discussing all the reviewers' comments together, I cherish those days and I also look forward to more cooperation with you in the future. Thank you Rick, Xiuqi, Jan, Tom, Maarten and Ting for all the help!

I would like to thank the Dutch research foundation STW (now part of NWO), Seatools B.V. and Tree-C Technology B.V. for all the sponsorships and effort into this project. Many thanks to Jan Frumau, Gerard Weder and Sandy Kalisingh for every time coming all the way to Delft for the meeting and giving very valuable advices. Besides, to the colleagues I co-worked with in the H-Haptics project, Roel Kuiper, David Abbink, Frans van der Helm and Tricia Gibo, the experience of working with you has opened a new door to me, you helped me to gain the knowledge about the haptics control system and to understand the human-machine interaction. Thank you!

To the colleagues we work or worked together, Bas, Ershad, Edwin, Geert, Arno, Rik, Rudy, Joep, Antonio, Thijs, Ralph, Jort, Stefano, Mohamed, Frans, Dave, Jian, Lynyrd, Henk. It has been so much fun working with you. We discuss our research together, we have coffee together, we make smart or silly jokes together, we drink tons of beer and some non-alcoholic beverages together. Geert, I learnt a lot about CFD from you and you helped me to understand the fluid behaviour in my problem, thanks a lot. Rudy, it is really beneficial for me to discuss with you about the whole research, because you understand all the details of the problem and you always give me very good advice, thank you very much. Bas, your photography skill is so good that I do believe you can develop a second job on that. Arno, it is surprisingly fun to find that you also know those out-of-box stories from Erich von Daniken. Thijs, remember the day you shaved off all your messy beard and moustache? That's the day you look like a decent gentleman. Dave, can AJAX win another European Champion before I have my grandchild? Edwin, we should not drink those free soda's because later I learnt that those were bought and reserved for the students union.

I would also give my appreciations to the kind friends from CEDA, Polite Laboyrie, Johan Pennekamp, Anna Csiti and Daan Rijks. I cannot remember how many times I asked for help from you when I was organising the symposiums and visits, you always hold a great patience on me and help me to as much as you can. Thank you so much!

To Xianguo Qian and Qingbo Zhang, I would express my appreciation for all the help and guidance I received from you, thank you very much gentlemen.

To my friends from the Master study, Santosh Kumar, Rafael Corona Tapia, Arnaud Verschelde, Stef Lommen, so many precious memories when we were studying and having fun together. Thanks for all the good times and I miss you a lot. To Dingena Schott, thank you Dingena for showing me into the DEM lab, and for all the help and guidance you gave me during my master thesis study.

To Yanrong Yu, Natalia Ermolaeva and Huijun Ren, thanks for all the help during my Allseas time. That is a precious memory.

To my friends in Delft, Qinghua Ye, Taoping Wan, Kun Yan, Shanshan Li, Hong Li, Wen Wang, Sien Liu, Sida Liu, Yuhan Rui, Wei Shi, Zheng Xu, Hui Chen, Zhi Yang, Chunqing Wang, Ao Chu, Shengyang Li, Liqing Zuo, Lu Zhang, Tao Zou, Xiaobo Zhang, Jun Ye, Pengpeng Xu, Jialun Liu, Jian Tan, Xu Chen, Zhe Du, Yapeng Li, Kai Wang, Yutian Yao, Hua Zhong, Qiang Xu, Xiaocheng Liu, Zhuo Xu, thanks for all the weekends, the diners, the trips, you have made my life colourful. Sometimes I just cannot believe you still see me as a friend since I eat so much but can hardly cook. Nevertheless I sincerely wish our friendship goes on and on.

To Xuan Zhu, my dear sister, you are always there with me, ups and downs. Because of you and Popo, I feel like I have families in The Netherlands. Give me a chance to say thank you and I will always love you. And Popo, you will become a dredging engineer.

To Yifan, you are the sunshine of my life.

Mom, Dad, I made it.

Curriculum Vitæ

Xiuhan CHEN

09-07-1985 Born in Jurong, China.

Education

2001–2004	High School Jurong High School of Jiangsu Province, China
2004–2008	BSc. Harbour, Waterway and Coastal Engineering Hohai University, Nanjing, China
2008–2009	MSc. Harbour, Coastal and Offshore Engineering Hohai University, Nanjing, China
2009–2011	MSc. Offshore and Dredging Engineering Delft University of Technology, The Netherlands
2012–2019	PhD. Dredging Engineering
Thesis:	Numerical Modelling for Underwater Excavation Process - A Method based on DEM and FVM
Promotor:	Prof. dr. ir. C. van Rhee and Dr. ir. S.A. Miedema

Work Experience

2008	Assistant Dredging Engineer Transport Planning and Design Institute of Jiangsu Province, China
2010–2011	Assistant Research Engineer Allseas Engineering B.V., Delft, The Netherlands
2019–	PostDoc Researcher Offshore and Dredging Engineering, Delft University of Technology